

Advances in Quantitative CEST MRI at 3T and 9.4T

Dissertation

der Mathematisch-Naturwissenschaftlichen Fakultät

der Eberhard Karls Universität Tübingen

zur Erlangung des Grades eines

Doktors der Naturwissenschaften

(Dr. rer. nat.)

vorgelegt von
Sebastian Müller
aus
Heidelberg

Tübingen
2022

Gedruckt mit Genehmigung der Mathematisch-Naturwissenschaftlichen Fakultät der
Eberhard Karls Universität Tübingen.

Tag der mündlichen Qualifikation:

27.06.2022

Dekan:

Prof. Dr. Thilo Stehle

1. Berichterstatter:

Prof. Dr. Klaus Scheffler

2. Berichterstatter:

Prof. Dr. Dr. Fritz Schick

Abstract

Magnetic Resonance Imaging (MRI) is a powerful modality that offers noninvasive imaging of biological tissue without any harmful radiation, but is based on the spin properties of hydrogen and other nuclei. Besides providing pure anatomical information, different techniques have been developed that make MRI a versatile tool for imaging tissue properties such as flow, diffusion or relaxation times. As nuclei experience different shielding of the external magnetic field dependent on their molecular environment, it is possible to derive spectroscopic information with Magnetic Resonance (MR) as well. The appearance of the spectra depends on factors such as spin-spin coupling, thus information about molecular structure can also be inferred. This information is of great interest especially when it comes to alterations of metabolism. Still, as all nuclei other than hydrogen have a relatively low gyromagnetic ratio and hydrogen in molecules other than water has low abundance in the human body, spectroscopic modalities require reduced spatiotemporal resolution to compensate for the low intrinsic Signal to Noise Ratio (SNR). A relatively new technique to retrieve metabolic information indirectly is Chemical Exchange Saturation Transfer (CEST) MRI. With specific Radio Frequency (RF) preparation, hydrogen protons that are not part of the bulk water pool are selectively labeled depending on their resonance frequency shift relative to bulk water. The labeled protons will subsequently exchange with protons in the bulk water pool and accumulate there. As the preparation might be executed over a longer time course, the magnetization of the bulk water can be continuously altered. The resulting signal changes in the bulk water pool are orders of magnitude larger than the direct signal from off-resonant protons. While CEST is advantageous compared to spectroscopic imaging in terms of SNR, it cannot provide the same spectral resolution. Moreover it is significantly slower than pure anatomic imaging due to repeated image acquisitions. Fast imaging is therefore crucial for applications of CEST MRI. Additionally, the lower spectral resolution of CEST causes entangled signal origins that require sophisticated data evaluation and design of the RF preparation schedules. While CEST MRI has high sensitivity, its specificity is low and false conclusions regarding the signal origin hamper the application as a diagnostic tool.

In the first step of this PhD project the signal origin in model solutions that mimic in vivo conditions is investigated in more detail. Experiments reveal that CEST MRI not only at spectrometers but even at whole body MR scanners is more sensitive than commonly assumed. Also, a novel background signal origin in model solutions is confirmed, which may help to avoid false interpretations during the transition from model solutions to in vivo applications. In the second project, the feasibility of a fast imaging method for CEST MRI at 3 T is investigated. The optimized MR sequence provides decent spatiotemporal resolution with high reproducibility for CEST MRI at clinical field strength of 3 T. To facilitate the reproducibility of CEST MRI across different sites and

MR scanners, in the third project, an open source sequence definition standard is proposed and implemented for both human and pre-clinical scanners. In the final project, the entire acquisition and reconstruction of MRI data is formulated as a model-free, supervised learning problem. This top-down approach autonomously optimizes both data acquisition and evaluation on a real MR scanner. Exemplary mapping of creatine concentration via CEST is learned without any analytical model. The proposed method also enables investigating whether MRI can be exploited as a tool for mapping arbitrary contrasts.

In the following sections, the main projects during the course of this PhD are briefly summarized.

Zusammenfassung

Magnetresonanztomographie ist ein leistungsfähiges Verfahren, das die nicht-invasive Darstellung von biologischem Gewebe ohne schädliche Strahlung, sondern basierend auf den Spineigenschaften von Wasserstoff und anderen Atomkernen ermöglicht. Neben dem Zugang zu rein anatomischer Information wurden unterschiedliche Methoden entwickelt, die MRT zu einem vielseitigen Instrument für die Darstellung von Gewebeeigenschaften wie etwa Fluss, Diffusion und Relaxationszeiten machen. Da Atomkerne abhängig von ihrer molekularen Umgebung eine unterschiedliche Abschirmung des externen Magnetfeldes erfahren, ist es zudem möglich, spektroskopische Information durch Magnetresonanz zu gewinnen. Das Erscheinungsbild der Spektren hängt von Faktoren wie der Spin-Spin Kopplung ab, weshalb auch Information über die Molekülstruktur abgeleitet werden kann. Diese Informationen sind vor allem dann von großem Interesse, wenn es um Veränderungen des Stoffwechsels geht. Da jedoch alle anderen Kerne als der von Wasserstoff ein vergleichsweise niedriges gyromagnetisches Verhältnis besitzen, und Wasserstoff außer in Wassermolekülen im menschlichen Körper selten vorkommt, erfordern spektroskopische Methoden eine Reduktion der räumlichen und zeitlichen Auflösung, um das intrinsisch niedrigere Signal-Rausch-Verhältnis (SNR) auszugleichen. Eine vergleichsweise neue Methode, um indirekt Informationen über den Stoffwechsel zu gewinnen, ist die Chemical Exchange Saturation Transfer (CEST) MRT. Durch spezielle Hochfrequenz-Präparation werden Wasserstoffprotonen, die nicht Teil des sogenannten freien Wassers sind, abhängig von der Verschiebung ihrer Resonanzfrequenz gegenüber der des freien Wassers selektiv markiert. Die so markierten Protonen tauschen anschließend mit Protonen des freien Wassers aus und reichern sich dort an. Da die Präparation über einen längeren Zeitraum hinweg ausgeführt werden kann, kann die Magnetisierung des freien Wassers kontinuierlich verändert werden. Die sich daraus ergebende Veränderung des Signals des freien Wassers ist um Größenordnungen größer als das direkt an den nicht-resonanten Protonen gemessene Signal. Während CEST MRT in Bezug auf das SNR im Vergleich zu spektroskopischer Bildgebung vorteilhaft ist, kann nicht dieselbe spektrale Auflösung erreicht werden. Außerdem ist CEST, aufgrund sich wiederholender Datenaufnahmen, signifikant langsamer als rein anatomische Bildgebung. Eine schnelle Bildgebung ist daher für die Anwendung von CEST MRT entscheidend. Zudem führt die geringere spektrale Auflösung von CEST zu einer Vermischung von Signalursprüngen, was wiederum eine anspruchsvolle Datenauswertung und Gestaltung der Hochfrequenz-Präparationen erfordert. Während die CEST MRT eine hohe Sensitivität besitzt, ist die Spezifität gering und falsche Rückschlüsse hinsichtlich des Signalursprungs erschweren die Anwendung als diagnostisches Hilfsmittel.

Im ersten Schritt des Promotionsprojekts wird der Signalursprung in Modellösungen, die in vivo Bedingungen nachahmen, genauer untersucht. Experimente zeigen, dass die

CEST-MRT nicht nur an Spektrometern, sondern sogar an Ganzkörper-MR-Scannern sensitiver ist, als gemeinhin angenommen. Außerdem wird ein neuartiger Ursprung des Hintergrundsignals in Modellösungen bestätigt, was helfen kann, Fehlinterpretationen während des Übergangs von Modellösungen hin zu in vivo Anwendungen zu vermeiden. Im zweiten Projekt wird die Umsetzbarkeit eines schnellen Bildgebungsverfahrens für CEST MRT bei 3T untersucht. Die optimierte MR-Sequenz bietet sowohl eine gute räumliche als auch zeitliche Auflösung mit hoher Reproduzierbarkeit für CEST MRT bei einer klinischen Feldstärke von 3T. Um die Reproduzierbarkeit von CEST MRT über verschiedene Standorte und MR-Scanner hinweg zu erleichtern, wird im dritten Projekt ein open-source Standard zur Definition von Sequenzen sowohl an Human als auch präklinischen Scannern vorgestellt und implementiert. Im letzten Projekt werden die gesamte Datenakquisition und -rekonstruktion als ein modellfreies, überwachtes Lernproblem formuliert. Dieser Top-down-Ansatz optimiert autonom sowohl die Datenakquisition als auch die Datenauswertung an einem echten MR-Scanner. Exemplarisch wird die Abbildung von Kreatinkonzentration mit CEST ohne irgendein analytisches Modell gelernt. Die vorgeschlagene Methode ermöglicht es außerdem zu untersuchen, ob die MRT als Werkzeug genutzt werden kann, um beliebige Kontraste abzubilden. In den folgenden Kapiteln werden die wesentlichen Projekte im Rahmen dieser Doktorarbeit kurz zusammengefasst.

Contents

	Page
1. Summarized Publications	1
2. Introduction	3
2.1. Spin	3
2.2. MR Image Formation	5
2.3. Chemical Exchange Saturation Transfer	10
3. Research Objectives	15
4. Publication Summaries	17
4.1. Publication 1	17
4.2. Publication 2	23
4.3. Publication 3	29
4.4. Publication 4	37
5. Conclusion and Outlook	45
A. Publication List	53
B. Appended Publications	55
B.1. Publication 1	56
B.2. Publication 2	70
B.3. Publication 3	86
B.4. Publication 4	102
References	113
Acknowledgments	123

Acronyms and Constants

ADC	Analog Digital Converter	MSE	Mean Squared Error
APT	Amide Proton Transfer	MTR _{asym}	Magnetization Transfer Ratio Asymmetry
B_0	Static Magnetic Field Strength	NOE	Nuclear Overhauser Effect
B_1	Magnetic Component of Transmit Fields	PCA	Principal Component Analysis
CEST	Chemical Exchange Saturation Transfer	PE	Phase Encoding
CAIPIRINHA	Controlled Aliasing in Parallel Imaging Results in Higher Acceleration	ppm	Parts Per Million
c.o.v.	Coefficient Of Variation	RF	Radio Frequency
EPI	Echo Planar Imaging	RMSE	Root Mean Squared Error
FA	Flip Angle	rNOE	exchange-relayed NOE
fMRI	functional Magnetic Resonance Imaging	RO	Readout
GM	Gray Matter	ROI	Region Of Interest
GRAPPA	Generalized Autocalibrating Partially Parallel Acquisitions	SD	Standard Deviation
GRE	Gradient Echo	SAR	Specific Absorption Rate
ω_L	Larmor Frequency	SE	Spin Echo
MR	Magnetic Resonance	SENSE	Sensitivity Encoding
MRI	Magnetic Resonance Imaging	SNR	Signal to Noise Ratio
MRS	Magnetic Resonance Spectroscopy	ssMT	semi-solid Magnetization Transfer
MRSI	Magnetic Resonance Spectroscopic Imaging	tSNR	temporal Signal to Noise Ratio
		T_1	Longitudinal Relaxation Constant
		T_2	Transversal Relaxation Constant
		UHF	Ultra-high Field
		WM	White Matter

Constants

$$N_A = 6.02214076 \cdot 10^{23} \quad \frac{1}{\text{mol}} \quad (\text{Avogadro Constant})$$

$$\gamma/2\pi \approx 42.577478518\dots \quad \frac{\text{MHz}}{\text{T}} \quad (\text{Proton Gyromagnetic Ratio})$$

$$\hbar \approx 1.054571817\dots 10^{-34} \quad \text{Js} \quad (\text{Reduced Planck Constant})$$

1. Summarized Publications

This dissertation is based on the following four publications, which can be found in Appendix B. A more detailed summary is given in this manuscript as well for all four publications in sections 4.1 to 4.4.

Publication 1

Mueller S, Scheffler K, Zaiss M. *On the interference from agar in chemical exchange saturation transfer MRI parameter optimization in model solutions*. NMR in Biomedicine, 2020;34(1):1–12. <https://doi.org/10.1002/nbm.4403>

Publication 2

Mueller S, Stirnberg R, Akbey S, et al. *Whole brain snapshot CEST at 3T using 3D-EPI: Aiming for speed, volume, and homogeneity*. Magnetic Resonance in Medicine 2020;00:1–15. <https://doi.org/10.1002/mrm.28298>

Publication 3

Herz K, Mueller S, Perlman O, et al. *Pulseq-CEST: Towards multi-site multi-vendor compatibility and reproducibility of CEST experiments using an open-source sequence standard*. Magnetic Resonance in Medicine 2021;00:1–14. <https://doi.org/10.1002/mrm.28825>

Publication 4

Glang F, Mueller S, Herz K, Loktyushin A, Scheffler K, and Zaiss M *MR-double-zero – proof-of-concept for a framework to autonomously discover MRI contrasts*. Journal of Magnetic Resonance 2022;(341) <https://doi.org/10.1016/j.jmr.2022.107237>

2. Introduction

In this chapter, a short introduction to the basic physics of MRI is given. It is not a general introduction but will mainly focus on the mechanisms that are necessary to explain the phenomena of CEST in the context of MRI. Comprehensive explanations of MR physics can for instance be found in [1], original descriptions of the CEST phenomenon are given in [2, 3] and reviews that focus on CEST MRI are for instance provided in [4, 5].

2.1. Spin

Spin is a property that can be assigned to all particles of the standard model. Atoms consist of an electron cloud and a nucleus that consists of protons (uud¹) and neutrons (udd) and therefore, for all atoms, a resulting spin S can be assigned. In an external magnetic field (Static Magnetic Field Strength (B_0)²), different spin quantum states result in shifted, discrete energy levels, known as *Zeeman effect*. For MRI, the Zeeman effect due to the spin \mathbf{I} of the atomic nucleus is important. The nuclear spin gives rise to the magnetic moment

$$\boldsymbol{\mu} = \gamma \mathbf{I} \quad (2.1)$$

for which the Hamiltonian $\mathbf{H} = \boldsymbol{\mu} \vec{B}_0$ can be used to determine the potential energy in the magnetic field as

$$E_{mag} = \gamma m_I \hbar B_0 \quad (2.2)$$

if it is assumed that $\vec{B}_0 = B_0 \cdot \vec{e}_z$ and considered that the projection of \mathbf{I} onto \vec{e}_z has to be quantized with $m_I = -I, -I + 1, \dots, I - 1, I$. Here, m_I is the magnetic quantum number.

For spin-1/2 particles such as protons, the energy difference of the two possible spin states *up* and *down* according to equation 2.2 is

$$\Delta E = \gamma \hbar B_0 = \hbar \omega_L \quad (2.3)$$

and the Larmor Frequency (ω_L)

$$\omega_L = \gamma B_0 \quad (2.4)$$

can be assigned. Even though the frequency ω_L associated with transitions between two quantum states in equation 2.3 equals the Larmor frequency, it should be noted that for

¹Characters *u* and *d* refer to up and down quarks.

²In this manuscript, the terms *magnetic field strength* and *magnetic field* actually refer to the magnetic flux density and not to the H-field.

2. Introduction

Larmor precession around \vec{e}_z the potential energy remains constant.

The electron cloud of the atom shields the nucleus against the external magnetic field. Because of this, the Larmor frequency differs when considering the same nucleus in environments of different electron densities. In molecules, which consist of multiple atoms, the same nuclei may experience different shielding at different locations within the same molecule. This is known as chemical shielding and forms the basis for CEST effects, for which *pools*³ of proton spins with same Larmor frequency are defined. Given an arbitrarily chosen pool with Larmor frequency $\omega_{L,a}$, one can define a chemical shift of another pool as

$$\delta = \frac{\omega_{L,a} - \omega_{L,b}}{\omega_{L,a}} . \quad (2.5)$$

The chemical shift is usually given in Parts Per Million (ppm).

In the above description a quantum mechanical property was described. This is not a suitable description when it comes to MR experiments of complex systems such as the human body. Instead, the expectation value $\langle \cdot \rangle$ of $\boldsymbol{\mu}$ (equation 2.1) is of interest and its temporal evolution can be described by application of the *Ehrenfest Theorem*. For the Hamiltonian $\mathbf{H} = -\boldsymbol{\mu}\vec{B}$ and spin operator \mathbf{I} it writes

$$\frac{d\langle \boldsymbol{\mu} \rangle}{dt} \stackrel{*}{=} \left\langle \left[-\gamma \mathbf{I} \vec{B}, \mathbf{I} \right] \right\rangle \stackrel{+}{=} \gamma \langle \mathbf{I} \times \vec{B} \rangle \stackrel{++}{=} \langle \boldsymbol{\mu} \rangle \times \vec{B} . \quad (2.6)$$

In the above equation the first equality (*) holds because of the Ehrenfest theorem⁴ when assuming $\partial \mathbf{I} / \partial t = 0$. The second equality (+) holds because of the general commutator relation $[\mathbf{I}_i, \mathbf{I}_j] = i\hbar \epsilon_{ijk} \mathbf{I}_k$ for any angular momentum \mathbf{I} . In the last step (++) , it was assumed that $\langle A + B \rangle = \langle A \rangle + \langle B \rangle$ and for a constant c it holds $\langle cA \rangle = c\langle A \rangle$. It can be seen from equation 2.6, that the expectation value of the magnetic moment $\langle \boldsymbol{\mu} \rangle$, caused by a spin, may be treated like a classical magnetic dipole. Therefore, in the following the expectation value of the magnetic moment of the spin is considered to be a classical magnetic dipole moment $\vec{\mu}$.

2.1.1. Macroscopic Magnetization and Relaxation

In equation 2.6 the magnetic moment of a single spin was considered. For all MRI applications, pools including a large number of spins are of interest. For these the so called *macroscopic magnetization* \vec{M} may be defined. It includes a total of N spins within a certain volume V , such that

$$\vec{M} = \frac{1}{V} \sum_{n=1}^N \vec{\mu}_n . \quad (2.7)$$

³Pools are defined as a group of nuclei of one type that have same spin properties. The nuclei do not necessarily have to belong to the same molecule. In this view, nuclei of the same pool are indiscernible.

⁴More generally, for any quantum mechanic operator \mathbf{A} and Hamiltonian \mathbf{H} it can be stated: $\frac{d\langle \mathbf{A} \rangle}{dt} = \frac{1}{i\hbar} \langle [\mathbf{A}, \mathbf{H}] \rangle + \langle \frac{\partial \mathbf{A}}{\partial t} \rangle$.

Only with slightly higher probability some of the $N = N^+ + N^-$ spins in volume V align parallel (N^+) but not antiparallel (N^-) with \vec{B}_0 . At room temperature T most of the spins have random orientation relative to \vec{B}_0 . The small difference of N^+ and N^- gives rise to the observed net magnetization, which can be shown (chapter 6.1 in [1]) to be

$$M_0 \propto \frac{N}{V} \cdot \frac{\gamma^2 \hbar^2}{4k_B T} B_0 \quad (2.8)$$

It increases for higher B_0 ⁵, which is why high and Ultra-high Field (UHF) ⁶ are beneficial in terms of SNR for MRI. If during an MR experiment the macroscopic magnetization is driven to *saturation*, this means the numbers N^- and N^+ become equal, thus resulting in $|\vec{M}| = 0$.

Combining equations 2.6 and 2.7 already yields a formulation for the temporal evolution of the macroscopic magnetization \vec{M} . Still, in a real-world experiment interaction between spins and of spins with their surrounding environment need to be taken into account. The interaction results in relaxation, first described by F. Bloch with the so-called phenomenological *Bloch Equations* [6]

$$\frac{d\vec{M}}{dt} = \gamma \vec{M} \times \vec{B} + \frac{1}{T_1} (M_0 - M_z) \vec{e}_z - \frac{M_x}{T_2} \vec{e}_x - \frac{M_y}{T_2} \vec{e}_y . \quad (2.9)$$

The Longitudinal Relaxation Constant (T_1) and Transversal Relaxation Constant (T_2) are also the governing parameters for the appearance of CEST Z-spectra introduced in section 2.3: T_2 as it includes both, dephasing of the transversal magnetization due to local inhomogeneity in B_0 as well as spin-spin interactions, and T_1 , as for CEST the prepared state of magnetization is investigated.

2.2. MR Image Formation

2.2.1. RF excitation, Gradients and k-space

The smallest temporally repeating unit of an MRI experiment typically starts with at least one (Gradient Echo (GRE)) or two (Spin Echo (SE) [7]) RF excitation pulses. Assuming the electromagnetic field is applied orthogonal (Magnetic Component of Transmit Fields (B_1) e.g. $B_{1,y} = B_{1,z} = 0$ and $B_{1,x} = B_1$) to the static magnetic field $\vec{B}_0 = B_0 \vec{e}_z$, it tips the macroscopic magnetization \vec{M} away from its equilibrium state $\vec{M}_0 = M_0 \vec{e}_z$ towards the x-y plane, as can for instance be seen from equations 2.6, 2.9. The RF pulse may either be applied as an *on-resonant* (at $\omega_{\text{RF}} = \omega_L$) or with $\omega_{\text{RF}} \neq \omega_L$ as *off-resonant* pulse. The resulting angle, around which \vec{M} is tilted against \vec{B}_0 , is re-

⁵Here $B_0 = \sqrt{\vec{B}_0 \cdot \vec{B}_0}$ and $M_0 = \sqrt{\vec{M}_0 \cdot \vec{M}_0}$ with \vec{M}_0 indicating the spin system being in thermal equilibrium.

⁶Currently, a field strength of $B_0 > 1.5$ T is considered as *high* and $B_0 \geq 7$ T as *ultra-high* field at least for in vivo MRI of the human body.

2. Introduction

ferred to as Flip Angle (FA). When \vec{M}^7 is tipped fully into the x-y plane, one observes $|\vec{M}_{||}| = 0$ and $|\vec{M}_{\perp}| = M_0$. As \vec{M} is tipped towards the x-y plane, the component \vec{M}_{\perp} may be seen as magnetic dipole that rotates with ω_L around \vec{e}_z . This causes a time-varying magnetic flux density and induces a voltage in the nearby receiver coil. This induced voltage is the detectable MR signal.

The induced MR signal of an object may be spatially resolved in MRI by the application of additional magnetic fields, so-called gradients \vec{B}^G that result in a spatially varying z-component of the magnetic field⁸

$$B_z(\vec{r}, t) = B_0 + \vec{r} \cdot \vec{G}(t) = B_0 + \vec{r} \cdot \vec{\nabla} B_z^G \text{ and } \vec{r} = (x, y, z) \quad (2.10)$$

The gradients therefore give rise to spatial and temporal changes of ω_L

$$\omega(\vec{r}, t) = \omega_L + \omega_G(\vec{r}, t) . \quad (2.11)$$

When a gradient is applied during signal acquisition, this leads to a spatial *frequency encoding* along the respective gradient's axis. Given the gradient was applied for a limited duration t , this is equivalent to a spatially varying accumulation of phase

$$\phi_G(\vec{r}, t) = - \int_0^t dt' \omega_G(\vec{r}, t') . \quad (2.12)$$

In the following, relaxation effects are neglected. Factors such as transmit and receive sensitivity or other electronic gain factors can be absorbed in an *effective spin density* ρ that may also include the relaxation effects [1]. With this abbreviation, assuming perfectly homogeneous \vec{B}_0 and after demodulation [8], the MR signal can be described as

$$s(t) \propto \int d^3r \rho(\vec{r}) e^{i\phi(\vec{r}, t)} . \quad (2.13)$$

In principle, the signal as described in equation 2.13 decays governed by T_2 , which in a real application would depend on \vec{r} and causes blurring in the image domain, especially for Echo Planar Imaging (EPI). Equations 2.11/2.12 and 2.13 can be combined when defining the vector \vec{k} such that

$$\vec{k} = \frac{\gamma}{2\pi} \int_0^t dt' \vec{G}(t') \stackrel{\pm}{=} \frac{\gamma}{2\pi} \vec{G}t . \quad (2.14)$$

⁷Often, the macroscopic magnetization \vec{M} is split into two components: $\vec{M}_{||}$ that is parallel to \vec{B}_0 , and \vec{M}_{\perp} that is perpendicular to \vec{B}_0 .

⁸It is assumed that $\vec{B}_0 = B_0 \vec{e}_z$ and that $B_0(\vec{r})$ is constant. Also $\vec{r} \cdot \vec{\nabla}$ should be read as $\vec{r} \cdot \vec{\nabla} = x \frac{\partial}{\partial x} + y \frac{\partial}{\partial y} + z \frac{\partial}{\partial z}$.

where temporally constant gradient amplitude was assumed in the second step (+). This finally yields

$$s(\vec{k}) \propto \int d^3r \rho(\vec{r}) e^{-i2\pi\vec{k}\cdot\vec{r}} \propto FT\{\rho(\vec{r})\} \quad (2.15)$$

From equation 2.15 it can be seen that the (effective) spin density that MRI tries to depict, and the acquired signal $s(\vec{k})$ are connected by a Fourier Transform (FT). The signal in MRI is therefore said to be acquired in *k-space* [9] referring to the definition of \vec{k} in equation 2.14. The signal in MRI always originates from a large number of spins within a small spatially encoded three dimensional volume rather than from a two dimensional pixel. Therefore, in MRI the smallest imaging unit is called a *voxel*. Even in a single voxel of 1 mm^3 , the number of ^1H spins is around $n \approx 111 \frac{\text{mol}}{\text{L}} \cdot 1 \text{ mL} \cdot N_A \approx 6.7 \cdot 10^{22}$. Besides their use for spatial encoding, gradients are also used for slice-selective excitation if they are applied during an RF pulse with a certain finite frequency bandwidth and off-resonance. For a pulse with sufficiently narrow bandwidth, only spins at certain spatial locations will be on-resonant and therefore get excited.

2.2.2. Sampling Trajectories and Undersampling

As the MRI signal is acquired in k-space, it is necessary to design *trajectories* in k-space that are both technically feasible and suitable for decent image reconstruction using the gradients as described in section 2.2.

From equation 2.14 it can be seen that if a gradient e.g. along x-direction is switched on during the data acquisition, one 1D projection in k-space along k_x can be acquired within the acquisition time interval t_{ADC} . This is considered one Readout (RO) or frequency encoded line of k-space. The Analog Digital Converter (ADC) may only sample with a limited temporal resolution t_{dwell} that defines the number of samples $n_{\text{RO}} = t_{\text{ADC}}/t_{\text{dwell}}$. For the Phase Encoding (PE) direction, the gradient amplitude G_{PE} is modified prior to the acquisition of the next RO line to subsequently sample all RO lines along this PE direction.

In terms of k-space sampling, *cartesian* and *non-cartesian* sampling trajectories can be distinguished. Only for cartesian sampling, the acquired signal can be reconstructed directly by uniform Fourier Transform. Still, non-cartesian spiral sampling [9, 10] allows for very fast acquisitions and radial sampling approaches [11, 12] are beneficial when it comes to motion correction. For the scope of this thesis, only cartesian sampling is of interest. In figure 2.1, very basic examples for different sampling trajectories are shown.

Recording an MR signal first of all requires an excitation RF pulse as mentioned in section 2.2.1. In case of spoiled GRE sequences, a single RO line in k-space is acquired following the RF pulse. Another possibility is to acquire multiple lines following a single excitation pulse, as for example done in EPI [13]. Instead of a single *echo*, a series of echos called *echo train* is generated and at each echo, one RO line can be acquired with the read gradient switched on for frequency encoding while the ADC records the signal. Even for 2D imaging, k-space is typically not entirely encoded following a single exci-

2. Introduction

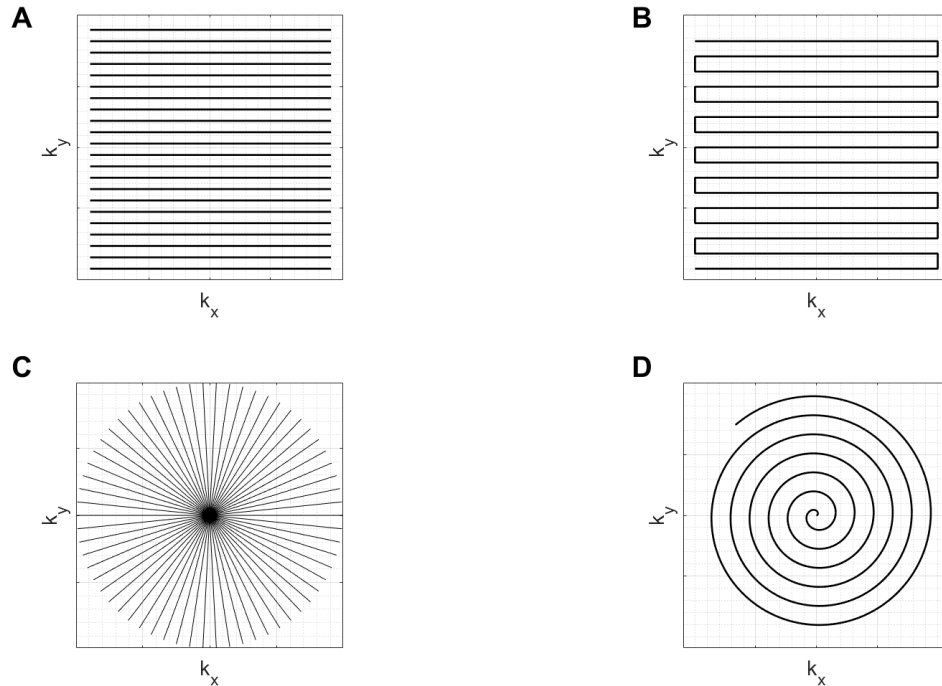


Figure 2.1.: Different 2D sampling trajectories in k-space. **(A)** shows multiple independently excited 1D lines that fill k-space as for example used in spoiled GRE sequences with RO along k_x . **(B)** shows a simple EPI trajectory with gradient *blips* along k_y . **(C)** and **(D)** are examples of non-cartesian radial and spiral trajectories. While (A) and (C) require multiple excitations, the trajectories as shown in (B) and (D) could be acquired following a single excitation. In all cases, the most simple version of the respective trajectory is shown. Undersampling was assumed in all cases to increase visibility.

tation RF pulse, but segmented using intermediate excitations for the generation of a certain number of echos. In the following, these repeated excitations are referred to as *segmentation* of k-space. The echos may be realized as either pure SE or GRE or a combination of both as first shown in [14].

For high-resolution 3D EPI, k-space cannot be fully sampled following a single excitation but needs to be split into multiple segments. Also, EPI data suffer from phase deviations between odd and even RO lines due to technical imperfections. These need to be corrected, as otherwise strong ghosting artifacts occur [15, 16].

To reduce the acquisition duration it is possible to *undersample* k-space, which means collecting less samples than required according to the Nyquist criterion, and reconstruct it making use of multi-coil receive arrays [17]. This process of making use of multiple coils is termed *parallel imaging*. Undersampling is performed along the PE directions and results in aliasing if the undersampled k-space is reconstructed from a single coil purely with Fourier Transformation as shown in figure 2.2. For instance, in figure 2.1 A/B it can be seen that actually not for all points required by the Nyquist theorem

along PE: k_y , a RO line is acquired. The two major approaches for reconstruction of such undersampled data are Sensitivity Encoding (SENSE) [18] and Generalized Autocalibrating Partially Parallel Acquisitions (GRAPPA) [19]. In terms of the location of aliasing artifacts in the image space, Controlled Aliasing in Parallel Imaging Results in Higher Acceleration (CAIPIRINHA) [20] is beneficial, which can be applied in both parallel multi-slice and 3D imaging with two PE directions k_y and k_z [21].

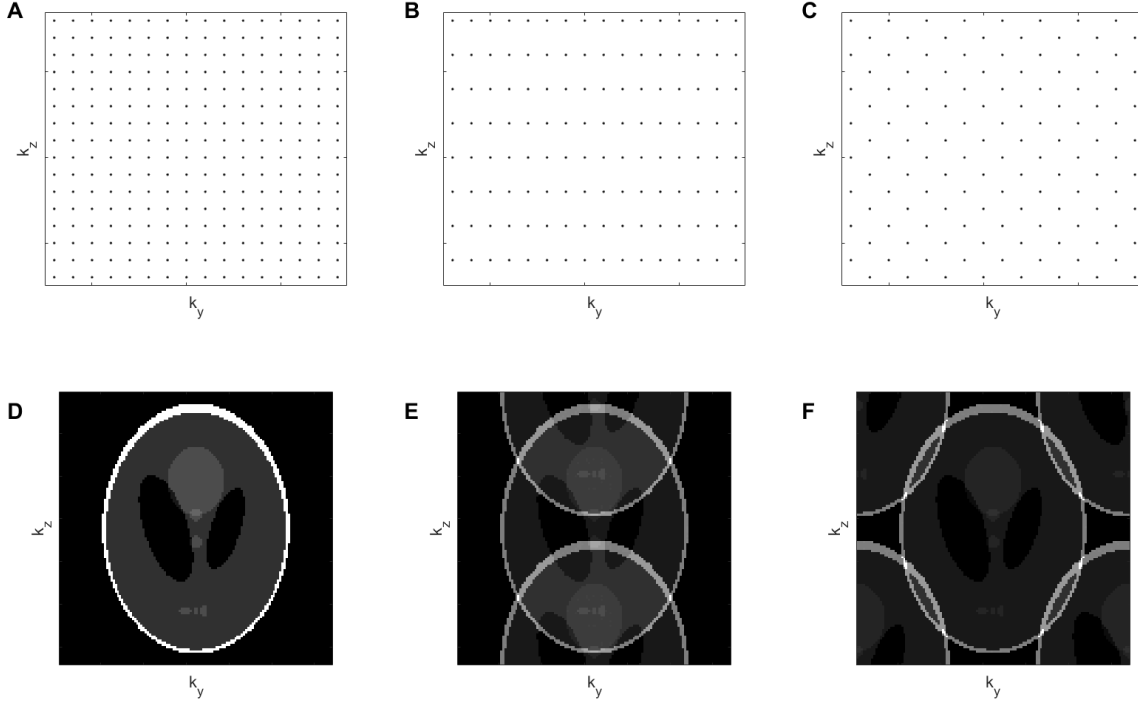


Figure 2.2.: Effect of different undersampling patterns on Fourier Transform of the respective data. In all cases twofold undersampling was applied. First column (**A,D**) shows fully sampled k -space. Second column (**B,E**) shows the effect of regular undersampling along k_z and last column (**C,F**) the effect of CAIPIRINHA with twofold undersampling and every other line shifted by one position in k -space. First row shows exemplary sampling pattern and second row the resulting image space data after application of Fourier Transformation. Aliasing occurs for both regular undersampling and CAIPIRINHA but at different locations in the image space. Simulated (MATLAB, The Mathworks, Natick, USA) data of a Shepp–Logan phantom [22] is shown.

For regular undersampling along either k_y or k_z or both directions, not all data but only subsets are sampled as shown exemplary for twofold undersampling along k_z in figure 2.2B. If Fourier Transformation was performed on this data, aliasing along the

2. Introduction

undersampled k_z direction occurs as shown in figure 2.2E. The same sampling pattern in k-space can be seen as a starting point for CAIPIRINHA. In addition to the regular undersampling pattern, every other point along k_y is shifted by one position along k_z as depicted in figure 2.2C. The resulting aliasing (figure 2.2F) occurs not only along k_z but also along k_y now, which is beneficial when it comes to actual multi-coil parallel imaging. Intuitively, one may consider that comparing the presented undersampling patterns, for CAIPIRINHA, the minimum distance to any neighboring sampled point in k-space is larger compared to the minimum distance in case of regular undersampling at the same undersampling factor. Therefore, k-space is covered more homogeneously. This will result in low correlation of the acquired data and therefore can improve the reconstruction.

2.3. Chemical Exchange Saturation Transfer

The use of Chemical Exchange Saturation Transfer (CEST) as a contrast mechanism is relatively new in the field of MRI. It relies on the chemical exchange of protons between the bulk water pool and additional smaller pools, which resonate at different Larmor frequency ω_L and by this can be investigated with MR [23]. First experiments and theoretical descriptions of systems including the exchange of spins were made by Slichter et al. [2, 3]. The exchange can be imaged spatially resolved with MRI [24], also in biological tissue [25]. The exchanging protons are bound to groups such as hydroxyl, amide, amine or guanidinium for example, which may have significantly different exchange rates (k_i) ranging from a couple of Hz to several kHz [26–32]. The kinetics of the exchange process will in general be governed by the temperature of the considered system. Same holds true for the pH value. A schematic example of exchanging pools is shown in figure 2.3. The exchange process is accessed by RF labeling of the smaller pool at $\Delta\omega \neq 0$, which due to the exchange alters the magnetization of the bulk water pool. Subsequently, the MR image is acquired on-resonant on the bulk water pool and by this making use of the larger pool size compared to the other pool. To acquire a full *Z-spectrum* [33], multiple offsets $\Delta\omega_{n=1\dots N}$ are acquired, each with RF preparation and potentially some relaxation time inbetween two consecutive offsets $M_{\text{sat},i}$ and $M_{\text{sat},i+1}$. Actually, not all CEST pools that are present in the spectrum will be equally well labeled. The labeling efficiency depends not only on T_2 of the bulk water pool but for instance also on the exchange rate of the CEST pool and the preparation B_1 [34]. The complete data typically consist of two or three spatial and one spectral dimension. In contrast to Magnetic Resonance Spectroscopy (MRS), the spectral domain is defined by the preparation offset and is therefore directly acquired and not linked to the measured time domain data via a Fourier Transform. For intensity normalization, additional data at one or multiple far off-resonant offsets (usually $\Delta\omega \geq 200$ ppm; named *unsaturated* M_0 image) are acquired in addition to the other offsets M_{sat} . The Z-spectrum is then defined as voxel-wise ratio $Z = M_{\text{sat}}/M_0$.

Mathematically, the exchange process depicted in figure 2.3 can be described by an extended version of the Bloch Equations [6], the so called Bloch-McConnell equations

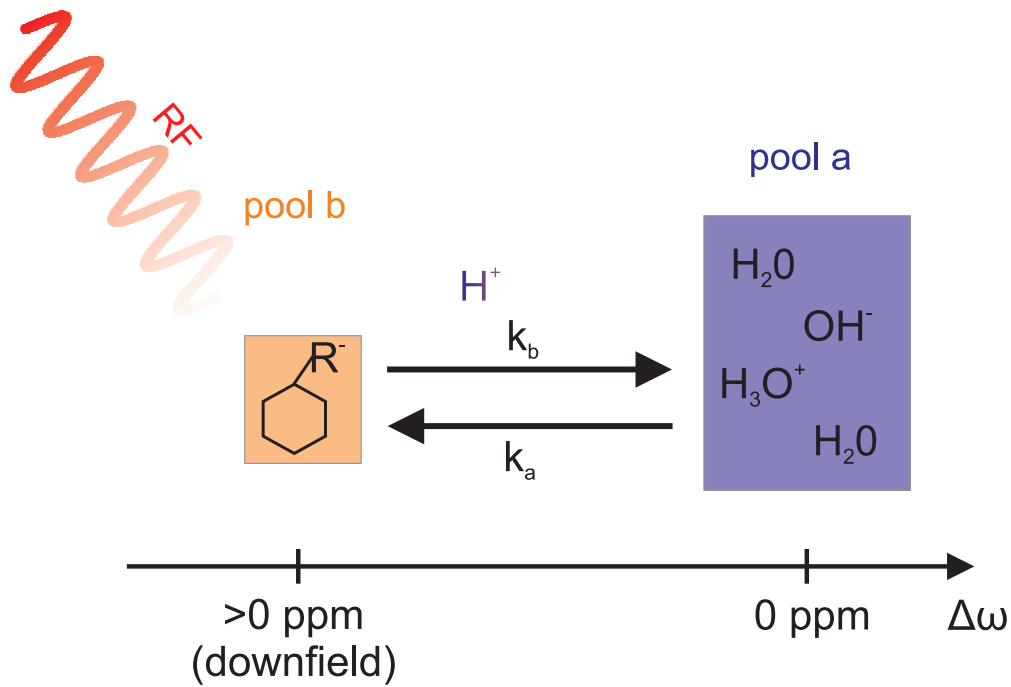


Figure 2.3.: Schematic depiction of a two pool system coupled by chemical exchange. Pool a was defined to resonate at 0 ppm while pool b is off-resonant. The exchange rate for the exemplary R group is labeled k_i ($i=a,b$).

[35]. This holds true for exchanging protons without spin-spin coupling and first order reactions as for example described in chapter 2.4 of [36]. In case of two exchanging pools a and b they may be written as:

$$\frac{d\vec{M}}{dt} = A \cdot \vec{M} + \vec{C} . \quad (2.16)$$

In equation 2.16 the magnetization is described as

$$\vec{M} = \begin{pmatrix} M_{xa} \\ M_{ya} \\ M_{za} \\ M_{xb} \\ M_{yb} \\ M_{zb} \end{pmatrix} \quad (2.17)$$

2. Introduction

in the rotating frame of reference ⁹. The longitudinal relaxation constant $T_{1i} = 1/R_{1i}$ is contained in the temporally constant vector

$$\vec{C} = \begin{pmatrix} 0 \\ 0 \\ R_{1a}M_{0a} \\ 0 \\ 0 \\ R_{1b}M_{0b} \end{pmatrix} \quad (2.18)$$

The chemical exchange and relaxation are described by the block matrix [4]

$$A = \begin{bmatrix} L_a - K_a & +K_b \\ +K_a & L_b - K_b \end{bmatrix} \text{ with } L_i = \begin{pmatrix} -R_{2i} & -\Delta\omega_i & 0 \\ +\Delta\omega_i & -R_{2i} & +\omega_1 \\ 0 & -\omega_1 & -R_{1i} \end{pmatrix} \text{ and } K_i = \mathbb{1} \cdot k_i \quad (2.19)$$

The different CEST pools are coupled via the off-diagonal exchange terms in matrix A (eq. 2.19), which are characterized by the chemical exchange rate k_i . The off-resonance $\Delta\omega_i$ is defined with respect to ω_L of pool i as $\Delta\omega_i = \omega_{RF} - \omega_{L,i}$. By definition, the bulk water pool ($\Delta\omega_a$) resonates at $\delta = 0$ ppm, thus, for other pools one may write (see definition of δ in eq. 2.5) $\Delta\omega_b = \omega_{RF} - \omega_{L,b} = \Delta\omega_a - \delta_b\omega_{L,a}$. The RF amplitude is $B_1 = \omega_1/\gamma$ and for the definition of matrix L in eq. 2.19 it was assumed that $B_{1,y} = 0$. In case that a semi-solid Magnetization Transfer (ssMT) pool (section 2.3.2) is added, one usually considers only the M_z component in eq. 2.19 for that pool as due to extremely short T_2 values the transversal components will decay rapidly.

For data evaluation, different approaches to solve (e.g. [37, 38]) or numerically simulate this set of coupled, first order, linear differential equations are applied. Numerical simulations are time-consuming, especially in case of multiple exchanging pools. Still, they are applied when trying to fit CEST data for quantification of exchange parameters. In addition to fitting the entire Bloch-McConnell equations, other, more simple metrics exist for quantifying CEST MRI data. Probably the most famous and most discussed is Magnetization Transfer Ratio Asymmetry (MTR_{asym}) [25]. In this case, the Z-spectrum is evaluated such that

$$MTR_{\text{asym}} = \frac{M_{\text{sat}}(-\Delta\omega) - M_{\text{sat}}(+\Delta\omega)}{M_0} \quad (2.20)$$

One problem of this metric is that if, for example, not only CEST (often $\Delta\omega > 0$) but also exchange-relayed NOE (rNOE) effects (often $\Delta\omega < 0$, section 2.3.1) are present, these will be entangled and may no longer be separated in MTR_{asym} . Also, if the data were acquired with some inhomogeneity of B_0 , this will result in a Z-spectrum shifted along $\Delta\omega$. A biased MTR_{asym} analysis that may look like a CEST effect close to the bulk water resonance is the result. Besides full Bloch-McConnell on the one hand and

⁹Instead of considering the laboratory frame of reference, the evolution of the magnetization is described in a coordinate system that rotates around \vec{e}_z at the frequency of the applied RF field.

MTR_{asym} on the other hand, CEST data may be described by a sum of Lorentzian line shapes [39]. In contrast to MTR_{asym} , fitting either the full Bloch-McConnell equations or Lorentzian line shapes allows to perform inverse Z-spectrum analysis, which is beneficial when quantitatively isolating CEST effects [40]. Still, as this is not the main focus of this thesis, the reader may refer to the literature for details on the different metrics and analyses.

2.3.1. Nuclear Overhauser Effect

Besides direct transfer of magnetization between pools a and b due to chemical exchange of saturated protons, indirect transfer of magnetization because of dipolar coupling (homo-nuclear Nuclear Overhauser Effect (NOE) [41]) may be observed between the pools [42]. Two different mechanisms are distinguished: intra- and intermolecular NOE. Intermolecular NOE requires that two different molecules are located next to each other for a sufficiently long time, the so-called correlation time. Intra-molecular NOE occurs for example between different atoms within a larger molecule. The intra-molecular NOE saturation transfer subsequently may result in a saturation transfer to another pool by chemical exchange. This may be termed rNOE, as both chemical exchange and NOE are involved in the magnetization transfer¹⁰. CEST effects originating from NOE may be observed on both sides of the Z-spectrum, that is downfield ($\Delta\omega > 0$) and upfield ($\Delta\omega < 0$) as shown in [44]. A more detailed description of NOE in CEST MRI can for instance be found in [45, 46].

2.3.2. Semi-Solid Magnetization Transfer

The ssMT effect describes the magnetization transfer between free bulk water molecules and a semi-solid matrix such as cell membranes or surface proteins [47] and may be exploited as a contrast mechanism in MRI [48]. Within the semi-solid matrix, magnetization can be efficiently transferred by intra-molecular NOE as described in section 2.3.1. The transfer to the bulk water pool can occur through inter-molecular NOE, as the water molecules are temporarily bound to the semi-solid matrix providing sufficiently long correlation time for dipolar-coupling. It is also possible that magnetization is transferred by chemical exchange from the semi-solid matrix to the bulk water pool. Quantitative investigations of ssMT have first been performed in agar gels [49]. Still, it is challenging to determine if the magnetization transfer to the bulk water is predominately due to molecular binding and inter-molecular NOE [50] or because of chemical exchange as may be expected from the pH dependence of the observed effects [51]. More recent studies conclude that there might be a CEST contribution to the ssMT, but the dominant magnetization transfer to bulk water is expected to originate from intermolecular NOE that is enabled by molecular binding of water molecules to the semi-solid matrix [43, 52].

¹⁰According to [43], *exchange relayed NOE* describes the process of intra-molecular NOE following a previous chemical exchange magnetization transfer. In contrast, it is termed *NOE-relayed exchange* (rNOE) if chemical exchange saturation transfer to the bulk water follows a previous intra-molecular NOE within another molecule.

2.3.3. Basic RF Prepared Sequence

CEST effects can be accessed by extending an MRI readout sequence by an RF preparation module. While in pre-clinical imaging continuous wave RF preparation is applied, for human in vivo examinations stricter Specific Absorption Rate (SAR) limitations typically only allow a pulsed RF preparation. In this case, the RF preparation is split into several pulses of duration t_p with inter-pulse delay t_d and the duty cycle (DC) is defined as

$$\text{DC} := \frac{t_p}{t_p + t_d} \quad (2.21)$$

Several different approaches for the actual image acquisition are possible. Two main techniques can be distinguished: either the entire k-space is acquired following a single RF preparation at off-resonance $\Delta\omega_i$ or only certain segments of the k-space are acquired.

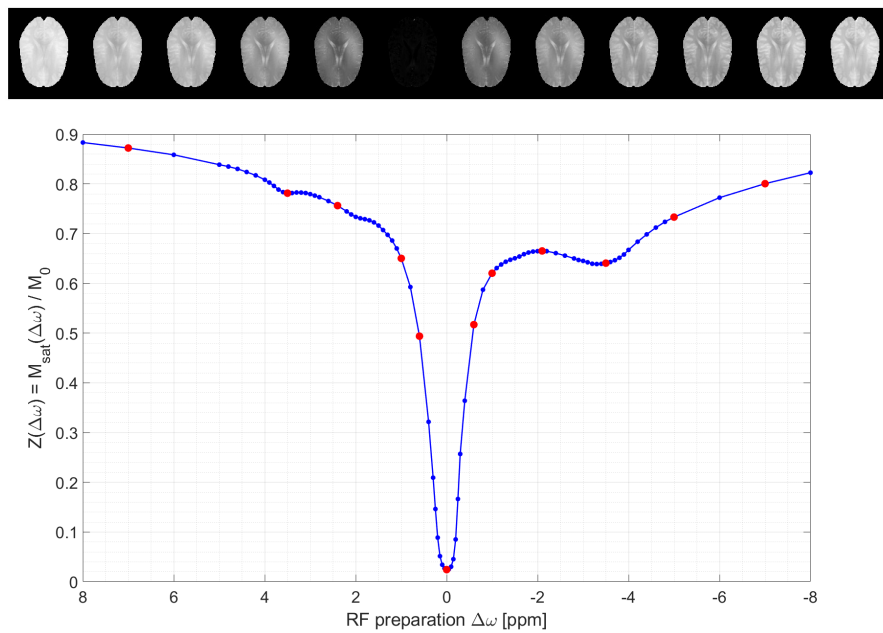


Figure 2.4.: Exemplary Z-spectrum (bottom) averaged over the voxels within a WM ROI in the human brain at $B_0=9.4$ T. Sampled RF preparation offsets are indicated by dots. For the red colored offsets, the corresponding CEST MRI images (normalized to M_{sat}/M_0) are shown above the Z-spectrum.

Typically, for each RF preparation offset the resulting k-space gets reconstructed independently. Still, in principle it is possible to perform a joint k - $\Delta\omega$ reconstruction of the data [53]. The resulting data are then normalized voxel-wise to $Z = M_{\text{sat}}/M_0$ in the image space and yield an entire Z-spectrum (see figure 2.4) for each voxel as described in section 2.3. It should be noticed that for an increased spectral resolution in CEST MRI, it is necessary to increase the number of acquired images. This automatically requires repeated RF preparation and optional recovery periods and significantly increases the acquisition duration.

3. Research Objectives

The goal of this thesis is to investigate and optimize CEST MRI at clinical field strength (3T) and UHF (9.4 T). In a first step, a closer look on the creation of well defined model solutions is taken. These model solutions are commonly used in the initial step of parameter optimization for CEST RF preparation schedules. It is shown that adding agar for setting realistic T_2 values might not be entirely unproblematic, as a bias is introduced. Investigations on the concomitant CEST effects are performed at different temperatures and field strengths to provide a detailed characterization of the bias. With these findings, it becomes possible to create precisely described model solutions that may be used as a baseline during the optimization of CEST experiments.

The second project targets the imaging of CEST effects at clinical field strength. Often CEST MRI acquisitions are infeasibly time consuming, or, at a trade-off against scan time, the data suffer from poor spatial resolution. It is shown that with optimized 3D EPI, both imaging speed and resolution requirements could be met with high reproducibility. The proposed readout is short enough to acquire the entire 3D k-space following a certain RF preparation and thus enables various different applications. This hopefully facilitates the application of CEST MRI further.

Not only are the observable CEST effects manifold especially in vivo, but also the number of adjustable parameters for a CEST examination is comparatively large. The third project therefore targets the widespread limitation of low reproducibility in CEST MRI. An open source CEST parameter definition standard was proposed, tested and agreed on within larger parts of the CEST community. Implementations for both human and pre-clinical applications are presented, which in parts make use of the findings of the first two projects.

Instead of describing the observed CEST effects numerically or analytically, the idea of model-free mapping to a target contrast is considered in the final project. It is shown that without any knowledge on the underlying mechanism, it is possible to formulate MRI as a target-driven, model-free problem that can be solved by an optimization that is based on automatized data acquisition on a real MR scanner. For proof-of-concept, it is assumed that CEST MRI was unknown. Absolute concentration of the metabolite creatine, which can be linked to the MR signal via CEST, is provided as a target and is mapped directly from MR data acquired in model solutions. Beyond this, the framework could be applied for optimizing CEST sequences, correcting for technical imperfections in MRI or maybe even to test hypotheses as to whether certain target contrasts could be accessed by MRI.

4. Publication Summaries

This thesis is written as an integrated accumulation of publications. In this chapter, the publications on which the thesis is based are briefly summarized. All figures shown here are reprinted with permission of John Wiley & Sons Ltd (Publication 1) and Wiley Periodicals LLC (Publication 2, 3), respectively. Publication 4 was submitted to the *Journal of Magnetic Resonance* (Elsevier Inc.) and permission to reprint figures was obtained, too.

The first publication describes the formation of a CEST signal in detail, while the second publication focuses on the data acquisition. The main topic of Publication 3 is the problem of missing reproducibility in CEST MRI. In Publication 4, CEST is exploited as a known effect to be discovered by and to benchmark the proposed model-free problem formulation of MRI experiments.

4.1. Publication 1

The appearance of a Z-spectrum is governed by the T_1 and T_2 values of the bulk water pool as mentioned in section 2.1.1. Typically, before applying CEST MRI in vivo, it is necessary to optimize the RF preparation in model solutions to get insights into the expected effect size. Also, in model solutions it is possible to investigate and modify the effect of external factors such as pH and temperature more easily than in vivo. To provide realistic model solutions, the adjustment of T_1 and T_2 is required before any CEST effect may be considered at all. Due to its convenient handling and availability, agar is often used to shorten T_2 in model solutions. It has also been shown that besides altering T_2 , agar introduces magnetization transfer effects [40, 49, 54]. Still, as the optimal RF preparation for an isolated CEST effect of a specific compound is of interest in the model solutions, it was previously assumed that agar does not provide any CEST contribution itself. When the presented publication was prepared, only [55] mentioned a potential interference of agar during the optimization of their CEST experiment. On the other hand Chávez and Halle [56] had already reported an exchange rate of 4 kHz at pH = 3.5 for agar before.

The goal of this study is to investigate the potential effect of agar on the optimization process of CEST RF preparation in model solutions in more detail. It is shown exemplarily for the CEST effect of L-glutamic acid that agar biases the optimization process significantly. The results of this study should hopefully provide a useful basis for interpreting the results of optimization processes for specific CEST effects in future applications.

To characterize the hypothesized CEST effect of agar, samples are created not only at

4. Publication Summaries

different concentrations of agar but also at different pH values. If there is a CEST effect this should depend on pH due to altered exchange rates at different pH levels. Additionally, the temperature of the samples is modified for different experiments to globally modify the exchange rates as discussed in section 2.1, 2.2 and 3.1 of the publication.

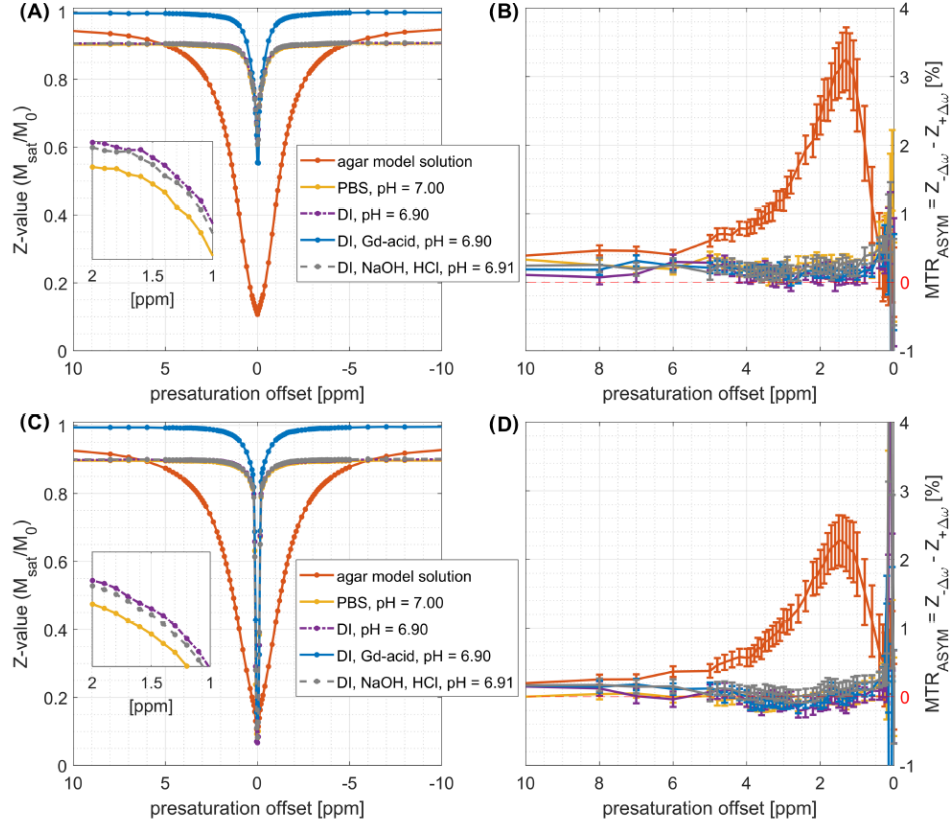


Figure 4.1.: (A), Z-spectra for different model solutions: orange – 2% (w/w) of agar, 1 X PBS, 0.1 mmol/L gadoteric acid at pH = 7.01; yellow – 1 X PBS at pH = 7.00; purple – deionized water at pH = 6.90; blue – deionized water, 0.1 mmol/L gadoteric acid at pH = 6.90; black – deionized water, hydrochloric acid, sodium hydroxide at pH = 6.91. Measured at $B_0 = 9.4$ T and $T = 25$ °C using 5×100 ms matched adiabatic spinlock pulses (see [57]) with DC = 50%, $B_1^+ = 4$ μ T. (B), the associated MTR_{ASYM} of the same samples. In (C) and (D), the same samples were measured under the same conditions upon presaturation using a train of Gaussian-shaped pulses. All data were measured with three interleaved M_0 scans and corrected both for $\Delta B_0(r, t)$ and $\Delta B_1(r)$.

Modified and reprinted with permission of John Wiley & Sons Ltd.

To ensure that indeed agar causes the hypothesized CEST effect, control samples are included as well. In figure 4.1 it can be seen that for the applied MTR_{ASYM} metric only

in the agar sample an effect is detectable. This is the first proof that with CEST MRI a significant effect due to agar can be observed. With further experiments, the CEST effect is characterized in more detail. In figures 3 and 4 of the publication, the observed effect at both different pH values and concentrations is shown for two different temperatures each. For the applied RF preparation as described in section 2.2 of the publication, MTR_{asym} values between 1 and 4% are observed.

It is demonstrated that the effect due to agar can bias the optimization of RF parameters for CEST preparation by considering a model solution that contained an additional 10 mmol/L of L-glutamic acid. The RF preparation is adjusted such that it comes close to what was reported in [29] but stays within the SAR restrictions of the 9.4 T human MR scanner. The continuous wave power equivalent therefore has to be reduced from 3.6 μT to 2.8 μT . Still, as shown in the Supporting Information of the publication, the observed effect due to agar is expected to even increase for higher preparation RF powers.

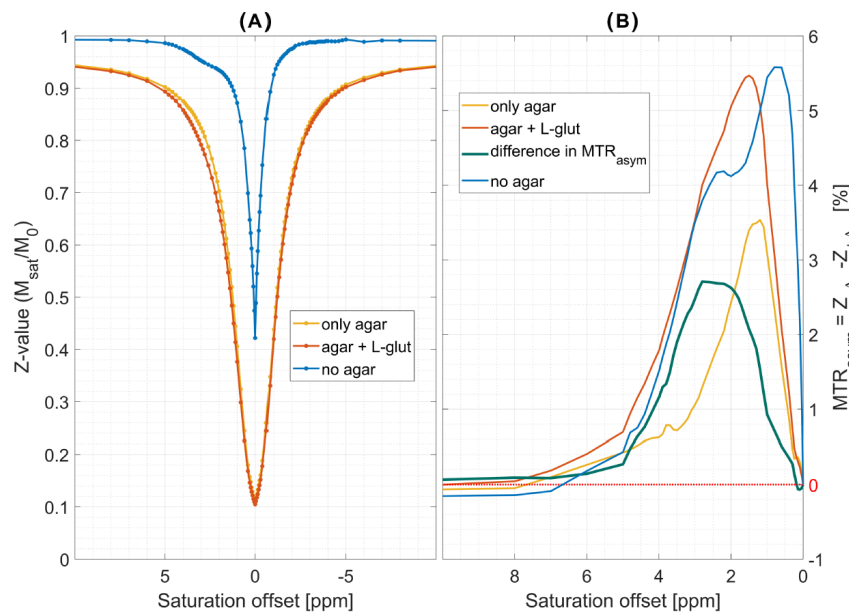


Figure 4.2.: (A), Z-spectra with (orange line) 10 mmol/L L-glutamic acid or without (yellow line). Both samples contained 2% (w/w) agar and 1 X PBS as buffer and 0.1 mmol/L gadoteric acid. pH was adjusted to pH = 7.00 in both samples. The blue line shows a sample with the same amount of L-glutamic and gadoteric acid but without agar (pH = 6.99). T_2 for this sample was (525 ± 131) ms and decreased to (60 ± 15) ms after adding agar. (B), the corresponding MTR_{asym} values of the samples and in addition the isolated MTR_{asym} of L-glutamic acid with the agar contribution removed by subtraction (green line). Presaturation: 5 x 100 ms matched adiabatic spinlock pulses (see [57]) at DC = 50%, $B_1^+ = 4 \mu\text{T}$. Measurement at 9.4 T at 25 °C with full postprocessing as described in the *Experimental* section of the publication.

Modified and reprinted with permission of John Wiley & Sons Ltd.

It can be seen in figure 4.2 that the observed effect of L-glutamic acid decreases by $\approx 50\%$ when correcting for the effect of agar. This means that if one would have transferred the applied RF preparation to in vivo, one could have falsely expected a CEST effect twice as large as it would actually be correct at the given pH and concentration of L-glutamic acid. In this case, the origin of potentially observed CEST effects in vivo could have been incorrectly assigned to L-glutamic acid, but may now be correctly interpreted considering the presented findings regarding the expected effect size.

To partly compensate for the bias due to agar, it is shown that agar might be replaced by pure agarose. It is shown in figure 6 of the publication that within the considered ranges of concentration, temperature and pH values, the CEST effect of pure agarose is significantly smaller compared to agar. The data acquired at different temperatures and pH values also allow conclusions on the exchange reaction itself. In section 3.1 of the publication it is discussed why the exchange reaction is likely to be base-catalyzed.

This information might be of interest when setting up other CEST experiments. In some cases, the data of a pH and concentration matched control sample can be used to correct the acquired data for the CEST effect of agar. This is shown in the Supporting Information of Publication 1.

The final conclusion of this project is that especially for high power RF preparation, agar can no longer be considered a neutral baseline for parameter optimization. Instead, pure agarose can be used for model solutions and control samples should be considered for quantitative data evaluation.

Statement of Contribution

- S. Mueller Study design, prepared the model solutions, performed the measurements and simulations and evaluated the data. Most of the manuscript was written by him.
- K. Scheffler Study design.
- M. Zaiss Study design, advice for both MR measurements and data evaluation. Parts of the manuscript were written by him.
- all authors Proofreading of the manuscript.

4.2. Publication 2

As mentioned in section 2.3, the acquisition of multiple MR images with different off-resonant RF preparations results in an inherently long acquisition time of CEST MRI. One approach to tackle this issue is to reduce the number of frequency offsets as for example shown in [58–60]. Still, this is a target-driven approach, which means reduction of scan time is only possible given that knowledge on a specific target contrast is provided. If the number of frequency offsets must not be reduced as the full spectral information is required or a specific target is not known, a snapshot approach [61] is appropriate. For this method, a fast MR image readout with large volume coverage is beneficial. The goal of this project is to optimize a segmented 3D EPI readout [62] for fast and reproducible CEST MRI of the whole brain at 3 T.

For the aforementioned snapshot approach, the readout needs to be fast compared to T_1 relaxation, therefore, for whole brain coverage, undersampling is required. If the readout duration is too long compared to T_1 , the RF induced magnetization preparation will decay. When a sufficiently short readout duration is not possible, steady-state CEST segmented readouts [63] might be feasible. Still, in these cases, the RF preparation is not very flexible. In contrast, with the snapshot approach, more flexible preparation, e.g. a different number of preparation pulses for different offsets is possible. This is beneficial when it comes to CEST fingerprinting [64] for instance.

In the presented work, both the optimized 3D EPI readout and a 3D spoiled GRE readout with sequence parameters as described in section 2.2 of the publication are applied. In a first step it is shown that EPI provides significantly higher temporal Signal to Noise Ratio (tSNR) than achieved by the GRE readout¹¹. With the desired matrix sizes, single shot EPI becomes infeasible. The optimized readout of 1201 k-space lines is therefore performed in a segmented fashion with 45 binomial-11 excitation pulses. At a readout bandwidth of 1930 Hz/pixel this yields a maximum echo train length of 24.3 ms.

¹¹Both readouts use gradient echos, still in the following GRE refers to the spoiled GRE readout only but not to the EPI readout.

4. Publication Summaries

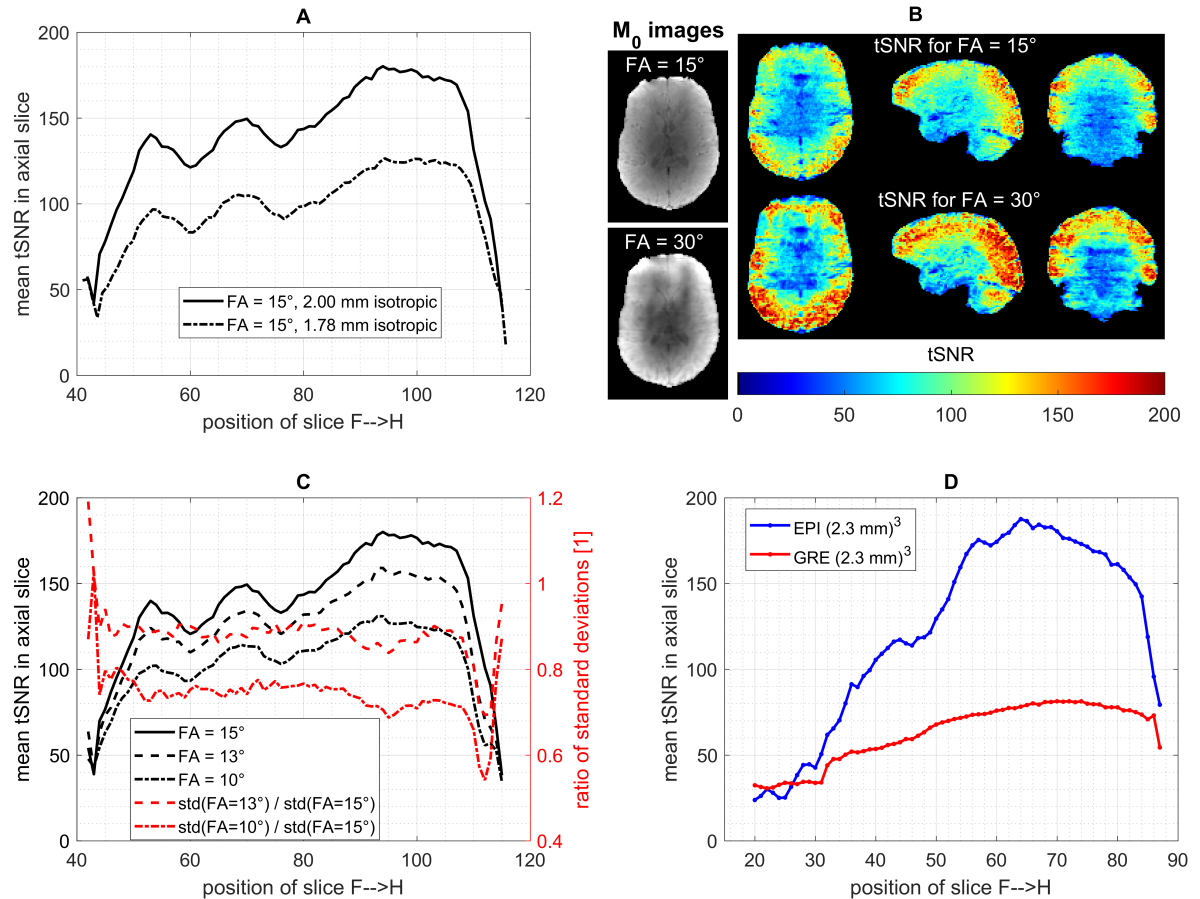


Figure 4.3.: (A) tSNR of EPI for different spatial resolutions. (B) tSNR maps of EPI for different FAs at $(1.8 \text{ mm})^3$ nominal isotropic resolution. Higher FAs provide higher average tSNR but at the cost of increased spatial heterogeneity (see also (C)), with very low tSNR in the center and lower regions of the brain. Additionally, a single image of the time series is shown for both FAs. (C) Closer look at FAs around 15 degrees with mean and SD in different axial slices. (D) Comparison to the GRE readout at $(2.34 \text{ mm})^3$. EPI at 1.8 mm isotropic resolution outperforms the 2.34 mm GRE in terms of tSNR. In the cerebellum, the tSNR is around 80. FA, flip angle; GRE, gradient echo; tSNR, temporal SNR.

Reprinted with permission of Wiley Periodicals LLC

The duration of the optimized readout is reduced by application of non-blipped CAIPIRINHA = $1 \times 6^{\text{shift}=2}$ [20]. Still, the images are not visibly biased by any undersampling artifacts as shown in figure 4.3 (B) or figure 7 in the paper. For optimizing tSNR, the matrix size, undersampling factor and FA are taken into account.

In addition to tSNR, the influence of B_1 is investigated. It is found that even at 3 T, a correction for spatial inhomogeneity of B_1 including data acquisition at three different,

nominal B_1 values is necessary as discussed in section 3.2 of the publication. To retrospectively increase the SNR before fitting, the CEST data are denoised by applying Principal Component Analysis (PCA) to the data as proposed by [65]. Besides the acquisition of CEST data, their evaluation may be of similar importance. In the presented study, fitting of multiple Lorentzian lines is performed as for instance demonstrated in [66] previously. While the volume coverage of other approaches was limited to a certain area within in the brain, the optimized readout provides whole brain coverage with homogeneous CEST contrast maps across the entire brain. Exemplary contrast maps are shown in figure 4.4.

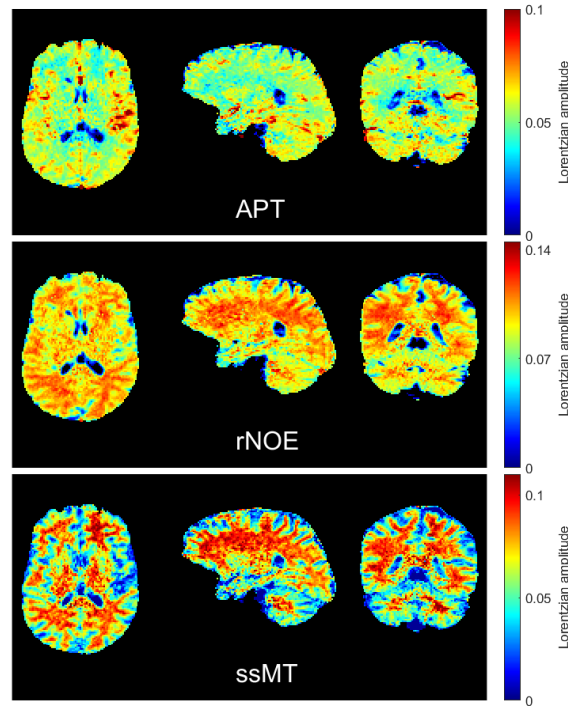


Figure 4.4.: CEST contrast (Lorentzian amplitude) of 1.8 mm isotropic EPI readout. Postprocessing included motion, ΔB_0 and ΔB_1 correction, and PCA denoising prior to B_1 correction. Maps show amplitudes derived from 4-pool Lorentzian fits: **upper** row is APT; **middle** is rNOE; and **lower** row is ssMT. Contrasts are homogeneous within a certain tissue type across the whole volume. Spatial resolution is high enough to, for example, recognize structures like caudate nucleus within the basal ganglia and at the same time distinguish GM and WM sections in the cerebellum. APT, amide proton transfer; GM, gray matter; PCA, principal component analysis; rNOE, relayed nuclear Overhauser enhancement; ssMT, semisolid magnetization transfer; WM, white matter.

Reprinted with permission of Wiley Periodicals LLC

4. Publication Summaries

Finally, the intra- and inter-subject reproducibility is considered. It is found that with the proposed data acquisition and postprocessing a significant ($P < 0.005$, Welch's t -test) contrast between GM and WM is achieved. More importantly, the largest Coefficient Of Variation (c.o.v.) is below 9% in case of two of the data sets for determining intra-subject reproducibility. For inter-subject reproducibility, the largest c.o.v. is below 4%. An overview over c.o.v. of the different CEST contrasts is shown in figure 4.5.

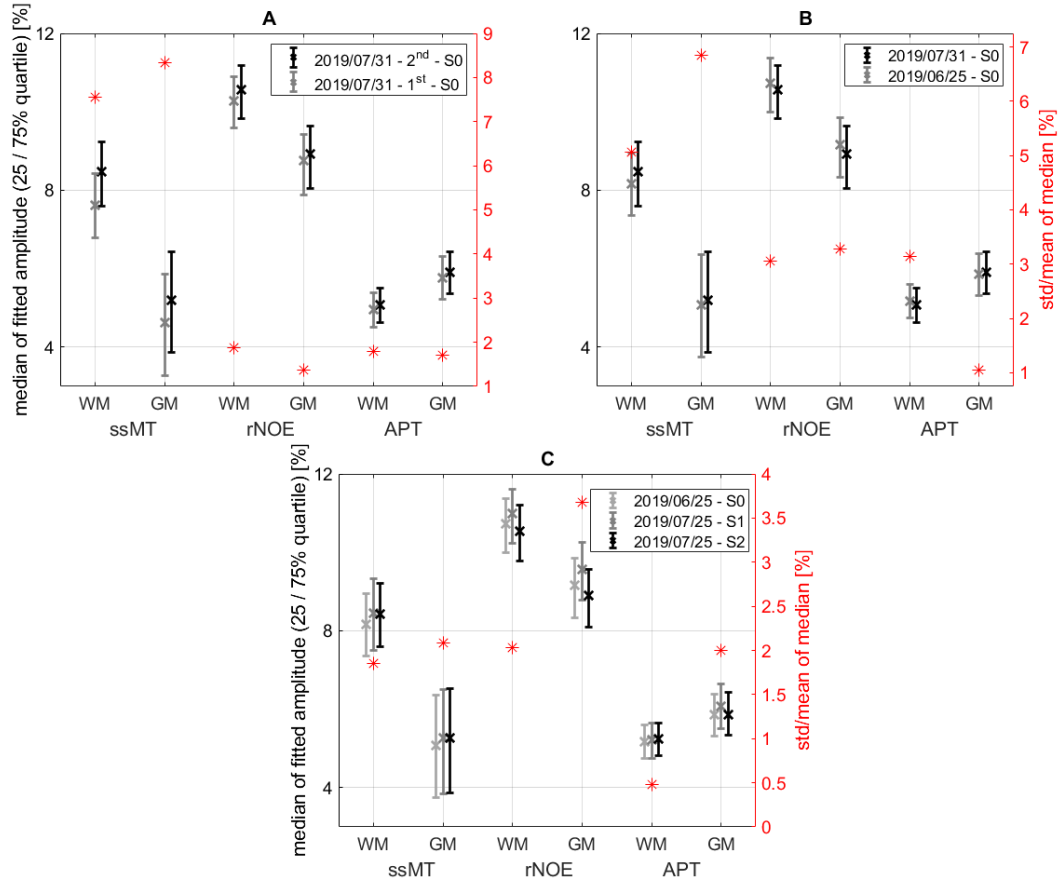


Figure 4.5.: Comparison of fitted CEST contrasts in GM and WM of healthy subjects. Within same session and volunteer (A) and across different sessions (B). Across $n = 3$ sessions and volunteers (C); variations in fitted CEST contrasts calculated as (SD/mean over tissue type) are comparable within the same volunteer and across volunteers. Fitted CEST contrasts are stable with coefficient of variation (SD/mean) less than 9%. APT, amide proton transfer; GM, gray matter; rNOE, relayed nuclear Overhauser enhancement; ssMT, semisolid magnetization transfer; WM, white matter. Reprinted with permission of Wiley Periodicals LLC

In the presented publication it is shown that the optimized 3D EPI readout allows for

fast and reproducible CEST MRI at 3 T with whole brain coverage. While in general the spectral resolution of CEST benefits from higher field strength, at lower field of 3 T, the increased T_2 values are beneficial for EPI readouts that rely on longer echo trains as for instance spoiled GRE readouts. Compared to the spoiled GRE readout, the number of excitation pulses could be reduced from 487 to 45, maintaining 6 % of the initially prepared magnetization at the end of the readout. For the spoiled GRE approach at lower resolution of $(2.34 \text{ mm})^3$, only 0.55 % are left as discussed in section 4 of the publication. Maintaining the prepared magnetization is crucial for getting CEST contrast and shows that EPI may be a suitable choice for CEST MRI at 3 T. The readout duration could be reduced to 1.2 s at a nominal isotropic resolution of $(1.8 \text{ mm})^3$. Including the applied RF preparation (described in section 1 of the publication), this allows the acquisition of one RF prepared image within 12 s, yielding a total duration of the examination at 3 different B_1 levels of around 15 min. In combination with the large volume coverage, this should hopefully bring CEST MRI closer to clinical applications.

Statement of Contribution

S. Mueller	Study design, sequence programming, performing all MR examinations, data evaluation and simulations. Wrote source code for data evaluation/simulation. Most of the manuscript was written by him.
R. Stirnberg	Study design, sequence programming and gave advice for the MR examinations as well as for the reconstruction of the MR data.
S. Akbey	Gave advice for performing MR examinations and data evaluation.
P. Ehses	Sequence programming.
K. Scheffler	Study design.
T. Stöcker	Study design.
M. Zaiss	Study design, sequence programming and performing examinations. He gave advice and assistance for data acquisition and evaluation. Wrote parts of the manuscript. Wrote source code for data evaluation/simulation.
all authors	Proofreading of the manuscript.

4.3. Publication 3

The CEST effect that can be accessed with MRI strongly depends on the applied RF preparation. As discussed in section 2.3, the labeling efficiency of a CEST-active proton pool depends both on the exchange rate and the RF amplitude. Also, the spillover dilution is affected by the applied RF power [67]. This shows that the RF preparation is one of the key features for CEST MRI and needs to be precisely defined. Unfortunately, in many cases it is not possible to reproduce preparation schemes based on the information provided by the publications themselves. One example is the phase of consecutive RF pulses in pulsed-CEST applications, which is rarely stated in any publication but has a significant effect on the acquired data as discussed below.

Why might sharing information on the parameters of CEST MRI sequences be important? Currently, there are two branches in the evolution of CEST MRI: on the one hand basic research is still going on, on the other hand studies with larger cohorts across different sites are emerging. In both cases sequence parameters need to be shared across sites and vendors. Especially in basic research a second issue may occur: often the very first optimization steps are performed in numeric simulations but at some later point the designed RF preparation module needs to be transferred to a real scanner. This is not straightforward, as either an entire new MR sequence needs to be implemented or one has to rely on the flexibility of existing implementations. As a result, discrepancies between measurements and simulation may originate from translation errors rather than actually being based on differences between real-world and simulated data.

To increase reproducibility, a common, comprehensive sequence definition standard needs to be defined. The Pulseseq project [68] offers an open-source standard for defining entire MR sequences and is proposed in the presented publication for sharing information on CEST RF preparation modules. Pulseseq files may also be used independently of the vendor on different MR scanners given a suitable interpreter sequence is installed on the scanner. With the proposed open-source Bloch-McConnell simulations it also becomes possible to directly simulate the RF preparation modules based on the Pulseseq files.

As mentioned, subtle modifications of the RF preparation module may alter the acquired data significantly. One example is shown in figure 4.6 for a pulsed CEST experiment. In one case the phase of the previously applied RF pulse ($n-1$) was taken into account when setting the phase for the n^{th} pulse, whereas in the second case the phase of each pulse was set to zero. In subplot 4.6E the effect on the resulting bulk water magnetization (Z -spectrum) can be seen.

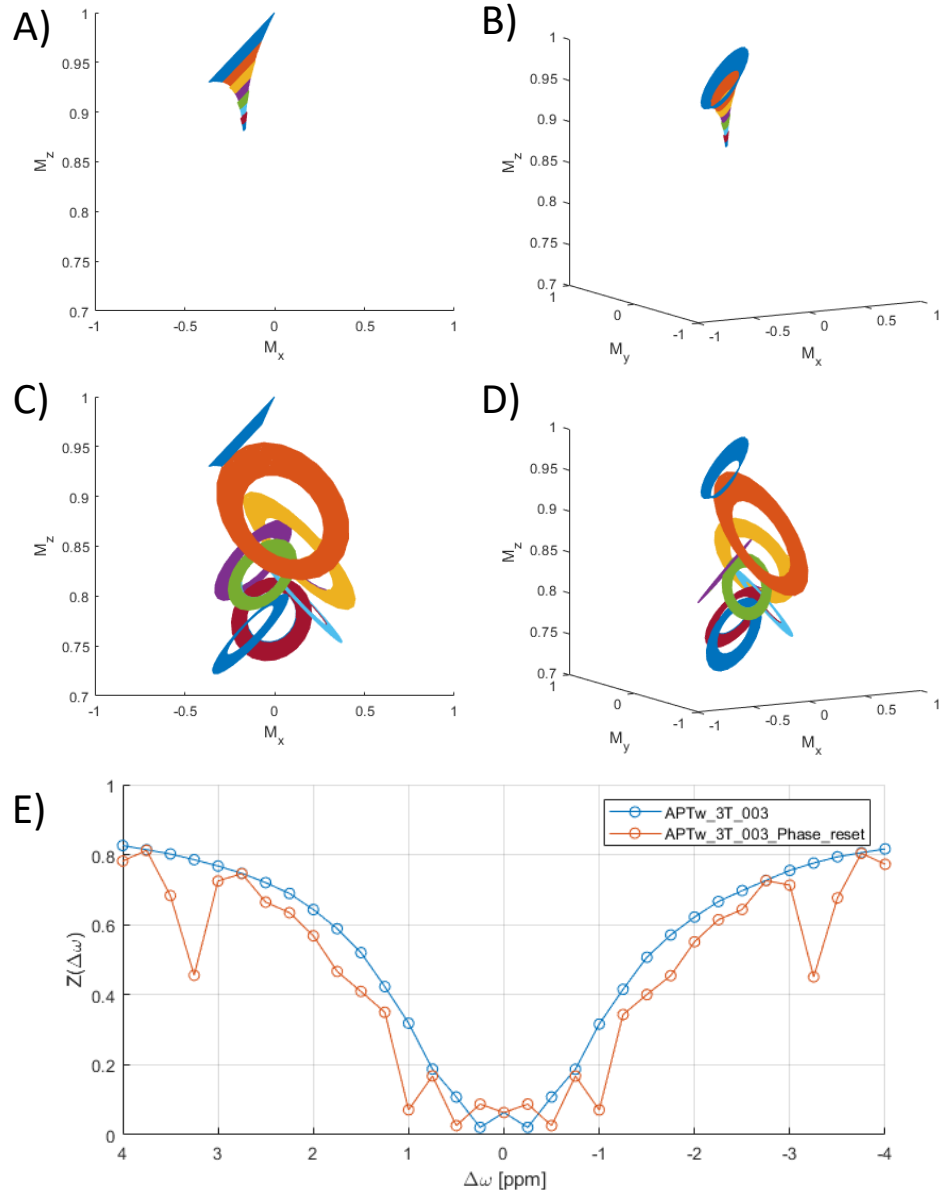


Figure 4.6.: Single magnetization vector trajectory during the CEST preparation period at 3.5 ppm with phase accumulation transfer during the saturation pulses (**A**, **B**) and without (**C**, **D**). The 8 different colors indicate the trajectory during the 8 different pulses. Due to the phase difference between magnetization vector and RF pulse in **C** and **D**, large oscillations can occur. (**E**) Z-spectra of a single magnetization vector for the sequences shown in **A**,**B** (blue) and **C**,**D** (red). Depending on the frequency offset $\Delta\omega$, the artifacts are more or less severe, since the accumulated phase and therefore the phase difference between magnetization vector and RF pulse is dependent on the frequency offset and the duration of the pulse. Figure was adapted. Reprinted with permission of Wiley Periodicals LLC.

Another parameter that is obviously of importance for the RF preparation is the B_1 amplitude. Still, as discussed in section 2.1 of the publication, there are several commonly used ways to define the amplitude e.g. pulse averaged power, average amplitude over the pulse train and average quadratic amplitude over the pulse train. Again, such differences might become problematic when sharing information on the MR sequence. While it may in principle be possible to avoid errors that originate from unclear definitions, there are deviations that are hard to avoid when comparing measurement and simulation. Typically, MR sequence source code is only partly written in a human readable way. In contrast, the proposed Pulseq files describe the MR experiment with as little as 8 parameters for each discrete time point. As can be seen in figure 4.7, the possible parameters for each time step are: an index, a delay, an RF event, an X, Y or Z gradient event, an ADC event and the extension table entry. This representation of the MR sequence parameters is close to a classical sequence diagram and might therefore be more easy to read. Different pulse shapes can be defined including information on both phase and amplitude for each custom shaped pulse within the file itself. The file therefore contains all information that is necessary to define and perform the experiment at the MR scanner. The files do not have to be compiled or processed but can directly be run using the interpreter sequence at the scanner. To make the proposed standard available for different vendors, a side project along with this publication was realized: an interpreter that reads both Pulseq files and Bruker source code and compiles it into a hybrid sequence [69].

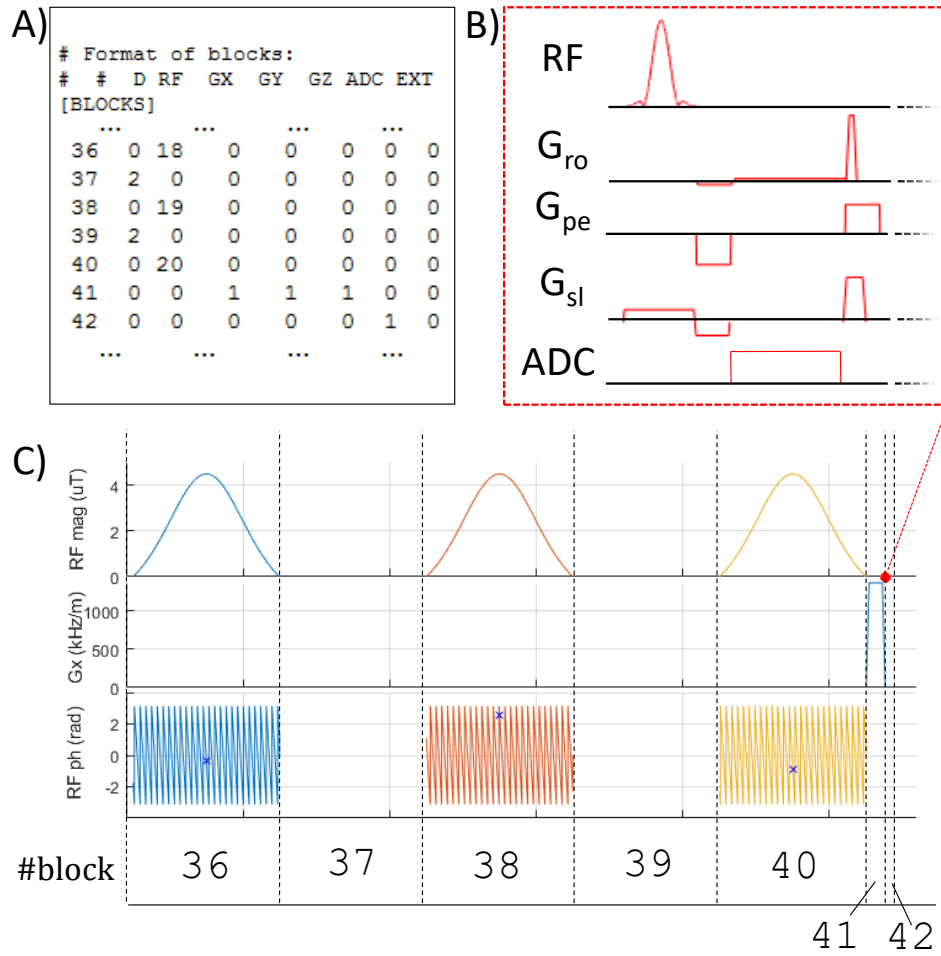


Figure 4.7.: Schematic sketch of the Pulseq-CEST hybrid sequence playing out the preparation period of protocol APTw_3T_002 (see: <https://pulseq-cest.github.io/>). **(A)**, Format of the pulseq-file with channels for time delay, RF pulse, gradient, ADC, and trigger events. The numbers link to entries in a lookup table, where the actual event parameters are defined. Note that the RF pulses have the same amplitude and frequency offset, but a different ID due to different phase offsets. **(B)**, Example gradient-echo readout sequence. **(C)**, Proposed combination of Pulseq events and the readout block using Pulseq as a sequence-building block (SBB). The RF events appear at blocks number 36, 38, and 40, spoiler gradients at block number 41, and delay events at blocks number 37 and 39. All Pulseq-CEST RF events are spatially nonselective. Blue crosses on the RF phase plots mark the RF phase at the moment of time when the peak RF magnitude is reached. For simplicity, GY and GZ gradient axes are not shown here. At every ADC event in the pulseq-file (block 42), the gradient-echo readout is played out. Modified and reprinted with permission of Wiley Periodicals LLC.

As mentioned previously, another challenge during the optimization or design of a sequence may be the comparison between measured and simulated data. This may not only be of interest for optimization but also for quantitative data evaluation. If an unexpected deviation between the assumed and actually executed RF preparation occurs, it may be impossible to correctly describe the observed data or false conclusions may be drawn based on fitting an analytical model to the data. Therefore, it is important to have both measurement and simulation in best possible agreement. With the provided

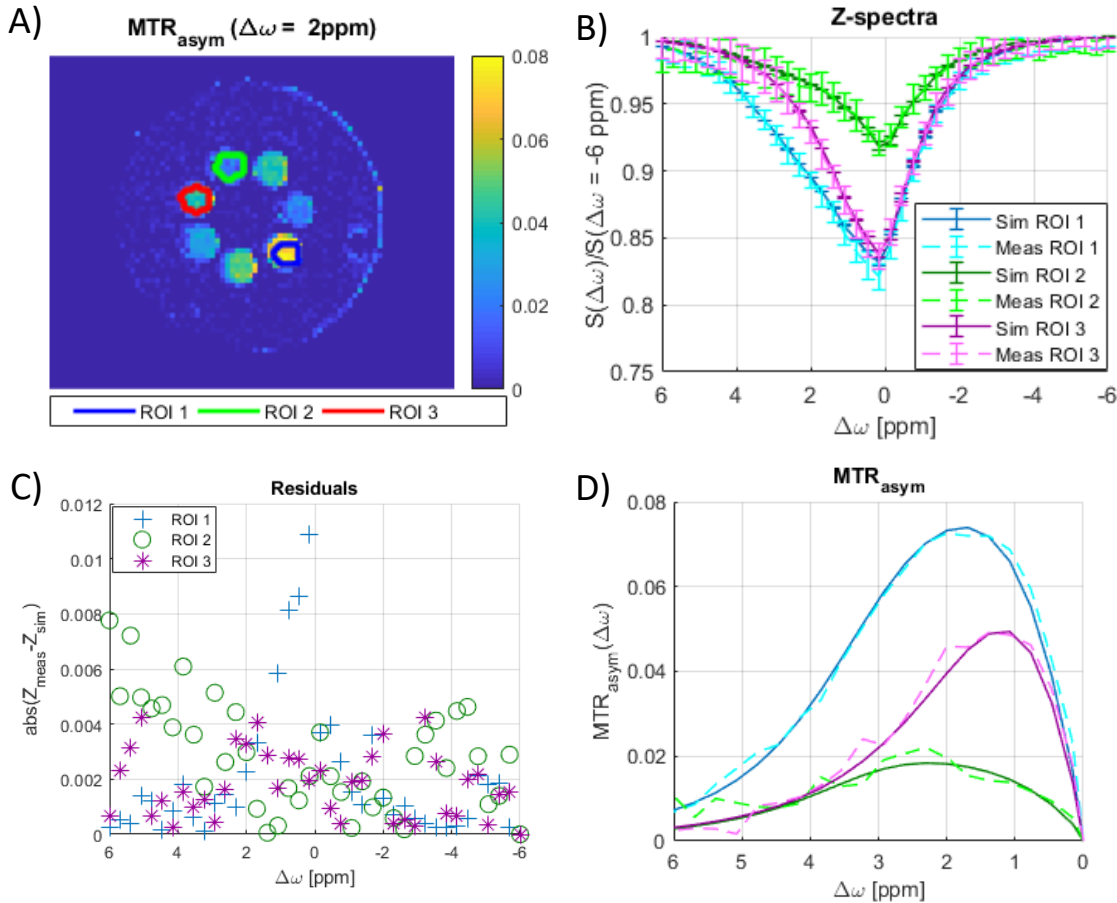


Figure 4.8.: (A) The $MTR_{asym}(\Delta\omega = 2\text{ppm})$ in slice 6. (B) Simulated and measured Z-spectra for ROI 1, 2 and 3, respectively. Error bars in the measured Z-spectra show the SD of Z-spectra across voxels. (C) Difference between the measured and simulated Z-spectra for each ROI. (D) The MTR_{asym} curves of simulated and measured Z-spectra for the three ROIs.

Reprinted with permission of Wiley Periodicals LLC.

open-source Bloch-McConnell simulation (<https://pulse-q-cest.github.io/>) it is possible to directly simulate the exact same Pulseseq files that were also executed at the MR scanner. By this it is made sure that the RF preparation is exactly the same for both

4. *Publication Summaries*

measurement and simulation and can therefore no longer be the source of any deviations. In figure 4.8 simulated and measured data of model solutions are shown. Both are in very good agreement as can be seen by the noise-like residuals shown in subplot 4.8C. Besides facilitating sequence development and assuring realistic simulations, the proposed sequence definition standard can easily be shared across sites without having to worry about any license issues, as the Pulseq files are open-source. In the presented publication CEST MRI examinations were performed at three different sites. In figure 5 of the publication the resulting CEST contrasts in three different healthy subjects are shown. Due to the proposed sequence standard it was possible to examine all of them with the exact same protocol. To facilitate this, the original Pulseq interpreter was modified such that it can be used as a sequence building block for Siemens (Siemens Healthineers, Erlangen, Germany). This allows combining the Pulseq interpreter with existing readouts without requiring extensive manual sequence programming. In principle, it would also be possible to define both CEST RF preparation module and the readout in Pulseq files. Still, in many cases sophisticated, optimized readouts have already been developed and may be used by adding Pulseq as a sequence building block. Admittedly, at the moment the sequence building block is only available for Siemens MR scanners. Still, a workaround for Bruker is presented [69] and transfer to GE devices is also possible [68]. For other providers such as Canon, United Imaging or Philips there is not yet an interpreter sequence available.

With the framework presented in this publication a complete solution for CEST MRI is presented. The Pulseq files for defining sequences allow sharing information in a standardized way. This should facilitate the transfer from development to clinical application and increase reproducibility. As all code is open-source, a widespread application of the framework should be possible with nearly no limitations across vendors and sites.

Statement of Contribution

K. Herz	Study design, sequence programming, MR examinations, data evaluation, programming for simulations. Most of the manuscript was written by him.
S. Mueller	Prepared the model solutions, sequence programming and assisted during the MR examinations.
O. Perlman	Designed CEST-MRF protocol, MR examinations, data evaluation.
M. Zaitsev	Provided support for the Pulseq interface and sequence programming.
L. Knutsson	Designed APT-weighted protocol.
P.Z. Sun	Designed APT-weighted protocol.
J. Zhou	Designed APT-weighted protocol.
P. van Zijl	Designed APT-weighted protocol.
K. Heinecke	Provided python Pulseq wrapper for simulation.
P. Schuenke	Provided python Pulseq wrapper for simulation.
C.T. Farrar	Designed CEST-MRF protocol, MR examinations.
M. Schmidt	Provided patient data.
A. Dörfler	Provided patient data.
K. Scheffler	Study design.
M. Zaiss	Designed APT-weighted protocol, MR examinations, programming for simulations.
all authors	proofreading of the manuscript.

4.4. Publication 4

MRI sequence development is usually performed in a trial-and-error manner based on the knowledge on the underlying physics. In a first step, an analytical model is derived to describe the effects that are of interest. Next, based on this model the parameters of the MR experiment are adapted such that for instance an increased T_2 weighting is expected. This obviously requires time consuming manual modifications of sequence parameters. Also, models that describe the measurement process in detail often become large in the number of potentially unknown parameters. One example of such a manual optimization process could be the design of the RF preparation module for CEST MRI of a specific metabolite. This requires knowledge on the chemical properties such as exchange rate, the properties of the bulk water pool such as T_1 and T_2 , estimates on effects such as ssMT and so on. For fast, simulation based optimization, in principle it is possible to describe such a system by the Bloch-McConnell equations. Still, in most cases the exact properties (e.g. exchange rate, T_1 , T_2 , CEST pool size) that would fully describe the system are unknown. Most likely one would need to have an educated guess for the parameters based on the known properties and the Bloch-McConnell equations. Anyways, finally one needs to go to the MR scanner, modify some of the parameters and see if a correlation of the MR signal with for instance the concentration of the metabolite in a model solution can be derived. This also requires to chose and apply a metric to quantify and extract the CEST effect based on the acquired data for each set of parameters as mentioned in section 2.3.

From a more general point of view, there might be cases in which it is not even known if a target may be accessed by MRI at all. It could be hypothesized that certain properties are somehow represented in the MR data but the underlying physics is unknown. One example where correlations in data are used to map to targets without necessarily knowing why this mapping should work is radiomics [70]. The question that arises is if it can be possible to automatize MR sequence design as a model-free optimization process. With this, it should be possible to perform the aforementioned hypothesis testing and instead of being limited to predefined acquisitions, one could also adapt the acquisition process and generate data that suits the respective hypothesis. Recently, Loktyushin et al. [71] demonstrated that optimization of MRI sequences may be performed automatically based on simulations. Still, this requires suitable models and is not based on measured data. In this work, MRI sequence design is formulated as a model free, target driven, supervised learning process based on measured data. The proposed framework should be applicable to any target of interest or for hypothesis testing, and as a proof-of-concept the discovery of CEST effects in MRI data was demonstrated as described below.

Instead of manual sequence parameter adjustments an automatized workflow is used. Pulseseq [68] files are sent to the scanner by the optimizer (CMA-ES optimizer [72] implemented in [73]; called *nevergrad* in the following) for each iteration of the optimization process. Subsequently, the acquired data flow back, are evaluated by the optimizer and the parameterized sequence gets updated. The human interaction reduces to providing the target contrast and a suitably parameterized MRI sequence. The workflow for up-

dating the sequence is depicted in figure 4.9.

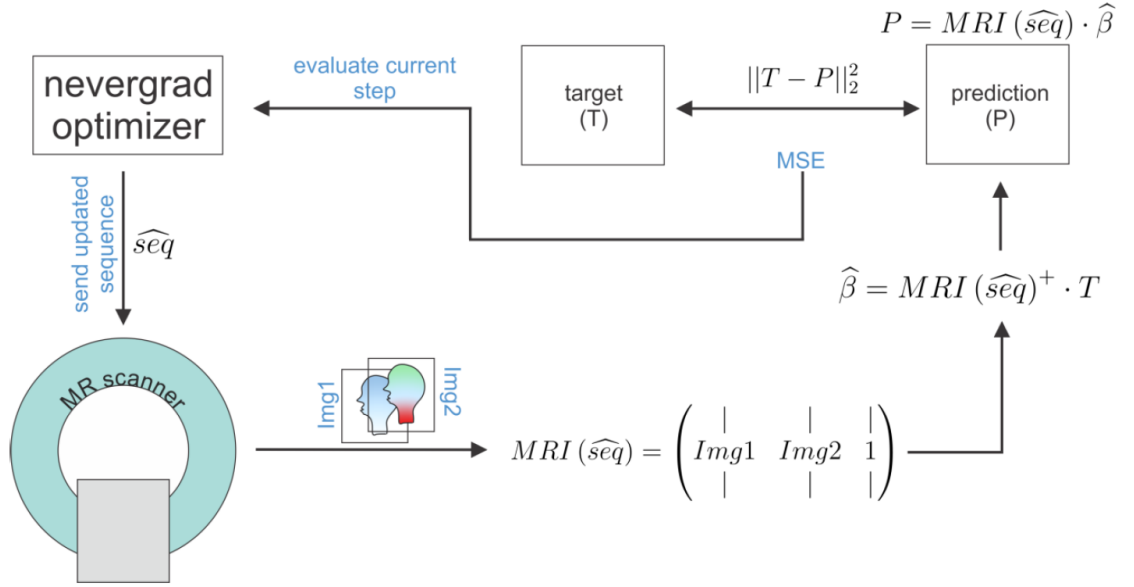


Figure 4.9.: Diagram of the proposed sequence development workflow termed MR-double-zero. The optimizer sends the parametrized sequence (seq) to a real MR scanner. The acquired data (in the depicted case for $R = 2$ images: $Img1$ and $Img2$) get flattened into the matrix $MRI(seq)$ which is used to determine coefficients β from linear regression of $MRI(seq)$ to the target. With these coefficients, the prediction (P) is determined and the deviation from the target (T) flows back to the optimizer. Our pipeline implements this using so called .seq-files of the Pulseseq standard [68] that are played out at the scanner by a Pulseseq interpreter sequence. Reprinted with permission of Elsevier Inc.

The automatized learning process can be formulated model-free, as it directly acquires data instead of simulating it. There are two separate optimization processes involved: the outer optimizer updates the sequence parameters (nevergrad), whereas in the inner optimization the acquired data get mapped to the desired target contrast by linear regression. Let T denote the provided target contrast and $MRI(seq)$ denote the acquired data for the parameter set seq after reshaping it into a 2D matrix as described in section 2.3 of the publication. The predicted target contrast (P) is then determined by applying the coefficients $\widehat{\beta} = MRI(\widehat{seq})^+ \cdot T$ such that $P = MRI(\widehat{seq}) \cdot \widehat{\beta}$ with X^+ denoting the Moore-Penrose pseudo-inverse $X^+ = (X^T X)^{-1} X^T$. The data matrix $MRI(seq)$ may in principle be created from any MR data. In this work, it consists of $n = 1, 2, \dots, N$ ($N_{\max} = 3$) RF prepared 2D images (Img_1, \dots, Img_N) and optionally higher order polynomials Img_n^k (with $k = 1, 2, \dots$) of the data. It should be noted that

even when including the higher order polynomials the inner optimization remains linear in the coefficients β .

For a first proof-of-concept, it is assumed that T_1 and T_2 relaxation are known but it is claimed that CEST itself is not known. Given this knowledge is provided, the idea of preparing a certain state of the magnetization with RF pulses before the MRI readout is no too far away. Consequently, the optimizer starts from an RF prepared sequence that is parameterized such that $n = 1, \dots, N$ images are acquired, each with np_n Gaussian-shaped RF pulses with amplitude $B_{1,n}$ and off-resonance $\Delta\omega_n$. As it is assumed T_1 and T_2 relaxation are known, the model solutions are prepared in a way that they are indiscernible with respect to T_1 and T_2 as shown in figure 4.10. The target contrast is the absolute concentration of creatine contained in the seven different vials. By this, a target that is not obviously linked to MR data is provided, assuming CEST effects are yet to be discovered by the proposed framework.

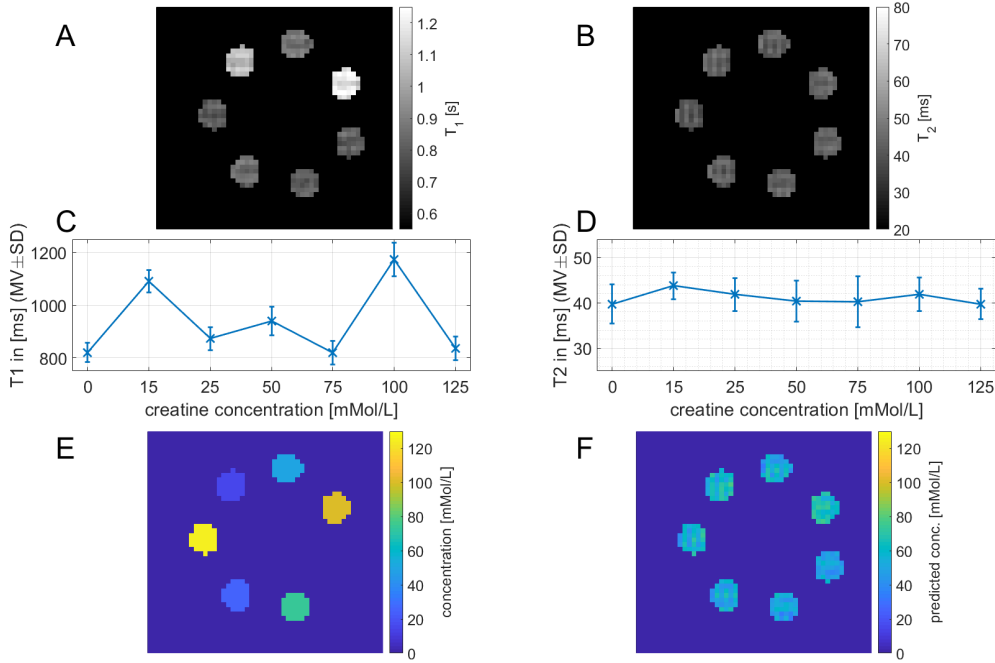


Figure 4.10.: Quantitative T_1 and T_2 maps of samples with different creatine concentration c_{Cr} . **Upper row:** different concentrations cannot be distinguished directly from T_1 (A) and/or T_2 (B) maps. **Center row:** evaluation of (C) T_1 and (D) T_2 values in different ROIs of data shown in (A)/(B) with mean (MV) and standard deviation (SD) for each vial. **Bottom row:** True creatine concentrations (E) cannot be predicted by linear regression $f([T_1, T_2, 1]) = c_{Cr}$ from T_1 and T_2 (F).

Reprinted with permission of Elsevier Inc.

4. Publication Summaries

Before considering the creatine concentration mapping the framework is tested on 1D problems. That is, out of the three parameters $\Theta = (B_{1,1}, \Delta\omega_1, np_1)$ two are fixed, one at a time is varied and the Root Mean Squared Error (RMSE) between $MRI(\Theta)$ and $MRI(\hat{\Theta})$ is determined within a certain parameter range as described in section 3 of the publication. Here $MRI(\hat{\Theta})$ denotes the data acquired with varying parameter $\hat{\Theta}$ given the other two parameters are fixed. It is proved that minima exist for all three 1D problems, which, if it was not observed, would have been a contraindication for the optimization process.

One exemplary optimization targeting the creatine concentration and therefore resulting in a novel RF preparation module is shown in figure 4.11. In this case $N = 2$ images and the pixel-wise images squared and cubed are used to extend the design matrix ($MRI(seq)$) as described in section 2.3 of the publication. As discussed in section 3 of the publication, this extension of the design matrix yields 50% smaller Mean Squared Error (MSE) loss. In contrast, extending the design matrix to $N = 3$ images but keeping the polynomial order at $k = 1$ does not reduce the MSE loss this much as shown in the Supplementary Material of the publication. This is potentially due to the additional non-linearity introduced for $k > 1$ as especially the mapping for different samples to the same concentration of 0 mmol/L improved.

Figure 4.11 proves that the goal of formulating MRI as a target driven, model-free learning process was reached by exploiting supposedly unknown CEST effects for mapping creatine concentration with MRI applied as an imaging tool. The whole framework is based on real and therefore noisy data used to solve a high-dimensional and potentially ill-conditioned problem. Still, it is shown that within 300 iterations on a smaller subset of maximum nine free parameters the optimizer could come up with a sufficiently good mapping to the given target contrast. A grid search with as little as 100 evaluations per parameter would have required an infeasible 10^5 measurements. This is infeasible as the estimated MRI scan time would be on the order of around three weeks. Also, when increasing the number of free parameters from six to nine, the MSE loss still decreased significantly within the limit of 300 iterations. This may be a hint that even more complicatedly parameterized MRI sequences could be feasible with the proposed framework. The inner optimization as described in section 2.3 of the publication was chosen to be a linear mapping for this proof-of-concept but could be extended as well to allow more complex mapping. Still, this may come at the cost of increased time demand and the potential risk of overfitting. The discovered RF preparation module and weighting parameters in the inner optimization closely reassemble a MTR_{asym} in case of a design matrix that contains only $N = 2$ images and no higher order polynomials ($k = 1$). This shows that in principle also known contrast mechanisms can be found. In case of $N = 2$ but $k = 3$, another set of parameters Θ is chosen. This may have the following reason: a stochastic optimizer is used and there might be several almost equivalent near-global minima. Consequently, the optimizer may also come up with solutions that are not trivial to find, in addition to solutions that are already expected from classical model driven approaches.

In the field of MRI there has already been an approach to jointly optimize acquisition

and reconstruction of data shown in [74] and [75]. Still, optimization of k-space sampling was performed retrospectively on previously fully sampled data, whereas the proposed approach allows full optimization of the data acquisition without being bound to existing data. This should hopefully facilitate to discover whole new strategies for MRI data acquisition. In the field of robotics real-world optimization is known to be beneficial, as it includes all potential sources of imperfections and noise that may be hard to model (e.g. see [76–78]). Modeling all imperfections may be tough in MRI as well. Therefore, the proposed framework could also be used not to discover completely new strategies, but for example to map directly to a fat-suppressed image instead of having to apply time and SAR intensive fat saturation pulses explicitly.

As a first proof-of-concept it was claimed that CEST effects are unknown. The proposed framework was then successfully applied to map creatine concentration with MRI by exploiting chemical exchange without providing any model or explanation of the underlying physics. The ultimate goal of the proposed approach would be to map to any target contrast of interest or at least test hypotheses as to whether or not the information contained in the target may be accessed by MRI. One potential future application for the proposed framework might be to approach radiomics [70] in a top-down manner: instead of evaluating existing data one could try to design the data in a way that the desired target information may directly be mapped. Still, the current approach with an MRI scan time of around three hours may not be suitable for in vivo applications. One way to tackle this issue might be to think about a hybrid approach that is partly based on simulations. In principle, it is also possible to split the learning process across multiple sessions. Still, similar as for traditional sequence design, it is always possible to stick to model solutions first and then directly translate to in vivo application. In any case, with the proposed framework, MRI sequence design is reduced to providing a suitable target while the entire optimization process is performed fully automatically and does not require any modeling of the underlying physics. The hope is that this facilitates and accelerates the process of sequence optimization and may at best even come up with completely novel sequence designs.

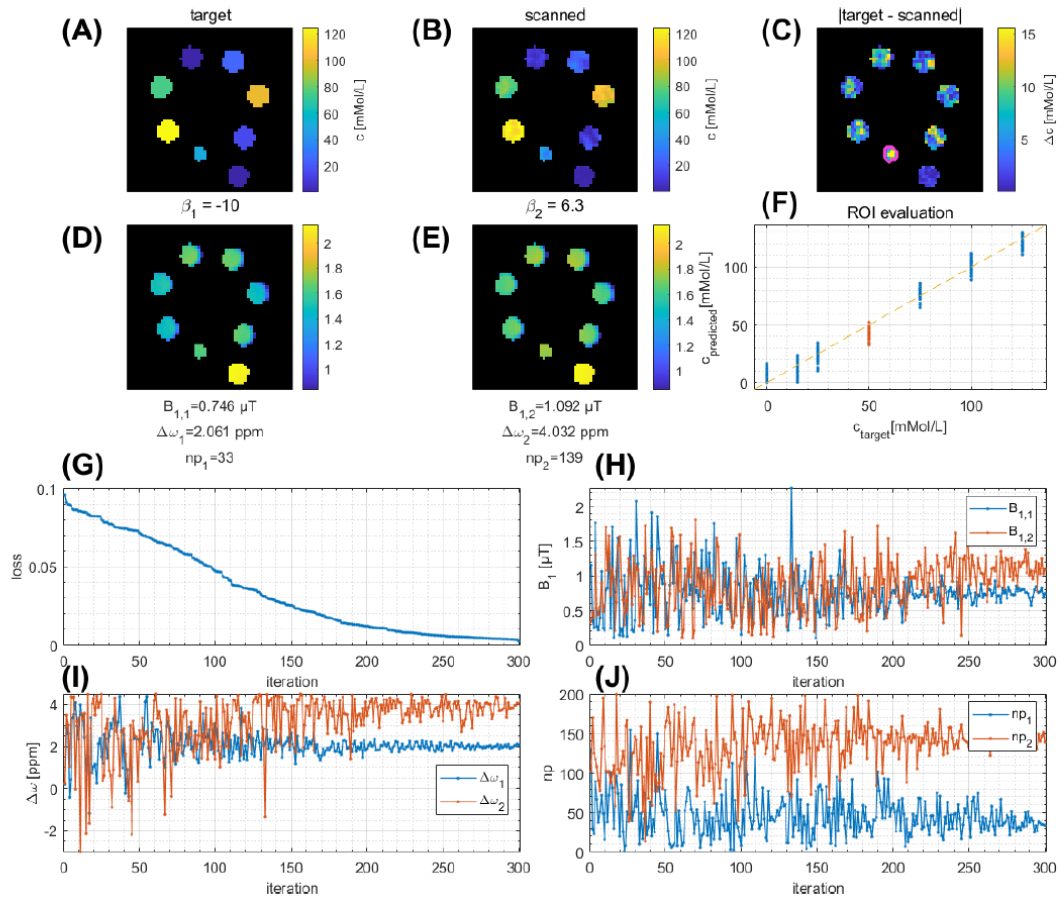


Figure 4.11.: Exemplary optimization process of a MR-double-zero sequence with 300 iterations (MRI scan time 3 h). The final parameter set here was $\text{seq} = (0.75 \mu\text{T}, 2.06 \text{ ppm}, 33 \mid 1.10 \mu\text{T}, 4.03 \text{ ppm}, 139)$. The design matrix contains in addition to the images ($\text{Img}_1, \text{Img}_2$) also the pixel-wise images squared ($\text{Img}_1^2, \text{Img}_2^2$) and cubed ($\text{Img}_1^3, \text{Img}_2^3$). The first row shows: (A) the target, (B) the experimentally derived and (C) the difference in concentrations. Second row shows the two images (C,D) with respective sequence parameters given below. In (F) the predicted and target data are scattered for ROIs within the different vials. The test vial (50 mmol/L) that was not included in the optimization process is highlighted in (C) and (F). Subplots (G-J) were retrospectively sorted by loss instead of the actual time course of acquisition. (G) shows the loss for the sequence parameters shown in (H)-(J). Subscripts 1 and 2 refer to the image number for all parameters.

Adapted. Reprinted with permission of Elsevier Inc.

Statement of Contribution

F. Glang*	Study design, performed measurements, set up code for optimization, evaluated data and wrote the manuscript.
S. Mueller*	Study design, performed measurements, prepared the model solutions, evaluated data and wrote the manuscript.
K. Herz	Provided assistance with the Pulseq framework.
A. Loktyushin	Provided assistance with the Pulseq framework and scanner interface.
K. Scheffler	Study design.
M. Zaiss	Study design.
all authors	Proofreading of the manuscript.

*S. Mueller and F. Glang contributed equally to this work.

5. Conclusion and Outlook

In Publication 1 (section 4.1), the bias due to the CEST effect of agar in model solutions for MRI parameter optimization was analyzed in detail. The dependence on temperature and pH values was considered, too, as these factors govern CEST effects in general. The introduced bias becomes larger for high power RF preparation modules and must in this case be taken into account. It was shown that it is possible to correct the bias in post-processing, given a sample for reference was provided, as demonstrated in the Supporting Information of [79]. Unfortunately, no other compound was found that could replace agar but does not introduce an undesired CEST effect. At least it could be shown that the use of pure agarose reduces the bias. It was challenging to observe the CEST effect of agar at lower field strength of 3T. Still, this does not mean that it is of minor importance there but rather emphasizes that CEST MRI benefits from UHF. The detailed description of the CEST effect both shows that it is necessary to precisely consider all possible contributions to CEST MRI and it hopefully provides useful information for future parameter optimizations.

The acquisition of CEST MRI data in vivo at a clinically relevant field strength of 3T was considered in Publication 2 (section 4.2). A readout that is fast compared to T_1 relaxation is crucial for CEST MRI and makes 3D EPI a suitable sequence as shown. As the CEST effects are on the order of some percent of the bulk water signal, a high tSNR is required. The optimized 3D EPI could provide a tSNR of at least 75 over the entire brain. By this, it outperformed established readouts that are currently applied for CEST MRI. A decent nominal resolution of $(1.8\text{ mm})^3$ with whole brain coverage should further facilitate clinical application. The scan time could be reduced to 4.3s per RF preparation frequency offset. This can be considered fast compared to state of the art approaches as for instance described in [66, 80–82]. Still, in most cases the readout itself has a similar or even shorter duration than the RF preparation. For Magnetic Resonance Spectroscopic Imaging (MRSI) there are approaches to jointly reconstruct data from two undersampled data sets [83, 84] and by this reduce the overall scan time. This is based on the idea of trading spatial against spectral resolution at fixed scan time and vice versa. For CEST MRI, this approach is not beneficial as even data with low spatial resolution requires the acquisition of multiple images each with lengthy RF preparation. If a certain target contrast is aimed for, there are chances to adapt the acquisition of CEST data accordingly as shown by Glang et al. [60]. With this, it is possible to reduce the number of RF prepared images and significantly decrease the scan time. Still, this comes at the loss of generality, as the target contrast is predefined. Other approaches apply compressed sensing [85] to reduce the acquisition duration, e.g. [53]. This reduces artifacts in the image reconstruction as it exploits redundancies of the acquired data across off-resonances, but cannot reduce the number of RF prepared

5. Conclusion and Outlook

images. In principle, it is possible to acquire several RF preparation offsets at the same time but at different spatial locations by applying an additional gradient during the RF preparation. This technique can be applied for both CEST MRS [86] and MRI [87] but it requires that the imaged object is homogeneous along the direction of the gradient applied during the RF preparation. This limits the application to model solutions. One possibility to actually reduce the scan time of CEST MRI could be to generalize the approach presented by Glang et al. [60]. Instead of mapping from a fully sampled Z-spectrum to a contrast, one could map from the undersampled (Z_{US}) to the fully sampled Z-spectra (Z_{full})¹³. This could for instance be done by simple linear regression such that $Z_{full}^{training} = A \cdot \beta$. The coefficients β may in the simplest case be determined by the Moore-Penrose pseudo inverse $A^+ = (A^T \cdot A)^{-1} \cdot A^T$ as $\beta = A^+ \cdot Z_{full}^{training}$.

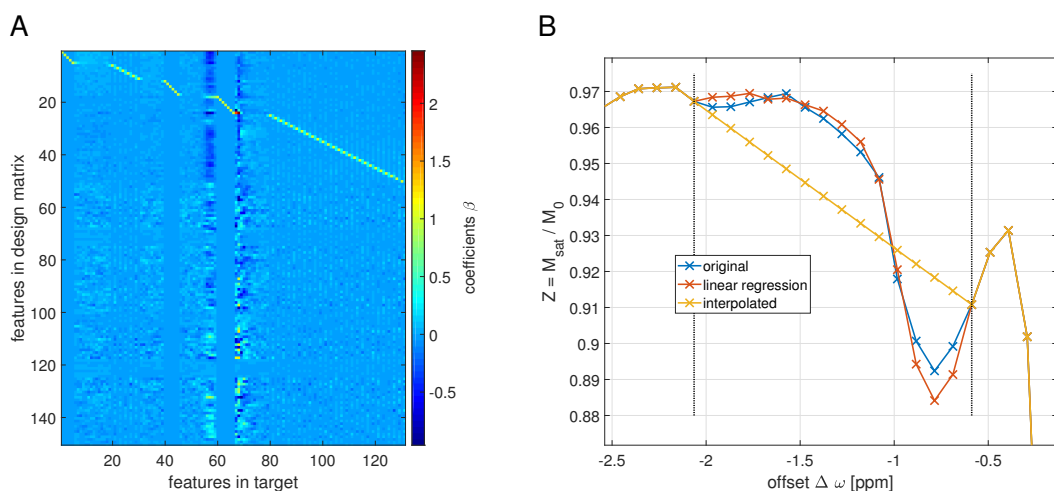


Figure 5.1.: **(A)** coefficients β for mapping the design matrix $A = [Z_{US}^{training}, (Z_{US}^{training})^2, (Z_{US}^{training})^3]$ containing undersampled spectral data to fully sampled data (Z_{full}) by linear regression $Z_{full}^{training} = A \cdot \beta$. Undersampling of off-resonances: for around half of the off-resonances every second was removed. Additionally, in some intervals, multiple neighboring off-resonance were either kept or removed. **(B)** original fully sampled and reconstructed data. For comparison, not only linear regression but also linear interpolation is shown. The vertical dashed lines in (B) indicate the interval in which no data was provided in the undersampled data set. Data acquired at $B_0 = 9.4$ T in egg white.

¹³Here, $Z_{full/US}$ denotes a single fully sampled or undersampled Z-spectrum, whereas $Z_{full/US}^{training}$ is an entire set of different spectra to learn the coefficients β from. This might for instance be a 2D matrix that contains spectra of all voxels of a measurement.

The design matrix A contains the undersampled data (Z_{US}) and optionally nonlinear transformations of these, such as Z_{US}^2 or $1/Z_{US}$. Instead of simply interpolating the spectral dimension of the undersampled data, the coefficients β can be learned on training data. By this, prior knowledge is included when β are applied to new data $Z_{full}^{new} = A^{new} \cdot \beta$. One example for such a learned set of coefficients β is shown in figure 5.1. Interpolation along the offset direction is possible for any undersampled data. Still, in contrast to the linear regression based approach, no prior knowledge is included. This causes severe deviations in the reconstructed data as can be seen in figure 5.1B. On the other hand, any approach based on supervised learning is based on prior knowledge and therefore requires the acquisition of training data. Even more sophisticated ways for mapping from undersampled to fully sampled data such as neural networks might be considered. Zaiss et al. [88] demonstrated that CEST data acquired at lower field strength of 3 T can be mapped to 9.4 T CEST contrast maps (Lorentzian amplitudes) with neural networks applied purely in the spectral but not in the spatial domain. In addition, for this approach different field strength, RF preparation modules (number of pulses, B_1 amplitude, offset frequencies) and bulk water T_1 and T_2 relaxation constants had to be implicitly interpolated by the neural network. Regarding this, increasing only the spectral resolution at same field strength and RF preparation should be possible. With this, one may significantly reduce the acquisition duration of CEST MRI compared to only decreasing the duration of the readout, but having the full Z-spectrum available. The readout proposed in Publication 2 (section 4.2) is flexible enough to acquire data with modified offset list and high reproducibility was proved as well, which would be important for comparing fully sampled and reconstructed spectra. Also, whole brain coverage is beneficial as this results in a larger set of voxels for the learning process. On the other hand, the question arises if the full Z-spectrum is of interest at all. In many cases, it is potentially sufficient to directly map to fitted CEST contrasts. For proof-of-principle, potentially model solutions are used and scan time is not a limiting factor. Still, it could be of interest to think about including prior knowledge, as there are quite some similarities that are observed in CEST data across different measurements. Approaches based on learning processes require that training and test data are acquired with the same acquisition parameters. This requirement would be a perfect application for the framework proposed in Publication 3 (section 4.3). As CEST MRI depends strongly on the RF preparation module, it was proposed to define these preparations in Pulseq files. This sequence definition standard is open-source and does not depend on the vendor of the MR hardware used to acquire data. In the presented publication a hybrid MRI sequence for Siemens scanners was described that is based either on the readout presented in Publication 2 or an established spoiled GRE sequence [61, 66]. The interpreter for the Pulseq files was modified and used as a sequence building block within the existing readouts. This allows combining the sophisticated readouts including their full flexibility of k-space sampling with the CEST RF preparation modules precisely defined in Pulseq. This overcomes the limitation of native Pulseq, which does not allow modifications of sequence parameters directly on the MR scanner. Given such a hybrid sequence is available, researchers may simply read Pulseq files provided by other research groups or define the Pulseq files themselves. In the publication, data were exemplarily

5. Conclusion and Outlook

acquired both for three different preparation modules in the same subject and with the same preparation module but in three different subjects at three different sites. The data acquired in three different subjects were evaluated with a CEST MR fingerprinting approach. In this case, data for the learning process had to be simulated. For this purpose, open-source Bloch-McConnell simulations are provided alongside the publication. They are implemented such that the same Pulseq files can be executed both at the scanner and in the simulations. While the potential of the proposed sequence definition standard was described in detail, one bottleneck of the entire workflow is the Pulseq interpreter sequence on the MR scanner itself. For Siemens and GE, such interpreter sequences were already presented [68]. For Bruker systems, a very basic implementation solely for CEST MRI was presented in the context of this publication as well [69]. For other vendors such as e.g. Philips, United Imaging or Canon, such interpreter or hybrid sequences are not yet available.

Besides the aforementioned limitations, Pulseq provides a great framework especially for sequence development, where usually the vendor provided framework requires time consuming programming in C++ and often does not offer full flexibility but is based on compiled libraries. The work presented in Publication 4 (section 4.4) therefore makes use of Pulseq files for sending updated sequence designs to the MR scanner automatically, too. This would not be possible within the vendor provided framework as the updated sequence would have to be compiled offline of the MR system and be installed on the scanner manually. For the proof-of-concept a hybrid approach similar to Publication 3 was chosen such that the readout itself remained untouched but only the RF preparation was modified. Still, both readout and RF preparation were entirely defined within a single Pulseq file in this case. The proposed framework formulates MRI sequence design as a model-free and fully automatized supervised learning process, which in contrast to other approaches works on real-world data instead of simulations. On the other hand, this requires suitably created model solutions. At this point, knowledge and experience from Publication 1 (section 4.1) was exploited when setting up the experiment. While in the first step it was only pretended that CEST effects were unknown, for future applications of the proposed framework it may indeed not be necessary anymore to have any knowledge on the underlying physics. A potential issue may be the number of free parameters required to describe any arbitrary MRI sequence. In the publication up to nine free parameters were used to parameterize the RF preparation module only. If for instance a FA array needs to be parameterized for an entire 3D GRE readout, this may soon approach orders of magnitude higher number of free parameters. Even though it was discussed in section 4.1 of the publication that increasing the number of free parameters from six to nine did not cause significantly different behavior of the MSE loss, this needs to be verified for much larger numbers of free parameters as well. For potential in vivo applications it may also be necessary to split the learning process across different MR examinations to reduce the scan time. In the presented study, linear regression was used to map to the target contrast but in principle other approaches would be possible as well. For example in figure 5.2, the proposed framework was modified such that the inner optimization - in contrast to the description in section 2.3 of the publication - was set up as multinomial logistic regression, which is a simple multi-class classification

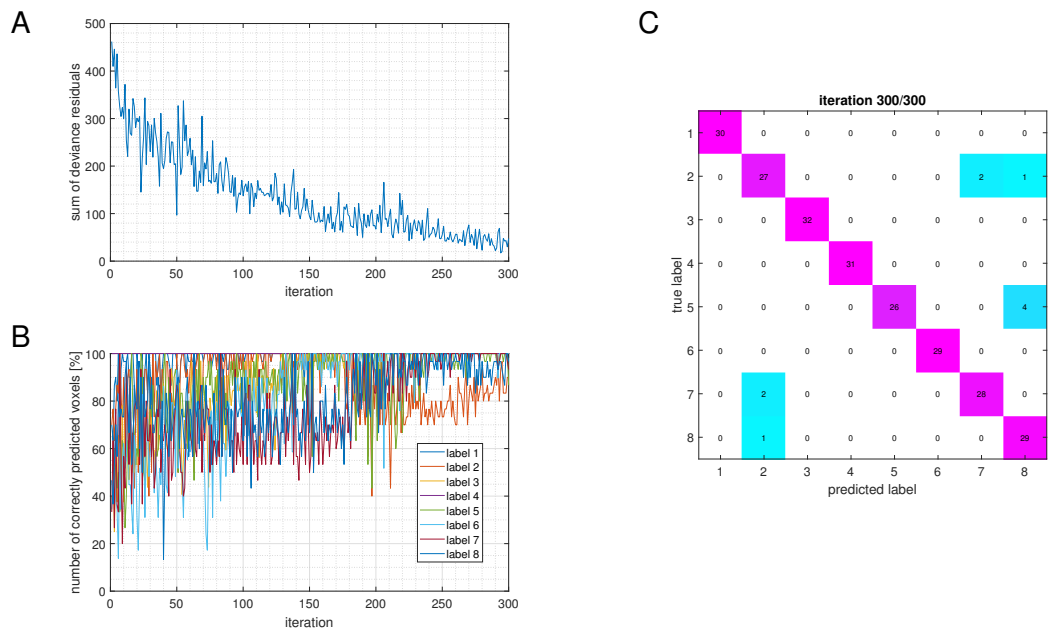


Figure 5.2.: Modified learning process for the real-world scanner optimization similar to what is proposed in Publication 4. Data are again resulting from an parametrized RF-prepared sequence with 2D spoiled GRE image readout. In contrast to the settings in Publication 4 an individual class label for each sample vial with different creatine concentration was provided as target. In **(A)** the summed residuals are shown. **(B)** shows the relative number of correctly predicted categories and in **(C)** a confusion chart for the last iteration is shown. Data was sorted by loss and not temporally as acquired at the scanner. Multinomial logistic regression was performed in MATLAB (The Mathworks, Natick, USA) for this figure but was executed in Python [89, 90] during the actual learning process.

5. Conclusion and Outlook

algorithm [91]. For that, instead of creatine concentration values, the target was set to be voxel-wise class labels, where each sample vial containing one concentration level was defined as one class. The loss is depicted sorted in descending order in figure 5.2A. The resulting predictions for each iteration are shown in figure 5.2B and a confusion chart for the iteration with lowest loss is shown in figure 5.2C. Multinomial linear regression does not require the targets to be sorted by for instance an unknown chemical exchange rate when mapping data. This may be beneficial if only classification is required, but obviously comes at the drawback that no interpolation or generalization to unknown labels is possible. Multinomial logistic regression is discussed at this point as it shows that for the inner optimization different mapping approaches up to neural networks might be applied.

During the course of thesis it was shown in another project that neural networks can map from classically acquired Z-spectra to absolute pH values in realistic model solutions made from pig brain [92]. Still, for in vivo applications, no ground truth pH maps are available as targets for the training. In principle, MRSI could provide absolute pH values [93] but the modality only provides significantly lower spatial resolution than CEST MRI, thus, no voxel-wise training would be possible. It is possible to apply the network that was only trained on model solutions directly to in vivo data, as shown in figure 5.3. Still, these results should be seen critically and may be misleading. The predicted pH values seem to be in a realistic range compared to values derived from MRSI (e.g. [94]). On the other hand, if the same neural network was trained with different random initializations, the predicted pH values based on the in vivo data differed, as shown in figure 5.3. This is a first hint that the mapping from the input data to pH values is not very reliable. The fact that the predicted pH values are not too unrealistic is potentially due to the range of pH values that the network was trained on. While the neural network was successfully applied in model solutions to predict absolute pH values [92], neither the training nor even the application to in vivo data are straightforward. The results derived at this point may rather be considered as an example for a drawback in the application of neural networks: some prediction is always returned but it may be difficult to tell if this is trustworthy. For data acquisition both in model solutions and in vivo, a low power RF preparation was applied [95], but in principle, the data acquisition was not specifically designed for the aim of mapping to absolute pH values.

At this point the approach presented in Publication 4 could be applied to experimentally figure out where most information on pH sensitivity can be encoded in the Z-spectra of these particular samples.

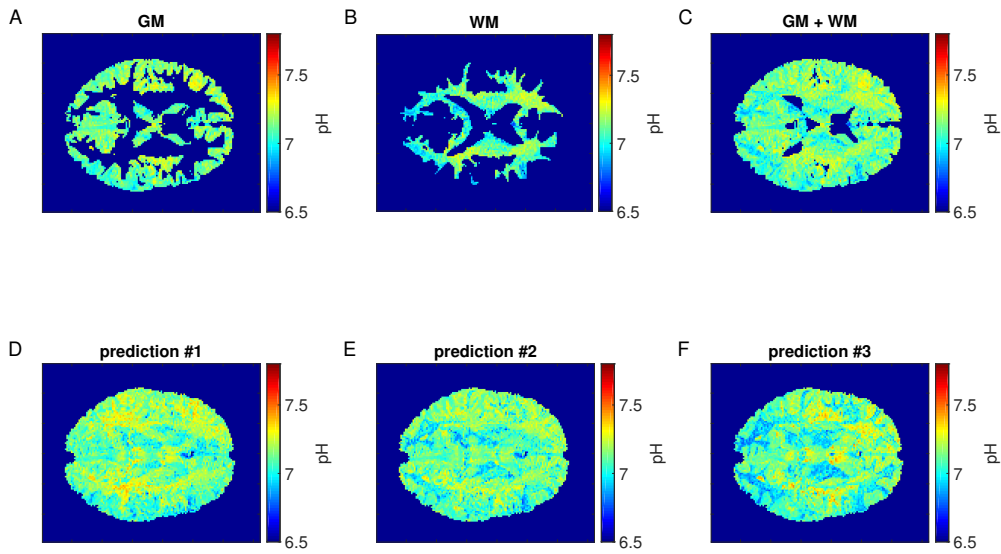


Figure 5.3.: pH values predicted by a neural network [92] based on CEST MRI data acquired at 9.4 T in a healthy subject. The network was trained only on samples made from pig brain homogenate for which the pH value could be determined exactly with a pH sensitive electrode (inoLab pH 720, WTW, Weilheim, Germany). Subplots (A-C) show the average prediction of four neural networks with different initializations during training. (D-F) show three of the four predictions which are averaged in (A-C).

As discussed in Publication 4, the presented work was a very first proof-of-concept study that provides no immediate benefits for MRI sequence design or application. On the other hand, at least it was shown for the first time that MRI sequence design does not necessarily have to be performed manually but could be fully automatized. With this, parameter optimization for existing sequences could potentially be facilitated and accelerated, too, for instance in projects such as the above mentioned pH mapping where the underlying system cannot be fully described.

To sum it up, we have started with a comprehensive description and analysis of model solutions for CEST MRI parameter optimization at different field strengths. This may hopefully be valuable information for the work of others as well. In the second publication, the benefits of an optimized, fast and stable readout at clinical relevant field strength was presented. On the other hand, to some extent it became clear once more that solely reducing the number of RF preparation offsets can effectively reduce the scan time for CEST examinations. Still, the readout meanwhile was successfully applied not only for CEST but also for other applications such as functional Magnetic Resonance Imaging (fMRI) at 9.4 T and the experience that was gained while working on the read-

5. Conclusion and Outlook

out for CEST was for sure helpful here as well. Insights gained in both the first and second publication also made their way into the third publication, where suitable model solutions and the optimized 3D EPI were used. In this work, an open source sequence definition standard for RF preparation based on Pulseseq is presented. The proposed framework should facilitate reproducibility and proved to be handy when sharing precise information with other MR research sites already. Also in the final project Pulseseq files turned out to be an elegant interface for communicating with the MR scanner during the automatized sequence design process. Admittedly, there is no immediate benefit for MRI from the presented proof-of-concept. As usual, all the results presented in here may have allowed considering further questions and gaining knowledge and experience rather than finally solving existing issues.

A. Publication List

Journal Articles

- [A] **Mueller, S.**; Scheffler, K.; Zaiss, M.: On the interference from agar in chemical exchange saturation transfer MRI parameter optimization in model solutions. *NMR in Biomedicine* 34 (1), p. 1 - 12 (2021)
- [B] **Mueller, S.**; Stirnberg, R.; Akbey, S.; Ehses, P.; Scheffler, K.; Stöcker, T.; Zaiss, M.: Whole brain snapshot CEST at 3T using 3D-EPI: Aiming for speed, volume, and homogeneity. *Magnetic Resonance in Medicine* 84 (5), p. 2469 - 2483 (2020)
- [C] Herz, K.; **Mueller, S.**; Perlman, O.; Zaitsev, M.; Knutsson, L.; Sun, P.; Zhou, J.; van Zijl, P.; Heinecke, K.; Schuenke, P. et al.: Pulseq-CEST: Towards multi-site multi-vendor compatibility and reproducibility of CEST experiments using an open-source sequence standard. *Magnetic Resonance in Medicine* 86 (4), p. 1845 - 1858 (2021)
- [D] Glang, F.; **Mueller, S.**; Herz, K.; Loktyushin, A.; Scheffler, K.; Zaiss, M.: MR-double-zero – proof-of-concept for a framework to autonomously discover MRI contrasts. *Journal of Magnetic Resonance* (341), p. 107237 (2022)

Conference Abstracts

- [E] **Mueller, S.**; Pohmann, R.; Chiaffarelli, R.; Hoffmann, S.; Martins, A.; Scheffler, K.; Zaiss, M.: An open source triggered CEST module for Bruker systems for reliable CEST MRI with efficient motion artifact mitigation. In *Magnetic Resonance Materials in Physics, Biology and Medicine*, 34 (Supplement 1), S3.O1, S. S18 - S19. 38th Annual Scientific Meeting of the European Society for Magnetic Resonance in Medicine and Biology (ESMRMB 2021), 07. Oktober 2021 - 09. Oktober 2021.
- [F] **Mueller, S.**; Pohmann, R.; Scheffler, K.; Zaiss, M.: CEST effect of agar: It's not a neutral baseline for realistic CEST-MRI parameter optimization. In *Magnetic Resonance Materials in Physics, Biology and Medicine*, 32 (Supplement 1), S10.04, S. S125 - S126. 36th Annual Scientific Meeting of the European Society for Magnetic Resonance in Medicine and Biology (ESMRMB 2019), Rotterdam, The Netherlands, 03. Oktober 2019 - 05. Oktober 2019.

A. Publication List

- [G] Herz, K.; **Mueller, S.**; Zaitsev, M.; Knutsson, L.; Zhou, J.; Sun, P.; van Zijl, P.; Scheffler, K.; Zaiss, M.: Pulseq-CEST: Towards multi-site multi-vendor compatibility and reproducibility of CEST experiments using an open source sequence standard. 2021 ISMRM & SMRT Annual Meeting & Exhibition (ISMRM 2021) (2021)
- [H] **Mueller, S.**; Herz, K.; Scheffler, K.; Zaiss, M.: Open source Pulseq interpreter for CEST MRI on Bruker systems. 2021 ISMRM & SMRT Annual Meeting & Exhibition (ISMRM 2021) (2021)
- [I] Herz, K.; **Mueller, S.**; Perlman, O.; Stirnberg, R.; Stoecker, T.; Scheffler, K.; Farrar, C.; Zaiss, M.: Towards clinical CEST-MRF: whole brain snapshot CEST MR Fingerprinting at 3T using spin-lock saturation and a centric 3D-EPI readout. 2020 ISMRM & SMRT Virtual Conference & Exhibition (2020)
- [J] **Mueller, S.**; Glang, F.; Scheffler, K.; Zaiss, M.: pH mapping of brain tissue by a deep neural network trained on 9.4T CEST MRI data: pH-deepCEST. 2020 ISMRM & SMRT Virtual Conference & Exhibition (2020)
- [K] **Mueller, S.**; Stirnberg, R.; Akbey, S.; Ehses, P.; Scheffler, K.; Stöcker, T.; Zaiss, M.: Snapshot whole brain CEST MRI at 3T with 3D-EPI. 2020 ISMRM & SMRT Virtual Conference & Exhibition (2020)
- [L] **Mueller, S.**; Deshmane, A.; Herz, K.; Scheffler, K.; Zaiss, M.: Development of whole-brain 3D snapshot CEST MRI at 3T. 27th Annual Meeting and Exhibition of the International Society for Magnetic Resonance in Medicine (ISMRM 2019), Montréal, QC, Canada (2019)
- [M] **Mueller, S.**; Glang F., Herz K., Scheffler K.; and Zaiss M.: MR-double-zero - Can a machine discover new MRI contrasts, such as metabolite concentration? 30th Annual Meeting and Exhibition of the International Society for Magnetic Resonance in Medicine (ISMRM 2022), London, GB (2022)

B. Appended Publications

B.1. Publication 1

On the interference from agar in chemical exchange saturation transfer MRI parameter optimization in model solutions

Mueller S., Scheffler K., and Zaiss M.

RESEARCH ARTICLE

On the interference from agar in chemical exchange saturation transfer MRI parameter optimization in model solutions

Sebastian Mueller¹  | Klaus Scheffler^{1,2} | Moritz Zaiss^{1,3} 

¹High-field Magnetic Resonance Center, Max Planck Institute for Biological Cybernetics, Tuebingen, Germany

²Department of Biomedical Magnetic Resonance, Eberhard Karls University Tuebingen, Tuebingen, Germany

³Department of Neuroradiology, University Hospital Erlangen, Erlangen, Germany

Correspondence

Sebastian Mueller, Max Planck Institute for Biological Cybernetics, High-field Magnetic Resonance Center, Max-Planck-Ring 11, 72076, Tuebingen, Germany.
Email: sebastian.mueller@tuebingen.mpg.de

Funding information

European Union's Horizon 2020 research and innovation programme, Grant/Award Number: 667510; German Research Foundation, Grant/Award Number: ZA 814/2-1

Chemical exchange saturation transfer (CEST) MRI is currently set to become part of clinical routine as it enables indirect detection of low concentrated molecules and proteins. Recently, intermediate to fast exchanging functional groups of glucose and its derivatives, glutamate and dextran, have gained attention as promising CEST contrast agents. To increase the specificity of CEST MRI for certain functional groups, the presaturation module is commonly optimized. At an early stage, this is performed in well-defined model solutions, in which, for instance, the relaxation times are adjusted to mimic in vivo conditions. This often involves agar, assuming the substance would not yield significant CEST effects by itself, which the current study proves to be an invalid assumption. Model solutions at different pH values and concentrations of agar were investigated at different temperatures at a 9.4 T human whole body MR scanner. High power presaturation of around 4 μ T, optimal for investigating intermediate to fast exchanging groups, was applied. Postprocessing included spatiotemporal corrections for B_0 and spatial corrections for B_1^+ . CEST effects of up to 3 % of the bulk water signal were observed. From pH, concentration and temperature dependency, it was concluded that the observed behavior reflects a CEST effect of agar. It was also shown how to remove this undesirable contribution from CEST MRI data. It was concluded that if agar is involved in the CEST MRI parameter optimization process, its contribution to the observed effects has to be taken into account. CEST agent concentration must be sufficiently high to be able to neglect the contribution of agar, or a control sample at matched pH is necessary for correction. Experiments on pure agarose showed reduced CEST effects compared with agar but did not provide a neutral baseline either.

KEYWORDS

CEST effect agar, CEST MRI parameter optimization, gluCEST MRI optimization, glutamate CEST

Abbreviations used: AP, anterior-posterior direction; CEST, Chemical Exchange Saturation Transfer; DC, duty cycle of (pulsed) CEST presaturation; HF, head-foot direction; LR, left to right; M_0 , MR image with far off-resonant CEST presaturation; M_{sat} , MR image after applying CEST presaturation; PBS, phosphate buffered saline; PE1, first phase-encoding direction; PE2, second phase-encoding direction; RO, frequency-encoding direction; t_p , duration of a single CEST presaturation pulse; $\delta\omega$, chemical shift relative to water (H₂O); $\Delta\omega$, frequency offset of CEST presaturation.

This is an open access article under the terms of the Creative Commons Attribution License, which permits use, distribution and reproduction in any medium, provided the original work is properly cited.

© 2020 The Authors. NMR in Biomedicine published by John Wiley & Sons Ltd

1 | INTRODUCTION

Chemical exchange saturation transfer (CEST) MRI enables noninvasive imaging of molecules and proteins at millimolar concentration in vivo. CEST effects occur after repeatedly applying off-resonant presaturation at the frequency offset of a proton pool that is in exchange with the bulk water protons.^{1,2} The resulting alteration of the bulk water signal through magnetization transfer can be detected by subsequent water proton MR image acquisition. In vivo, many different CEST active groups are apparent (e.g., see³⁻⁸). To increase the specificity for a certain CEST active proton pool, the presaturation module can be optimized. This is due to the fact that the CEST labeling efficiency depends on both the exchange rate of specific CEST pools and presaturation power.^{9,10} Recently glucose,¹¹ its derivatives,^{12,13} glucosamine,¹⁴ dextran¹⁵ and glutamate⁵, have gained attention as promising CEST MRI contrast agents. All of these five contrast agents have fairly high exchange rates of the order of a few kilohertz. This study will exemplarily investigate L-glutamic acid. Since the transfer of magnetization is governed by the exchange rates between the bulk water and the CEST pools, the CEST MRI signal is also sensitive to external parameters such as pH¹⁶ or temperature. Moreover, as CEST effects are measured indirectly via the bulk water signal, longitudinal and transversal relaxation time (T_1 , T_2) of the water pool also affect the CEST signal directly.¹⁷⁻²² Therefore, when in vivo optimization is not possible, it is necessary to perform the optimization of presaturation parameters in precisely defined model solutions that closely mimic in vivo conditions. At least T_1 , T_2 , pH, temperature and semisolid magnetization transfer have to be adjusted to ensure the optimized parameters transfer to in vivo application. To control the temperature of the sample is a rather technical task. The pH value may be adjusted using suitable base and acid combinations along with a buffer such as phosphate buffered saline (PBS). T_1 can be modified using paramagnetic MRI contrast agents. For modifications of T_2 , agar made its way into CEST MRI parameter optimization and is frequently used in model solutions. Besides altering T_2 , agar also introduces relaxation due to magnetization transfer effects.^{21,23,24} Adjustment of T_2 is of major importance for the optimization process, since T_2 directly influences spillover effects,¹⁹ which will finally be reflected in the presaturation module optimized for a specific CEST pool. All substances used to adjust the external parameters of the model solutions share one prerequisite: they should not introduce significant, specific CEST effects themselves. For agar this was implicitly—in some cases even explicitly—assumed to be generally fulfilled. To date, only Li et al. have explicitly mentioned a significant proton exchange-related contribution of agar to the CEST MRI signal, but they did not provide any further discussion on this issue.²⁵ Besides that study, an exchange rate of 4 kHz in agarose samples at an acid pH of 3.5 was reported by Chávez and Halle²⁶ when characterizing the exchange-mediated orientational randomization (EMOR)²⁷ model on MR spectrometers. In the current study, the contribution of agar to the observed CEST MRI signal was investigated in detail. This was carried out at a 9.4 T human whole body MR system at in vivo-like pH, T_1 and T_2 values using an established gradient echo-based CEST MRI sequence²⁸ as it is also applied in vivo. With this setup it was shown that agar does not provide a neutral baseline for CEST MRI parameter optimization prior to translating the latter to in vivo. It was exemplarily demonstrated that optimizing the presaturation of CEST MRI for the CEST effect of L-glutamic acid was significantly biased by agar and provided misleading optimization results. So although agar was successfully used in model solutions for CEST MRI in the past, its CEST effect has to be taken into account again when faster exchanging agents are studied. Especially at a higher field, these have become increasingly important over the last few years. The detailed characterization of the observed CEST effects of agar help to interpret and correct the results of L-glutamic acid obtained in agar gels.

2 | EXPERIMENTAL

2.1 | Preparation of model solutions

Model solutions were prepared using agar (Agar-Agar, Kobe I, powdered, for microbiology, art. no. 5210.1, Carl Roth, Germany) that was dissolved in 1X PBS (prepared according to²⁹ but containing only KCl, Na_2HPO_4 , KH_2PO_4 and 140 mmol/L NaCl). After boiling, the pH value was adjusted while the mixture cooled down to $\sim 44^\circ\text{C}$ under constant stirring. To minimize dilution, hydrochloric acid (HCl) and sodium hydroxide solution (NaOH) were both applied at 1 mol/L concentration (Sigma-Aldrich Laborchemikalien, Germany, and Fisher Scientific, UK). The pH value was monitored along with temperature using a pH electrode with an integrated temperature sensor (inoLab pH 720, WTW, Germany). To set T_1 to in vivo-like values, 0.105 mmol/L gadoteric acid (gadoterate meglumine [dotarem 500 mmol/L], Guerbet, Germany) was added. If the model solution contained 10 mmol/L L-glutamic acid (Fluka Chemie, Switzerland), the latter was added at a temperature below 44°C to avoid damaging the molecule. Afterwards, the mixture was cooled further and solidified on an orbital shaker (Titramax 100, Heidolph Instruments, Germany) or was centrifuged for around 4 seconds at 3490 rpm (Multifuge 1 S-R, Heraeus, Germany) to remove residual air bubbles.

In addition, model solutions were made from pure agarose (Agarose NEEO ultra-quality, art. no. 2267.2, Carl Roth, Germany) in the same manner as described for agar. Agarose is a polysaccharide and together with agaropectin forms agar. These samples also contained 0.105 mmol/L gadoteric acid to reduce T_1 values.

2.2 | CEST MRI parameters

Measurements were performed at a 9.4 T ultra-high field, human whole body MR scanner (Magnetom 9.4 T, Siemens Healthineers, Erlangen, Germany) using a custom-built 18/32 Tx/Rx head coil.³⁰ To maintain stable temperatures ($\Delta T_{\max} \sim 1$ K) during the measurements, a thermos jug was used, in which the model solutions were placed on a custom-built, circular-shaped rack surrounded by water that contained ~ 50 mmol/L sodium chloride.

MRI was performed using a 3D gradient echo-based sequence (centric reordered, rectangular-spiral readout) realized in a snapshot manner.²⁸ The basic sequence parameters were: flip angle (FA) = 5° , TE/TR = 1.91/3.76 ms, nominal matrix size $96 \times 78 \times 8$ (RO = AP \times PE = LR \times 3D = HF; GRAPPA = 2) with FOV = $147 \times 119 \times 40$ mm³. The presaturation module consisted of five Gaussian-shaped $t_p = 100$ ms pulses at a duty cycle (DC = $t_p/(t_p + t_d)$; t_d : delay after single pulse) of 50% or matched adiabatic spinlock pulses³¹ with the same duration and DC. The adiabatic tipping pulses swept over a bandwidth of 3 kHz and took 8 ms both for tip-up/-down and only the locking time is considered as t_p . The spinlock pulses were chosen because they provide reduced direct water saturation and are beneficial in terms of specific absorption rate (SAR) compared with Gaussian pulses. This is because the rectangular locking pulse requires a lower peak B_1 compared with a Gaussian-shaped pulse. The resulting Fourier width of both the spinlock and Gaussian-shaped pulses was $1/t_p = 10$ Hz (Figure S1). For the widths of the resonances in the Z-spectrum, it is the continuous wave power equivalent which is important and not the pulse duration (e.g., see³²). The continuous wave power equivalent was found to be 20% smaller for the spinlock pulses (see the supporting information for more details). The transmit B_1 (B_1^+) values stated in this study are the average B_1^+ values of a single presaturation pulse, such that $FA = t_p B_1^+ \gamma$ independent of the pulse shape. The presaturation offset list can be found in the supporting information. For both pulse types the recovery times for un-/saturated images were 12/5 seconds. All measurements were performed for three different nominal B_1^+ values to enable interpolation-based B_1^+ -correction.³³ Interleaved WASABI³⁴ scans (single rectangular pulse of duration $t_p = 3.7$ ms at $B_1^+ = 5$ μ T; recovery times [un-/saturated]: 12/5 ms) before and after each CEST acquisition were performed to track spatiotemporal changes of the static magnetic field. Image readout parameters for WASABI were the same as for the CEST acquisitions and data were acquired with the same 3D gradient echo-based sequence.

2.3 | Data evaluation

Unless stated otherwise, data were normalized, including multiple unsaturated images (M_0). These were acquired before the first, after half of all, and after the last saturated image. During postprocessing the intensities of the different M_0 images were interpolated (linear) to match the acquisition times of the saturated images. This yielded an individual $M_{0,i}$ for each presaturation offset i . So each saturated image was normalized to $Z_i = M_{\text{sat},i}/M_{0,i}$. Afterwards, data were corrected for spatiotemporal changes in $\Delta B_0(r,t)$ ³⁵ combining the different $\Delta B_0(r)$ maps derived from the interleaved WASABI scans. Next, data were corrected for spatial inhomogeneity in transmit $B_1^+(r)$ using averaged relative B_1^+ maps derived from WASABI scans by a two-point Z- B_1 correction³³ including data acquired at three different nominal B_1^+ . Since the observed CEST effects were located close to the water resonance ($\delta\omega < 2$ ppm) and no discrete peaks could be resolved, a simple and therefore meaningful asymmetry analysis² was performed on the corrected Z-spectra³⁶

$$\text{MTR}_{\text{asym}} = \frac{M_{\text{sat}}(-\Delta\omega) - M_{\text{sat}}(+\Delta\omega)}{M_0}$$

This is justified if (a) inhomogeneity of B_0 was completely corrected, (b) measurement was stable over time and (c) the Z-spectrum does not contain multiple pools both up- and downfield of the bulk water resonance.

2.3.1 | Bloch-McConnell simulations

To determine the approximate CEST effect of agar at a clinically more popular field strength of 7 T, the Bloch-McConnell equations were simulated numerically.³⁷ To determine suitable parameters, both measurements at 3 and 9.4 T were modeled with the same CEST and ssMT pool parameters but different longitudinal and transversal relaxation rates for the water pool. Afterwards, these values were interpolated to 7 T and the simulations were performed again. Additionally, the data measured at 3 and 9.4 T were directly interpolated to 7 T for comparison. Detailed model parameters can be found in the supporting information.

3 | RESULTS

3.1 | Agar

Figure 1 shows the effect of the suggested postprocessing on Z-spectra. It was found that normalization including multiple M_0 scans (yellow line) reduced MTR_{asym} for larger offsets compared with normalization including only a single M_0 image (orange line). The effect of both spatial $\Delta B_0(r)$ and spatiotemporal $\Delta B_0(r,t)$ correction (blue and purple lines) was most prominent directly around 0 ppm, where it shifted MTR_{asym} from negative to positive values. Comparing both methods, the spatiotemporal correction gave reduced MTR_{asym} values (Figure 1C). The applied $\Delta B_1^+(r)$ correction (black line) did not substantially alter either the Z-spectra or MTR_{asym} in addition to the $\Delta B_0(r,t)$ correction in this particular case.

To make sure the observed MTR_{asym} effects were not caused by contributions of PBS, NaOH, HCl or gadoteric acid, measurements of samples that contained solely these compounds were performed (Figure 2). For these samples pH was adjusted to comparable values between 6.90 and 7.00 and the measurement was performed at 25°C. Figure 2B shows that neither PBS, NaOH, HCl nor gadoteric acid yielded a maximum MTR_{asym} of more than 0.4%, but 2% (w/w) agar caused an almost 10-fold larger maximum MTR_{asym} of 3.3%. In Figure 2C,D the same samples are shown for Gaussian-shaped instead of matched adiabatic spinlock pulses but with identical nominal $B_1^+ = 4 \mu\text{T}$, t_p and number of pulses. The average of absolute values of MTR_{asym} in the range of 0.5 to 10.0 ppm over samples that contained no agar was $(0.08 \pm 0.02) \%$ for Gaussian and $(0.18 \pm 0.04) \%$ for matched adiabatic spinlock pulses. For the sample that contained agar the same metric revealed 1.05% and 1.43% of average MTR_{asym} . In all cases, data were processed according to the suggested full postprocessing as described above and evaluated at a corrected B_1^+ of $4 \mu\text{T}$. From Figure 2A,C it can be observed that for some of the samples the Z-values do not approach $Z = 1$, even for offsets farther away from

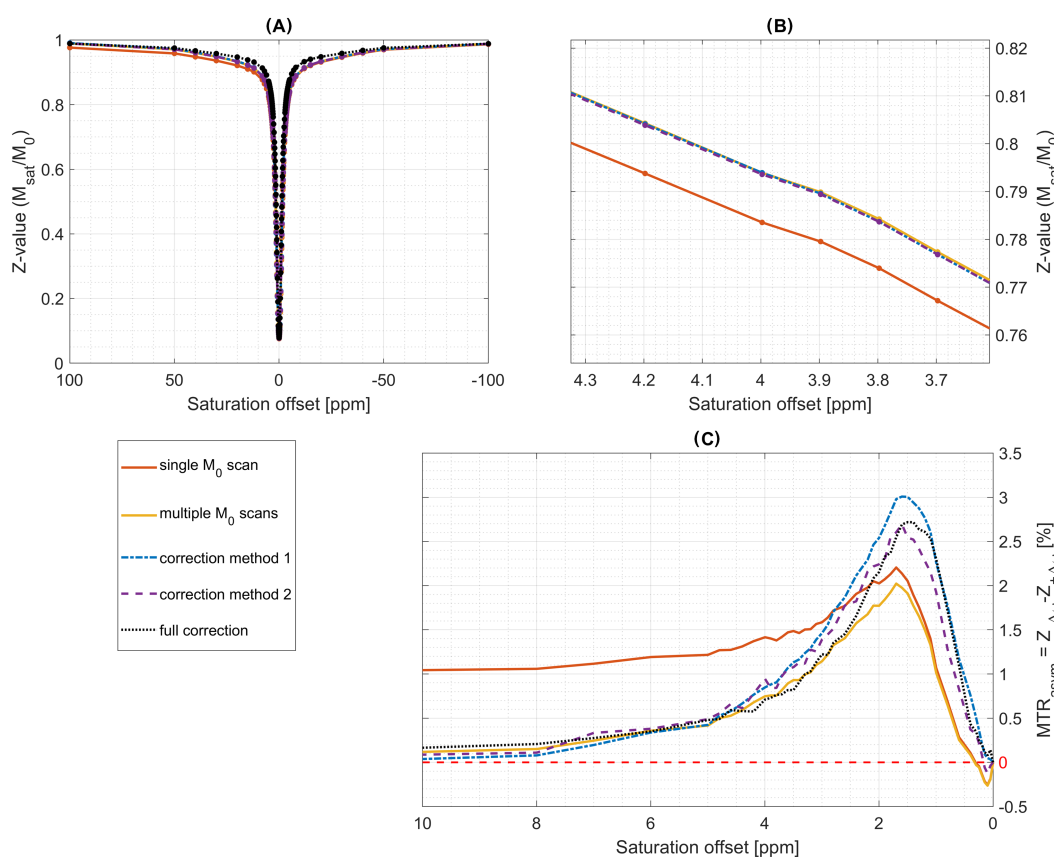


FIGURE 1 A, effect of different postprocessing methods on Z-spectra of agar. B, the Z-spectra in an 0.72 ppm presaturation offset interval to emphasize differences between the postprocessing stages. C, the resulting MTR_{asym} for different postprocessing and the red dashed line highlights $MTR_{\text{asym}} = 0$. Key: “single M_0 scan”/orange – no ΔB_0 or ΔB_1^+ correction and single M_0 scan for normalization; “multiple M_0 scans”/yellow – no ΔB_0 or ΔB_1^+ correction but using three interleaved M_0 scans for normalization; “correction method 1”/blue – additionally including $\Delta B_0(r)$ correction; “correction method 2”/purple – not only $\Delta B_0(r)$ but spatiotemporal $\Delta B_0(r,t)$ correction included; “full correction”/black – $\Delta B_0(r,t)$ and $\Delta B_1^+(r)$ correction included. Data acquired at $B_0 = 9.4 \text{ T}$ and $T = 37^\circ\text{C}$ using $5 \times 100 \text{ ms}$ matched adiabatic spinlock pulses with $DC = 50\%$. All samples contained 2.0% (w/w) of agar, 1 X PBS and $\sim 0.1 \text{ mmol/L}$ gadoteric acid with adjusted $\text{pH} = 7.00$ at 43.5°C

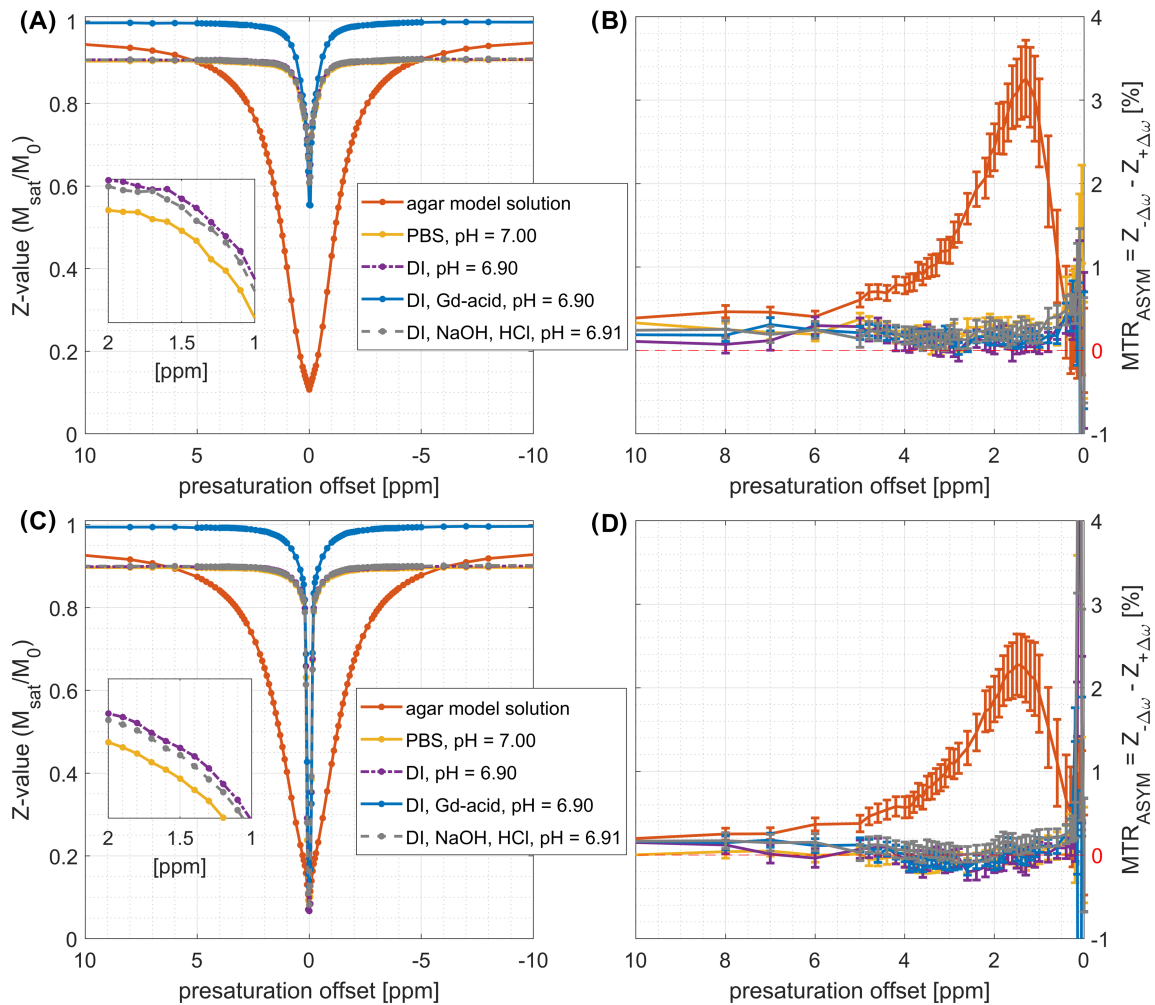


FIGURE 2 A, Z-spectra for different model solutions: orange – 2% (w/w) of agar, 1 X PBS, 0.1 mmol/L gadoteric acid at pH = 7.01; yellow – 1 X PBS at pH = 7.00; purple – deionized water at pH = 6.90; blue – deionized water, 0.1 mmol/L gadoteric acid at pH = 6.90; black – deionized water, hydrochloric acid, sodium hydroxide at pH = 6.91. Measured at $B_0 = 9.4$ T and $T = 25^\circ\text{C}$ using 5×100 ms matched adiabatic spinlock pulses with DC = 50%, $B_1^+ = 4$ μT . B, the associated MTR_{ASYM} of the same samples. In C and D, the same samples were measured under the same conditions upon presaturation using a train of Gaussian-shaped pulses. All data were measured with three interleaved M_0 scans and corrected both for $\Delta B_0(r,t)$ and $\Delta B_1(r)$

water of around ± 10 ppm. This is a known relaxation effect, because some samples (the ones without gadoteric acid) had long T_1 of ~ 3.2 seconds but the recovery times were 5.5 seconds, which prevented full relaxation in these cases. More data on this observation can be found in Figure S4.

Figure 3 shows Z-spectra of agar samples acquired at 9.4 T including the described postprocessing along with the determined MTR_{ASYM} for different temperatures (25°C in A and B and 37°C in C and D) and pH values. Twice as high maximum MTR_{ASYM} was observed for lower temperature at nominal pH = 7.40 (Figure 3E). The maximum value of MTR_{ASYM} constantly increased with decreasing pH at 37°C (Figure 3E). Compared with this, MTR_{ASYM} was found to be rather stable across pH at 25°C with overall higher maximal values (Figure 3E). This temperature dependency of MTR_{ASYM} at different pH values reveals more details of the underlying exchange reaction, as explained below.

First, MTR_{ASYM} , as a function of the exchange rate (k_{ex}), increases with k_{ex} if $k_{ex} < \gamma B_1$ (correlation), but decreases with k_{ex} if $k_{ex} > \gamma B_1$ (anticorrelation).³² Second, in the majority of cases, exchange rates correlate with temperature³⁸ (Arrhenius equation), which is also assumed here. Additionally, in³ increasing k_{ex} was confirmed experimentally for various exchangeable groups. As decreasing MTR_{ASYM} was observed with higher temperature and therefore higher exchange rate (anticorrelation), it can be concluded that the exchange reaction was in the regime $k_{ex} > \gamma B_1$. The fact that MTR_{ASYM} values at 25°C were almost unaffected by pH indicates that the exchange reaction was close to the regime of maximum possible MTR_{ASYM} , where $k_{ex} = \gamma B_1$ ($B_1 = 4$ μT in this study).

At 37°C , MTR_{ASYM} values showed highest signal for lowest pH. As MTR_{ASYM} was still anticorrelated with k_{ex} , this means that the exchange rates correlate with pH. This makes the exchange reaction base-catalyzed.

The average observed shift in offset position of maximum MTR_{ASYM} (Figure 3F) was 0.1 ppm, which was around four times smaller than the average shift introduced by altered concentrations (Figure 4F).

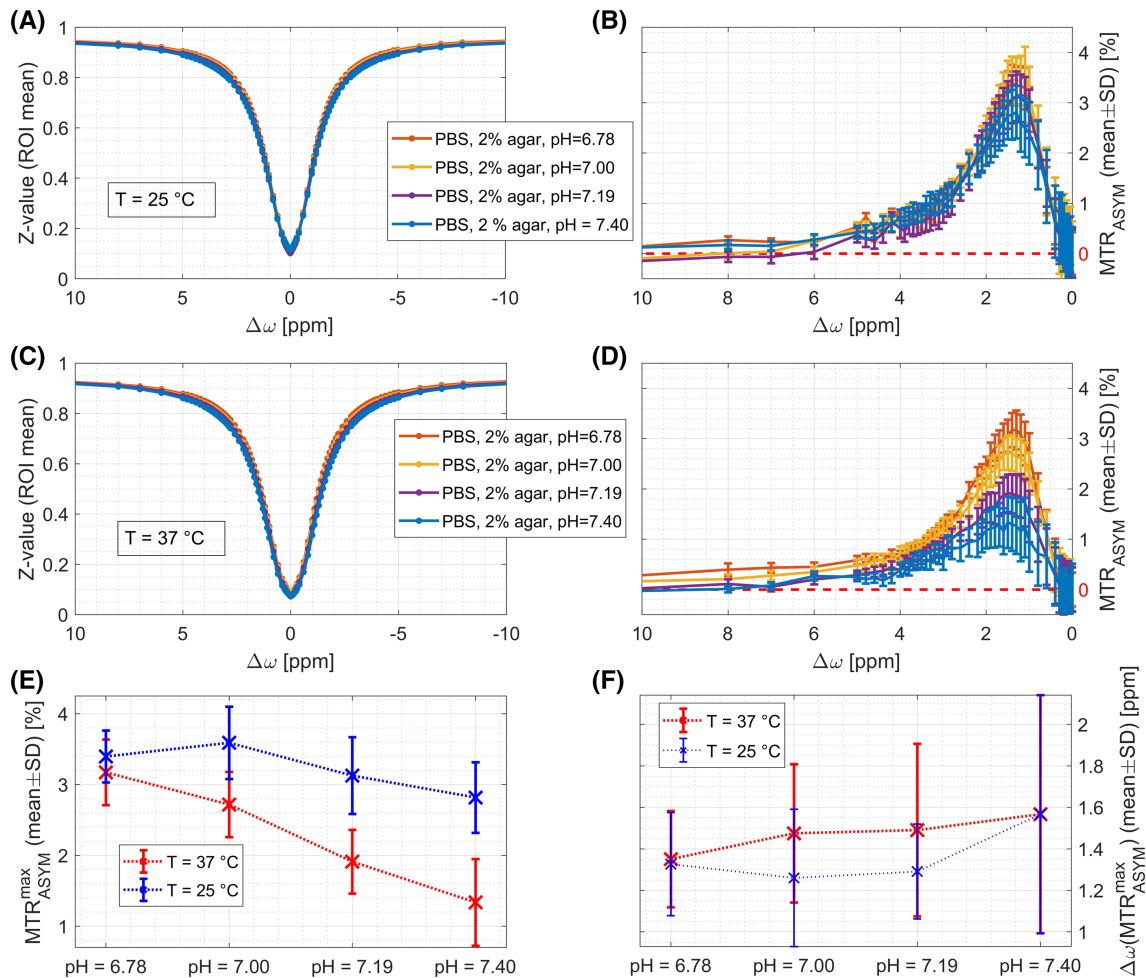


FIGURE 3 Model solutions of agar with different pH values measured at $B_0 = 9.4$ T and $T = 25/37$ °C. Upper row shows A, Z-spectra and B, MTR_{asym} at $T = 25$ °C. A temperature of $T = 37$ °C is shown in C and D. The last row shows E, the maximum observed MTR_{asym} value and F, its offset position. The axis limits of B and D are similar to those in Figure 4B,D for better comparability. Presaturation module: 5×100 ms matched adiabatic spinlock pulses (DC = 50%). Data were acquired including three interleaved M_0 scans and corrected both for $\Delta B_0(r,t)$ and $\Delta B_1(r)$ with linear Z- B_1 correction to $B_1^+ = 4$ μ T

Z-spectra and MTR_{asym} values for different concentrations and temperatures at constant pH are shown in Figure 4A,B, again for 25°C (A and B) and 37°C (C and D). All the samples were measured at the same time but over two different sessions for the different temperatures. The maximum MTR_{asym} value, in general, increased with agar concentration (Figure 4E), on average by 18%, increasing from 1.0% to 2.5% (w/w) of agar. Whereas for low concentrations (increasing from 1.0% to 1.5% of agar) it did not change significantly ($P > 0.9$), it increased by $\sim 13\%$, increasing from 1.5% to 2.0% (w/w) agar. The observed changes in maximum MTR_{asym} were significant at a global $\alpha = 0.003$ (Holm-Bonferroni method) for pairwise comparison of concentrations except for the comparison of 1.0% and 1.5% (w/w). MTR_{asym} was evaluated in single voxels at the presaturation frequency of maximum MTR_{asym} of the ROI-averaged Z-spectrum. The frequency offset of maximum MTR_{asym} shifted away from the bulk water resonance at 0 ppm for both temperatures as the agar concentration increased (Figure 4F). Shifts were 0.4 and 0.6 ppm for 25 and 37°C, respectively. More linear shift dependence on concentration was observed for higher temperatures.

The conclusions derived from maximum MTR_{asym} could also be confirmed analyzing the area under the curve (AUC) of MTR_{asym} within 0.5 to 4.0 ppm. This metric should be more stable against noise, though maximum MTR_{asym} already represented a ROI average. The associated results are shown in Figure S10.

To determine the undesired contribution of agar to the observed CEST effect of L-glutamic acid, model solutions with matched pH values both with and without agar were investigated. As can be seen from Figure 5, the position of maximum MTR_{asym} value shifted 0.7 ppm away from water when T_2 was reduced from (525 ± 131) ms to more in vivo-like values of (60 ± 15) ms using agar (T_2 values determined from repeated 2D spin echo sequences with different T_E). Still, the absolute maximum value was reduced by less than 2% due to adjusted T_2 . For the sample in which T_2 was not adjusted, two peaks can be seen in MTR_{asym} . This is due to chemical shift averaging, as described by Cai et al.⁵ and can be understood by $T_{1\rho}$ theory (see equation 23 in Zaiss et al.¹⁹). To isolate the contribution of agar in these data, a control sample without L-glutamic

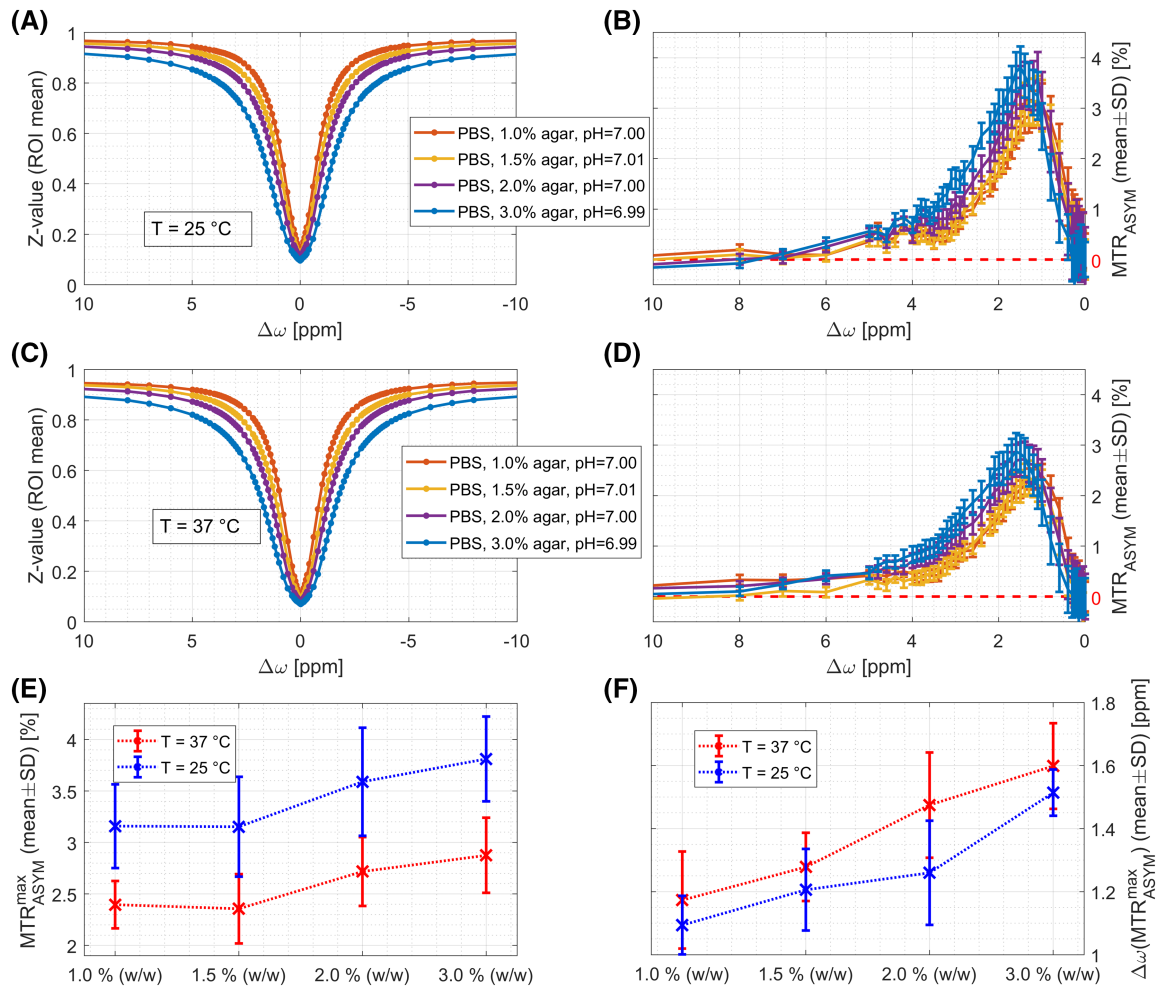


FIGURE 4 Different concentrations of agar measured at $B_0 = 9.4$ T and $T = 25/37^\circ\text{C}$. Upper row shows A, Z-spectra and B, MTR_{ASYM} at $T = 25^\circ\text{C}$. A temperature of $T = 37^\circ\text{C}$ is shown in C and D. The last row shows E, maximum observed MTR_{ASYM} value and F, its offset position. The axis limits of B and D are similar to those in Figure 3B,D for better comparability. Presaturation module: 5×100 ms matched adiabatic spinlock pulses (DC = 50%). Data were acquired including three interleaved M_0 scans and corrected both for $\Delta B_0(r,t)$ and $\Delta B_1^+(r)$ with linear Z-B1 correction to $B_1^+ = 4 \mu\text{T}$

acid was created and Z-values were subtracted from the referring Z-spectrum of the sample that contained agar and L-glutamic acid. It was found that the maximum MTR_{ASYM} decreased by 50% when the contribution of agar was removed (Figure 5B, green curve). This leads to two important conclusions. First, it was shown that (as expected from theory) T_2 does significantly affect the observable CEST effect of L-glutamic acid. And second, without taking into account the CEST effect of agar, one could have falsely concluded that the applied presaturation would yield nearly identical MTR_{ASYM} independent of T_2 .

From the Bloch-McConnell simulations (Figures S2 and S3) it was estimated that 2.0% (w/w) of agar should result in maximum MTR_{ASYM} of the order of 2% at $B_0 = 7$ T given a saturation with 5×100 ms matched adiabatic spinlock pulses at $B_1 = 4 \mu\text{T}$, DC = 50%. It was found that both simulations and straightforward interpolation of 3 and 9.4 T data yielded comparable results even although the experimentally applied saturation differed in terms of number of pulses ($n = 4$ at 3 T vs. $n = 5$ at 9.4 T).

3.2 | Pure agarose

The agarose samples were measured with the same matched adiabatic spinlock pulses used for the agar samples: DC = 50%, $t_p = 100$ ms, $B_1^+ = 4 \mu\text{T}$. Again, all samples were measured at both 25°C and 37°C . A detailed presentation of the Z-spectra and MTR_{ASYM} for different concentrations and pH values of pure agarose is shown in Figures S5 and S6. It was found that the agarose samples yielded on average 61% / 56% lower maximum MTR_{ASYM} for the same concentrations measured at $25^\circ\text{C}/37^\circ\text{C}$ (Figure 6A,B) compared with agar. The maximum MTR_{ASYM} observed in pure agarose was between 0.9% and 1.4%.

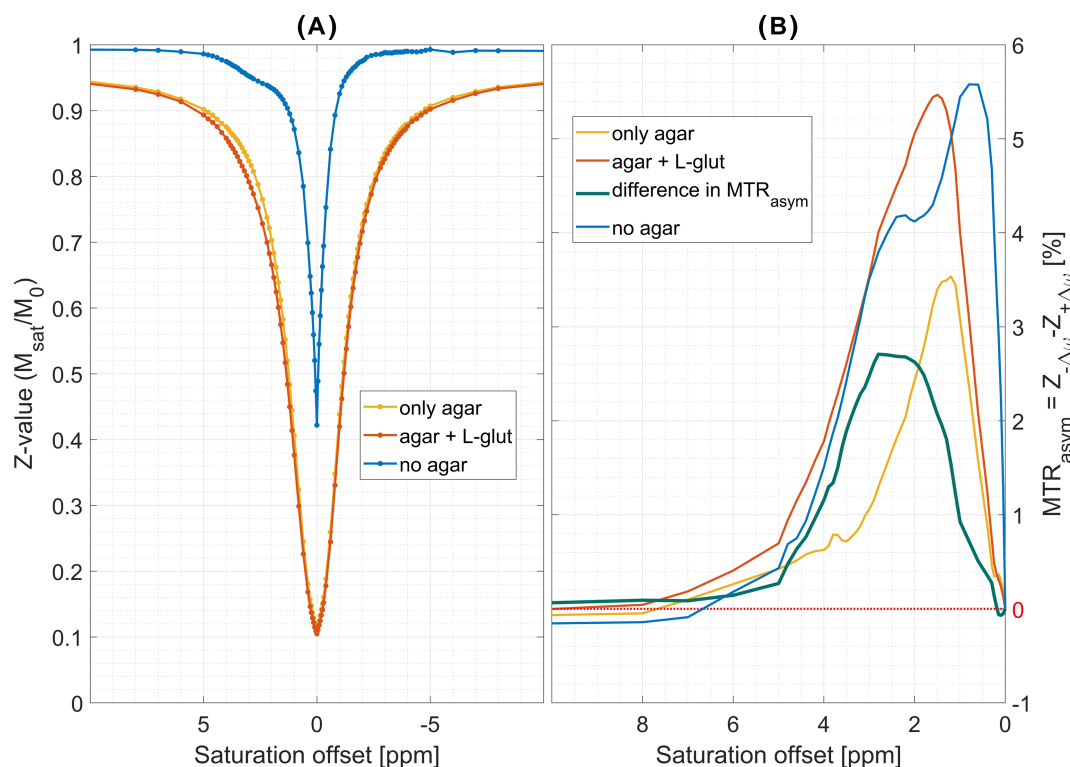


FIGURE 5 A, Z-spectra with (orange line) 10 mmol/L L-glutamic acid or without (yellow line). Both samples contained 2% (w/w) agar and 1 X PBS as buffer and 0.1 mmol/L gadoteric acid. pH was adjusted to pH = 7.00 in both samples. The blue line shows a sample with the same amount of L-glutamic and gadoteric acid but without agar (pH = 6.99). T_2 for this sample was (525 ± 131) ms and decreased to (60 ± 15) ms after adding agar. B, the corresponding MTR_{asy} values of the samples and in addition the isolated MTR_{asy} of L-glutamic acid with the agar contribution removed by subtraction (green line). Presaturation: 5×100 ms matched adiabatic spinlock pulses at DC = 50%, $B_1^+ = 4 \mu\text{T}$. Measurement at 9.4 T at 25°C with full postprocessing as described in the Experimental section

At different pH values, the maximum MTR_{asy} was reduced on average by 60% for $T = 25^\circ\text{C}$ in pure agarose compared with agar (Figure 6C). For higher temperatures, MTR_{asy} showed a stronger dependency on pH for agar compared with the dependency observed for agarose (Figure 6D). MTR_{asy} showed a slight increase of $\Delta MTR_{\text{asy}} = 0.25\%$ when going towards more alkaline pH in agarose. For agar it decreased by $\Delta MTR_{\text{asy}} = 1.26\%$ over the same range of pH (Figure 6D).

As both agar and agarose may be used to adjust T_2 in model solutions, their influence on T_2 was compared (Figure S7A). It was found that at the same pH and concentration, both compounds yielded the same T_2 values. While the T_2 values did depend on the concentration, they were not significantly different within the investigated pH range (Figure S7B). The latter remark holds true for both pure agarose and agar, each at a global significance level of $\alpha = 0.05$.

4 | DISCUSSION

The observed MTR_{asy} did not vanish even after application of multiple corrections during postprocessing (Figure 1). This proved that there is indeed a significant CEST contribution from agar that can be detected even with CEST MRI at a human whole body scanner. At the same time, control experiments did not yield significant MTR_{asy} (Figure 2B,D) for samples that did not contain agar. This assured that no contribution from substances other than agar, which were used to adjust T_1 and pH, could be detected. The employed gadoterate meglumine had five potentially exchangeable hydroxyl groups per molecule, but still no significant MTR_{asy} was observed. This could be attributed to the fact that the concentration necessary to decrease T_1 to in vivo-like values is very low (~ 0.1 mmol/L) and that exchange rates could potentially be very high. Therefore, a possible contribution could be expected to be not significant. This would be tolerable for optimization of CEST MRI parameters. Regarding the pulse shape, it was first shown that both Gaussian-shaped and matched adiabatic spinlock pulses yielded consistent results (Figure 2). Still, the matched adiabatic spinlock pulses provided 45% higher maximum MTR_{asy} , which is related to a reduced spillover contribution, which made it easier to investigate the CEST effects of agar.

The influence of pH, concentration and temperature further supported the hypothesis that agar shows a specific, significant CEST effect under in vivo-like conditions. The observed MTR_{asy} increased for more acid pH values at 37°C but was more stable at 25°C (Figure 3). This is

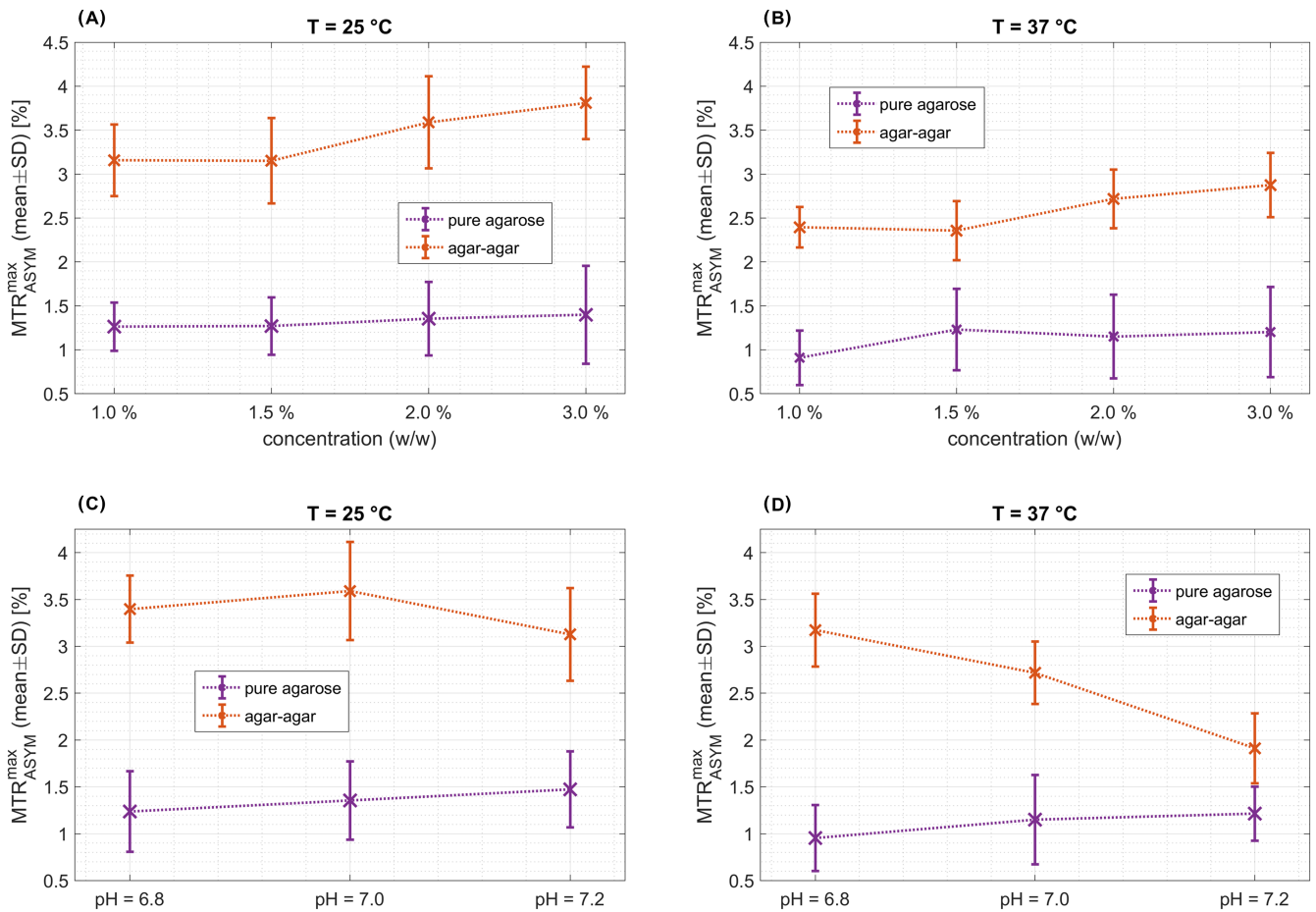


FIGURE 6 Comparison of data acquired in both agar and agarose at different pH values and concentrations for $T = 25^{\circ}\text{C}$ and 37°C . CEST presaturation consisted of 5×100 ms matched adiabatic spinlock pulses at $\text{DC} = 50\%$, $B_1^+ = 4 \mu\text{T}$. Full Z-spectra are shown in Figures 3 and 4, S5 and S6

because both temperature and pH are able to alter exchange rates and may balance with each other. For increasing agar/agarose concentrations T_2 was decreased (Figure S7A), which pronounced spillover effects. The latter is why adjusting T_2 properly in model solutions is of major importance for presaturation parameter optimization. As the concentration of agar increased, the contribution of semi-solid magnetization transfer also increased, to a factor of 2.8 (Figure S8).

It was observed that both MTR_{ASYM} and the frequency offset of maximum MTR_{ASYM} depended on the agar concentration (Figure 4). The shift of maximum observed MTR_{ASYM} is expected as the spectrum becomes broader for shorter T_2 . In particular, this interplay of both scaled CEST pool size, and because of this the modified T_2 -related spillover effects for different agar concentrations, might cause problems if one is actually optimizing parameters for another CEST pool. For instance, for concentrations of 1.0% and 1.5% (w/w), the maximum MTR_{ASYM} value was stable but increased by 13% for an additional 0.5% (w/w) of agar. This was most likely due to the fact that increased spillover effects at lower concentrations still counterbalanced the effects of increased pool size. The AUC (Figure S10) at 25°C already showed a significant ($P < 0.05$) increase for a concentration of 1.5% compared with one of 1.0% (w/w). This demonstrates that it is not trivial to predict the expected behavior of the agar CEST contribution in model solutions, especially if different presaturation schemes are to be compared. At least it could be concluded that for the pH (6.8 to 7.4) and concentration (1.0%-2.5% w/w) ranges studied, the underlying exchange rates are base-catalyzed, which might be of interest depending on the behavior of the other CEST pools for which parameters should actually be optimized.

The contribution of agar at lower powers ($B_1^+ < 1 \mu\text{T}$) may be negligible (Figure S9). On the other hand, recently published studies that deal with glucose or its chemical derivatives rely on high power presaturation for CEST MRI. Also, other compounds, such as glutamate^{5,39} need a high presaturation power of $\sim 3 \mu\text{T}$. In the current study, continuous wave power equivalents of 2.8 and $3.4 \mu\text{T}$ for spinlock and Gaussian-shaped pulses were applied for a total saturation duration of 1 second. Given the SAR restrictions at 9.4 T, this was comparable with the continuous wave saturation ($B_{1,\text{rms}} = 3.6 \mu\text{T}$, optimal $t_{\text{sat}} = 1$ second) that Cai et al.⁵ reported for in vivo GluCEST imaging at $B_0 = 7$ T.

As an alternative to agar one may use pure agarose, which has also been used in previous CEST MRI studies. We found that the use of pure agarose instead of agar can be beneficial as it showed less than half of the MTR_{ASYM} observed for agar. Still, with maximum MTR_{ASYM} of up to 1.4%

for certain concentrations and pH values, it does not yet provide a fully neutral baseline for CEST parameter optimization. In terms of adjusting T_2 it was found that both agar and agarose performed equally well. Therefore, pure agarose should be preferably chosen when performing parameter optimization for CEST MRI in model solutions.

Regarding the origin of the CEST effect, hydroxyl groups may be responsible for the observed saturation transfer. These are known for rather high exchange rates and resonate close to the bulk water (e.g., Jin et al.⁴⁰), which is what was observed in the current study. Furthermore, agarose, which makes up the main part of agar, has five exchangeable hydroxyl groups (e.g., see Gamini et al.⁴¹) that could contribute. The observed effects in pure agarose were smaller in terms of both AUC and maximum MTR_{asym} compared with agar. This shows that agarose by itself probably does not provide all the exchanging sites observed in agar. Agar is derived from a natural product and also contains agaropectine. It is therefore likely that additional exchanging sites are available. Still, the exact composition of agaropectine is unknown and the spectral resolution of CEST MRI does not enable any further insights. Therefore, it is not possible to exactly assign a particular exchanging group to the observed effects.

It should also be emphasized that the applied postprocessing is crucial, especially when MTR_{asym} is evaluated. For instance, even spatial $\Delta B_0(r)$ or spatiotemporal $\Delta B_0(r,t)$ correction³⁵ yielded a 10% difference in MTR_{asym} (Figure 1C).

This study benefited from the availability of an ultra-high field 9.4 T whole body MR scanner that is not typically used in clinical CEST MRI studies. However, also at 3 T (Prisma^{fit}, Siemens Healthineers, Erlangen, Germany), MTR_{asym} of up to 0.5%, most likely originating from agar, was observed (Figure S11). Due to reduced absolute frequency separation at lower field strength, CEST pools resonating close to the bulk water are strongly affected by spillover, making quantification challenging. From the 3 T data alone it would not have been possible to characterize the CEST contribution of agar and agarose. Still, it was at least shown that the AUC of MTR_{asym} differed significantly from zero ($P < 0.001$) in the case of agar, but not for the control sample without agar ($P > 0.5$). Small effect sizes will occur for all CEST effects, but not only for agar or agarose at lower field strength. Although it will not be obvious to see, it is even more important to be aware that there is a possible contribution from agar and/or agarose, even at 3 T. As an estimate for the effect size at more commonly used 7 T scanners, numerical simulations of the Bloch-McConnell equations showed that the expected effect (maximum observed MTR_{asym}) size for an identical saturation scheme was reduced by ~30% compared with 9.4 T.

To show that neglecting the CEST effect of agar can lead to errors when optimizing CEST MRI parameters in model solutions, samples containing 10 mmol/L glutamic acid were prepared exemplarily. As shown, the effect of agar contributed 50% to the observed maximum MTR_{asym} (Figure 5B). Considering MTR_{asym} at 3 ppm, it was found that the observed MTR_{asym} (3 ppm) value originated from agar by one-third and from glutamic acid by two-thirds. This means that even although larger contributions from agar were found closer to water, for offsets farther away, the contribution also remains significant. It is also shown (see the supporting information) that for the discussed setup the relaxation-compensated MTR_{ex} and MTR_{asym} provide the same results with regard to the relative contribution of agar. The contribution of agar to CEST MRI depended on B_1^+ , pH, concentration and temperature in a nonlinear manner (Figures 3 and 4, Figure S9). To remove its contribution, a baseline sample which contained no glutamic acid was suggested for correction. Another way to bypass the bias introduced by agar would be to find another suitable way to modify T_2 in CEST model solutions. On the other hand, there are many practical reasons which encourage the continued use of agar for the creation of CEST MRI model solutions. Therefore, we suggest creating control samples with corresponding pH, T_1 and T_2 values to correct for the bias attributable to agar in CEST MRI parameter optimization by simply subtracting the corresponding Z-values. As agarose displayed ~50% smaller CEST effects, instead of using agar, pure agarose should be chosen as the first step in model solutions.

5 | CONCLUSION

The presented findings proved that agar shows a significant CEST effect for in vivo-like pH and temperature at a human MR scanner. Therefore, it does not a priori provide a neutral baseline for CEST MRI parameter optimization in the case of strong presaturation. CEST effects of agar showed a complex dependency on the interplay of concentration, pH, temperature and B_1^+ , which made the creation of control samples necessary. Otherwise, misleading results in presaturation parameter optimization may be derived, as well as incorrectly assigned CEST effect strengths. It was exemplarily shown—and corrected using the control sample—that for 10 mmol/L glutamic acid, 50% of the observed MTR_{asym} was due to agar. It was also found that pure agarose yields 50% reduced CEST effects compared with agar and is therefore preferable when creating model solutions.

FUNDING INFORMATION

The financial support of the Max Planck Society, German Research Foundation (DFG, grant ZA 814/2-1), and European Union's Horizon 2020 research and innovation programme (grant agreement no. 667510), is gratefully acknowledged.

ACKNOWLEDGEMENTS

The financial support of the Max Planck Society, German Research Foundation (DFG, grant ZA 814/2-1), and European Union's Horizon 2020 research and innovation programme (grant agreement no. 667510), is gratefully acknowledged. Open access funding enabled and organized by Projekt DEAL.

ORCID

Sebastian Mueller  <https://orcid.org/0000-0003-2699-9214>Moritz Zaiss  <https://orcid.org/0000-0001-9780-3616>

REFERENCES

1. Wolff SD, Balaban RS. NMR imaging of labile proton exchange. *J Magn Reson.* 1990;86(1):164-169.
2. Guivel-Scharen V, Sinnwell T, Wolff SD, Balaban RS. Detection of proton chemical exchange between metabolites and water in biological tissues. *J Magn Reson.* 1998;133(1):36-45.
3. Liepinsh E, Otting G. Proton exchange rates from amino acid side chains— implications for image contrast. *Magn Reson Med.* 1996;35(1):30-42. <https://doi.org/10.1002/mrm.1910350106>
4. Zhou J, Payen J-F, Wilson DA, Traystman RJ, van Zijl PCM. Using the amide proton signals of intracellular proteins and peptides to detect pH effects in MRI. *Nat Med.* 2003;9(8):1085-1090. <https://doi.org/10.1038/nm907>
5. Cai K, Haris M, Singh A, et al. Magnetic resonance imaging of glutamate. *Nat Med.* 2012;18(2):302-306. <https://doi.org/10.1038/nm.2615>
6. Kogan F, Haris M, Singh A, et al. Method for high-resolution imaging of creatine in vivo using chemical exchange saturation transfer. *Magn Reson Med.* 2014;71(1):164-172. <https://doi.org/10.1002/mrm.24641>
7. Ling W, Regatte RR, Navon G, Jerschow A. Assessment of glycosaminoglycan concentration in vivo by chemical exchange-dependent saturation transfer (gagCEST). *Proc Natl Acad Sci.* 2008;105(7):2266-2270. <https://doi.org/10.1073/pnas.0707666105>
8. Ling W, Regatte RR, Schweitzer ME, Jerschow A. Characterization of bovine patellar cartilage by NMR. *NMR Biomed.* 2008;21(3):289-295. <https://doi.org/10.1002/nbm.1193>
9. Zhou J, Wilson DA, Sun PZ, Klaus JA, van Zijl PCM. Quantitative description of proton exchange processes between water and endogenous and exogenous agents for WEX, CEST, and APT experiments. *Magn Reson Med.* 2004;51(5):945-952. <https://doi.org/10.1002/mrm.20048>
10. Sun PZ, van Zijl PCM, Zhou J. Optimization of the irradiation power in chemical exchange dependent saturation transfer experiments. *J Magn Reson.* 2005;175(2):193-200. <https://doi.org/10.1016/j.jmr.2005.04.005>
11. Xu X, Yadav NN, Knutsson L, et al. Dynamic glucose-enhanced (DGE) MRI: translation to human scanning and first results in glioma Patients. *Tomography.* 2015;1(2):105-114. <https://doi.org/10.18383/j.tom.2015.00175>
12. Nasrallah FA, Pagès G, Kuchel PW, Golay X, Chuang K-H. Imaging brain deoxyglucose uptake and metabolism by glucoCEST MRI. *J Cereb Blood Flow Metab.* 2013;33(8):1270-1278. <https://doi.org/10.1038/jcbfm.2013.79>
13. Rivlin M, Tsarfaty I, Navon G. Functional molecular imaging of tumors by chemical exchange saturation transfer MRI of 3-O-Methyl-D-glucose. *Magn Reson Med.* 2014;72(5):1375-1380. <https://doi.org/10.1002/mrm.25467>
14. Rivlin M, Navon G. Glucosamine and N-acetyl glucosamine as new CEST MRI agents for molecular imaging of tumors. *Sci Rep.* 2016;6(1):1-7, 32648. <https://doi.org/10.1038/srep32648>
15. Li Y, Qiao Y, Chen H, et al. Characterization of tumor vascular permeability using natural dextrans and CEST MRI. *Magn Reson Med.* 2018;79(2):1001-1009. <https://doi.org/10.1002/mrm.27014>
16. Ward KM, Balaban RS. Determination of pH using water protons and chemical exchange dependent saturation transfer (CEST). *Magn Reson Med.* 2000;44(5):799-802.
17. Baguet E, Roby C. Off-resonance irradiation effect in steady-state NMR saturation transfer. *J Magn Reson.* 1997;128(2):149-160. <https://doi.org/10.1006/jmre.1997.1230>
18. Horská A, Spencer GS. Correctly accounting for radiofrequency spillover in saturation transfer experiments: application to measurement of the creatine kinase reaction rate in human forearm muscle. *MAGMA.* 1997;5(2):159-163. <https://doi.org/10.1007/BF02592247>
19. Zaiss M. Chemical exchange saturation transfer (CEST) and MR Z-spectroscopy in vivo: a review of theoretical approaches and methods. *Phys Med Biol.* 2013;58(22):221-269. <https://doi.org/10.1088/0031-9155/58/22/R221>
20. Sun PZ, Sorensen AG. Imaging pH using the chemical exchange saturation transfer (CEST) MRI: Correction of concomitant RF irradiation effects to quantify CEST MRI for chemical exchange rate and pH. *Magn Reson Med.* 2008;60(2):390-397. <https://doi.org/10.1002/mrm.21653>
21. Zaiss M, Xu J, Goerke S, et al. Inverse Z-spectrum analysis for spillover-, MT-, and T1 -corrected steady-state pulsed CEST-MRI—application to pH-weighted MRI of acute stroke. *NMR Biomed.* 2014;27(3):240-252. <https://doi.org/10.1002/nbm.3054>
22. Zaiß M, Schmitt B, Bachert P. Quantitative separation of CEST effect from magnetization transfer and spillover effects by Lorentzian-line-fit analysis of z-spectra. *J Magn Reson.* 2011;211(2):149-155. <https://doi.org/10.1016/j.jmr.2011.05.001>
23. Jin T, Kim S-G. Advantages of chemical exchange-sensitive spin-lock (CESL) over chemical exchange saturation transfer (CEST) for hydroxyl- and amine-water proton exchange studies. *NMR Biomed.* 2014;27(11):1313-1324. <https://doi.org/10.1002/nbm.3191>
24. Henkelman RM, Huang X, Xiang Q-S, Stanisz GJ, Swanson SD, Bronskill MJ. Quantitative interpretation of magnetization transfer. *Magn Reson Med.* 1993;29(6):759-766. <https://doi.org/10.1002/mrm.1910290607>
25. Li Y, Chen H, Xu J, et al. CEST theranostics: label-free MR imaging of anticancer drugs. *Oncotarget.* 2016;7(6):6369-6378. <https://doi.org/10.18632/oncotarget.7141>
26. Chávez FV, Halle B. Molecular basis of water proton relaxation in gels and tissue. *Magn Reson Med.* 2006;56(1):73-81. <https://doi.org/10.1002/mrm.20912>
27. Halle B. Molecular theory of field-dependent proton spin-lattice relaxation in tissue. *Magn Reson Med.* 2006;56(1):60-72. <https://doi.org/10.1002/mrm.20919>
28. Zaiss M, Ehse P, Scheffler K. Snapshot-CEST: Optimizing spiral-centric-reordered gradient echo acquisition for fast and robust 3D CEST MRI at 9.4 T. *NMR Biomed.* 2018;31(4):1-14, e3879. <https://doi.org/10.1002/nbm.3879>
29. Phosphate-buffered saline (PBS). *Cold Spring Harb Protoc.* 2006;2006(1). <https://doi.org/10.1101/pdb.rec8247>
30. Avdievich NI, Giapitzakis I-A, Bause J, Shajan G, Scheffler K, Henning A. Double-row 18-loop transceive–32-loop receive tight-fit array provides for whole-brain coverage, high transmit performance, and SNR improvement near the brain center at 9.4T. *Magn Reson Med.* 2019;81(5):3392-3405. <https://doi.org/10.1002/mrm.27602>

31. Herz K, Gandhi C, Schuppert M, Deshmane A, Scheffler K, Zaiss M. CEST imaging at 9.4 T using adjusted adiabatic spin-lock pulses for on- and off-resonant T1 ρ -dominated Z-spectrum acquisition. *Magn Reson Med*. 2019;81(1):275-290. <https://doi.org/10.1002/mrm.27380>
32. Zaiss M, Bachert P. Exchange-dependent relaxation in the rotating frame for slow and intermediate exchange - modeling off-resonant spin-lock and chemical exchange saturation transfer: MODELING SL AND CEST. *NMR Biomed*. 2013;26(5):507-518. <https://doi.org/10.1002/nbm.2887>
33. Windschuh J, Zaiss M, Meissner J-E, et al. Correction of B1-inhomogeneities for relaxation-compensated CEST imaging at 7 T. *NMR Biomed*. 2015; 28(5):529-537. <https://doi.org/10.1002/nbm.3283>
34. Schuenke P, Windschuh J, Roeloffs V, Ladd ME, Bachert P, Zaiss M. Simultaneous mapping of water shift and B1 (WASABI)-Application to field-Inhomogeneity correction of CEST MRI data. *Magn Reson Med*. 2017;77(2):571-580. <https://doi.org/10.1002/mrm.26133>
35. Windschuh J, Zaiss M, Ehses P, Lee J-S, Jerschow A, Regatte RR. Assessment of frequency drift on CEST MRI and dynamic correction: application to gagCEST at 7 T. *Magn Reson Med*. 2019;81(1):573-582. <https://doi.org/10.1002/mrm.27367>
36. Grad J, Bryant RG. Nuclear magnetic cross-relaxation spectroscopy. *J Magn Reson*. 1990;90(1):1-8. [https://doi.org/10.1016/0022-2364\(90\)90361-C](https://doi.org/10.1016/0022-2364(90)90361-C)
37. ESMRMB 2019, 36th Annual Scientific Meeting, Rotterdam, NL, October 3–October 5: Abstracts, Friday. *Magn Reson Mater Phys Biol Med*. 2019; 32(S1):107–233. <https://doi.org/10.1007/s10334-019-00754-2>
38. Bechmann W, Bald I. Wechselwirkung zwischen elektromagnetischer Strahlung und Stoff – Grundlagen der Spektroskopie. In: Bechmann W, Bald I, eds. *Einstieg in die Physikalische Chemie für Naturwissenschaftler*. Studienbücher Chemie. Berlin, Heidelberg: Springer; 2018:303-440. https://doi.org/10.1007/978-3-662-55858-4_4
39. Cui J, Zu Z. Towards the molecular origin of glutamate CEST (GluCEST) imaging in rat brain. *Magn Reson Med*. 2020;83(4):1405-1417. <https://doi.org/10.1002/mrm.28021>
40. Jin T, Autio J, Obata T, Kim S-G. Spin-locking versus chemical exchange saturation transfer MRI for investigating chemical exchange process between water and labile metabolite protons. *Magn Reson Med*. 2011;65(5):1448-1460. <https://doi.org/10.1002/mrm.22721>
41. Gamini A, Toffanin R, Murano E, Rizzo R. Hydrogen-bonding and conformation of agarose in methyl sulfoxide and aqueous solutions investigated by ¹H and ¹³C NMR spectroscopy. *Carbohydr Res*. 1997;304(3):293-302. [https://doi.org/10.1016/S0008-6215\(97\)00232-2](https://doi.org/10.1016/S0008-6215(97)00232-2)

SUPPORTING INFORMATION

Additional supporting information may be found online in the Supporting Information section at the end of this article.

How to cite this article: Mueller S, Scheffler K, Zaiss M. On the interference from agar in chemical exchange saturation transfer MRI parameter optimization in model solutions. *NMR in Biomedicine*. 2021;34:e4403. <https://doi.org/10.1002/nbm.4403>

B.2. Publication 2

Whole brain snapshot CEST at 3T using 3D-EPI: Aiming for speed, volume, and homogeneity

Mueller S., Stirnberg R., Akbey S., Ehses P., Scheffler K., Stöcker T., and Zaiss M.

Whole brain snapshot CEST at 3T using 3D-EPI: Aiming for speed, volume, and homogeneity

Sebastian Mueller¹  | Rüdiger Stirnberg²  | Suzan Akbey² | Philipp Ehses² | Klaus Scheffler^{1,3}  | Tony Stöcker^{2,4}  | Moritz Zaiss^{1,5} 

¹High-field Magnetic Resonance Center, Max Planck Institute for Biological Cybernetics, Tuebingen, Germany

²German Center for Neurodegenerative Diseases (DZNE), Bonn, Germany

³Department of Biomedical Magnetic Resonance, Eberhard Karls University Tuebingen, Tuebingen, Germany

⁴Department of Physics and Astronomy, University of Bonn, Bonn, Germany

⁵Department of Neuroradiology, University Hospital Erlangen, Erlangen, Germany

Correspondence

Sebastian Mueller, Max Planck Institute for Biological Cybernetics, High-field Magnetic Resonance Center, Max-Planck-Ring 11, 72076 Tuebingen, Germany.
Email: sebastian.mueller@tuebingen.mpg.de

Funding information

This work received support from the Max Planck Society, German Research Foundation (DFG), grant ZA 814/2-1; and European Union's Horizon 2020 research and innovation program, grant agreement No. 667510

Purpose: CEST MRI enables imaging of distributions of low-concentrated metabolites as well as proteins and peptides and their alterations in diseases. CEST examinations often suffer from low spatial resolution, long acquisition times, and concomitant motion artifacts. This work aims to maximize both resolution and volume coverage with a 3D-EPI snapshot CEST approach at 3T, allowing for fast and robust whole-brain CEST MRI.

Methods: Resolution and temporal SNR of 3D-EPI examinations with nonselective excitation were optimized at a clinical 3T MR scanner in five healthy subjects using a clinical head/neck coil. A CEST presaturation module for low power relayed nuclear Overhauser enhancement and amide proton transfer contrast was applied as an example. The suggested postprocessing included motion correction, dynamic B_0 correction, denoising, and B_1 correction and was compared to an established 3D-gradient echo-based sequence.

Results: CEST examinations were performed at 1.8 mm nominal isotropic resolution in 4.3 s per presaturation offset. In contrast to slab-selective 3D or multislice approaches, the whole brain was covered. Repeated examinations at three different B_1 values took 13 minutes for 58 presaturation offsets with temporal SNR around 75. The resulting CEST effects revealed significant gray and white matter contrast and were of similar quality across the whole brain. Coefficient of variation across three healthy subjects was below 9%.

Conclusion: The suggested protocol enables whole brain coverage at 1.8 mm isotropic resolution and fast acquisition of 4.3 s per presaturation offset. For the fitted CEST amplitudes, high reproducibility was proven, increasing the opportunities of quantitative CEST investigations at 3T significantly.

KEYWORDS

3D CEST MRI, chemical exchange saturation transfer MRI 3T, chemical exchange saturation transfer MRI EPI, high resolution CEST MRI, whole-brain CEST MRI

1 | INTRODUCTION

CEST MRI allows indirect detection of low concentrated solutes. CEST uses two properties of these low concentrated solutes: their chemical exchange with the bulk water proton pool, and their chemical shift relative to water by a certain frequency offset $\delta\omega$. In contrast to purely anatomical MRI, a frequency selective presaturation module with RF irradiation at $\delta\omega$ precedes each image readout. Given presaturation at different frequencies, the resulting bulk water signals may be combined to a Z-spectrum,¹ which contains information on all interacting metabolites resonating in the covered frequency range. To extract all information, the Z-spectrum should be sampled densely, and the presaturation and readout block are thus repeated 10 to 100 times. The major problem of the combination of CEST presaturation and classic line-by-line MRI readout is that the repeated excitations will successively destroy the prepared magnetization state. The number of excitations can be reduced by k-space segmentation or by a small matrix size (small FOV or low resolution). Recently, a snapshot CEST approach with centric reordered 3D-gradient echo (GRE) readout scheme was proposed that was optimized for maximized number of k-space lines being acquired following a single presaturation.² Still, this GRE-based method was limited to 16 slices and a resolution of $1.7 \times 1.7 \times 5 \text{ mm}^3$. When extending the volume coverage to whole brain, even at 3T CEST effects become sensitive to the inhomogeneity of B_1 RF irradiation. To correct for spatial inhomogeneity in B_1 , repeated measurements at different nominal B_1 values are needed.³ In this work, encouraged by recent findings at 7T,⁴ we extended a 3D-EPI readout to allow semielliptical scanning along with CAIPIRINHA⁵ undersampling. It was then optimized with centric reordering and nonselective excitation for whole-brain snapshot CEST MRI at 3T. This increased temporal SNR (tSNR) by 20% compared to the 7T protocol applied at 3T. In addition, a novel saturation scheme at low power B_1 was applied to minimize side bands in the Z-spectrum. Together with the proposed postprocessing, this enables multipool CEST MRI with whole brain coverage and isotropic resolution of 1.8 mm in less than 4:30 minutes for a fully sampled Z-spectrum at a clinical MR system.

2 | METHODS

2.1 | MR examinations

All examinations were performed at a clinical whole-body MR system (3T Magnetom Prisma^{fit}, Siemens Healthineers, Germany). The vendor-provided 1Tx/64Rx-channel head/neck coil was used for MR image acquisition on six healthy subjects with written informed consent and approval by the local ethics committee.

The CEST presaturation module was optimized for relayed nuclear Overhauser enhancement (rNOE) and amide proton transfer (APT) contrast by modifying a scheme suggested by Deshmane et al.⁶ To reduce sidebands and increase selectivity, rather long Gaussian pulses of $16 \times 100 \text{ ms}$ were applied in the present study at a duty cycle of 50% and $B_1 = 0.65 \mu\text{T}$. The offset distribution can be found in the Supporting Information. To correct for B_1 inhomogeneity, data were acquired at [0.75, 1.00, 1.25] times the nominal B_1 by adjusting the reference voltage. This covered 95% of all measured relative B_1 values in vivo using the body coil as transmit coil. For imaging, both a 3D-GRE² and the 3D-EPI⁷ sequence were investigated with nonselective excitation applied in both cases.

2.2 | MR readout parameters

The 3D-EPI readout was accelerated using parallel acquisition with CAIPIRINHA acceleration 1×6 (shift = 2, 36×36 reference lines) along both phase-encoding directions (PE, 3D) and 6/8 partial Fourier along the first PE direction. Semielliptical k-space sampling,⁷ along with centric reordering of the 3D phase-encoding steps, were used. A non-blipped CAIPIRINHA sampling strategy for high spatiotemporal resolution⁸ was chosen for which each CAIPIRINHA offset was realized with a separate excitation instead of 3D gradient blips. This resulted in a maximum EPI-factor of 32 and 45 excitations for the readout of 1201 k-space lines per 3D volume at a nominal matrix size of $144 \times 126 \times 88$ (RO \times PE \times 3D: head-foot \times anteroposterior \times left-right). A readout bandwidth of 1930 Hz/pixel with TE/echo train length = 11.0/24.3 ms lead to a total readout duration of 1.2 s for an isotropic nominal resolution of 1.8 mm at a FOV of $256 \times 224 \times 156 \text{ mm}^3$. The nominal excitation flip angle (FA) was set to 15 degrees. Nonselective binomial-11 water excitation was applied instead of fat saturation to minimize chemical shift artifacts and maximize readout efficiency.⁹ The acquisition duration was 4.3 s per presaturation offset, plus an additional 12 s recovery time for the unsaturated M_0 image. Fifty-seven offsets and one M_0 image could be measured in 4:22 min, including the CAIPIRINHA reference lines.

The 3D-GRE readout was accelerated using GRAPPA¹⁰ 3×2 in both phase-encoding directions. Further undersampling was achieved by applying partial Fourier (6/8 along both phase-encoding directions) and omitting the corners of k-space (elliptical sampling). The number of acquired k-space lines for a nominal matrix size of $96 \times 78 \times 72$ (RO \times PE \times 3D: head-foot \times anteroposterior \times left-right) was therefore 487, and thus only 15% above the maximum of 424 lines derived according to the work of Zaiss et al.² ($T_{1,\text{WM}} = 950 \text{ ms}^{11}$; FA = 5°; TR = 3.1 ms). The whole readout duration was 1.7 s. These optimized settings of the 3D-GRE (TE = 1.3 ms; TR = 3.1 ms; bandwidth = 660 Hz/pixel; FA = 5°)¹²

allowed to acquire one presaturation offset in 5.1 s (additional relaxation in case of M_0 image) with a nominal spatial resolution of 2.34 mm isotropic.

Field mapping was performed applying the simultaneous water shift and B_1 mapping (WASABI) approach of Schuenke et al.¹³ ($t_p = 5000 \mu\text{s}$, $B_1 = 3.7 \mu\text{T}$, recovery time (saturated/ M_0): 3 s/12 s, 31 equally spaced presaturation offsets from -1.8 to $+1.8$ ppm). This was executed with the same imaging parameters as the CEST MRI sequences. To enable correction for spatiotemporal changes in B_0 ,¹⁴ interleaved WASABI acquisitions were performed before and after each CEST examination.

For quantification of tSNR, 16 repeated measurements were performed without any presaturation module and a pause of 3 seconds in between consecutive image acquisitions. Different voxel sizes, acceleration factors, and nominal excitation FAs with otherwise identical parameters, unless stated differently, were investigated in preparation of the final 3D-EPI CEST protocol.

2.3 | CEST data evaluation

Data processing was performed using in-house written MatLab R2018a (The MathWorks, Inc., Natick, MA, USA) code, if not stated differently.

For both imaging methods, 3D-EPI and 3D-GRE, the post-processing was identical. All images of the same examination were registered to the unsaturated image of the first WASABI to correct for subject movement during the acquisition. This was done automatically using the AFNI toolbox of Cox et al.¹⁵ Afterward, the brain data were segmented automatically using SPM12¹⁶ in case of the EPI and manually in case of the GRE readout to extract only the brain volume (including CSF, gray [GM], and white matter [WM]). The segmentation was of importance for the subsequently performed principal component analysis (PCA) based denoising. The CEST data sets were then corrected for dynamic changes in B_0 ¹⁴ using $\Delta B_0(r,t)$ maps derived from the interleaved WASABI measurements. To reduce noise in the images, PCA denoising¹⁷ was applied next. Median criterion with correction factor $\beta = 1.29$ ¹⁸ was used to determine the cutoff eigenvalue in the reconstruction. Malinowski indicator function was exemplarily applied to one data set as well. With the so-called real error RE,¹⁹ the cutoff eigenvalue k_{ind} can be derived as the minimum of $\text{RE}(k)/(c-k)^2$, where c is the number of columns (rows are observations in Casorati notation; columns are reshaped 3D volumes at a single offset frequency) in the considered matrix.²⁰ The denoised data were then corrected for spatial B_1 inhomogeneity, including three different nominal B_1 values for Z- B_1 correction.³

To quantify the CEST effects, a 4-pool Lorentzian model²¹ was fitted to the postprocessed data voxel by voxel using a nonlinear least squares algorithm. The peak positions of APT, rNOE, and semisolid magnetization transfer

(ssMT) were fixed with respect to the frequency offset of direct water saturation (Supporting Information Table S1). To evaluate CEST effects within a certain tissue type, the tissue probability maps as derived with SPM12 were cut at a certain threshold (50% for GM and WM; 25% in case of CSF). Lower threshold for CSF was chosen to ensure contributions by CSF were separated from GM and WM.

For estimations on the point spread functions (PSF) of different readouts, numeric simulations had been performed for which a description can be found in the Supporting Information. These simulations were also used to investigate the effect of different FAs.

To evaluate the reproducibility of the derived results the Lorentzian amplitudes of APT, rNOE and ssMT pools were compared for different acquisitions. Within the tissue masks of GM and WM, the median amplitudes were determined. These were in the next step compared to the results of the other acquisitions in terms of mean value and SD, combined as a coefficient of variation (COV), which is the ratio of SD over mean value.

3 | RESULTS

3.1 | tSNR evaluation

tSNR was determined in each voxel as the ratio of mean value over SD for repeated measurements. As shown in Figure 1A, the tSNR decreased on average by approximately 30% going from $(2.0 \text{ mm})^3$ to $(1.8 \text{ mm})^3$ isotropic resolution. The increased average tSNR for higher FAs went along with a less homogeneous spatial distribution (Figure 1B,C and Supporting Information Figure S1). For $\text{FA} > 20^\circ$ a significant decrease of tSNR in the center and in lower regions of the brain was observed. For the final protocol, a FA of 15° was chosen. The PSF simulations (Figure 2) revealed a relative FWHM² of on average 1.33 for $\text{FA} = 15^\circ$. The maximum relative magnitude was found to be 4.4% for $\text{FA} = 17.5^\circ$ (Supporting information Figure S4A). These numbers also prove a FA of 15° to be suitable. Increasing the total acceleration factor from 4 to 6 decreased tSNR by around 17% (Supporting Information Figure S2), which approximately corresponds to the expected thermal noise increase, that is, the expected additional g-factor penalty seems to be compensated for by reduced physiological noise (ratio of square root of undersampling factors: 18%). The non-blipped sixfold CAIPIRINHA acceleration nearly preserved signal with similar echo train length (24.3 vs. 23.9 ms, same EPI factor of 32) and allowed fewer excitations for the complete readout (45 vs. 66). The latter likely reduced physiological contributions to the tSNR.²² For the final protocol ($\text{FA} = 15^\circ$, non-blipped CAIPIRINHA = $1 \times 6^{(\text{shift} = 2)}$, partial Fourier = 6/8, 1.8 mm isotropic resolution), the tSNR of the EPI readout was ≈ 75 even in the cerebellum. In contrast to the previously published protocol for 7T⁴, we worked out and optimized a modified 3D-EPI readout, for example,

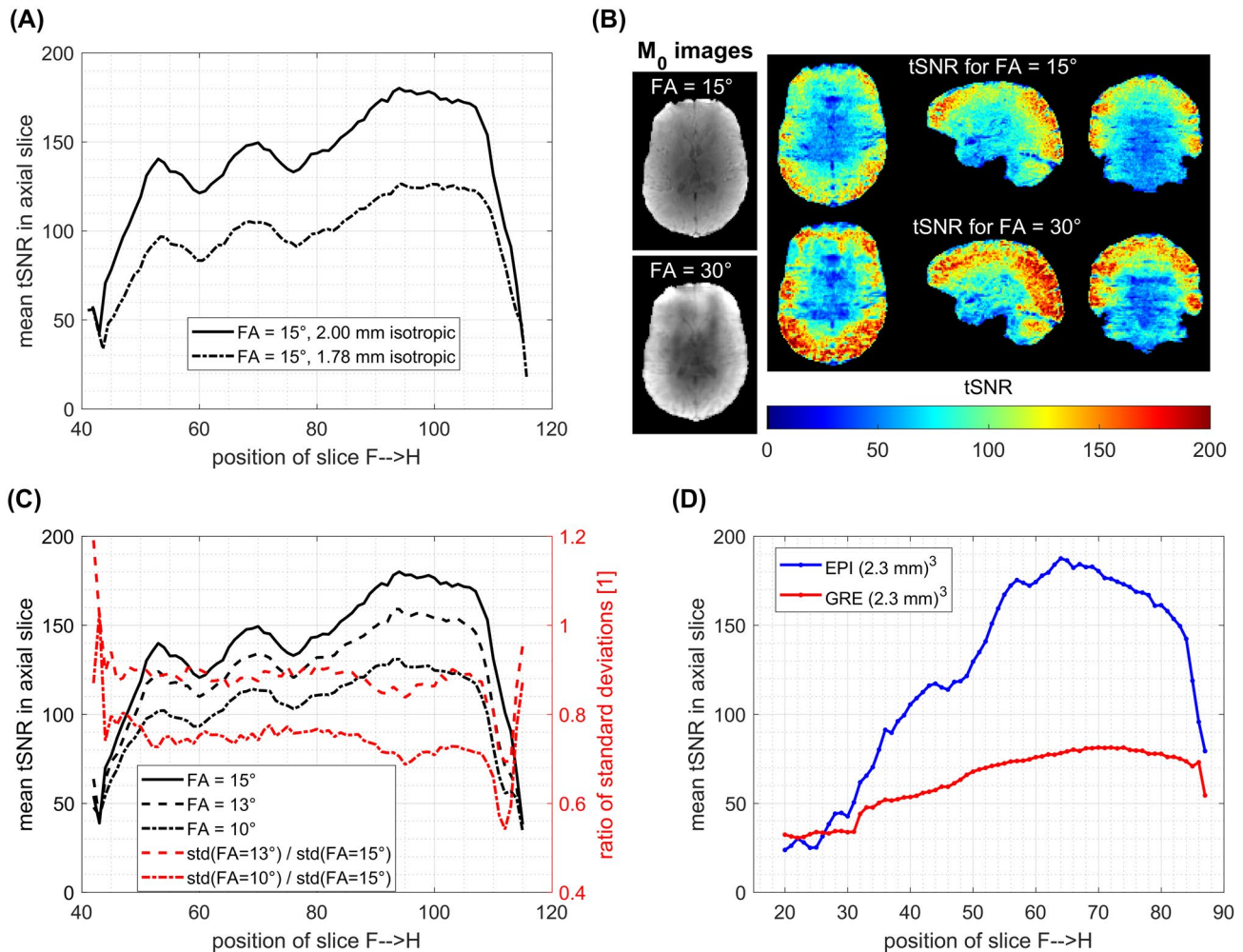


FIGURE 1 (A) tSNR of EPI for different spatial resolutions. (B) tSNR maps of EPI for different FAs at (1.8 mm)³ nominal isotropic resolution. Higher FAs provide higher average tSNR but at the cost of increased spatial heterogeneity (see also (C)), with very low tSNR in the center and lower regions of the brain. Additionally, a single image of the time series is shown for both FAs. (C) Closer look at FAs around 15 degrees with mean and SD in different axial slices. (D) Comparison to the GRE readout at 2.34 mm. EPI at 1.8 mm isotropic resolution outperforms the 2.34 mm GRE in terms of tSNR. In the cerebellum, the tSNR is around 80. FA, flip angle; GRE, gradient echo; tSNR, temporal SNR

in terms of undersampling (GRAPPA vs. CAIPIRINHA), full versus elliptical sampling, and segmentation of one versus three. This yielded $\approx 20\%$ higher tSNR for the novel 3T protocol (Supporting Information Figure S3). The PSF analysis revealed that the referring FWHM increased by 8.7% in the first and 9.5% in the second phase-encoding direction (compared to the 7T protocol) with maximum 1.75 pixels in the first PE direction (Figure 2E,F). Compared to the unfiltered PSF, the two protocols yielded a relative FWHM of 132 and 143%, respectively, in the first phase-encoding direction and 112 and 123% in the second.

3.2 | Inhomogeneity of B_1^+

As shown in Figure 3A to C, the B_1 amplitude varied by approximately 50% across the whole brain volume. The

deviation along the head-foot direction was larger than the deviation along the other two (left-right and anteroposterior) directions (Figure 3A).

If the data were not corrected for B_1 inhomogeneity, fitted CEST contrasts were significantly altered as shown for rNOE in Figure 3D,E. For comparison of B_1 correction methods, the FWHM of Z-value distribution in GM and WM was determined by fitting a Gaussian distribution at each presaturation offset. In Supporting Information Figure S5A, it is shown that using as little as $n = 2$ B_1 values for correction already yielded 40/48% narrower FWHM in Z-value distributions in GM and WM than without B_1 correction. The FWHM decreased by 44.0/49.8% when including $n = 3$ B_1 values, but only by an additional 0.4/1.0 and 1.3/2.4% for $n = 4$ and $n = 5$ included B_1 values (spline interpolation; average over all offsets in GM/WM segments. Data not shown.). However, a 2-point correction

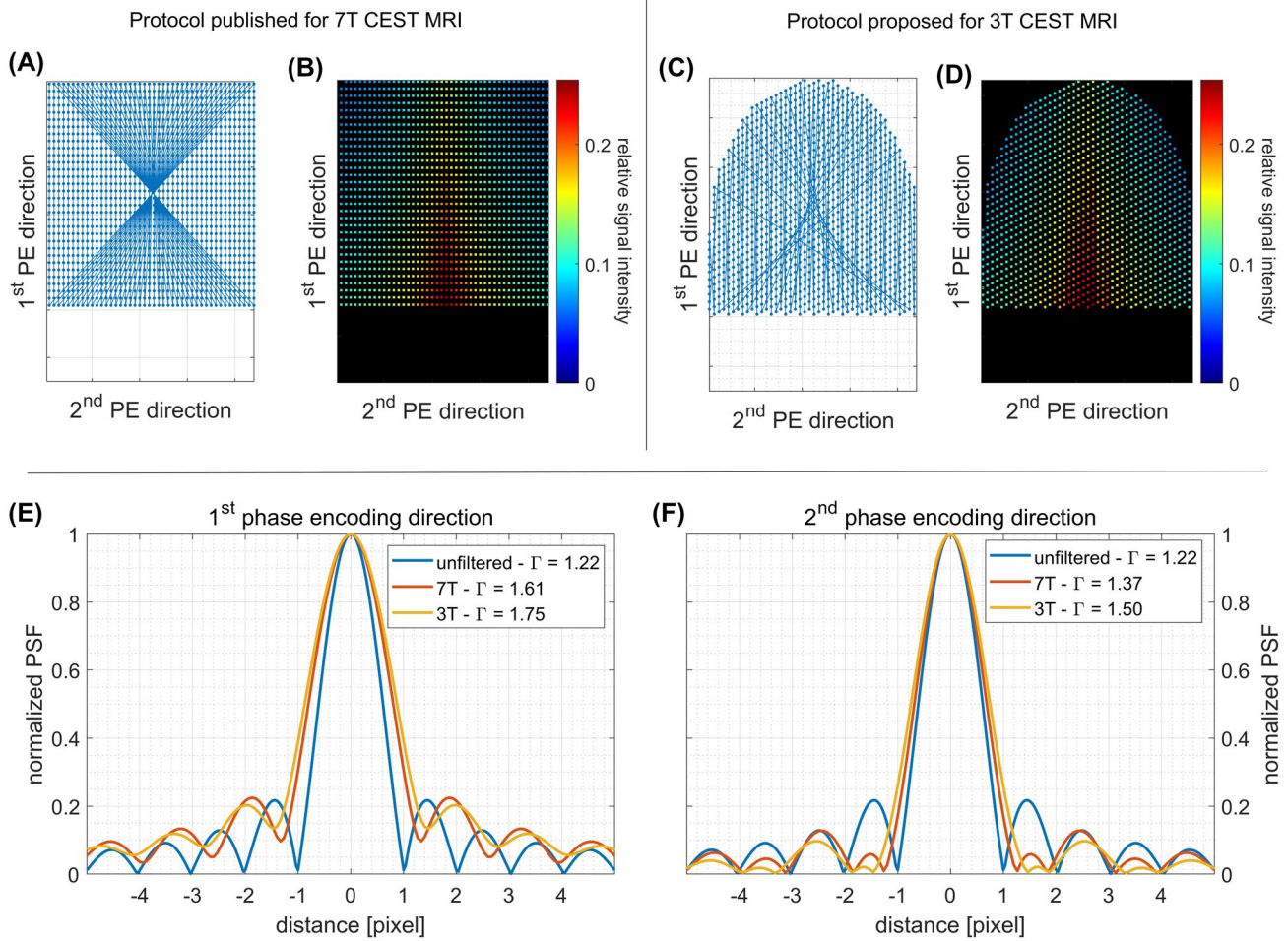


FIGURE 2 Comparing the PSFs of the established 7T protocol (A,B) and the novel 3T readout (C,D). (A,C) show the sampling trajectories, with CAIPIRINHA sampling in (C); and in (B,D) the resulting relative signal intensity is shown. PSFs (E,F) were determined from Fourier transformation of a 2D delta function that was convoluted with the signal evolution (B,D) determined from k space sampling taking into account both T_1 and T_2 (nominal matrix size (RO \times PE \times 3D): 144 \times 126 \times 88, FA = 15°, T_1 = 1300 ms, T_2^* = 45 ms and initial magnetization $M_0 = 1$ for both protocols. Variable TR for different excitations in 3T protocol with semielliptical sampling). Gamma is the FWHM of the PSF in both subplots. For the 3T protocol, like regular centric-out sampling, each 3D phase encoding slice starts with a new excitation; however, the first phase encoding is offset by ± 1 line according to the CAIPIRINHA pattern. CAIPIRINHA, controlled aliasing in parallel imaging results in higher acceleration; PE, phase-encoding directions; PSF, point spread function; RO, readout; T, tesla

assumes linear behavior of Z-spectra over a 50% change in B_1 . If only $n = 2$ B_1 values were included, the fitted amplitudes were altered (Supporting Information Figure S5B). Supporting information Figure S5B to E also show that including an increasing number of B_1 values in the correction reduced noise in the fitted contrast maps. This held true for spline but not necessarily for linear interpolation. We therefore suggest to measure at three different B_1 amplitudes and to use spline interpolated Z- B_1 correction.

3.3 | CEST contrast

With the Z- B_1 corrected whole brain 3D-EPI approach, CEST contrast maps (fitted amplitudes) with high homogeneity over the whole FOV were generated. As shown in Figure 4,

the contrast maps covered the whole brain volume with high spatial resolution. Fine anatomical structures, such as GM and WM regions in the cerebellum, could be distinguished in all fitted contrasts (APT, ssMT, and rNOE). In agreement with previous studies,^{6,23,24} higher rNOE ($\times 1.17$) and ssMT ($\times 1.61$) amplitudes in WM compared to GM were found (Table 1), as well as the inverse relationship ($\times 0.88$) for APT (see also Figure 5). On average ($n = 3$ healthy subjects examined with final protocol) the median fitted Lorentzian amplitudes in GM and WM were (mean \pm SD): $\{(5.9 \pm 0.1)\% / (5.21 \pm 0.02)\% \}$ for APT, $\{(9.2 \pm 0.3)\% / (10.8 \pm 0.1)\% \}$ for rNOE, and $\{(5.21 \pm 0.09)\% / (8.4 \pm 0.1)\% \}$ for ssMT.

As shown in Figure 6, fitted CEST pool amplitudes revealed reproducible GM/WM contrast for different healthy subjects. Reproducibility was investigated both across the same subject at different sessions and for direct repetition within the same

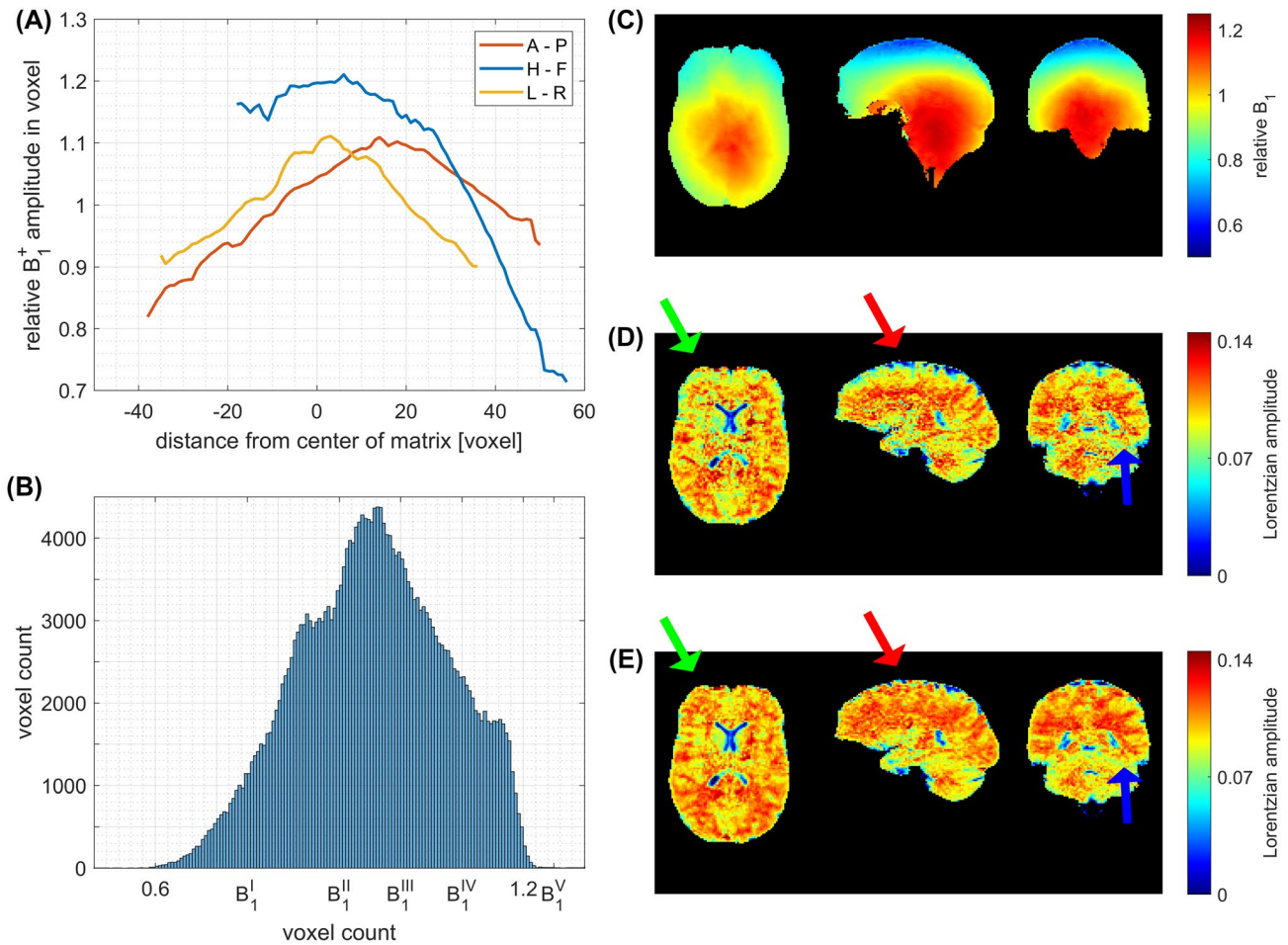


FIGURE 3 (A) Spatial distribution of relative B_1 along different directions at $B_0 = 3T$. (B) Labels B_1^I, \dots, B_1^V indicate the different nominal B_1 values that were measured for B_1 correction in this case. (C) B_1 distribution in slices of different orientation. Fitted rNOE CEST amplitudes without (D) B_1 correction and with Z- B_1 correction including three B_1 values (E). rNOE, relayed nuclear Overhauser enhancement

session (intrasubject) as well as across different subjects (intersubject). The intrasubject coefficients of variation (COV) in fitted amplitudes were below 8.5% for examinations in the same session and below 7% for examinations in different sessions for APT, ssMT, and rNOE both in GM and WM (Figure 7A,B). It was found that ssMT showed four times higher COV than the other fitted amplitudes when evaluated for examinations within same session. The intersubject COV was below 4% for $n = 3$ subjects (Figure 6C) for all tissues and CEST pool amplitudes. In this case, none of the fitted amplitudes showed a manifold increased COV as compared to the others within both tissue types at the same time.

3.4 | Comparison with 3D-GRE protocol

Both GRE and EPI readout were compared at an isotropic resolution of 2.34 mm with same CEST presaturation module. Still, even at a higher resolution of 1.8 mm, the EPI (black dash-dotted line, Figure 1A) outperformed the GRE at 2.34 mm isotropic resolution (red dashed line, Figure 1D) in

terms of tSNR. At $(2.34 \text{ mm})^3$, the tSNR of EPI was approximately two times higher than that of the GRE (Figure 1D). CEST measurements were acquired in the same volunteer but in different sessions. EPI was applied with matrix size $110 \times 96 \times 72$ (RO \times PE \times 3D: head-foot \times anteroposterior \times left-right) and had a total acquisition time of 4:09 minutes for 58 offsets including the unsaturated M_0 image. On the contrary, the GRE was executed with matrix size $96 \times 78 \times 72$ (RO \times PE \times 3D: head-foot \times anteroposterior \times left-right) and took 4:59 minutes. Readout durations were 1.7 seconds for GRE and 0.8 seconds for EPI, which also showed less blurring in the raw images (Figure 7, last row).

Considering the fitted CEST amplitude maps (Figure 7), it was found that the EPI readout allowed to detect finer anatomical structures in the brain. Especially the fitted amplitudes of rNOE were more blurry using the GRE readout. Still, both readouts yielded fitted CEST amplitudes in GM and WM segments that deviated by less than 10% (Table 1). The contrast ratios between GM/WM were found to be comparable with $\{0.9, 1.2, 1.6\}$ (EPI) and $\{0.9, 1.1, 1.4\}$ (GRE) for APT, rNOE and ssMT.

FIGURE 4 CEST contrast (Lorentzian amplitude) of 1.8 mm isotropic EPI readout. Postprocessing included motion, B_0 and B_1 correction, and PCA denoising prior to B_1 correction. Maps show amplitudes derived from 4-pool Lorentzian fits: upper row is APT; middle is rNOE; and lower row is ssMT. Contrasts are homogenous within a certain tissue type across the whole volume. Spatial resolution is high enough to, for example, recognize structures like caudate nucleus within the basal ganglia and at the same time distinguish GM and WM sections in the cerebellum. APT, amide proton transfer; GM, gray matter; PCA, principal component analysis; rNOE, relayed nuclear Overhauser enhancement; ssMT, semisolid magnetization transfer; WM, white matter

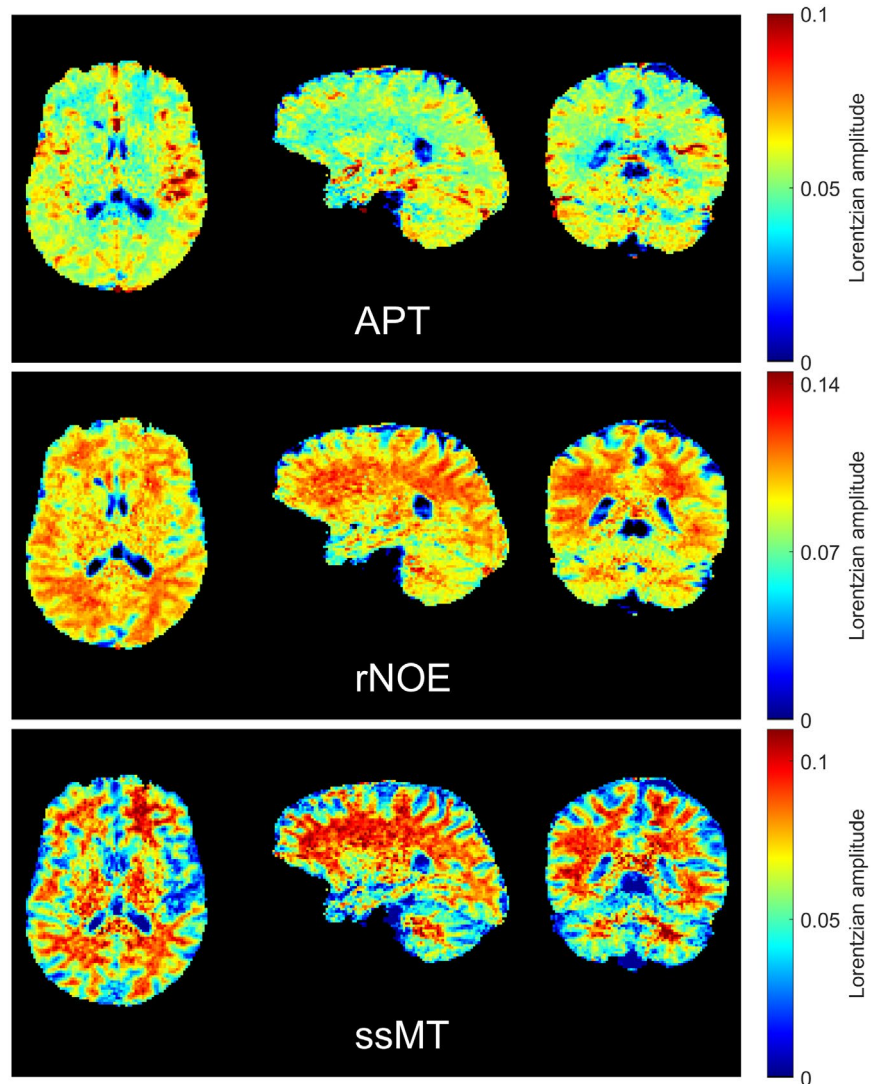


TABLE 1 Comparison of derived CEST contrast to other study

	APT		rNOE		ssMT	
	GM	WM	GM	WM	GM	WM
Deshmane et al ⁶	(2.92 ± 0.24)	(2.44 ± 0.24)	(6.08 ± 0.47)	(6.44 ± 0.44)	(7.52 ± 0.04)	(10.96 ± 0.43)
GM/WM ratio	1.20		0.94		0.69	
This study EPI RO	(5.9 ± 0.1)	(5.21 ± 0.02)	(9.2 ± 0.3)	(10.8 ± 0.1)	(5.21 ± 0.09)	(8.4 ± 0.1)
GM/WM ratio	1.13		0.85		0.62	
Deshmane et al/this study	0.49	0.47	0.66	0.60	1.44	1.30
This study GRE RO	5.58	5.26	8.97	10.03	5.42	7.64
GM/WM ratio	1.06		0.89		0.71	

APT, amide proton transfer; GM, gray matter; GRE, gradient echo; rNOE, relayed nuclear Overhauser enhancement; RO, readout; ssMT, semisolid magnetization transfer; WM, white matter.

3.5 | Influence of denoising

To estimate systematic effects of PCA denoising on the appearance of the Z-spectrum, the average spectrum in a homogeneous WM region of interest was considered. Supporting

information Figure S6 shows that the residual Z-values due to PCA denoising according to Median criterion^{17,18} are noise-like across different presaturation offsets. The maximum difference with and without denoising was 0.4% at 0.1 ppm. The average value of residual Z-value across all offsets was

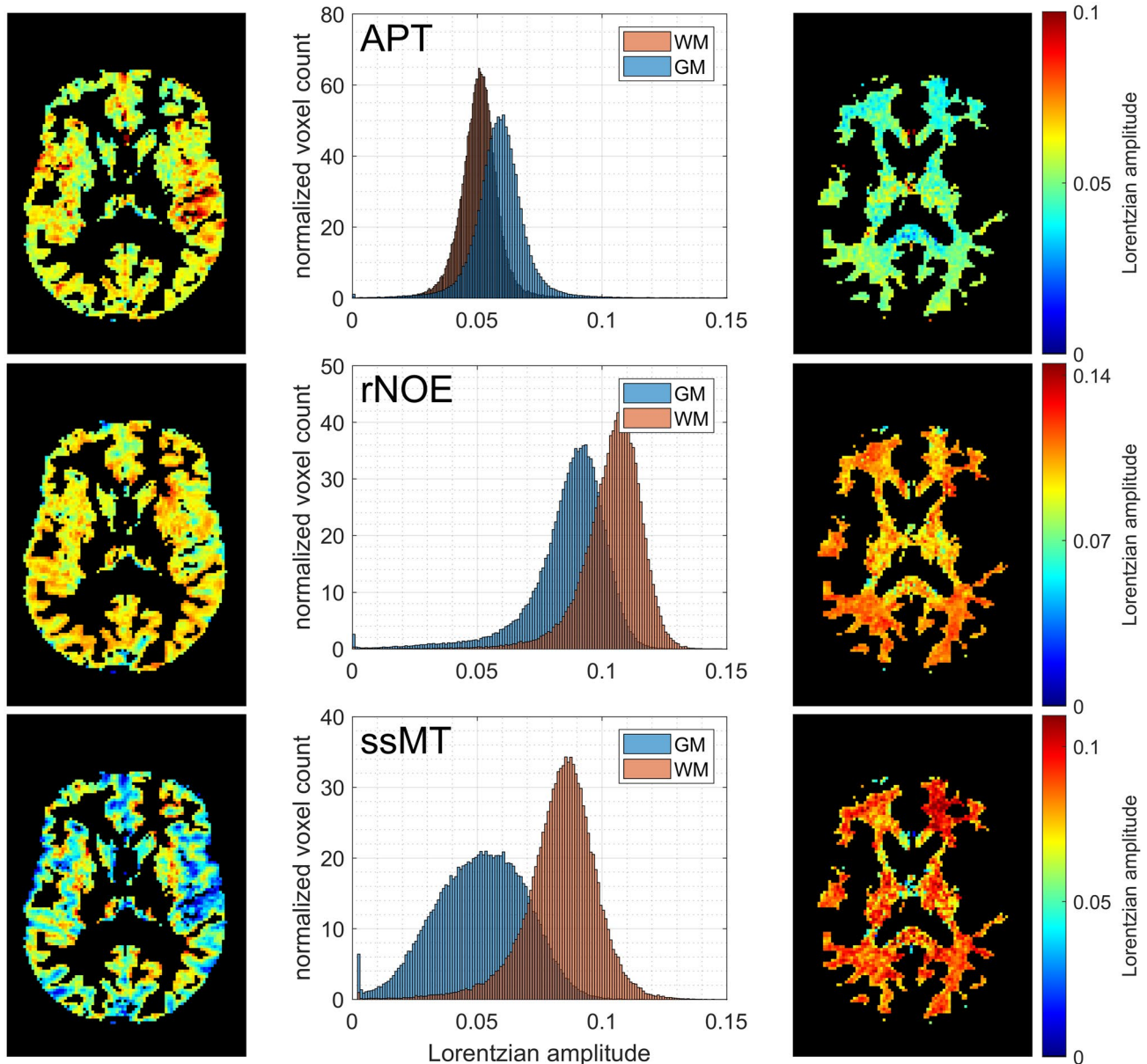


FIGURE 5 Exemplary distribution of fitted CEST contrasts (Lorentzian amplitude) in GM and WM regions: APT, rNOE, and ssMT. GM and WM regions show significant differences in distribution of all three CEST contrasts ($P < .005$). APT, amide proton transfer; GM, gray matter; rNOE, relayed nuclear Overhauser enhancement; ssMT, semisolid magnetization transfer; WM, white matter

-5.6×10^{-6} , and the average spatial SD in the non-denoised Z-spectrum was 1.0×10^{-3} . The resulting fitted amplitudes did not reveal anatomical structures depending on the denoising, as shown in Supporting Information Figure S7 and S8. In addition to the suggested postprocessing that includes PCA denoising using the Median criterion, stronger denoising with application of Malinowski's indicator function²⁰ was investigated. This had previously been applied in the studies of Goerke et al²⁴ and Deshmans et al.⁶ In our study, Malinowski's indicator function suggested to include roughly 40% of the number of components suggested by the Median criterion. It was observed that this made, for example, the structures in the striatum—especially the putamen—more clearly visible in

the fitted amplitude maps (Figure 8). The differences in fitted amplitudes between the two cutoff criteria did not show obvious anatomical structure besides some areas in the CSF (Supporting Information Figure S9B,C,D). The coefficients of variation of the medians of fitted amplitudes in GM and WM for both cutoff criteria were less than 1.4% for APT, rNOE, and ssMT (Supporting Information Figure S9A).

4 | DISCUSSION

It was shown that with the worked-out 3D-EPI readout, a tSNR of 75 could be achieved in all regions of the brain,

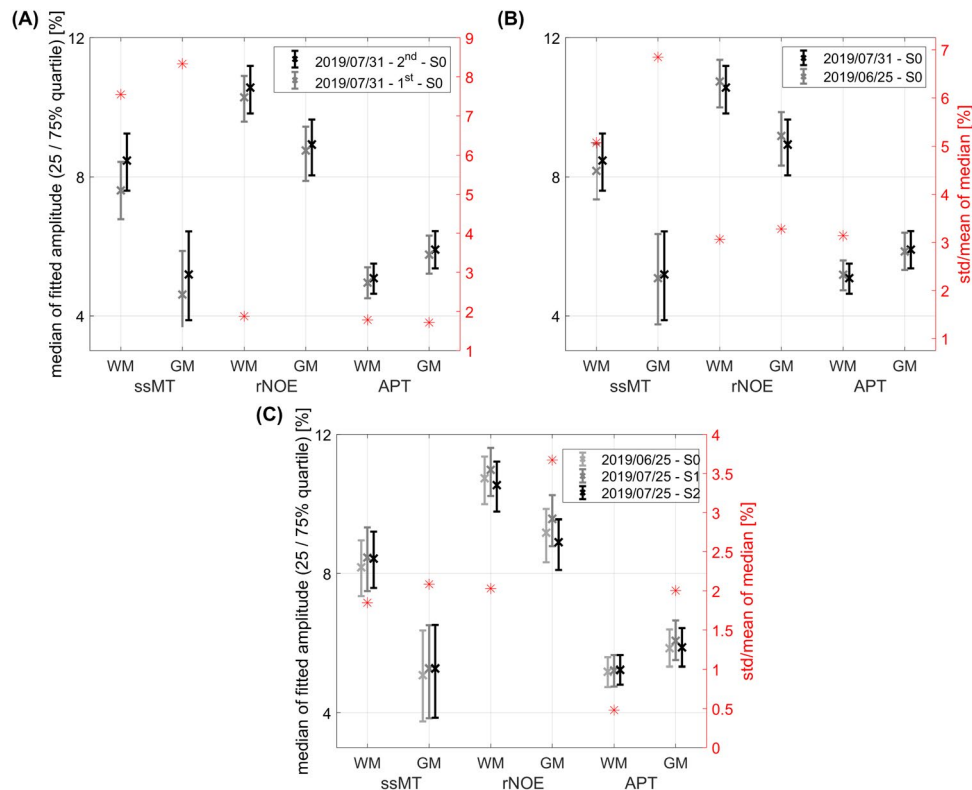


FIGURE 6 Comparison of fitted CEST contrasts in GM and WM of healthy subjects. Within same session and volunteer (A) and in different sessions (B). Across $n = 3$ sessions and volunteers (C); variations in fitted CEST contrasts calculated as (SD/mean over tissue type) are comparable within the same volunteer and across volunteers. Fitted CEST contrasts are stable with coefficient of variation (SD/mean) less than 9%. APT, amide proton transfer; GM, gray matter; rNOE, relayed nuclear Overhauser enhancement; ssMT, semisolid magnetization transfer; WM, white matter

even at 1.8 mm isotropic resolution at sixfold acceleration. Compared to higher field strengths (for example: Ref. 4), the approach at $B_0 = 3T$ benefits from more homogeneous saturation and excitation, especially in lower regions of the brain. In addition, the 3D-EPI readout benefits from lower field strength such that T_2 is increased by about 65% compared to 7T.¹¹ Assuming T_2^* scales similar as T_2 with field strength, at the given echo train length of ≈ 25 ms this is 30% higher residual transversal magnetization at the end of the readout (assuming monoexponential decay and linear scaling of magnetization with field strength), compensating partly for lower SNR as compared to ultrahigh field. The final protocol based on 3D-EPI allowed to perform CEST MRI at 1.8 mm isotropic resolution within 4.3 s per presaturation offset (1.2 s readout duration) with $256 \times 224 \times 156$ mm³ whole brain coverage. A previous approach of Zhu et al²⁵ at 3T enabled a FOV = $212 \times 212 \times 132$ mm³ at (2.2 mm)² in-plane resolution in 20 s per presaturation offset. A more recent 2D-EPI-based study of Ellingson et al²⁶ reported (2 mm)² in-plane resolution with FOV = $256 \times 256 \times 100$ mm³ in approximately 14 s per presaturation offset, also at $B_0 = 3T$. Krishnamoorthy et al²⁷ had chosen a FLASH approach with two shots per readout volume at $B_0 = 7T$. This enabled high in-plane resolution of (0.6 mm)² with a FOV of

$140 \times 140 \times 48$ mm³ for 16 slices but took 16 s per saturation offset and did not provide whole brain coverage. Deshmane et al⁶ worked with a 3D-GRE based snapshot approach, yielding (1.7 mm)² in-plane resolution for 18 slices with FOV = $220 \times 180 \times 54$ mm³ and 2.9 s readout. In general, snapshot-based approaches benefit from additional freedom in the pre-saturation such that no specific magnetization preparation has to be achieved for the image readout. It can be seen that our suggested protocol offers one of the highest spatial resolutions combined with a large FOV, it is significantly faster than most of the reported approaches and is flexible due to its snapshot realization.

One remaining drawback that all whole brain approaches share is the increased B_1 inhomogeneity within the large FOV even at clinical field strength. It has been shown previously^{3,28} that an effective B_1 correction strategy is a necessary prerequisite for reliable CEST quantification at ultra-high field. However, if homogeneity over the whole brain volume is aimed at, then B_1 correction becomes necessary even at 3T, as shown in this study. This prolongs the scan time significantly because it demands repeated CEST acquisitions with different B_1 scaling. Similar to the ultra-high field study,⁴ in the present study measurements at [0.75, 1.00, 1.25] times the nominal B_1 were shown to

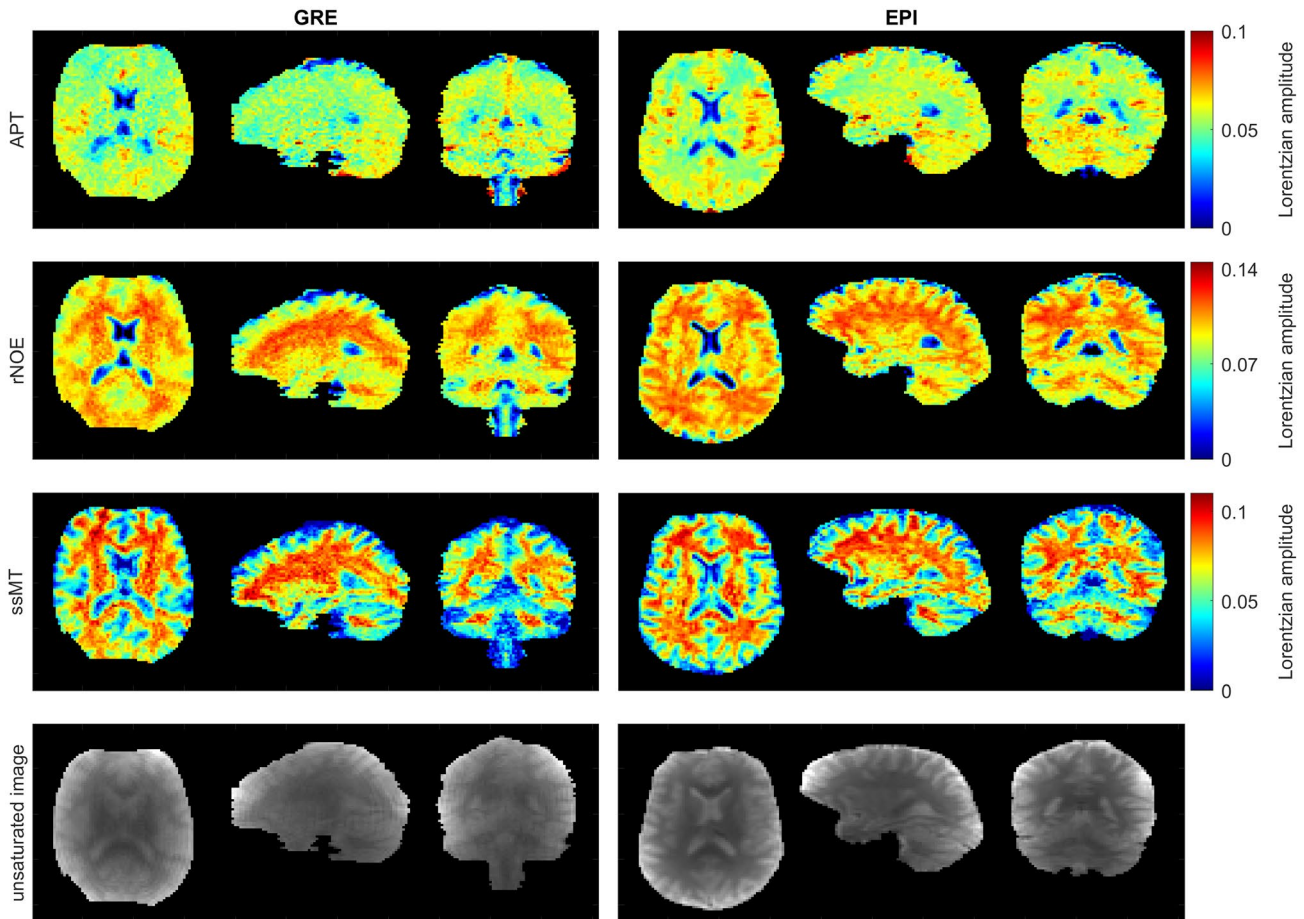


FIGURE 7 Fitted amplitudes of CEST pools: APT, rNOE, and ssMT. 2.34 mm isotropic resolution GRE (left) and EPI (right) both with same CEST presaturation module, same postprocessing, and in the same volunteer. Different segments were chosen for GRE and EPI readout, respectively, because data were not coregistered onto each other. Both readouts reveal similar GM and WM contrast in the fitted amplitudes of APT, rNOE, and ssMT. With the EPI readout, more detailed anatomical structures are visible. Additionally, in the last row unsaturated images are shown for both readouts. APT, amide proton transfer; GM, gray matter; GRE, gradient echo; rNOE, relayed nuclear Overhauser enhancement; ssMT, semisolid magnetization transfer; WM, white matter

be sufficient for spline interpolated Z - B_1 correction. The range of nominal B_1 values covered 95% of all occurring B_1 values and avoided extrapolation of the Z -spectra when correcting for B_1 inhomogeneity. The FWHM of the distributions of Z -values for all offsets were investigated in GM and WM separately after Z - B_1 correction. Including the three different B_1 values mentioned above and performing spline interpolation gave smaller FWHM than linear interpolation from five different B_1 values. On the contrary, including up to five B_1 values for spline interpolation only marginally decreased the FWHM further, indicating that the width of the natural distribution within the region of interest was already reached. Correction using two B_1 values yielded 44% smaller FWHM of Z -values than without correction. Still, in this case the fitted Lorentzian amplitudes were visibly altered. If parallel transmit systems are available, B_1 inhomogeneity might be further mitigated using B_1 shimming²⁹ or the MIMOSA approach,³⁰ which could directly be combined with our protocol.

If only certain brain areas are of interest, the number of scans at different presaturation B_1 values may be reduced given by the B_1 inhomogeneity in the considered slices. For example, for a single, more cranially located axial slice in which also B_0 distortions due to the air cavity of the mouth are less dominant, the B_1 deviation was below 20% (Figure 3A, Supporting Information Figure S10).

We also suggest to perform interleaved B_0 measurements after each CEST scan. This might not be of major importance as long as peaks can be fitted to the Z -spectrum. But in case that high power presaturation modules are used or asymmetry analysis is performed for evaluation,³¹ alteration of B_0 inhomogeneity over time should be taken into account.¹⁴ Necessity of repeated acquisitions at different presaturation B_1 also increased examination time, and therefore, the sensitivity to temporal variations in B_0 inhomogeneity. With accelerated field mapping methods, for example, DREAM/3DREAM^{32,33} for B_1 and dual-echo EPI for B_0 mapping instead of WASABI, the duration of field mapping

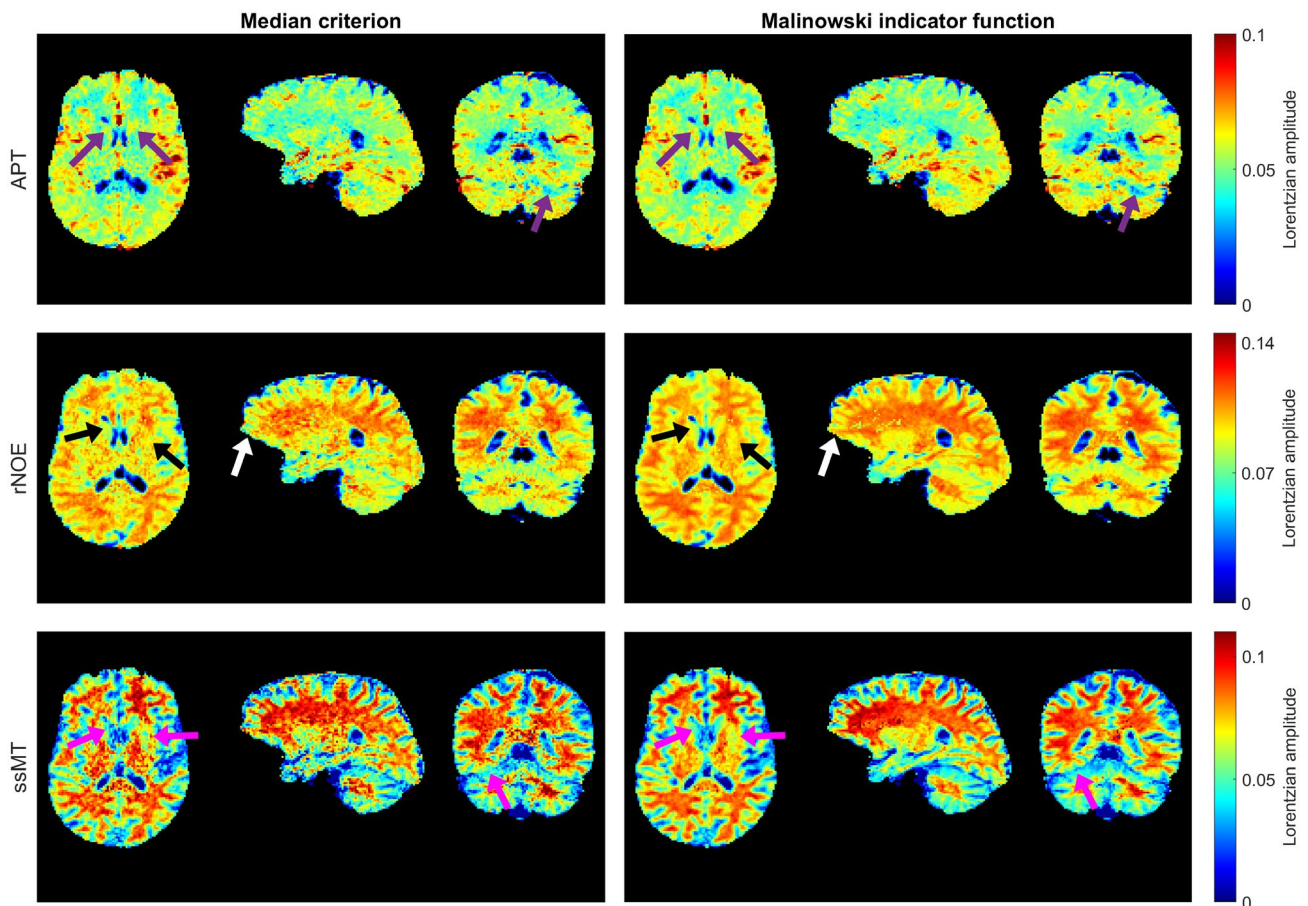


FIGURE 8 Effect of denoising on the subsequently fitted CEST pool amplitudes. APT, rNOE, and ssMT amplitudes fitted after postprocessing that included denoising according to Median (left) and Malinowski (right) criterion. Arrows highlight areas where denoising causes substantial differences in the spatial distribution of fitted amplitudes. Especially in the striatum, structures that might be of similar shape as caudate nucleus or putamen become visible when denoising with the more aggressive Malinowski criterion. APT, amide proton transfer; rNOE, relayed nuclear Overhauser enhancement; ssMT, semisolid magnetization transfer

could be strongly reduced. Assuming this enables field mapping within one minute, the total duration for the suggested procedure would be reduced by 25%. Although shorter scan durations may result in less intervolumetric head motion over time, retrospective motion correction before CEST analysis is still required (see Supporting Information Figure S12). Strong imaging acceleration is also an effective means to reduce intravolumetric motion sensitivity. Here, whole-brain k-space acquisition in only 1.2 s over 45 excitations resulted in no apparent motion artifacts. However, this may have to be reevaluated for motion-prone subject groups.

To quantify CEST effects, the amplitudes of the fitted 4-pool Lorentzian model²¹ were considered. Comparable fit models had recently been applied by, for example, Deshmene et al.,⁶ Goerke et al.,²⁴ and Akbey et al.⁴ Medians of fitted amplitudes in GM and WM were determined separately for each subject (Supporting Information Table S2). In Table 1, the mean values over different subjects are listed. In Figures 4, 5, and 8, as well as Supporting Information Figure S13, it can be observed that especially the APT

maps show some areas of strongly increased amplitudes in all healthy subjects. These match the expected spatial distribution of vessels known to have different CEST properties compared to brain tissue,^{34,35} which might explain the observations in APT maps. More data on this issue can be found in Supporting Information Figure S13 to S15. Comparing the fitted CEST amplitudes to the results of Deshmene et al.⁶ ($B_0 = 3T$, 3D-GRE readout) showed similar behavior in GM relative to WM for APT, rNOE, and ssMT (Table 1). Nonetheless, absolute values of fitted amplitudes differed. For APT and rNOE, we derived about twice as high amplitudes as reported by Deshmene et al.⁶ For ssMT, we found 1.4 times smaller amplitudes. This can be explained by the use of inversion pulses in the other study, which are known to generate strong MT effects,³⁶ whereas we used longer pulses for the sake of spectral selectivity. Additionally, a different number of pools was fitted to the data in both studies. Recently, Akbey et al.⁴ presented a CEST study at ultra-high field ($B_0 = 7T$, 3D-EPI readout). The reported GM/WM ratios (MTR_{LD} metric²³;

data extracted from Figure 9 in Ref. 4) of APT, rNOE, and ssMT {1.1, 0.9, 0.8} were similar to what we observed at $B_0 = 3T$. Nevertheless, it becomes obvious at this point that for all different presaturation and Lorentzian models used, standardization is missing. Most importantly, the compared EPI and GRE readouts yielded the same contrast for the same CEST presaturation and postprocessing used (Supporting Information Figure S14).

To investigate reproducibility of the suggested CEST pipeline, the median of the fitted amplitudes was considered. The COV across three subjects and sessions was below 4% for APT, rNOE, and ssMT. Still, it was up to 8.3% for ssMT in GM when comparing the results of repeated examinations of the same subject in the same session. On the contrary, for APT and rNOE amplitudes, it was below 2% for these two data sets. The increased deviation in the ssMT amplitudes may have several contributions. One explanation could be different GM and WM segmentation that was performed independently for different examinations. Segmentation tissue volume of both data sets differed by 0.45% for WM and 0.87% for GM. Because ssMT amplitudes show larger GM/WM contrast than those of APT and rNOE, a different segmentation should affect ssMT stronger. Still, segmentation could not exclusively be concluded to explain the observed deviations in the ssMT amplitudes. The deviations rather indicate that with the suggested CEST pipeline fitted amplitudes can at worst be reproduced with a COV of less than 8.5%.

The determined Lorentzian peaks might be used to calculate more sophisticated CEST contrasts such as the apparent exchange-dependent relaxation,³⁷ which additionally considers differences in T_1 relaxation times. One exemplary apparent exchange-dependent relaxation evaluation is shown in the Supporting Information Figure S11, with T_1 estimated using the proposed 3D-EPI readout in a saturation recovery protocol.

We also directly compared the proposed 3D-EPI protocol to an established 3D-GRE-based whole brain protocol.¹² EPI outperformed the GRE readout in terms of tSNR by a factor of two at the highest possible nominal resolution of the GRE, which was 2.34 mm isotropic. In addition, for the described settings the EPI readout was more than two times faster than the GRE. This gain in tSNR, along with the reduction in measurement time, allowed increased spatiotemporal resolution in the CEST acquisition as presented in this work. Fitted CEST amplitudes revealed much more detailed anatomical structures of the brain in case of the EPI readout, as shown in Figure 7. Still, GM/WM ratios of fitted amplitudes derived with the established GRE readout {1.06, 0.89, 0.71} were comparable to that observed with EPI (Table 1). It seems that actually the 3D-GRE was at its limits in case of the presented whole brain settings, for example, leading to more blurry images compared to the 3D-EPI and an established slab-selective

3D-GRE. The latter revealed contrast maps very similar to the nonselective 3D-EPI (Supporting Information Figure S14).

CEST spectra can be strongly affected by direct saturation of fat signals.^{38,39} Thus, a water excitation enables mitigation of this artifact. However, binominal water excitation pulses⁹ are rather long (additional ≈ 1.1 ms per excitation for both GRE and EPI) and would prolong a GRE readout significantly. Fortunately, for the EPI much fewer excitations are needed compared to GRE (45 at 1.8 mm isotropic resolution vs. 487 for the GRE at 2.34 mm), and these longer pulses can easily be afforded regarding scan time for EPI. Thus, artifacts in the Z-spectrum originating from fat signals are directly suppressed in snapshot EPI. In general, the faster readout of EPI is beneficial when comparing the PSF of GRE and EPI. Overall T_1 signal decay during readout can be described by a Look-Locker decay^{2,40,41} in both cases. Assuming a T_1 of 950 ms,¹¹ this yields a decay to 6.4% of the initial signal amplitude for EPI after acquisition of one 3D volume and 0.55% for GRE (EPI at 1.8 mm and GRE at 2.34 mm isotropic resolution). For EPI along the first PE direction (anteroposterior), signal decay is governed by T_2^* . Still, with $T_2^* = 30$ ms, approximately 40% of the initial signal remains at the end of the considered PE-line (one PE-line containing up to 32 readout lines was encoded per excitation).

To improve SNR, PCA denoising¹⁷ was applied during the postprocessing for both GRE and EPI, with cutoff eigenvalue determined according to Median criterion. A more aggressive denoising as introduced by Malinowski²⁰ was found to provide better visibility of anatomical structures in the striatum. We found that the COV due to different denoising was below 1.4% for the fitted Lorentzian amplitudes. Difference maps of amplitudes revealed no anatomical structures, but contiguous areas with larger deviations that are not noise-like (Supporting Information Figure S9) were observed. Also, Breitling et al¹⁷ reported that Malinowski indicator function can be problematic if applied to determine the cutoff eigenvalue for CEST data. In accordance with their findings, we therefore suggest to apply the more conservative Median criterion. The chosen denoising yielded noise-like residuals when considering a region of interest in WM with and without denoising and did not alter the fitted amplitudes (Supporting Information Figure S6 to S8), which provides strong evidence for the assumption that the denoising did indeed only remove noise but did neither remove nor add systematic features to the Z-spectra.

5 | CONCLUSION

It was demonstrated that it is possible to acquire reproducible (coefficient of variation of less than 9%) CEST contrasts with whole brain coverage at $B_0 = 3T$ in 4:22 minutes per

presaturation B_1 . In addition, with 1.8 mm isotropic resolution we were able to decrease the voxel size by 60% compared to currently used multislice or 3D CEST protocols. The suggested protocol is adaptable and may be used for any CEST presaturation module and fit model of interest. It therefore increases the opportunities of CEST investigations at $B_0 = 3T$ widely.

ACKNOWLEDGMENT

The financial support of the Max Planck Society, German Research Foundation (DFG) (grant ZA 814/2-1), and European Union's Horizon 2020 research and innovation program (grant agreement No. 667510) is gratefully acknowledged.

ORCID

Sebastian Mueller  <https://orcid.org/0000-0003-2699-9214>

Rüdiger Stirnberg  <https://orcid.org/0000-0001-7021-1063>

Klaus Scheffler  <https://orcid.org/0000-0001-6316-8773>

Tony Stöcker  <https://orcid.org/0000-0002-8946-9141>

Moritz Zaiss  <https://orcid.org/0000-0001-9780-3616>

REFERENCES

- Grad J, Bryant RG. Nuclear magnetic cross-relaxation spectroscopy. *J Magn Reson* (1969). 1990;90:1-8.
- Zaiss M, Ehes P, Scheffler K. Snapshot-CEST: Optimizing spiral-centric-reordered gradient echo acquisition for fast and robust 3D CEST. *NMR Biomed*. 2018;31:e3879.
- Windschuh J, Zaiss M, Meissner J-E, et al. Correction of B_1 -inhomogeneities for relaxation-compensated CEST imaging at 7 T. *NMR Biomed*. 2015;28:529-537.
- Akbe S, Ehes P, Stirnberg R, Zaiss M, Stöcker T. Whole-brain snapshot CEST imaging at 7 T using 3D-EPI. *Magn Reson Med*. 2019;82:1741-1752.
- Breuer FA, Blaimer M, Heidemann RM, Mueller MF, Griswold MA, Jakob PM. Controlled aliasing in parallel imaging results in higher acceleration (CAIPIRINHA) for multi-slice imaging. *Magn Reson Med*. 2005;53:684-691.
- Deshmane A, Zaiss M, Lindig T, et al. 3D gradient echo snapshot CEST MRI with low power saturation for human studies at 3T. *Magn Reson Med*. 2019;81:2412-2423.
- Stirnberg R, Huijbers W, Brenner D, Poser BA, Breteler M, Stöcker T. Rapid whole-brain resting-state fMRI at 3 T: Efficiency-optimized three-dimensional EPI versus repetition time-matched simultaneous-multi-slice EPI. *Neuroimage*. 2017;163:81-92.
- Poser BA, Ivanov D, Kannengiesser SA, Uludag K, Barth M. Accelerated 3D EPI using 2D blipped-CAIPI for high temporal and/or spatial resolution. In Proceedings of the 22nd Annual Meeting of ISMRM, Milan, Italy, 2014. p. 1506.
- Stirnberg R, Brenner D, Stöcker T, Shah NJ. Rapid fat suppression for three-dimensional echo planar imaging with minimized specific absorption rate. *Magn Reson Med*. 2016;76:1517-1523.
- Griswold MA, Jakob PM, Heidemann RM, et al. Generalized auto-calibrating partially parallel acquisitions (GRAPPA). *Magn Reson Med*. 2002;47:1202-1210.
- Zhu J, Klarhöfer M, Santini F, Scheffler K, Bieri O. Relaxation measurements in brain tissue at field strengths between 0.35T and 9.4T. In Proceedings of the 22nd Annual Meeting of ISMRM, Milan, Italy, 2014. Abstract 3208.
- Mueller S, Deshmane A, Herz K, Scheffler K, Zaiss M. Development of whole-brain 3D snapshot CEST MRI at 3T. In Proceedings of the 27th Annual Meeting of ISMRM, Montréal, Québec, Canada, 2019. Abstract 3995.
- Schuenke P, Windschuh J, Roeloffs V, Ladd ME, Bachert P, Zaiss M. Simultaneous mapping of water shift and B_1 (WASABI)—Application to field—Inhomogeneity correction of CEST MRI data. *Magn Reson Med*. 2017;77:571-580.
- Windschuh J, Zaiss M, Ehes P, Lee J-S, Jerschow A, Regatte RR. Assessment of frequency drift on CEST MRI and dynamic correction: Application to gagCEST at 7 T. *Magn Reson Med*. 2019;81:573-582.
- Cox RW. AFNI: Software for analysis and visualization of functional magnetic resonance neuroimages. *Comput Biomed Res*. 1996;29:162-173.
- Ashburner J, Friston KJ. Unified segmentation. *NeuroImage*. 2005;26:839-851.
- Breitling J, Deshmane A, Goerke S, et al. Adaptive denoising for chemical exchange saturation transfer MR imaging. *NMR Biomed*. 2019;e4133.
- Manjón JV, Coupé P, Buades A. MRI noise estimation and denoising using non-local PCA. *Med Image Anal*. 2015;22:35-47.
- Malinowski ER. Theory of error in factor analysis. *Anal Chem*. 1977;49:606-612.
- Malinowski ER. Determination of the number of factors and the experimental error in a data matrix. *Anal Chem*. 1977;49:612-617.
- Zaiß M, Schmitt B, Bachert P. Quantitative separation of CEST effect from magnetization transfer and spillover effects by Lorentzian-line-fit analysis of z-spectra. *J Magn Reson*. 2011;211:149-155.
- van der Zwaag W, Marques JP, Kober T, Glover G, Gruetter R, Krueger G. Temporal SNR characteristics in segmented 3D-EPI at 7T. *Magn Reson Med*. 2012;67:344-352.
- Jones CK, Huang A, Xu J, et al. Nuclear overhauser enhancement (NOE) imaging in the human brain at 7 T. *NeuroImage*. 2013;77:114-124.
- Goerke S, Soehngen Y, Deshmane A, et al. Relaxation-compensated APT and rNOE CEST-MRI of human brain tumors at 3 T. *Magn Reson Med*. 2019;82:622-632.
- Zhu H, Jones CK, van Zijl PCM, Barker PB, Zhou J. Fast 3D chemical exchange saturation transfer (CEST) imaging of the human brain. *Magn Reson Med*. 2010;64:638-644.
- Ellingson BM, Yao J, Raymond C, et al. pH-weighted molecular MRI in human traumatic brain injury (TBI) using amine proton chemical exchange saturation transfer echoplanar imaging (CEST EPI). *NeuroImage Clin*. 2019;22:101736.
- Krishnamoorthy G, Nanga RPR, Bagga P, Hariharan H, Reddy R. High quality three-dimensional gagCEST imaging of in vivo human knee cartilage at 7 Tesla. *Magn Reson Med*. 2017;77:1866-1873.
- Singh A, Cai K, Haris M, Hariharan H, Reddy R. On B_1 inhomogeneity correction of in vivo human brain glutamate chemical exchange saturation transfer contrast at 7T. *Magn Reson Med*. 2013;69:818-824.
- Tse DHY, da Silva NA, Poser BA, Shah NJ. B_1+ Inhomogeneity mitigation in CEST using parallel transmission. *Magn Reson Med*. 2017;78:2216-2225.

30. Liebert A, Zaiss M, Gumbrecht R, et al. Multiple interleaved mode saturation (MIMOSA) for B1+ inhomogeneity mitigation in chemical exchange saturation transfer. *Magn Reson Med.* 2019;82:693-705.
31. Guivel-Scharen V, Sinnwell T, Wolff SD, Balaban RS. Detection of proton chemical exchange between metabolites and water in biological tissues. *J Magn Reson.* 1998;133:36-45.
32. Ehses P, Brenner D, Stirnberg R, Pracht ED, Stöcker T. Whole-brain B1-mapping using three-dimensional DREAM. *Magn Reson Med.* 2019;82:924-934.
33. Nehrke K, Börnert P. DREAM – A novel approach for robust, ultrafast, multislice B1 mapping. *Magn Reson Med.* 2012;68:1517-1526.
34. Shah SM, Mougin OE, Carradus AJ, et al. The z-spectrum from human blood at 7T. *Neuroimage.* 2018;167:31-40.
35. Zheng S, van der Bom IMJ, Zu Z, Lin G, Zhao Y, Gounis MJ. Chemical exchange saturation transfer effect in blood. *Magn Reson Med.* 2014;71:1082-1092.
36. McLaughlin AC, Ye FQ, Pekar JJ, Santha AKS, Frank JA. Effect of magnetization transfer on the measurement of cerebral blood flow using steady-state arterial spin tagging approaches: A theoretical investigation. *Magn Reson Med.* 1997;37:501-510.
37. Zaiss M, Xu J, Goerke S, et al. Inverse Z-spectrum analysis for spillover-, MT-, and T1 -corrected steady-state pulsed CEST-MRI—application to pH-weighted MRI of acute stroke. *NMR Biomed.* 2014;27:240-252.
38. Zimmermann F, Korzowski A, Breitling J, et al. A novel normalization for amide proton transfer CEST MRI to correct for fat signal-induced artifacts: Application to human breast cancer imaging. *Magn Reson Med.* 2020;83:920-934.
39. Lu J, Zhou J, Cai C, Cai S, Chen Z. Observation of true and pseudo NOE signals using CEST-MRI and CEST-MRS sequences with and without lipid suppression. *Magn Reson Med.* 2015;73:1615-1622.
40. Look DC, Locker DR. Time saving in measurement of NMR and EPR relaxation times. *Rev Sci Instrum.* 1970;41:250-251.
41. Ganter C. Analytical solution to the transient phase of steady-state free precession sequences. *Magn Reson Med.* 2009;62:149-164.

SUPPORTING INFORMATION

Additional Supporting Information may be found online in the Supporting Information section.

FIGURE S1 tSNR evaluation at $B_0 = 3T$ for 63 images with 3 s idle time between subsequent acquisitions. Final protocol as described in the paper was applied with different nominal flip angles ranging from 10 to 30 degree. All data were corrected for motion during post processing. Besides the flip angle all parameters remained unchanged: $(1.78 \text{ mm})^3$ nominal resolution, CAIPIRINHA = $1 \times 6^{\text{shift}=2}$, half elliptical scanning, BW = 1930 Hz/pix, phase partial Fourier and FOV = $256 \times 224 \times 156 \text{ mm}^3$

FIGURE S2 tSNR determined for 63 images with 3 s idle time between subsequent acquisitions. Final protocol was used besides the deviations stated in the legend with the dark blue line being the final settings. Data were corrected for motion

FIGURE S3 Comparison of tSNR across 63 images with 3 s idle time in between subsequent acquisitions. The novel

3D-EPI protocol worked out for 3 T yields approximately 20% higher tSNR as the published 7T protocol.¹ Both protocols were executed at $(1.78 \text{ mm})^3$ nominal resolution, FA = 15° and BW = 1930 Hz/pix and motion correction was performed

FIGURE S4 (A) shows the relative magnitude rMag for different FA with its maximum value of 4.4% for a FA = 17.5° . (B) shows the relative FWHM (rFWHM) for the 3T protocol with different flip angles (FA). It can be seen that for FA = 15° the average rFWHM is increased to ≈ 1.34

FIGURE S5 (A) Effect of Z-B₁ correction (3) on the distribution of Z-values in gray matter at presaturation offset -3.5 ppm. Effect of 2 (B) to 5 (E) B₁ values included in Z-B₁ correction on fitted rNOE amplitudes. Including 2 (B) values (linear interpolation) shows deviations as compared to 5 values (spline interpolation) included. Difference between 3 and 4 or 5 values included (all: spline interpolation) is only little

FIGURE S6 Influence of denoising according to the Median criterion on the mean Z-spectrum in a white matter region of interest in a healthy volunteer. The mean Z-spectrum did not significantly differ after denoising which is shown, for example, in the difference of the Z-spectra. The mean value of difference is -5.6×10^{-6} , whereas the spatial standard deviations are on average $1.0 \times 10^{-3\text{max}}$ (without PCA) and 9.4×10^{-4} (including PCA), respectively

FIGURE S7 Comparison of fit results in a healthy volunteer with respect to the effect of PCA denoising (cut off eigenvalue determined according to the Median criterion). Plots show correlation of fitted Lorentzian amplitudes with and without PCA denoising. Legends provide: Pearson r, P-value as well as slope and offset of a linear fit to the data. High correlation of $r > 0.92$ for all contrasts (APT, rNOE, ssMT and (direct saturation) DS) indicates that PCA denoising does not introduce any systematical bias to the fit results

FIGURE S8 Fitted Lorentzian amplitudes of APT, rNOE, SSMT and DS (direct saturation) are shown in the same axial slice separately with and without PCA denoising (cut off eigenvalue determined according to the Median criterion). Last row shows the difference between the two sets of fitted amplitudes. The difference maps do not reveal any significant anatomical structure that would have potentially been introduced due to the PCA denoising

FIGURE S9 Effect of different cut off criteria during PCA denoising (17) on the fitted CEST amplitudes of one healthy subject (S0). (A): median of ssMT, rNOE and APT amplitudes in gray and white matter for cut off according to Malinowski's indicator function (20) and Median criterion (18). The maps in (B), (C) and (D) show spatial distribution of the difference in fitted amplitudes of the same data shown in (A). Arrows indicate contiguous areas of deviations

FIGURE S10 Fitted amplitudes of APT (A), rNOE (B) and ssMT (C) for a different number of B₁ values included in the B₁ correction (3). Maps show axial slice in more cranially situated

region of the brain that had more homogeneous B_1 distribution than other areas of the brain. B_1 correction including only two different B_1 values (linear interpolation) might, therefore, be sufficient. Still including five B_1 values and applying spline interpolation yields smoother maps due to averaging

FIGURE S11 CEST MRI acquired according to the final protocol combined with a saturation recovery sequence to determine T_1 and from this calculate the T_1 corrected AREX (37) contrast

FIGURE S12 Same data and post processing but once with and once without motion correction. Arrows highlight areas where substantial differences in the fitted Lorentzian amplitudes can be seen if motion correction is not applied. Even though the optimized protocol allows relatively fast CEST MRI acquisition motion would significantly corrupt the results if not corrected

FIGURE S13 Fitted Lorentzian amplitudes (rNOE, APT, ssMT and (DS) direct saturation) of four healthy volunteers. For all volunteers only in the APT maps voxels with much larger amplitudes are visible

FIGURE S14 Fitted Lorentzian amplitudes and maximum intensity projections for an established slab selective 3D-GRE (2,6) and the novel non-selective 3D-EPI readout. In both cases only in the APT maps similarly shaped and located areas show higher amplitudes (see arrows). Both readouts were acquired in different volunteers, and therefore, have different slice orientations. Data includes slices 2 to 11 (GRE) and 87 to 100 (EPI), respectively

FIGURE S15 Same 3D-EPI measurement as shown in Supporting Information Figure S15. Residual sum of squares (RSS) was determined in slice 87 to 100. It is found that RSS does not increase with increasing APT amplitudes (A) and that highest RSS is observed in the ventricles

TABLE S1 Fit parameters for all $i = 0, \dots, 3$ amplitudes (A_i), peak widths (G_i), initial magnetization (Z_i) and position of the bulk water pool (d_{wi}). Positions for $i = 1, \dots, 3$ were fixed at 3.1, -1.25 and -3.1 ppm relative to d_{wi} . Other parameters fitted with lower bond (l_b), upper bond (u_b) and start values (p_0)

TABLE S2 Resulting amplitudes of 4-pool Lorentz fit for $n = 5$ different examinations in 3 different subjects (S_0 , S_1 and S_2). All values are given in percent to increase visibility. For each examination and subject median and standard deviation (std) were determined in gray (GM) and white matter (WM) for APT, rNOE and ssMT. In the 3 bottom lines mean, standard deviation and coefficient of variation (c.o.v.) across the five different examinations are shown

How to cite this article: Mueller S, Stirnberg R, Akbey S, et al. Whole brain snapshot CEST at 3T using 3D-EPI: Aiming for speed, volume, and homogeneity. *Magn Reson Med.* 2020;84:2469–2483. <https://doi.org/10.1002/mrm.28298>

B.3. Publication 3

Pulseq-CEST: Towards multi-site multi-vendor compatibility and reproducibility of CEST experiments using an open-source sequence standard

Herz K., Mueller S., Perlman O., Zaitsev M., Knutsson L., Sun P. Z., Zhou J., van Zijl P., Schmidt M., Dörfler A., Scheffler K., and Zaiss M.

Pulseq-CEST: Towards multi-site multi-vendor compatibility and reproducibility of CEST experiments using an open-source sequence standard

Kai Herz^{1,2}  | Sebastian Mueller^{1,2}  | Or Perlman³  | Maxim Zaitsev⁴ |
 Linda Knutsson^{5,6}  | Phillip Zhe Sun⁷  | Jinyuan Zhou⁶ | Peter van Zijl^{6,8} |
 Kerstin Heinecke⁹  | Patrick Schuenke⁹  | Christian T. Farrar³  |
 Manuel Schmidt¹⁰ | Arnd Dörfler¹⁰ | Klaus Scheffler^{1,2}  | Moritz Zaiss^{1,10} 

¹Magnetic Resonance Center, Max Planck Institute for Biological Cybernetics, Tuebingen, Germany

²Department of Biomedical Magnetic Resonance, University of Tuebingen, Tuebingen, Germany

³Athinoula A. Martinos Center for Biomedical Imaging, Department of Radiology, Massachusetts General Hospital and Harvard Medical School, Charlestown, Massachusetts, USA

⁴High Field MR Center, Center for Medical Physics and Biomedical Engineering, Medical University of Vienna, Vienna, Austria

⁵Department of Medical Radiation Physics, Lund University, Lund, Sweden

⁶Russell H. Morgan Department of Radiology and Radiological Science, Johns Hopkins University School of Medicine, Baltimore, Maryland, USA

⁷Yerkes Imaging Center, Yerkes National Primate Research Center, Emory University, Atlanta, Georgia, USA

⁸F.M. Kirby Research Center for Functional Brain Imaging, Kennedy Krieger Institute, Baltimore, Maryland, USA

⁹Physikalisch-Technische Bundesanstalt, Braunschweig and Berlin, Germany

¹⁰Department of Neuroradiology, Friedrich-Alexander Universität Erlangen-Nürnberg, University Hospital Erlangen, Erlangen, Germany

Correspondence

Kai Herz, Magnetic Resonance Center, Max Planck Institute for Biological Cybernetics, Max-Planck-Ring 11, 72076 Tuebingen, Germany.
 Email: kai.herz@tuebingen.mpg.de

Funding information

Max Planck Society, German Research Foundation (ZA 814/5-1, SCHU 3468/1-1, SFB 1340 project C03, and Reinhart Koselleck project DFG SCHE 658/12); National Institutes of Health (P41 EB015909, RO1EB019934, RO1 EB015032, R01 CA203873, and P41 EB024495); Swedish Research Council (2015-04170 and 2019-03637); Swedish Cancer Society (CAN 2015/251 and 2018/550); and European Union's Horizon 2020 Research and Innovation Program (Marie Skłodowska-Curie Grant No. 836752)

Purpose: As the field of CEST grows, various novel preparation periods using different parameters are being introduced. At the same time, large, multisite clinical studies require clearly defined protocols, especially across different vendors. Here, we propose a CEST definition standard using the open *Pulseq* format for a shareable, simple, and exact definition of CEST protocols.

Methods: We present the benefits of such a standard in three ways: (1) an open database on GitHub, where fully defined, human-readable CEST protocols can be shared; (2) an open-source Bloch-McConnell simulation to test and optimize CEST preparation periods in silico; and (3) a hybrid MR sequence that plays out the CEST preparation period and can be combined with any existing readout module.

Results: The exact definition of the CEST preparation period, in combination with the flexible simulation, leads to a good match between simulations and measurements. The standard allowed finding consensus on three amide proton transfer-weighted protocols that could be compared in healthy subjects and a tumor patient. In

This is an open access article under the terms of the Creative Commons Attribution License, which permits use, distribution and reproduction in any medium, provided the original work is properly cited.

© 2021 International Society for Magnetic Resonance in Medicine

addition, we could show coherent multisite results for a sophisticated CEST method, highlighting the benefits regarding protocol sharing and reproducibility.

Conclusion: With *Pulseq*-CEST, we provide a straightforward approach to standardize, share, simulate, and measure different CEST preparation schemes, which are inherently completely defined.

KEYWORDS

CEST, open-source, *Pulseq*, standardization

1 | INTRODUCTION

Chemical exchange saturation transfer MRI uses the exchange transfer of magnetization from solutes to water to increase the sensitivity of detection through a saturation effect on the water signal.¹⁻³ The CEST method uses a molecular amplification mechanism that accumulates its effect on the spin system during a saturation period (T_{sat}), consisting of one or more RF pulses with or without interpulse delays, followed by an imaging sequence. Detectable CEST effects in vivo have been reported for instance for proteins,^{4,5} glutamate,⁶ and different sugars.⁷⁻⁹ The choice of a specific saturation period is crucial for an optimal CEST experiment, as the maximum effect depends not only on the tissue and solute pool of interest, but also on the efficiency of the saturation imposed by the RF pulse scheme¹⁰ and of its transfer during T_{sat} ^{11,12} as well as on concomitant saturation effects, such as direct saturation and magnetization-transfer contrast associated with the semisolid pool.^{13,14} Moreover, differences in approaches for data analysis in terms of normalization or spectral regions considered can further affect the final image contrast calculated from Z-spectra.¹⁵

Thus, the saturation period has to be precisely defined by such parameters as RF pulse shape (both magnitude and phase), pulse duration (t_p), saturation duty cycle (DC_{sat}), total saturation time (T_{sat}), saturation field strength (B_1), and offset from the water resonance frequency ($\Delta\omega$). However, these parameters vary significantly in the current literature,¹⁶ and are not always provided in sufficient detail. In addition, the literature uses different definitions or terminology to describe saturation “power,” such as the flip angle of the pulse,¹⁷ pulse peak B_1 amplitude,¹⁸ B_1 root mean square ($B_{1,\text{rms}}$) amplitude,¹⁹ or continuous wave power equivalent ($B_{1,\text{cwpe}}$),²⁰ potentially leading to confusion when implementing a comparable CEST MRI experiment. Therefore, it is not always possible to faithfully reproduce a CEST experiment without corresponding with the authors, and even then, the method could still be prone to errors. Thus, a common, easy-to-use format for researchers to provide and share the precise saturation parameters is desirable, especially regarding the current focus on reproducibility in MR research.²¹ Moreover,

a growing number of deep learning-based evaluation approaches for large multi-site, multi-vendor data sets make a proper definition of input data even more important.²²

A vendor-independent, human-readable, and sharable file format for MR sequences has been introduced with the *Pulseq* framework.²³ In *Pulseq*, all sequence parameters are defined in a text file (hereafter called *pulseq-file*), which can be created with various popular programming applications such as *MATLAB* (The MathWorks, Natick, MA) or *Python*.²⁴ This *pulseq-file* is then read and played out on the scanner using a vendor-specific interpreter sequence. Although *Pulseq* is a great tool that enables a flexible implementation of complex sequence patterns,²⁵ it is complicated to incorporate vendor-provided image reconstruction functions, which are generally proprietary. However, having the source code of a full interpreter sequence at hand, a capsulated interpreter can be included into other existing sequences for imaging readout. For example, a 3D snapshot gradient echo^{26,27} can be equipped with an encapsulated *Pulseq* interpreter that solely plays out a CEST preparation block defined in a *pulseq-file*. This makes the *Pulseq* file format a perfect candidate for sharing CEST preparation periods. The established MRI readout following the saturation period can be used with the familiar user interface and all possibilities of adjustments and image reconstruction. This procedure enables four major advantages:

1. The CEST preparation period definition in *Pulseq* is complete. It is defined in a human-readable text file that is easy to interpret and allows direct comparison of different protocols. Thus, exchanging and comparing such files allows total reproducibility;
2. The definition of the RF pulses can be done in *MATLAB* or *Python* instead of implementing it in the sequence using a vendor-specific language (often C++), which, depending on the vendor, can be time-consuming and can require the compilation of a new sequence library;
3. The CEST preparation period can be used directly in simulations in the same framework (eg, *MATLAB* or *Python*), eliminating possible sources of error from transferring simulation results to the sequence source code and vice versa; and

4. The CEST preparation period can be used directly at the scanner with different state-of-the-art readouts, bridging the gap from first publication to reproducible multi-site application not only for research, but also for clinical applications. In addition, novel developments and work-in-progress approaches can be compared much faster and more reliably than with existing approaches.

Using *Pulseq* for the CEST preparation part in the sequence theoretically enables a vendor-independent approach, provided that a *Pulseq* interpreter sequence is available for each vendor. In this work, we implemented such a hybrid *Pulseq*-CEST sequence for the Siemens IDEA (Integrated Development Environment for Applications; Siemens Healthineers, Erlangen, Germany) framework and tested it on three Siemens scanners at three sites, with two scanner models running very different software baselines. In addition, we present a fast and flexible open-source simulation for the same *pulseq-files* that are played out on the MR scanner. Moreover, we provide a platform for researchers to share and test their saturation protocols in the *Pulseq* format. As a first illustration of these steps, we show applications at clinically available MR scanners including adiabatic spin lock-prepared imaging, well-defined and original-author-approved amide proton transfer-weighted (APT_w) imaging, and a CEST MR fingerprinting (MRF) protocol measured at three different MR sites in Europe and the United States.

2 | METHODS

2.1 | Pulseq to standardize CEST preparation periods

Originally intended as a hardware-independent MRI sequence prototyping framework, *Pulseq* allows for rapid and simple sequence definitions from within *MATLAB*, *Python*, and other software programming packages, which are usually open source.^{23,24,28} Within these programs, RF pulse, gradient, ADC, and trigger events can easily be defined and are written to a *pulseq-file*, which is then read and played out by a native interpreter sequence on the scanner. Because *Pulseq* includes built-in functions to generate block, Gaussian, apodized sinc, and arbitrary user-defined pulse shapes, theoretically, every excitation or saturation CEST preparation scheme can be defined with only a few lines of code. Thus, defining saturation periods in *Pulseq* is a general and easy approach. Example codes to create different CEST preparation periods in *MATLAB* and *Python* are provided at the projects' website (<https://pulseq-cest.github.io>).

The *pulseq-file* contains the full definition of all sequence objects, which makes it a perfectly suitable candidate for

sharing protocol parameters of preparation periods for generating different types of contrast before readout, such as a CEST contrast here. Moreover, these *pulseq-files* are human-readable, and the aforementioned *MATLAB* and *Python* packages include plot functions to compare preparation schemes directly. The benefit of such a direct comparison becomes obvious in Figure 1. Here, RF magnitude and phase of different CEST preparation periods used in this study are shown. For instance, Figure 1A,B shows the shape of an off-resonant adiabatic spin-lock pulse scheme previously used for in vivo DGE_p studies²⁹ and phantom measurements herein. While such a pulse shape would be rather complex to describe in a publication, it is completely defined in the *pulseq-file*. Figure 1C-H shows three different saturation preparation protocols (APT_w_3T_001,³⁰ APT_w_3T_002,³¹ and APT_w_3T_003³²) that were recently recommended for APT-weighted tumor applications.³³ For comparison of the CEST preparation pulses, we use the following definitions for the B_1 pulse average ($B_{1,pa}$), B_1 average amplitude over pulse train ($B_{1,cwae}$), and B_1 average quadratic amplitude over pulse train ($B_{1,rms}$ or $B_{1,cwpe}$)^{34,35}:

$$B_{1,pa} = \frac{1}{t_p} \int_0^{t_p} B_1(t) dt \quad (1)$$

$$B_{1,cwae} = \frac{1}{t_p + t_d} \int_0^{t_p} B_1(t) dt \quad (2)$$

$$B_{1,rms} = \sqrt{\frac{1}{t_p + t_d} \int_0^{t_p} (B_1(t))^2 dt} \quad (3)$$

where t_p is the pulse duration, and t_d is the delay between preparation pulses. For the three different APT_w protocols in Figure 1C-H, $B_{1,rms}$ was set to 2 μ T. The different peak amplitudes of the saturation pulses due to the different shapes and duty cycles are directly observable. For instance, in Figure 1C,E, sinc-Gauss pulses with the same shape are shown, but in Figure 1E, the peak amplitude of the pulse is higher, as this protocol uses a saturation duty cycle (DC_{sat}) of 0.5 compared with 0.9 for the protocol in C.

Figure 1I,J shows the RF magnitude and phase over multiple repetitions of the CEST-MRF schedule.³⁶⁻³⁸ Here, the amplitude of the spin-lock saturation pulses changes over the different repetitions.

Full details about the protocols can be found in the *pulseq-files* in the Supporting Information. In addition, the RF phase evolution during saturation pulses is available, a parameter that is rarely provided in CEST literature, although it can have an influence on the experiment, as shown in more detail in Supporting Information Figures S1 and S2.

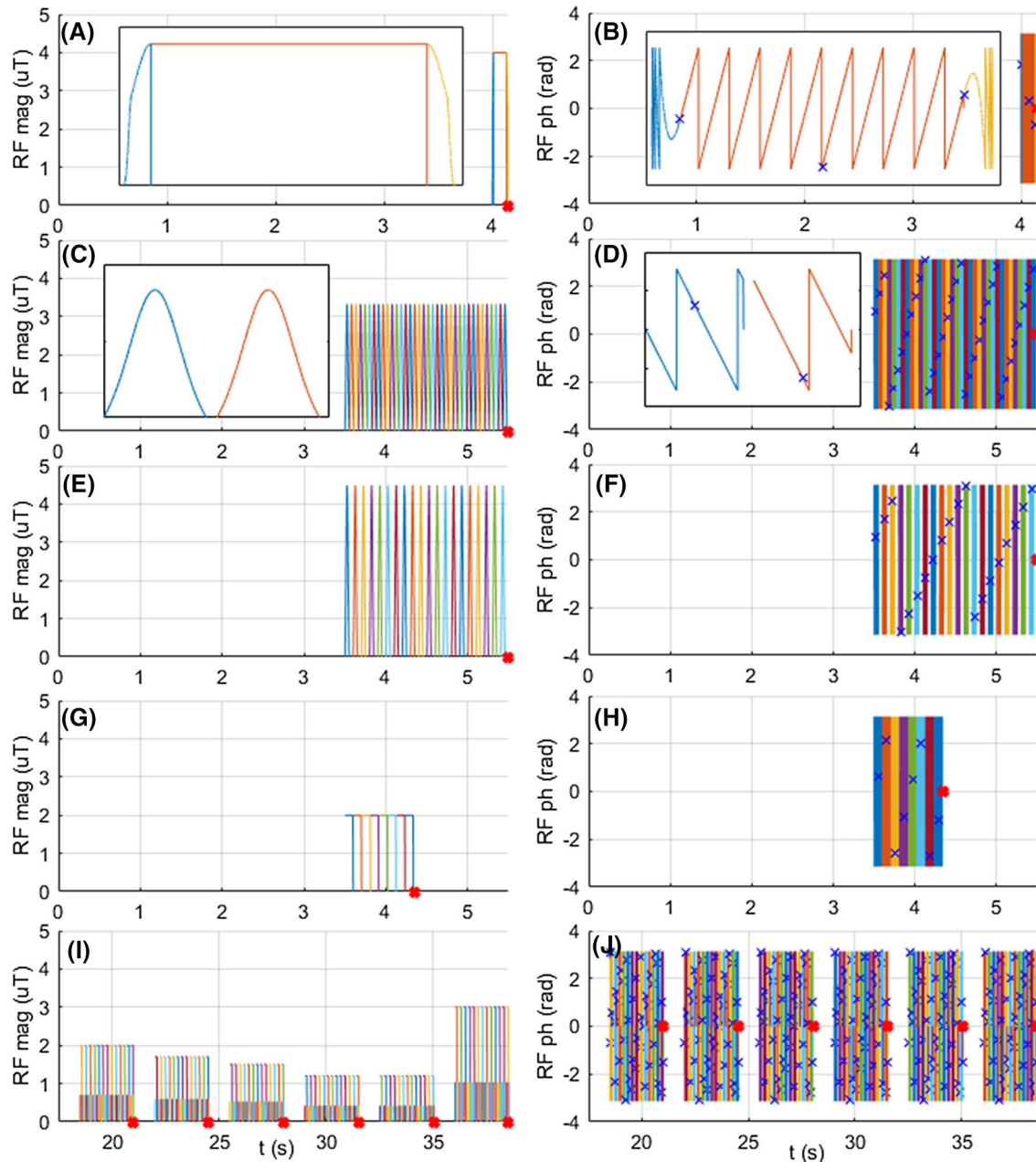


FIGURE 1 A,B, The RF magnitude and phase of the HSExp spin-lock saturation at 0.6 ppm. Adiabatic tip-down (blue) and tip-up (yellow) pulses surround the locking pulse (red). The frequency modulation can be seen in the zoomed plot (black box) from the changing phase. The red dot marks the beginning of the readout period, which can be an FID or a full 3D gradient echo for instance; spoiler gradients are not shown for simplicity. The RF magnitude (C,E,G) and phase (D,F,H) during three different amide proton transfer–weighted (APT_w) protocols: APT_w_3T_001 (C,D), APT_w_3T_002 (E,F), and APT_w_3T_003 (G,H)—all with $B_{1,rms} = 2 \mu\text{T}$ and recovery time (T_{rec}) = 3.5 seconds. Due to the different pulse shapes and DC_{sat} during the preparation periods, the peak amplitudes of the pulses differ. In (C) and (D), a zoomed graph for two RF pulses is shown in the black rectangles. The phase accumulation due to the off-resonance character of the pulses is taken into account, as shown between the blue and red phase curve. The blue “x” marks the phase at the center of the RF pulse. I,J, The RF magnitude and phase of multiple repetitions during an amide–MR fingerprinting spin-lock saturation at 3.5 ppm

2.2 | Bloch-McConnell simulations

To be able to not only compare protocol parameters, but also simulate them, an application was written in C++ that loops through the *pulseq-files*, performs Bloch-McConnell

simulations for the respective sequence events,³⁷ and returns the current magnetization vector after preparation. The compiled code is callable as a *mex* function for an easy integration into a *MATLAB*-based pipeline. The *Python* implementation wraps the C++ code with SWIG (Simplified Wrapper and

Interface Generator) and is simplified by a *Python* parser. This setup ensures input and output compatibility between the *MATLAB* and *Python* implementation. Where not specified explicitly, the *mex* function was used for the simulations in this study. Due to the flexible design, it is possible to simulate an arbitrary number of CEST pools and an additional semisolid magnetization-transfer contrast pool with either a Lorentzian or super-Lorentzian line shape. In combination with the flexible *Pulseq* saturation period definition, any number of CEST pools can be simulated for any kind of preparation period in a relatively short amount of time, thanks to the native C++ implementation. For this study, the simulation program was compiled for a 64-bit *Microsoft Windows* 10 OS, using the *Microsoft Visual C++* 2017 compiler. Simulations were performed on a PC with an Intel i7-7700K Kaby Lake CPU. The source code is available on the project's website (<https://pulseq-cest.github.io/>).

2.3 | Pulseq sequence building block

By adapting the source code of the original *Pulseq* sequence for the Siemens IDEA framework, we were able to play out the *pulseq-files*, containing the definition of the CEST preparation period, directly on the scanner, followed by different readout sequences. Adaptions were implemented to use the code as a so-called sequence-building block (SBB). For example, (1) the FOV positioning options are removed, as this information is defined in the readout sequence; and (2) during the *Pulseq* building block, no data are acquired, as indicated by the ADC event; instead the ADC event is used internally as marker to interrupt the *Pulseq* sequence and switch to the readout sequence, which is then played out (Figure 2). Note that the *Pulseq* block containing an ADC event is skipped entirely, and therefore is not allowed to contain any other events. With this design of the *Pulseq* SBB, it can be implemented in every MR sequence where the source code is available. Because timing and specific absorption rate calculations are handled by the interpreter sequence, the workload for such implementation is small. Only a few lines of code need to be implemented in the main sequence for initialization, preparation, and running of the *Pulseq* SBB. For instance, to implement the SBB to an established, native EPI sequence,^{39,40} only 30 lines of C++ code were necessary, including code regarding communication with the user interface.

The *Pulseq* interpreter sequence for Siemens IDEA contains vendor-specific code, and can therefore only be obtained through the customer-to-customer partnership program (co-called C2P procedure). The interpreter sequence can be provided upon request to interested researchers. The current *Pulseq* C2P package supports multiple software and hardware platforms of Siemens, including Numaris4 vb15, vb17,

vb19(a,b), vd11d, ve11(a,b,c,e,k,u), ve12u, and NumarisX va11 and va20. For other vendors, different "interpreter" approaches need to be developed or already exist, such as the TOPPE interpreter for GE (GE Healthcare, Chicago, IL) systems.⁴¹

2.4 | Phantom preparation

A phantom was prepared using multiple 6-mL tubes with either L-arginine or D-glucose. Five tubes were filled with 50 mmol/L L-arginine (Fluka Chemie, Buchs, Switzerland) dissolved in phosphate-buffered saline (according to Cold Spring Harbor Protocols,⁴² but containing 2.7 mM KCl, 10 mM Na₂HPO₄, 1.8 mM KH₂PO₄, and 140 mM NaCl). The pH of the L-arginine tubes was adjusted between 4 and 6 using HCl (Sigma-Aldrich Laborchemikalien, Germany) and NaOH (Riedel-de Haën, Seelze, Germany). Two additional tubes were filled with a D-glucose solution (Glucosteril 20%; Fresenius Kabi Deutschland, Germany) and diluted to 33 mmol/L or 66 mmol/L using phosphate-buffered saline. To shorten T₁, gadoterate meglumine (Dotarem 500 mmol/L; Guerbet, Villepinte, France) was added to each tube in this phantom, yielding a final concentration of approximately 0.054 mmol/L.

2.5 | Magnetic resonance imaging measurements

The MRI measurements were performed on three clinical 3T scanners: two 3T Prismas and one 3T Trio (Siemens Healthineers). For all Prisma measurements, the 64-channel head coil for signal reception and the body coil for transmission were used. All in vivo measurements were performed under approval by the local ethics committee. Each subject gave written, informed consent before the study. Where not specified explicitly, measurements were done on a Siemens 3T Prisma scanner at the Max Planck Institute Tuebingen). Following the *Pulseq* SBB, a 3D gradient-echo readout,^{26,27} was used. A table with relevant imaging parameters for the readout sequence can be found in Supporting Information Table S1. In addition, all *pulseq-files* used in this study are provided in the Supporting Information.

For the phantom experiment, a spin-lock (SL) Z-spectrum acquisition was performed using HSExp pulses⁴³ with the pulse shape parameters recently optimized for 3 T²⁹ (see Figure 1A,B and SLExp_3T_Phantom.seq in the Supporting Information). For each saturation, a single spin-lock pulse with a duration of 100 ms was played out after a recovery delay (T_{rec}) of 5 seconds. For this protocol, 39 evenly distributed offsets between ±6 ppm were acquired, together with an unsaturated S₀ scan. To enable realistic simulations,

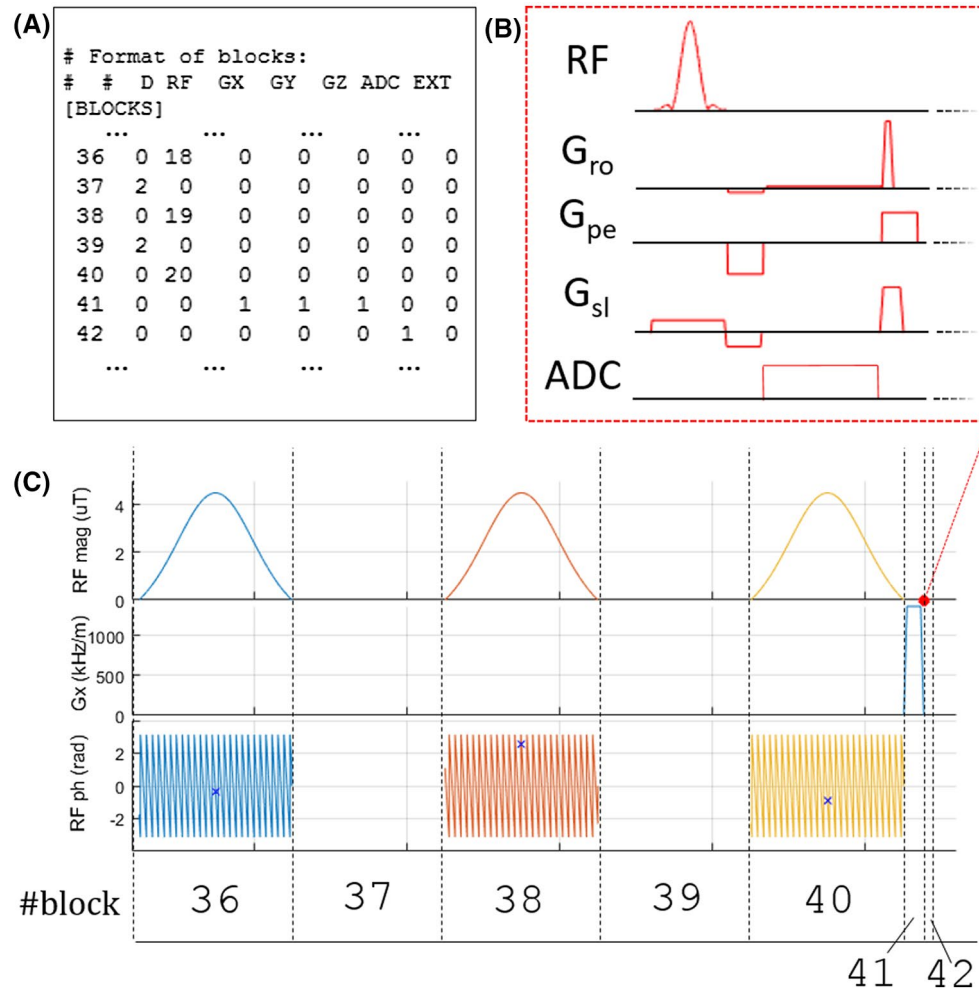


FIGURE 2 Schematic sketch of the *Pulseq*-CEST hybrid sequence playing out the preparation period of protocol APTw_3T_002. A, Format of the *pulseq*-file with channels for time delay, RF pulse, gradient, ADC, and trigger events. The numbers link to entries in a lookup table, where the actual event parameters are defined. Note that the RF pulses have the same amplitude and frequency offset, but a different ID due to different phase offsets. B, Example gradient-echo readout sequence. C, Proposed combination of *Pulseq* events and the readout block using *Pulseq* as a sequence-building block (SBB). The RF events appear at blocks number 36, 38, and 40, spoiler gradients at block number 41, and delay events at blocks number 37 and 39. All *Pulseq*-CEST RF events are spatially nonselective. Blue crosses on the RF phase plots mark the RF phase at the moment of time when the peak RF magnitude is reached. For simplicity, GY and GZ gradient axes are not shown here. At every ADC event in the *pulseq*-file (block 42), the gradient-echo readout is played out

a WASABI (simultaneous mapping of water shift and B_1),⁴⁴ saturation recovery, and T_2 magnetization-preparation⁴⁵ sequence were applied to determine B_0 , B_1 , T_1 , and T_2 maps. The phantom was scanned at a room temperature of about 25°C.

The three different APTw protocols shown in Figure 1C-H (APTw_3T_001.seq, APTw_3T_002.seq, and APTw_3T_003.seq in the Supporting Information) were scanned for direct comparison in vivo in a healthy volunteer. In addition, a WASABI measurement was performed to correct the Z-spectra for B_0 field inhomogeneity. To generate magnetization-transfer asymmetry (MTR_{asym}) maps with higher SNR in vivo, all APTw protocols were acquired with repeated acquisitions (three repetitions) at the offsets of interest and a dummy scan at the beginning (APTw_3T_001_AVG.

seq, APTw_3T_002_AVG.seq, and APTw_3T_003_AVG.seq in the Supporting Information). This averaged protocol was additionally measured in a patient with a glioblastoma (World Health Organization grade IV, IDH mutation, and methylation of MGMT (O(6)-methylguanine-DNA methyltransferase) promoter) at the University Hospital Erlangen under approval of the local ethics committee.

Finally, we performed a whole-brain, in vivo CEST-MRF³⁶ measurement at three different sites. For this purpose, the *Pulseq* SBB was implemented into a 3D-EPI sequence.^{39,40} All relevant readout parameters can be found in Supporting Information Table S1. The protocol consisted of the following measurements: (1) an APTw MRF protocol with 31 scans, using spin-lock pulses with a B_1 varying between 0 μ T and 4 μ T at a constant offset of 3.5 ppm (Figure 1I,J); (2)

a semisolid magnetization-transfer contrast-weighted MRF protocol with 31 scans, using spin-lock pulses with B_1 varying between 0.2 μT and 4 μT at offsets varying between 6 ppm and 14 ppm; (3) a WASABI measurement for B_0 and B_1 field inhomogeneity maps; (4) a saturation-recovery measurement for T_1 maps; and (5) a T_2 preparation measurement for T_2 maps. All *pulseq-files* for this experiment can be found in the Supporting Information (MRF_Amide.seq, MRF_MT.seq, T1prep.seq, T2prep.seq, and WASABI.seq). The protocol was applied at three different sites for one healthy volunteer each (two Siemens 3T Prisma Scanners at MPI Tuebingen and Massachusetts General Hospital, and a Siemens 3T Trio scanner at University Hospital Erlangen). For the Trio system, a 32-channel coil was used for reception, whereas a 64-channel coil was used at both Prisma systems.

2.6 | Postprocessing

For the phantom experiment, MTR_{asym} maps were generated voxel-wise, with $MTR_{\text{asym}}(\Delta\omega) = (S(-\Delta\omega) - S(\Delta\omega))/S_0$, after a ΔB_0 correction using a linear interpolation between acquired offsets. Additionally, three regions of interest (ROIs) were drawn in the center slice in the tubes listed in Table 1. Z-spectra in these ROIs were simulated as described in section 2.2. All simulation parameters can be found in Supporting Information Tables S2-S4). Both simulated and measured Z-spectra were normalized by the measurement at -6 ppm.

For the in vivo APTw experiment, all measurements were motion-corrected using *elastix*.⁴⁶ The applied *elastix* parameter file can be found in the Supporting Information (Rigid_MMI.txt). The MTR_{asym} maps were generated in the same way as for the phantom but with applying an additional principal component analysis denoising approach⁴⁷ using the Malinowski criterion and a spatial 2D in-plane Gaussian filter ($\sigma = 0.6$) to smooth the images. A white-matter ROI was generated automatically by segmenting the image at -4 ppm using *SPM* (statistical parameter mapping).⁴⁸

For the CEST-MRF experiment, all images were again motion-corrected and registered to the T_1 measurement using *elastix*. The T_1 maps were generated by fitting a mono-exponential function to the data of the saturation-recovery measurement. The T_1 map was then used to generate a synthetic T_1 -weighted image, which was subsequently used to

generate gray-matter and white-matter segmentation masks using *SPM*. Dictionary generation and calculation of amide and semisolid magnetization transfer-contrast concentration and exchange-rate maps were performed according to Perlman et al.³⁸ A major advantage in using the *Pulseseq* SBB in this context is that for both measurement and dictionary generation, the same *pulseq-file* describing the saturation period definition is used. This reduces possible error sources from transferring the measurement parameters to the simulation or vice versa.

3 | RESULTS

3.1 | Simulation and phantom measurement

The first experiment demonstrates how the same *pulseq-file* can be used for simulation and phantom measurements. Figure 3 shows the MTR_{asym} map (Figure 3A) at 2 ppm, as well as the measured Z-spectra ($Z(\Delta\omega) = S(\Delta\omega)/S(-6$ ppm)) and simulated Z-spectra ($Z(\Delta\omega) = M_z(\Delta\omega)/M_z(-6$ ppm) (Figure 3B) and the MTR_{asym} (Figure 3D) curve for the three different ROIs. The residuals between these measured and simulated normalized intensities are displayed in Figure 3C. The maximum residuals were 0.009, 0.008, and 0.004 for ROIs 1, 2, and 3, respectively. Simulation of the *pulseq-file*, using 500 samples per pulse (60 000 pulse samples per Z-spectrum) took approximately 0.19 seconds for a single amide CEST pool Z-spectrum (ROIs 1 and 2) and 0.77 seconds for four different D-glucose CEST pools (ROI 3).

3.2 | In vivo APT-weighted measurements

The second experiment demonstrates the value of well-defined *pulseq-files* for comparison of different author-approved APTw CEST implementations. The APTw ($MTR_{\text{asym}}(3.5$ ppm)) results for the volunteer and the tumor patient can be found in Figure 4. The MTR_{asym} maps for the three different protocols are shown in Figure 4A-C, and despite different saturation, they show similar contrast in the healthy volunteer. The contrast in healthy brain is very low, which is expected, as the APTw-imaging parameters are designed to yield almost no contrast in healthy tissue.^{4,49-51} Corresponding Z-spectra, with $Z(\Delta\omega) = S(\Delta\omega)/S(-1560$ ppm), and MTR_{asym} spectra can be found in Figure 4H,I, respectively. Comparison with simulation can be found in Supporting Information Figure S3. While the intensity in the MTR_{asym} maps of the healthy volunteer is similar for all three protocols, a clear contrast can be seen in the tumor region (Figure 4D-F) of the glioblastoma patient. These protocols are all in use at clinical scanners, but were, to our knowledge,

TABLE 1 Region of interest and phantom information

ROI	Solute	Concentration (mmol/L)	pH	Voxels (N)
1	L-arginine	50	5.55	18
2	L-arginine	50	4.01	23
3	D-glucose	66	6.52	23

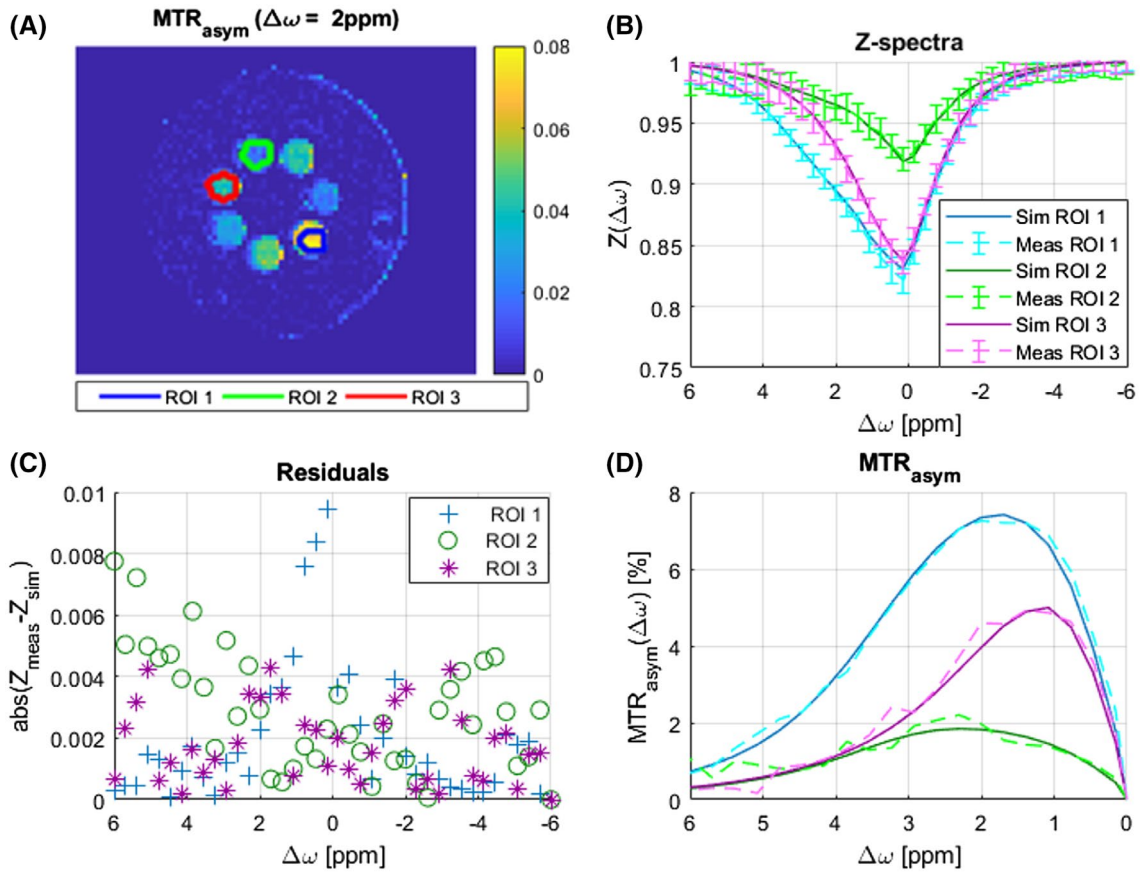


FIGURE 3 A, The $MTR_{asym}(\Delta\omega = 2\text{ppm})$ in slice 6. B, Simulated and measured Z-spectra for regions of interest (ROIs) 1, 2 and 3, respectively. Error bars in the measured Z-spectra show the SD of Z-spectra across voxels. C, Difference between the measured and simulated Z-spectra for each ROI. D, The MTR_{asym} curves of simulated and measured Z-spectra for the three ROIs

never compared side by side. Such a comparison can now be performed in different pathologies, to validate different protocols and their relation to previous work.

3.3 | In vivo CEST-MRF measurements

The final experiment demonstrates that with *Pulseseq*-CEST, sophisticated CEST sequences can be shared between sites, for both simulation (and training of reconstruction networks in this CEST-MRF example) as well as for measurement of work-in-progress developments at different systems. The spin-lock based CEST-MRF scheme with whole-brain EPI readout was applied in three healthy volunteers and at three different MR sites. The resulting maps for the semisolid proton fraction (f_{MT}), the semisolid proton to water proton exchange rate (k_{MT}), the amide proton fraction (f_{Amide}), and the amide proton to water proton exchange rate (k_{Amide}) are shown in Figure 5. The mean values for gray matter and white matter across the entire brain are shown in Table 2. A visual as well as quantitative comparison indicates reproducibility of effects across multiple sites.

4 | DISCUSSION

By adapting the source code of the *Pulseseq* interpreter sequence to the SBB concept of the Siemens IDEA framework, we were able to use it as a sequence building block in established MR sequences and subsequently run CEST experiments at different clinical 3T scanners. Hence, we combined the full flexibility of *Pulseseq* and the sophisticated readout methods from native sequences to generate an easy-to-use and flexible method for reproducible CEST measurements. For instance, it was directly possible to perform CEST-MRF experiments at three different sites on scanners with distinctly different software versions using identical CEST preparation periods defined in *Pulseseq*. Thus, a sophisticated and still work-in-progress protocol could be reliably shared between research sites using *Pulseseq*-CEST, without being limited by hard-coded user interface interactions. The quantitative results of the applied CEST-MRF method are consistent across sites, although the maps generated from the Trio system appear noisier. We attribute this primarily to the used 32-channel receive coil, leading to lower SNR compared with the 64-channel coil used on the Prisma system.

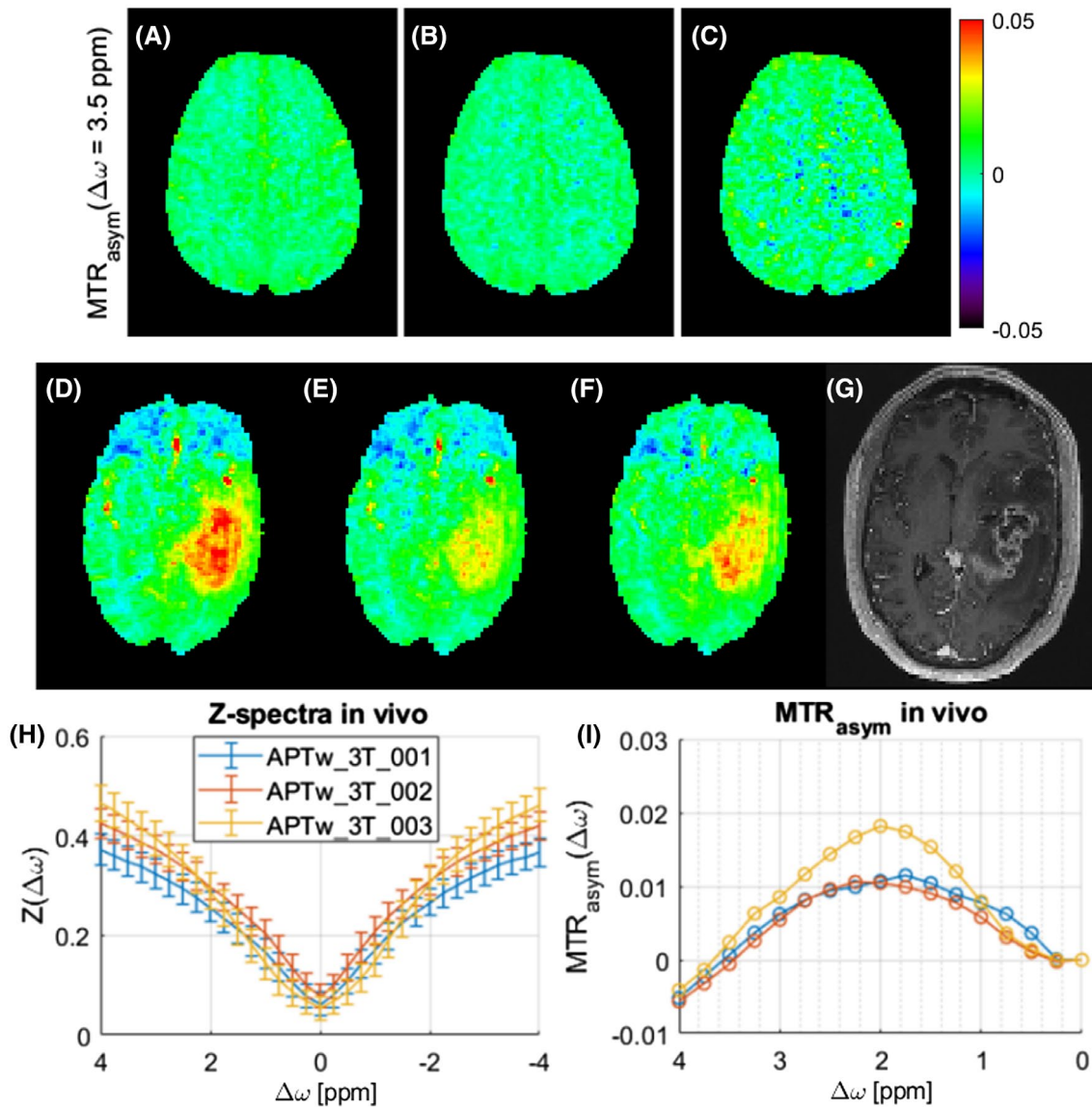


FIGURE 4 A-C, The MTR_{asym} maps at 3.5 ppm for the APTw_3T_001_AVG (A), APTw_3T_002_AVG (B), and APTw_3T_000_AVG3 (C) protocols in a healthy volunteer. D-F, The MTR_{asym} maps at 3.5 ppm for the APTw_3T_001_AVG (D), APTw_3T_002_AVG (E), and APTw_3T_003_AVG (F) protocols in a glioblastoma patient. G, Contrast-enhanced MPRAGE image for this patient. Z-spectra (H) and MTR_{asym} curve (I) for a white-matter ROI in the volunteer. Due to the rectangular saturation, residual artifacts in the ventricle regions can be observed in (C). Error bars in (H) show the SD in the white-matter ROI

In addition, the actual amplitude of the RF pulses is not only determined by the defined pulse shape in the *pulseq-file*, but also by the reference voltage of the system. It is therefore possible that different reference voltages lead to different results. Such MRF differences can now be evaluated and handled. While larger, further studies using this protocol should compare and discuss results with previous CEST-MRF studies,^{38,52} it is beyond the scope of the work presented here, as Bloch-McConnell-based quantification is extremely challenging in vivo. Results presented here represent a work-in-progress state of a sophisticated method undergoing an active development. The *Pulseq*-CEST standard allows for efficient and active exchange between the research sites, even in such

an early stage of development, accelerating generation and refinement of simulation databases and improving model training. The *Pulseq* SBB presented in this paper allows convenient though reliable multi-center collaboration to further investigate the method in detail in a larger cohort.

In addition, our software provides a Bloch-McConnell simulation tool for *pulseq-files* to simulate the exact same CEST preparation period that is played out by the interpreter on the scanner. The fast, native C++ implementation allows for pulsed CEST simulations, also with multiple isochromats, an application discussed in more detail in Supporting Information Figures S4 and S5. To ensure broad applicability, we provide implementations of the Bloch-McConnell simulation in both

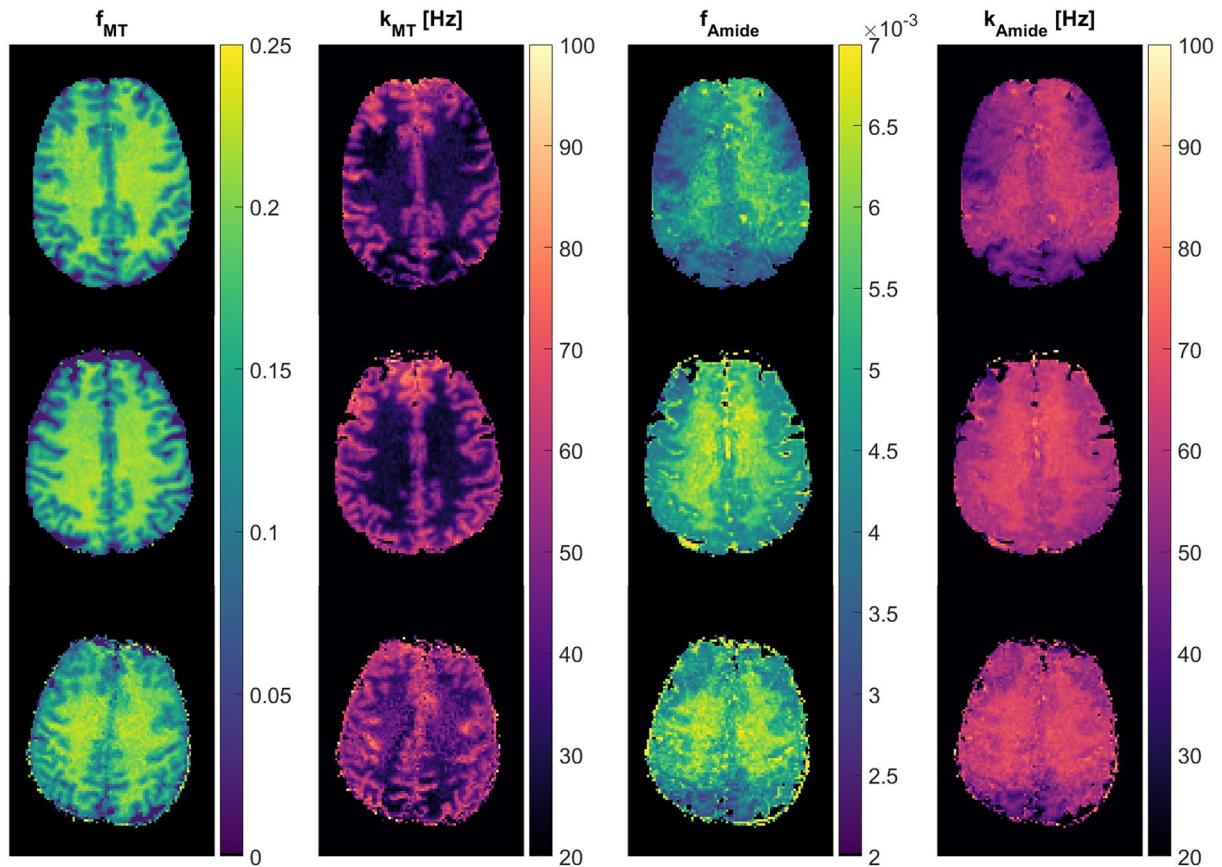


FIGURE 5 Semisolid magnetization-transfer (MT) contrast water fraction (first column) and exchange rate (second column), amide water fraction (third column), and exchange rate (fourth column) for measurements at a 3T Prisma in Tuebingen (first row), 3T Prisma in Boston (second row), and 3T Trio in Erlangen (third row)

MATLAB and *Python*, which are the most frequently used programming languages in research. Confirmation that both implementations yield identical results is provided in Supporting Information Table S5. We hope that with this work, we provide the first version of a valuable and needed tool for the CEST community, to exchange and test CEST preparation periods for the many different types of different CEST experiments. For instance, a researcher publishing data could share a *pulseq-file* containing all RF pulse, gradient, and delay parameters through the Supporting Information, and it could subsequently be used by other researchers. Additionally, all *pulseq-files* can be made available on the project's website (<https://pulseq-cest.github.io>).

Moreover, the *Pulseq* sequence building block can be used to test all of these CEST-preparation blocks with a minimum workload, even with different readout sequences, such as gradient echo, EPI or RARE, which have been optimized with regard to their imaging performance beforehand. Although the SBB is so far only available for Siemens scanners, it already demonstrated its multiplatform capabilities by executing the same CEST preparation periods on scanners built on different hardware components and running different software versions. Furthermore, it is generally possible

to transfer the approach to GE and Bruker (Bruker Biospin, Ettlingen, Germany) systems, where *Pulseq* implementations have been demonstrated.²³ For Bruker systems, we recently proposed an initial approach to combine CEST preparation periods from *pulseq-files* with native Bruker readouts automatically with *MATLAB*.⁵³ By doing so, we were able to measure the above-mentioned APTw protocols on a Bruker 14.1T scanner with *ParaVision* 6. This will be useful for comparison between preclinical and clinical trials, especially for pulsed CEST approaches.

A design of the interpreter software for other manufacturers (eg, Philips, United Imaging, or Canon) is needed for a universal application. However, even without actually applying *pulseq-files* on the scanner, the possibility to share, edit, display, and simulate saturation periods can be very insightful and beneficial for the design of CEST experiments. Because the *pulseq-file* guarantees a completely defined CEST preparation period inherently, which we believe is needed to improve the reproducibility of data in the CEST community, this will be a valuable tool especially when designing multisite clinical trials of technology, such as APTw MRI of brain tumors, which is being performed currently at many sites but often with different protocols.

TABLE 2 Mean values for quantitative CEST-MRF parameters and relative B_1 values of gray matter and white matter at the three different sites (Tuebingen, Boston, and Erlangen)

	f_{MT} GM	k_{yMT} GM (Hz)	f_{MT} WM	k_{yMT} WM (Hz)	$f_{A_{mid}} GM$	$k_{A_{mid}} GM$ (Hz)	$f_{A_{mid}} WM$	$k_{A_{mid}} WM$ (Hz)	Rel. B_1 (GM)	Rel. B_1 (WM)
TUE Prisma	0.140 ± 0.033	47.3 ± 10.8	0.201 ± 0.017	31.7 ± 6.7	0.0046 ± 0.0010	54.6 ± 10.0	0.0052 ± 0.0009	60.7 ± 7.5	1.03 ± 0.10	1.05 ± 0.09
BOS Prisma	0.142 ± 0.038	47.7 ± 11.3	0.203 ± 0.019	32.0 ± 6.6	0.0049 ± 0.0010	58.3 ± 8.8	0.0055 ± 0.0008	63.2 ± 6.0	0.99 ± 0.09	1.02 ± 0.08
ERL Trio	0.142 ± 0.034	48.6 ± 11.2	0.197 ± 0.022	35.2 ± 8.6	0.0047 ± 0.0011	55.8 ± 10.3	0.0054 ± 0.0009	61.9 ± 7.3	1.01 ± 0.10	1.03 ± 0.09

Abbreviations: BOS, Boston; ERL, Erlangen; GM, gray matter; TUE, Tuebingen; WM, white matter.

The *Pulseq* interpreter sequence has been adapted and used as a sequence building block in native readout sequences herein, but it is also possible to use readouts implemented directly in *Pulseq*. The current version of the *Pulseq* interpreter allows for the images to be reconstructed directly on the scanner, which makes the development of novel imaging sequences even more convenient. As the presented approach is compatible with the “parent” *Pulseq* project, the previously published *Pulseq*-CEST preparation periods could be trivially integrated with these novel readout modules, implemented directly in *Pulseq*. This will allow full reproducibility, as the complete sequence (including preparation and readout) can be published in the *pulseq-file* format in the same database.

While native *Pulseq* readout modules can be considered for measurements in the future, it is already possible to combine them with CEST preparation modules for more realistic simulations. In that case, the pseudo ADC event needs to be replaced by a full readout sequence. Various examples of possible readout sequences implemented with *Pulseq* can be found on the project’s website (<https://pulseq.github.io/>). By explicitly including the readout, it becomes possible to simulate the influence of the RF pulses during the readout with the provided simulation (Supporting Information Figure S6). It is also possible to use a different *Pulseq*-compatible simulation software, such as *JEMRIS*,⁵⁴ which supports Bloch-McConnell simulations, and provides a full MRI simulation framework. In addition, if the readout module is included in the *pulseq-file*, it is possible to estimate the expected specific absorption rate value using *sar4seq*⁵⁵ before the scanning session. In general, the open format of *Pulseq* allows for a broad development of useful applications.

With regard to the growing number of applications of neural networks to CEST data reconstruction,^{22,38,56-58} often trained on simulated data, a match of the sequences used in silico and in vivo becomes crucial. In fact, the CEST-MRF reconstruction network used to infer the quantitative maps of Figure 5 was trained using simulated data with exactly the same *pulseq-file* as used at the MR scanner. This is just one example showing that *Pulseq*-CEST could be valuable for many emerging machine and deep learning-based approaches.

Finally, the method is obviously not limited to CEST applications. In principle, any magnetization-preparation sequence can be realized, as exemplified in Supporting Information Figure S7, for the WASABI field-mapping approach and a T_1 saturation-recovery sequence.

5 | CONCLUSIONS

We present a *Pulseq*-based sequence framework for CEST preparation pulse sequences and an accompanying simulation tool, the use of which in combination with available MRI sequences allows for straightforward sharing, implementing,

testing, optimizing, and running of CEST MRI studies. Because the *pulseq-files* inherently include a complete CEST parameter definition, this fosters faster comparison and facilitates reproducibility—not only between different MR sites, but also between real and simulated environments.

Source code for the Siemens IDEA interpreter sequence is available on request. All code for creating and simulating *pulseq-files* is open source and can be obtained on the project's website (<https://pulseseq-cest.github.io/>).

ACKNOWLEDGMENT


The authors thank the developers of *Pulseq* and *pypulseq* (<https://github.com/imr-framework/pypulseq>). This paper reflects the authors' views only; the Research Executive Agency of the European Commission is not responsible for any use that may be made of the information it contains. Open access funding enabled and organized by ProjektDEAL.

DATA AVAILABILITY STATEMENT

All source code used for *pulseq-file* generation and simulation in this study is openly available at <https://pulseseq-cest.github.io/>, where links to the corresponding GitHub repositories can be found.

ORCID

Kai Herz  <https://orcid.org/0000-0002-7286-1454>

Sebastian Mueller  <https://orcid.org/0000-0003-2699-9214>

Or Perlman  <https://orcid.org/0000-0002-3566-569X>


Linda Knutsson  <https://orcid.org/0000-0002-4263-113X>

Phillip Zhe Sun  <https://orcid.org/0000-0003-4872-1192>

Kerstin Heinecke  <https://orcid.org/0000-0003-4024-4811>

Patrick Schuenke  <https://orcid.org/0000-0002-3179-4830>

Christian T. Farrar  <https://orcid.org/0000-0001-6623-8220>

Klaus Scheffler  <https://orcid.org/0000-0001-6316-8773>

Moritz Zaiss  <https://orcid.org/0000-0001-9780-3616>

Moritz Zaiss  <https://orcid.org/0000-0001-9780-3616>

REFERENCES

- Wolff SD, Balaban RS. NMR imaging of labile proton exchange. *J Magn Reson*. 1990;86:164-169.
- van Zijl PCM, Yadav NN. Chemical exchange saturation transfer (CEST): what is in a name and what isn't? *Magn Reson Med*. 2011;65:927-948.
- Zaiss M, Bachert P. Chemical exchange saturation transfer (CEST) and MR Z-spectroscopy *in vivo*: a review of theoretical approaches and methods. *Phys Med Biol*. 2013;58:R221-R269.
- Zhou J, Payen J-F, Wilson DA, Traystman RJ, van Zijl PCM. Using the amide proton signals of intracellular proteins and peptides to detect pH effects in MRI. *Nat Med*. 2003;9:1085-1090.
- Zhou J, Lal B, Wilson DA, Larter J, van Zijl PCM. Amide proton transfer (APT) contrast for imaging of brain tumors. *Magn Reson Med*. 2003;50:1120-1126.
- Cai K, Haris M, Singh A, et al. Magnetic resonance imaging of glutamate. *Nat Med*. 2012;18:302-306.
- Chan KWY, McMahon MT, Kato Y, et al. Natural D-glucose as a biodegradable MRI contrast agent for detecting cancer. *Magn Reson Med*. 2012;68:1764-1773.
- Rivlin M, Navon G. CEST MRI of 3-O-methyl-D-glucose on different breast cancer models. *Magn Reson Med*. 2018;79:1061-1069.
- Nasrallah FA, Pagès G, Kuchel PW, Golay X, Chuang K-H. Imaging brain deoxyglucose uptake and metabolism by glucocest MRI. *J Cereb Blood Flow Metab*. 2013;33:1270-1278.
- van Zijl PCM, Sehgal AA. Proton chemical exchange saturation transfer (CEST) MRS and MRI. *eMagRes*. 2016;5:1307-1332.
- McMahon MT, Gilad AA, Zhou J, Sun PZ, Bulte JWM, van Zijl PCM. Quantifying exchange rates in chemical exchange saturation transfer agents using the saturation time and saturation power dependencies of the magnetization transfer effect on the magnetic resonance imaging signal (QUEST and QUESP): pH calibration for poly. *Magn Reson Med*. 2006;55:836-847.
- Zaiss M, Angelovski G, Demetriou E, McMahon MT, Golay X, Scheffler K. QUESP and QUEST revisited—fast and accurate quantitative CEST experiments. *Magn Reson Med*. 2018;79:1708-1721.
- Sun PZ, Sorensen AG. Imaging pH using the chemical exchange saturation transfer (CEST) MRI: correction of concomitant RF irradiation effects to quantify CEST MRI for chemical exchange rate and pH. *Magn Reson Med*. 2008;60:390-397.
- Zaiss M, Schmitt B, Bachert P. Quantitative separation of CEST effect from magnetization transfer and spillover effects by Lorentzian-line-fit analysis of z-spectra. *J Magn Reson*. 2011;211:149-155.
- Grad J, Bryant RG. Nuclear magnetic cross-relaxation spectroscopy. *J Magn Reson*. 1990;90:1-8.
- Jones KM, Pollard AC, Pagel MD. Clinical applications of chemical exchange saturation transfer (CEST) MRI. *J Magn Reson Imaging*. 2018;47:11-27.
- Sun PZ, Wang E, Cheung JS, Zhang X, Benner T, Sorensen AG. Simulation and optimization of pulsed radio frequency irradiation scheme for chemical exchange saturation transfer (CEST) MRI-demonstration of pH-weighted pulsed-amide proton CEST MRI in an animal model of acute cerebral ischemia. *Magn Reson Med*. 2011;66:1042-1048.
- Harris RJ, Cloughesy TF, Liau LM, et al. pH-weighted molecular imaging of gliomas using amine chemical exchange saturation transfer MRI. *Neuro Oncol*. 2015;17:1514-1524.
- Cai K, Singh A, Roalf DR, et al. Mapping glutamate in subcortical brain structures using high-resolution GluCEST MRI. *NMR Biomed*. 2013;26:1278-1284.
- Evans VS, Torrealdea F, Rega M, et al. Optimization and repeatability of multipool chemical exchange saturation transfer MRI of the prostate at 3.0 T. *J Magn Reson Imaging*. 2019;50:1238-1250.
- Stikov N, Trzasko JD, Bernstein MA. Reproducibility and the future of MRI research. *Magn Reson Med*. 2019;82:1981-1983.
- Glang F, Deshmane A, Prokudin S, et al. DeepCEST 3T: robust MRI parameter determination and uncertainty quantification with neural networks—application to CEST imaging of the human brain at 3T. *Magn Reson Med*. 2020;84:450-466.
- Layton KJ, Kroboth S, Jia F, et al. Pulseq: a rapid and hardware-independent pulse sequence prototyping framework. *Magn Reson Med*. 2017;77:1544-1552.
- Sravan Ravi K, Geethanath S, Vaughan JT. PyPulseq: a python package for MRI pulse sequence design. *J Open Source Softw*. 2018;4:1725.

25. Loktyushin A, Herz K, Dang N, Glang F, Deshmane A, Weinmüller S, Doerfler A, Schölkopf B, Scheffler K, Zaiss M. MRzero - Automated discovery of MRI sequences using supervised learning. *Magn Reson Med.* 2021;86:709-724
26. Zaiss M, Ehses P, Scheffler K. Snapshot-CEST: Optimizing spiral-centric-reordered gradient echo acquisition for fast and robust 3D CEST MRI at 9.4 T. *NMR in Biomedicine.* 2018;31:e3879.
27. Deshmane A, Zaiss M, Lindig T, et al. 3D gradient echo snapshot CEST MRI with low power saturation for human studies at 3T. *Magn Reson Med.* 2019;81:2412-2423.
28. Stöcker T, Vahedipour K, Pflugfelder D, Shah NJ. High-performance computing MRI simulations. *Magn Reson Med.* 2010;64:186-193.
29. Herz K, Lindig T, Deshmane A, et al. T1 ρ -based dynamic glucose-enhanced (DGE ρ) MRI at 3 T: method development and early clinical experience in the human brain. *Magn Reson Med.* 2019;82:1832-1847.
30. APTw_3T_001_2uT_36SincGauss_DC90_2s_brainumor.seq. <https://pulseseq-cest.github.io/>. Accessed January 10, 2021
31. APTw_3T_002_2uT_20SincGauss_DC50_2s_brainumor.seq. <https://pulseseq-cest.github.io/>. Accessed January 10, 2021
32. APTw_3T_003_2uT_8block_DC95_834ms_brainumor.seq. <https://pulseseq-cest.github.io/>. Accessed January 10, 2021
33. Herz K, Knutsson L, Zhou J, et al. Towards a reproducible definition of APTw MRI saturation preparation using an open source sequence standard. In: Proceedings of the 8th International Workshop on Chemical Exchange Saturation Transfer Imaging, 2020.
34. Zu Z, Li K, Janve VA, Does MD, Gochberg DF. Optimizing pulsed-chemical exchange saturation transfer imaging sequences. *Magn Reson Med.* 2011;66:1100-1108.
35. Ramani A, Dalton C, Miller DH, Tofts PS, Barker GJ. Precise estimate of fundamental in-vivo MT parameters in human brain in clinically feasible times. *Magn Reson Imaging.* 2002;20:721-731.
36. Cohen O, Huang S, McMahon MT, Rosen MS, Farrar CT. Rapid and quantitative chemical exchange saturation transfer (CEST) imaging with magnetic resonance fingerprinting (MRF). *Magn Reson Med.* 2018;80:2449-2463.
37. Perlman O, Herz K, Zaiss M, Cohen O, Rosen MS, Farrar CT. CEST MR-fingerprinting: practical considerations and insights for acquisition schedule design and improved reconstruction. *Magn Reson Med.* 2020;83:462-478.
38. Perlman O, Ito H, Herz K, et al. AI boosted molecular MRI for apoptosis detection in oncolytic virotherapy. bioRxiv. 2020. <https://doi.org/10.1101/2020.03.05.977793>
39. Akbey S, Ehses P, Stirnberg R, Zaiss M, Stöcker T. Whole-brain snapshot CEST imaging at 7 T using 3D-EPI. *Magn Reson Med.* 2019;82:1741-1752.
40. Mueller S, Stirnberg R, Akbey S, et al. Whole brain snapshot CEST at 3T using 3D-EPI: aiming for speed, volume, and homogeneity. *Magn Reson Med.* 2020;84:2469-2483.
41. Nielsen JF, Noll DC. TOPPE: a framework for rapid prototyping of MR pulse sequences. *Magn Reson Med.* 2018;79:3128-3134.
42. Phosphate-buffered saline (PBS). *Cold Spring Harb Protoc.* 2006;2006.pdb.rec8247. <http://dx.doi.org/10.1101/pdb.rec8247>
43. Herz K, Gandhi C, Schuppert M, Deshmane A, Scheffler K, Zaiss M. CEST imaging at 9.4 T using adjusted adiabatic spin-lock pulses for on- and off-resonant T1 ρ -dominated Z-spectrum acquisition. *Magn Reson Med.* 2019;81:275-290.
44. Schuenke P, Windschuh J, Roeloffs V, Ladd ME, Bachert P, Zaiss M. Simultaneous mapping of water shift and B1 (WASABI)—application to field-inhomogeneity correction of CESTMRI data. *Magn Reson Med.* 2017;77:571-580.
45. Zhu J, Bornstedt A, Merkle N, et al. T2-prepared segmented 3D-gradient-echo for fast T2-weighted high-resolution three-dimensional imaging of the carotid artery wall at 3T: a feasibility study. *Biomed Eng Online.* 2016;15:165.
46. Klein S, Staring M, Murphy K, Viergever MA, Pluim J. elastix: a toolbox for intensity-based medical image registration. *IEEE Trans Med Imaging.* 2010;29:196-205.
47. Breitling J, Deshmane A, Goerke S, et al. Adaptive denoising for chemical exchange saturation transfer MR imaging. *NMR Biomed.* 2019;32:e4133.
48. Ashburner J, Friston KJ. Unified segmentation. *Neuroimage.* 2005;26:839-851.
49. Zhou J, Heo HY, Knutsson L, van Zijl PCM, Jiang S. APT-weighted MRI: techniques, current neuro applications, and challenging issues. *J Magn Reson Imaging.* 2019;50:347-364.
50. Togao O, Yoshiura T, Keupp J, et al. Amide proton transfer imaging of adult diffuse gliomas: correlation with histopathological grades. *Neuro Oncol.* 2014;16:441-448.
51. Jones CK, Schlosser MJ, Van Zijl PCM, Pomper MG, Golay X, Zhou J. Amide proton transfer imaging of human brain tumors at 3T. *Magn Reson Med.* 2006;56:585-592.
52. Heo HY, Han Z, Jiang S, Schär M, van Zijl PCM, Zhou J. Quantifying amide proton exchange rate and concentration in chemical exchange saturation transfer imaging of the human brain. *Neuroimage.* 2019;189:202-213.
53. Mueller S, Herz K, Scheffler K, Zaiss M. Open source Pulseseq interpreter for CEST MRI on Bruker systems. In: Proceedings of the 2021 ISMRM & SMRT Virtual Conference & Exhibition [Online], 2021. Abstract 1453.
54. Stöcker T, Vahedipour K, Pflugfelder D, Shah NJ. High-performance computing MRI simulations. *Magn Reson Med.* 2010;64:186-193.
55. sar4seq. <https://github.com/imr-framework/sar4seq>. Accessed March 01, 2021
56. Zaiss M, Deshmane A, Schuppert M, et al. DeepCEST: 9.4 T chemical exchange saturation transfer MRI contrast predicted from 3 T data—a proof of concept study. *Magn Reson Med.* 2019;81:3901-3914.
57. Chen L, Schär M, Chan KWY, Huang J, Wei Z, Lu H, Qin Q, Weiss RG, van Zijl PCM, Xu J. In vivo imaging of phosphocreatine with artificial neural networks. *Nat Commun.* 2020;11. <http://dx.doi.org/10.1038/s41467-020-14874-0>
58. Kim B, Schär M, Park H, Heo H-Y. A deep learning approach for magnetization transfer contrast MR fingerprinting and chemical exchange saturation transfer imaging. *Neuroimage.* 2020;221:117165. <http://dx.doi.org/10.1016/j.neuroimage.2020.117165>

SUPPORTING INFORMATION

Additional Supporting Information may be found online in the Supporting Information section.

FIGURE S1 Single magnetization vector trajectory during the CEST preparation period at 3.5 ppm with phase accumulation transfer during the saturation pulses (A,B) and without (C,D). The eight different colors indicate the trajectory during the eight different pulses. Due to the phase difference

between magnetization vector and RF pulse in (C) and (D), large oscillations can occur

FIGURE S2 Z-spectra of a single magnetization vector for the sequences from Supporting Figure 1A,B (blue) and C,D (red). Depending on the frequency offset $\Delta\omega$, the artifacts are more or less severe, as the accumulated phase and therefore the phase difference between magnetization vector and RF pulse is dependent on the frequency offset and the duration of the pulse

FIGURE S3 Measured (A,B) and simulated (C,D) Z-spectra (A,C) and magnetization-transfer asymmetry (MTR_{asym}) curves (B,D) for the three different amide proton transfer-weighted (APT_w) protocols from the main paper

FIGURE S4 Comparison of simulation results between a single (blue) and multiple isochromats (red) in different tissue environments. The red curve shows the mean Z-spectrum of all 200 isochromats, and the error bars indicate the SD between isochromats

FIGURE S5 Trajectory during a rectangular saturation pulse of a single isochromat with short (left) and long T_2 (right)

FIGURE S6 Evolution of the z-magnetization after different CEST-preparation periods at 3.5 ppm during a 2D gradient-echo readout

FIGURE S7 Comparison of simulation results from the *MATLAB* implementation (solid blue) and the *Python* implementation (dashed orange) for a WASABI (A) and a T_1 saturation-recovery (B) example

TABLE S1 Basic imaging parameters of readouts used for the presented Pulseq-hybrid sequence

TABLE S2 Simulation parameters for first region of interest (ROI)

TABLE S3 Simulation parameters for second ROI

TABLE S4 Simulation parameters for third ROI

TABLE S5 Currently available pulseq-files in the Pulseq-CEST open database with the RMS error of the spectra simulated in *MATLAB* and *Python*

How to cite this article: Herz K, Mueller S, Perlman O, et al. Pulseq-CEST: Towards multi-site multi-vendor compatibility and reproducibility of CEST experiments using an open-source sequence standard. *Magn Reson Med.* 2021;86:1845–1858. <https://doi.org/10.1002/mrm.28825>

B.4. Publication 4

MR-double-zero - proof-of-concept for a framework to autonomously discover MRI contrasts

Glang F., Mueller S., Herz K., Loktyushin A., Scheffler K., and Zaiss M.



MR-double-zero – Proof-of-concept for a framework to autonomously discover MRI contrasts



Felix Glang^{a,1}, Sebastian Mueller^{a,b,1}, Kai Herz^{a,b}, Alexander Loktyushin^a, Klaus Scheffler^{a,b}, Moritz Zaiss^{a,c,*}

^a High-field Magnetic Resonance Center, Max Planck Institute for Biological Cybernetics, Tuebingen, Germany

^b Department of Biomedical Magnetic Resonance, Eberhard Karls University Tuebingen, Tuebingen, Germany

^c Institute of Neuroradiology, University Hospital Erlangen, Friedrich-Alexander University Erlangen-Nürnberg (FAU), Erlangen, Germany

ARTICLE INFO

Article history:

Received 30 November 2021

Revised 2 April 2022

Accepted 10 May 2022

Available online 16 May 2022

Keywords:

Contrast mechanism

Sequence design

Supervised learning

Automatic MR

ABSTRACT

Purpose: A framework for supervised design of MR sequences for any given target contrast is proposed, based on fully automatic acquisition and reconstruction of MR data on a real MR scanner. The proposed method does not require any modeling of MR physics and thus allows even unknown contrast mechanisms to be addressed.

Methods: A derivative-free optimization algorithm is set up to repeatedly update and execute a parametrized sequence on the MR scanner to acquire data. In each iteration, the acquired data are mapped to a given target contrast by linear regression.

Results: It is shown that with the proposed framework it is possible to find an MR sequence that yields a predefined target contrast. In the present case, as a proof-of-principle, a sequence mapping absolute creatine concentration, which cannot be extracted from T1 or T2-weighted scans directly, is discovered. The sequence was designed in a comparatively short time and with no human interaction.

Conclusions: New MR contrasts for mapping a given target can be discovered by derivative-free optimization of parametrized sequences that are directly executed on a real MRI scanner. This is demonstrated by 're-discovery' of a chemical exchange weighted sequence. The proposed method is considered to be a paradigm shift towards autonomous, model-free and target-driven sequence design.

© 2022 The Authors. Published by Elsevier Inc. This is an open access article under the CC BY-NC-ND license (<http://creativecommons.org/licenses/by-nc-nd/4.0/>).

1. Introduction

The discovery of new MRI contrasts often happened hitherto by 'trial-and-error' using educated guesses directly at the MR system. We consider here whether such a trial-and-error approach can be formulated as a machine learning or optimization approach, that still makes use of the MRI system directly. Traditionally, the design of an MR sequence yielding a certain target contrast is performed manually, often by considering an analytical description of the contrast mechanism (subsequently referred to as a 'model') and adapting parameters such as the echo time (TE) or flip angle (FA) at the scanner. This approach is inherently limited by having to describe and understand the contrast mechanism before designing

a sequence for it. In addition, this workflow requires time-consuming human interaction with the scanner.

Within this traditional approach, often a single potentially specific target, e.g. quantitative relaxation, diffusion or magnetization transfer parameters is aimed for during sequence optimization. When considering one of these targets in isolation, there are often very precise models available to describe the underlying physics, such as the Bloch, Bloch-Torrey or Bloch-McConnell equations. However, in most cases, some assumptions do have to be made to apply these models, such as ignoring concomitant effects. A more general description requires the combination of different models, which may result in models that are too large and complicated to solve, and that anyway involve making many assumptions. Furthermore, the choice of model explicitly defines the targets which one may optimize, as the only possible targets are the ones described by the model itself. This ultimately means that the entire MR experiment, including the object of interest, the MR scanner hardware and the data reconstruction need to be included into a comprehensive, universal model that, to be practical, should be evaluated within as little time as possible.

* Corresponding author at: Institute of Neuroradiology, University Hospital Erlangen, Friedrich-Alexander University Erlangen-Nürnberg (FAU), Erlangen, Germany.

E-mail address: moritz.zaiss@uk-erlangen.de (M. Zaiss).

¹ Mueller and Glang contributed equally to this work.

We recently proposed a self-learning framework to discover MRI sequences based on a differentiable MRI physics simulation, which was dubbed *MRzero*, because zero sequence programming experience, but only knowledge of the Bloch equations was required [1]. Progressing further, the approach presented here requires neither a model nor human interaction with the scanner; thus, we call this approach *MR-double-zero*.

Instead of starting from a theoretical model and optimizing for a certain contrast, here, the model-free learning process is based solely on the desired target contrast, and performs automated, explorative real-scanner acquisitions. This allows optimization for any given target, even if the physical contrast mechanism in the MR signal might yet be unknown. With such a target-driven approach, a pure ‘optimization’ can be extended to become a ‘discovery’, as it may now be possible to test hypotheses as to whether (and how) a certain target might become visible by exploiting MRI as a tool. The proposed method can therefore be considered as a paradigm shift towards automatic target-driven sequence design. The ability to initially find an MR sequence solely guided by a desired target is the novelty of the presented work. In a first step, it is necessary to consider a mechanism which is known to result in an alteration of the MR signal and therefore may in principle be used to generate MR contrast. To mimic the discovery of a novel MRI effect, we assume that we know about water relaxation and have relaxation-weighted sequences. We then pretend that another specific contrast mechanism, namely the chemical exchange saturation transfer effect (CEST) of creatine guanidine protons, is unknown and needs to be discovered with *MR-double-zero* autonomously. In contrast to classical sequence design, no signal equation or analytical model are included. Instead, only the final target, which is not even an MR signal anymore, but rather absolute creatine concentration, is provided. The necessary human interaction is reduced to creating the samples and providing a suitable target, which in the present case is a manually generated map of the known creatine concentrations. To the best of our knowledge, this is the first realization of a MR sequence optimization framework with direct and automatized data acquisition and feedback on a real MR scanner in a target-contrast-driven manner; for pulse profile optimization a similar setup was proposed by Scheffler [2].

2. Methods

2.1. Samples

Samples were prepared with varying concentration of creatine. Seven samples with different creatine concentration values (0, 15, 25, 50, 75, 100, 125 mMol/L) were created from creatine monohydrate (Fisher Scientific GmbH, Schwerte, Germany). By adding T1 contrast agent (dotarem® 500 mMol/L, Guerbet, Germany) and agarose (Carl Roth, Karlsruhe, Germany) [3] it was made sure that in quantitative T1 and T2 maps obtained from conventional sequences these samples were indiscernible as shown in Fig. 3A-D.

To add another test case, the sample at 100 mMol/L concentration was designed in a way that it actually had a significantly longer T1 value than the other samples. This was achieved by not adding any contrast agent at all to this sample. Still, agar was added such that its T2 value approximately matches that of the other samples. Quantitative T1 and T2 values can be found in Fig. 3. Full Z-spectra acquired with low power preparation [4] are shown in Supplementary Fig. 1 for the seven different samples. For comparison of classical Z-spectra and Z-values explored with the proposed framework, an overlay plot of those can be found in Supplementary Fig. 5/6.

2.2. Scanner interface

To enable real measurements for the optimization process, the MR scanner was remotely controlled by the optimizer. Pulseseq [5] files were used to automatically execute the sequence of each iteration at the scanner. The actual optimization was run on a local computer (Intel Xeon W-2145 3.7 GHz CPU, 8 cores and 128 GB RAM) but not on the scanner host computer. This reduces the interaction with the scanner software to reading Pulseseq files from a network drive. The Pulseseq files additionally facilitate numerical simulations of the optimized sequence parameters [6]. Measurements were performed on a 3 T PRISMA scanner (Siemens Healthineers, Erlangen, Germany) using the vendor’s 20Ch head coil for receive and the body coil for transmit.

2.3. Optimization process

The actual optimization is based on an RF-prepared sequence with fixed 2D gradient and RF spoiled GRE readout (TE = 3.3 ms, TR = 6.6 ms, FA = 8°, BW = 300 Hz/pixel, RO × PE = 96 × 96, FoV = 128 × 128 mm², slice thickness: 10 mm). The CMA-ES optimization algorithm [7] implemented in nevergrad [8] was employed to explore the sequence parameter space including possible RF-preparation events such as number of pulses, amplitude, duration, phase/frequency, and delay times. This type of stochastic optimization algorithm is particularly designed for derivative-free, non-convex, noisy optimization problems as posed by sequence optimization at a real scanner. Every sequence generated by the optimizer is executed directly at the scanner and the intermediate images flow back to the algorithm influencing the next sequence iteration.

For the present work, each sequence iteration consisted of several (indexed by $r = 1, 2, \dots, R$) RF-prepared readouts with the pulse train parameters peak saturation amplitude $B_{1,r}$, frequency offset $\Delta\omega_r$, and number of pulses np_r , as optimized sequence parameters (seq) with $\text{seq} = (B_{1,1}, \Delta\omega_1, np_1 | B_{1,2}, \Delta\omega_2, np_2 | \dots | B_{1,R}, \Delta\omega_R, np_R)$.

Initial and boundary conditions for the optimization algorithm used with this parametrization are given in Table 1.

The duration of each Gaussian-shaped pulse was fixed to $t_p = 20$ ms and the duty cycle to $DC = t_p / (t_p + t_d) = 50\%$, i.e. a $t_d = 20$ ms gap between pulses. Still, with the number of pulses as free parameter, a large range of different total saturation times can be achieved. This choice of parametrization ensured that the explored sequences stay within the specific absorption rate limits throughout the optimization. The reconstructed images $\text{Img}_r(B_{1,r}, \Delta\omega_r, np_r)$ at each iteration were assembled in a design matrix.

$$\text{MRI}(\text{seq}) = \begin{pmatrix} \vdots & \vdots & \vdots & \vdots & \vdots \\ \text{Img}_1 & \text{Img}_2 & \dots & \text{Img}_R & 1 \\ \vdots & \vdots & \vdots & \vdots & \vdots \end{pmatrix}$$

of shape #voxels-by-($R + 1$). Only voxels within ROIs of the sample vials were considered, to avoid bias by the larger number of surrounding water-only voxels. Still, voxels within an ROI of the same size in the surrounding water were included as well.

Linear regression onto the voxel-wise targets T (shape: #voxels-by-1), was performed by pseudo-inversion of the relation $T = \text{MRI}(\text{seq}) \cdot \beta \Rightarrow \hat{\beta}(\text{seq}) = \text{MRI}(\text{seq})^+ \cdot T$ (with the Moore-Penrose pseudo-inverse $X^+ = (X^T X)^{-1} X^T$). This mapping process is referred to as ‘inner’ optimization in the following. The difference between the linear prediction and the true target determined how the CMA-ES optimization algorithm updated the sequence

Table 1

Initial and boundary conditions for the creatine mapping experiments, corresponding to $seq = (B_{1,1}, \Delta\omega_1, np_1 | B_{1,2}, \Delta\omega_2, np_2)$ in the case of $R = 2$ images per iteration and $seq = (B_{1,1}, \Delta\omega_1, np_1 | B_{1,2}, \Delta\omega_2, np_2 | B_{1,3}, \Delta\omega_3, np_3)$ in case of $R = 3$ images per iteration.

	lower bound	initial value	upper bound
$B_{1,1}$	0.1 μ T	1 μ T	3 μ T
$B_{1,2}$	0.1 μ T	1 μ T	3 μ T
$B_{1,3}$	0.1 μ T	1 μ T	3 μ T
$\Delta\omega_1$	-4.5 ppm	+1 ppm	+4.5 ppm
$\Delta\omega_2$	-4.5 ppm	-1 ppm	+4.5 ppm
$\Delta\omega_3$	-4.5 ppm	0 ppm	+4.5 ppm
np_1	1	80	200
np_2	1	80	200
np_3	1	80	200

parameters by solving the following non-linear minimization problem:

$$\widehat{seq} = \underset{seq}{\operatorname{argmin}} \left(\left\| T - \operatorname{MRI}(seq) \cdot \widehat{\beta}(seq) \right\|_2^2 \right)$$

$$= \underset{seq}{\operatorname{argmin}} \left(\left\| (1 - \operatorname{MRI}(seq) \cdot \operatorname{MRI}(seq)^+) \cdot T \right\|_2^2 \right)$$

With this problem formulation, the optimizer has to find sequence parameters that yield images that allow the best possible linear mapping to the target (Fig. 1). The optimization of sequence parameters is referred to as ‘outer’ optimization in the following.

To enable a more flexible mapping function from acquired images to targets, the design matrix $\operatorname{MRI}(seq)$ can be extended by non-linear transforms of the acquired images as additional features, i.e. columns. For example, by adding the squares and cubes of the acquired pixel intensities, respectively, a third-order polynomial representation is formed:

$$\operatorname{MRI}(seq) = \begin{pmatrix} \vdots & \vdots & \vdots & \vdots & \vdots & \vdots & \vdots & \vdots & \vdots & \vdots & \vdots & \vdots & \vdots & \vdots & \vdots \\ \operatorname{Img}_1 & \operatorname{Img}_2 & \cdots & \operatorname{Img}_R & \operatorname{Img}_1^2 & \operatorname{Img}_2^2 & \cdots & \operatorname{Img}_R^2 & \operatorname{Img}_1^3 & \operatorname{Img}_2^3 & \cdots & \operatorname{Img}_R^3 & 1 & \vdots & \vdots \\ \vdots & \vdots & \vdots & \vdots & \vdots & \vdots & \vdots & \vdots & \vdots & \vdots & \vdots & \vdots & \vdots & \vdots & \vdots \end{pmatrix}$$

Note that, while being non-linear in the image intensities, such a representation is still linear in the regression coefficients β , which allows obtaining them by simple pseudo-inversion.

As exemplary targets, known creatine concentrations were chosen with samples prepared as described in the above section.

3. Results

As a first feasibility check, simple experiments to investigate the behavior of the MSE loss function evaluated directly at the scanner were performed. To that end, a single target image with fixed saturation parameters $seq = (1 \mu\text{T}, +1.9 \text{ ppm}, 80)$ was acquired. Subsequently, three series of presaturated images were acquired, for which two of the parameters were fixed to their original values, respectively, while the remaining parameter was linearly incremented. This approach explores the loss landscape along each of these three axes ($B_1, \Delta\omega, np$) individually. For each of the acquired images, MSE to the target was calculated to see if this loss function actually exhibits a minimum at the respective target parameter value. Fig. 2 shows the resulting 1D loss curves. For the saturation amplitude B_1 , there is a clear global minimum at the target value and the loss curve appears smooth and largely convex. In case of the frequency offset $\Delta\omega$, there are several local minima and a more complex oscillatory behavior of the loss curve. Still, the global minimum in the explored range is located at the target value of $\Delta\omega = +1.9 \text{ ppm}$. For the number of pulses np , the global minimum is at a higher number ($np \sim 100$) than the actual target value ($np = 80$), and the loss curve exhibits small periodic oscillations.

From these experiments it can be concluded that the MSE loss landscapes acquired at the real scanner with respect to a given

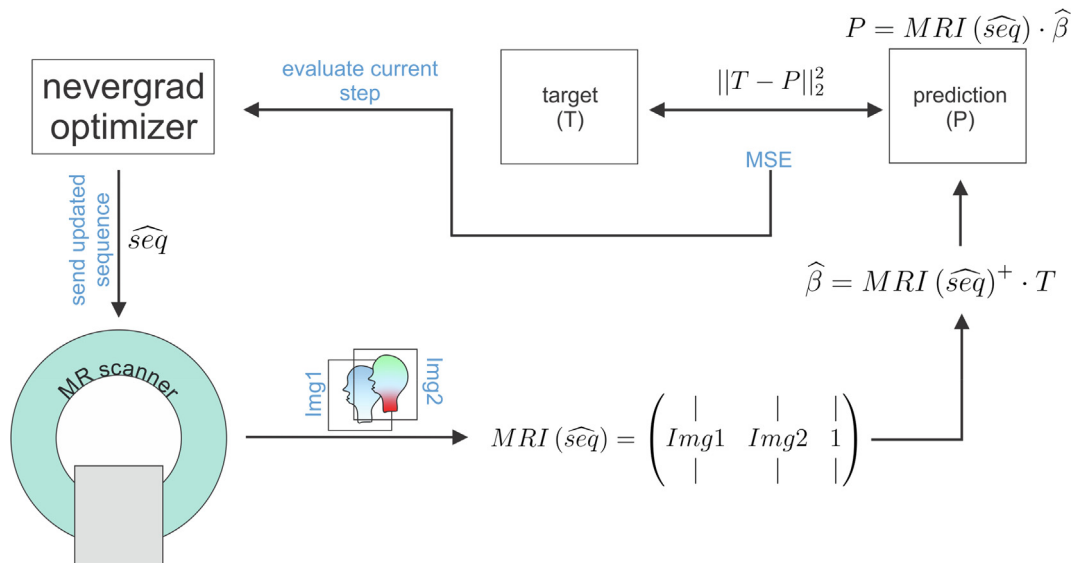


Fig. 1. Diagram of the proposed sequence development workflow termed MR-double-zero. The optimizer sends the parametrized sequence (seq) to a real MR scanner. The acquired data (in the depicted case for $R = 2$ images: Img_1 and Img_2) get flattened into the matrix $\operatorname{MRI}(seq)$ which is used to determine coefficients β from linear regression of $\operatorname{MRI}(seq)$ to the target. With these coefficients, the prediction (P) is determined and the deviation from the target (T) flows back to the optimizer. Our pipeline implements this using so called .seq-files of the Pulseseq standard that are played out at the scanner by a Pulseseq interpreter sequence.

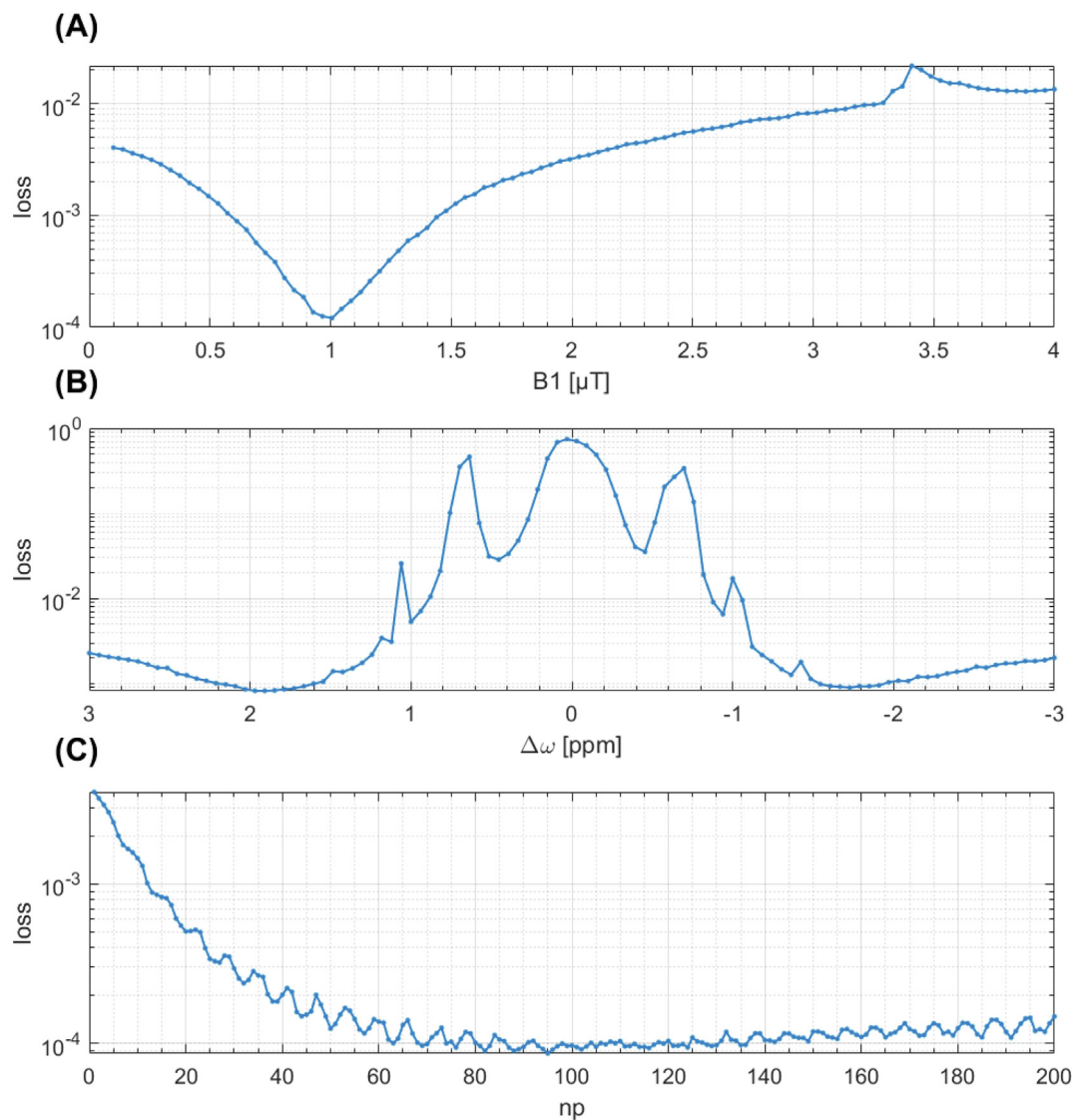


Fig. 2. Preliminary sanity checks of the MSE loss function evaluated directly at the scanner. As a target, a CEST-weighted image with predefined parameters $\text{seq} = (1 \mu\text{T}, +1.9 \text{ ppm}, 80)$ was acquired. Subsequently, a set of weighted images was acquired with two of these three parameters fixed to their target values, respectively, and the remaining parameter incremented with constant step size across a predefined range. For each of these images, MSE to the original target is shown (only evaluated within the sample vials, not in the surrounding water).

target contrast may exhibit multiple local minima, but still show somewhat smooth behavior and global minima that closely reflect the ground truth parameters. This means that these target parameter values can also be found by an optimization algorithm, however, a gradient descent might get stuck in the observed local minima.

To make sure that the MR-double-zero agent has to find a new sequence concept, and that the creatine concentration cannot be inferred only from T1- or T2-weighted contrasts, the samples were built such that T1 and T2 is not governed by creatine proton exchange. This invariance can already be seen in the T1 and T2 maps in Fig. 3, and was verified by the unsuccessful linear estimation using only T1 and T2 as input (Fig. 3F). Interestingly, it was not even possible to map the vial that had longer T1 values (see Fig. 3A/C) to its target concentration.

An exemplary optimization process is depicted in Fig. 4. Due to the stochastic behavior of the optimizer, the iterations were retrospectively sorted by loss instead of acquisition number. It can be seen that with decreasing loss at some point the optimized param-

eters converge towards a specific value. Still, for different runs, different sets of parameters are found (Supplementary Figure 7), which reflects that there are different strategies to generate the same contrast. In this specific case, the optimized sequence consists of two images at $+2.09 \text{ ppm}$ and -2.11 ppm with similar saturation strength (i.e., B_1 and np), which approximately get subtracted by the linear regression. This closely resembles the asymmetry metric, which is a classical model-based description of CEST effects [9]. If not stated differently, for all data shown in the following, the iteration that yielded smallest loss was chosen.

Fig. 4B shows the creatine concentration map generated based on the newly discovered sequence, which was formed by linear regression from the two RF-prepared images (Fig. 4D/E) with optimized sequence parameters. Remarkably, the method generalizes to the vial with 50 mMol/L , which was excluded from the ‘training’ procedure, i.e. not considered in the loss function during optimization (Fig. 4F).

Fig. 5 shows the optimization result for the concentration mapping experiment in which the design matrix was augmented by

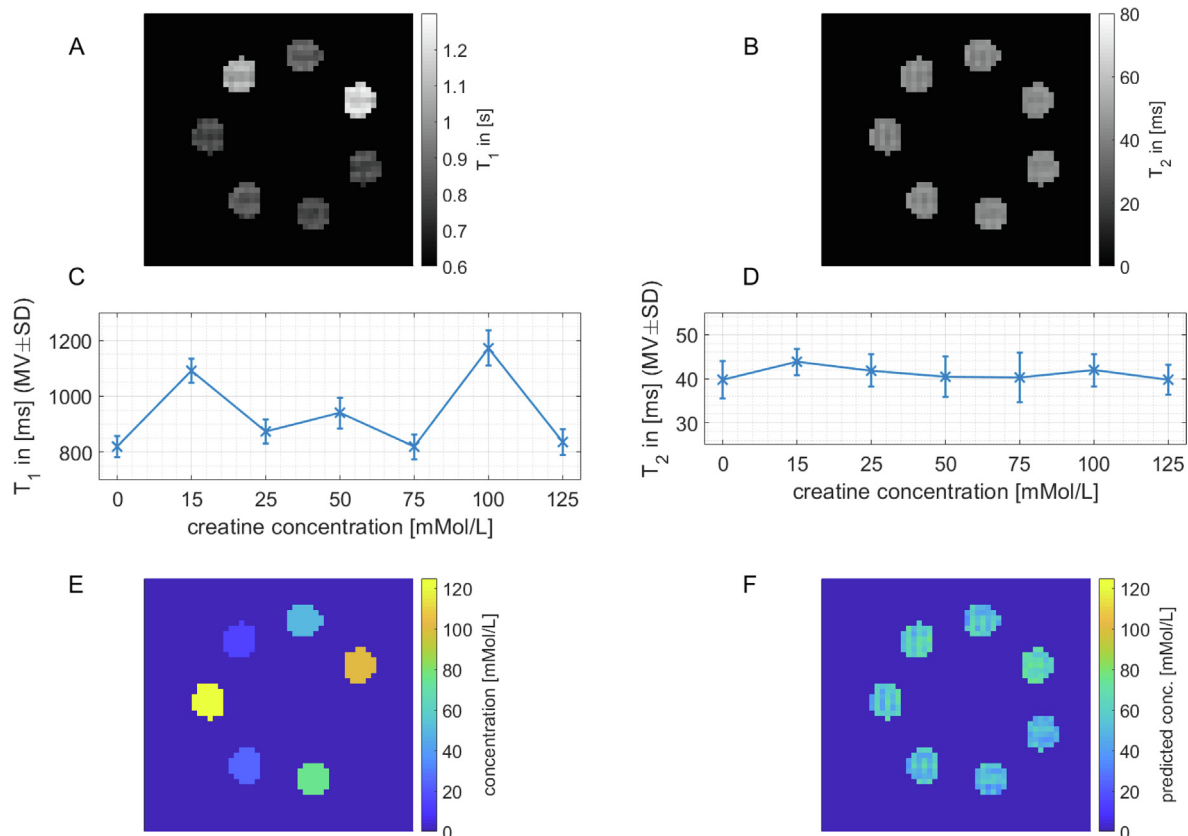


Fig. 3. Quantitative T1 and T2 maps of samples with different creatine concentration (c_{Cr}). Upper row: different concentrations cannot be distinguished directly from T1 (A) and/or T2 (B) maps. Center row: evaluation of (C) T1 and (D) T2 values in different ROIs of data shown in (A)/(B) with mean (MV) and standard deviation (SD) for each vial. Bottom row: True creatine concentrations (E) cannot be predicted by linear regression $f([T1, T2, 1]) = c_{Cr}$ from T1 and T2 (F).

square and cube terms. It can be seen that the more flexible polynomial mapping results in a more accurate mapping ($\sim 50\%$ smaller MSE loss, see [Supplementary Fig. 4](#)) to the target concentrations, which is especially pronounced for the ROIs with no creatine (both within the sample and in the surrounding water) and the two vials with highest concentrations (for which one even had different T1). The sequence parameters found by the optimization in this case were substantially different from the ones found in the experiment with simple non-augmented design matrix ([Fig. 5](#) vs. [Fig. 4](#)). On the one hand, the non-linear mapping function allows for different contrast extraction schemes compared to the case of a simple linear mapping, which may lead to different sequence schemes generating the input for this specific extraction. On the other hand, the stochastic optimization process itself will yield different seq-ectors for different runs in a loss-landscape with potentially multiple, equivalent local minima. This is demonstrated in [Supplementary Figure 7](#), from which it can be seen that the observed fluctuations in the final parameters could be attributed to the stochastic nature of the chosen optimizer rather than to the influence of non-linear extensions to the design matrix.

The accuracy of predicted concentrations can be further increased by extending the sequence to three differently prepared images ([Supplementary Figs. 2, 3, 4](#)), however, at the expense of increased acquisition and thus optimization duration. Also, it was found that extending the design matrix to a third image performs similarly well as extending the design matrix by higher order terms of only two images actually acquired at the scanner. However, extending the design matrix by higher order terms only requires very little additional computation time compared to the additional scan time required for a larger number of images. A

comparison of loss curves for all shown experiments (2 scans vs. 3 scans and linear vs. polynomial regression) is given in [Supplementary Fig. 4](#).

3.1. Samples including creatine plus glucose as confounding factor

The above experiments were conducted in samples that contained only creatine as a unique compound of interest. However, in a typical in vivo situation, multiple metabolites are present, which raises the question if this might skew the optimization process. To investigate this further, an additional set of samples was created similar to the first set that only contained creatine, but adding variable concentrations of glucose as a potential confounding factor. Indeed, when applying optimized GlucoCEST RF preparation [10], some of the creatine concentrations can no longer be distinguished by the conventional MTR_{asym} approach ([Supplementary Figure 8](#)).

As demonstrated in [Fig. 6](#), also for these samples, the proposed optimization pipeline comes up with a solution that accurately maps to creatine concentration with no apparent interference from the different glucose concentration levels. Runs with $R = 3$ images per iteration as well as non-linearly extended design matrix are shown in [Supplementary Figures 10–12](#). As can be seen in [Supplementary Figure 9](#), also for these samples, non-linear extension of the design matrix leads to lower loss values even with $R = 2$ images compared to only linear design matrix with $R = 3$ images. The concept found by MR-double-zero is qualitatively different from conventional MTR_{asym} , and the chosen different B_1 levels and offsets seem to enable the robustness against glucose contamination.

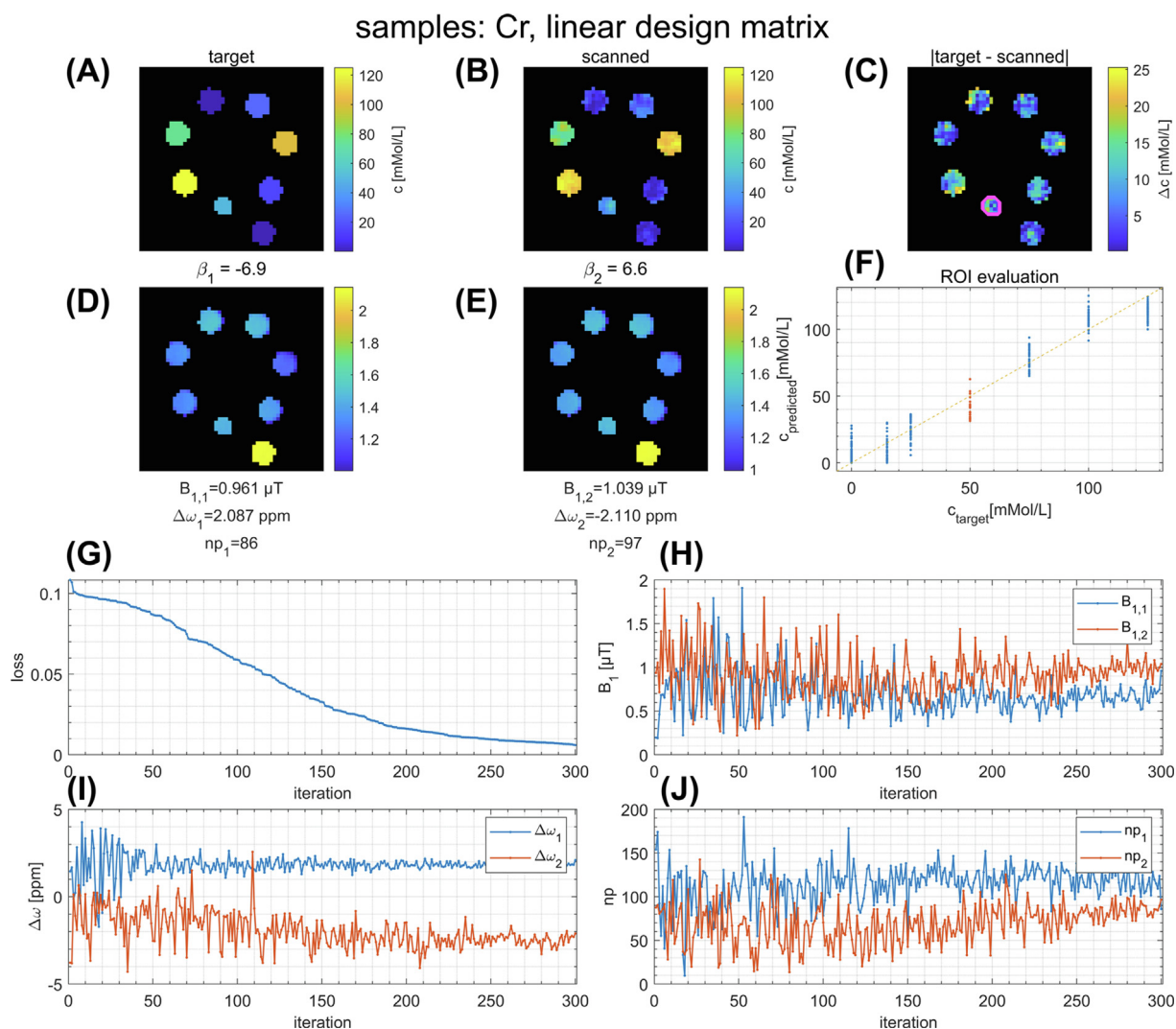


Fig. 4. Exemplary optimization process of a MR-double-zero sequence with 300 iterations (MRI scan time: 3 h). The final parameter set was here $\text{seq} = (0.96 \mu\text{T}, +2.09 \text{ ppm}, 86 | 1.04 \mu\text{T}, -2.11 \text{ ppm}, 97)$. The design matrix contained two images acquired with different RF-preparations. The first row shows quantitative concentration maps: (A) the target, (B) the experimentally derived and (C) the difference in concentrations. Second row shows the two images (D,E) with respective sequence parameters given below. In (F) the predicted and target data are scattered for ROIs within the different vials. The test vial (50 mMol/L) that was not included in the optimization process, is highlighted in (C) and (F). Subplots (G-J) were retrospectively sorted by loss instead of the actual time course of acquisition. (G) shows the loss for the parameter parameters shown in (H)-(J). Subscripts 1 and 2 refer to the image number for all parameters. An animated version of this figure can be found as [Supplementary Material](#).

4. Discussion

4.1. General comments on the proposed method

In the present work, we have shown a proof-of-principle for MRI sequence parameter optimization with the goal to discover a target contrast solely based on acquisitions at a real scanner system, without any knowledge of a theoretical signal model. In general, such an optimization problem is difficult, i.e. noisy, non-convex, high-dimensional and potentially ill-conditioned. However, the very first feasibility checks of the MSE loss function for a single parameter sweep showed that running an optimization based on real data could in principle converge towards global minima (Fig. 2). Additionally, stochastic gradient-free evolutionary algorithms like the employed CMA-ES are known to be particularly suited for this class of optimization problems [8].

MR-double-zero can be seen as advanced, sophisticated and efficient search in the MR parameter space to figure out if a certain

contrast can be generated by MRI. A grid search with $S = 100$ entries in each of the $N = 3$ dimensions would lead to $S^N = 10^5$ necessary measurements, and the problem of defining suitable grid boundaries. In contrast, the autonomous MR-double-zero learning required only 300 iterations, which took around 3 h at the MRI scanner. This is still long for an MRI scan, but fast for the discovery of a novel MRI contrast.

In general, the search space grows with the power of the number of dimensions, thus, reduction of dimensions N is an important step. The present optimization problem was reduced to the optimization of as little as $3 \cdot R$ parameters (with the number of scans per iteration $R = 2, 3$), which defined the preparation phase before R fixed 2D readouts. This is a significantly smaller subset of parameters as compared to the set of parameters required to define an entire MR sequence. Doing so, we still gave some reasonable boundaries by the definition of these few dimensions. Still, going from $N \cdot R = 6$ to $N \cdot R = 9$ degrees of freedom, a similar decrease of the MSE loss function was observed over the fixed number of

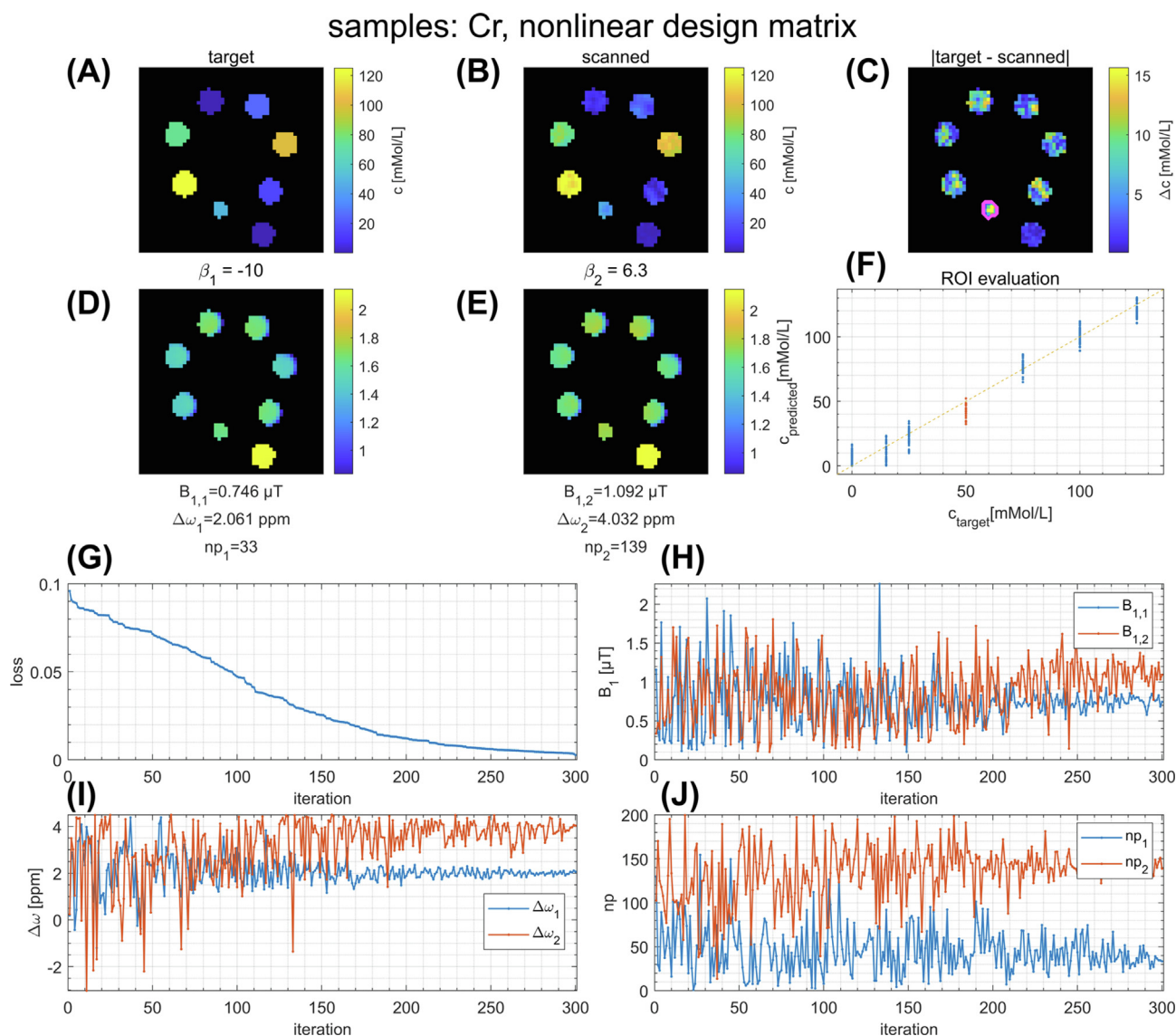


Fig. 5. Exemplary optimization process of a MR-double-zero sequence with 300 iterations (MRI scan time 3 h). The final parameter set was here $\text{seq} = (0.75 \mu\text{T}, +2.06 \text{ ppm}, 33 | 1.10 \mu\text{T}, +4.03 \text{ ppm}, 139)$. In contrast to Fig. 4, the design matrix contains in addition to the images ($\text{Img}_1, \text{Img}_2$) also the pixel-wise images squared ($\text{Img}_1^2, \text{Img}_2^2$) and cubed ($\text{Img}_1^3, \text{Img}_2^3$). The first row shows: (A) the target, (B) the experimentally derived and (C) the difference in concentrations. Second row shows the two images (C,D) with respective sequence parameters given below. In (F) the predicted and target data are scattered for ROIs within the different vials. The test vial (50 mMol/L) that was not included in the optimization process is highlighted in (C) and (F). Subplots (G-J) were retrospectively sorted by loss instead of the actual time course of acquisition. (G) shows the loss for the sequence parameters shown in (H)-(J). Subscripts 1 and 2 refer to the image number for all parameters. An animated version of this figure can be found as [Supplementary Material](#).

300 iterations for both cases ([Supplementary Fig. 4](#)). Thus, it is conceivable that also higher-dimensional problems could be addressed by a feasible number of iterations, such that they are solvable with reasonable effort and scan time. However, this must be investigated in detail, also with regard to the hyper-parameters of the optimizer.

4.2. Contrast mapping function (inner optimization)

Note that a linear representation was assumed to map from contrast-prepared images to the target map, such that the coefficients could be directly obtained by pseudo-inversion of acquired and target data and do not need to be *learned* by the outer optimizer. For more sophisticated tasks, however, also non-linear representations like neural networks might be used instead. As a first step towards such more sophisticated mapping functions, it could be observed that augmenting the design matrix by

non-linear transforms of the acquired signal intensities (here by power functions, thus forming a polynomial regression) increased the accuracy of the predicted concentrations ([Supplementary Fig. 4](#)). Potentially, the accuracy can be improved even more by adding more of such transforms e.g. $1/x$, as inverse metrics have proven useful for CEST data evaluation [11]. This, however, would mean to incorporate CEST-specific knowledge into the reconstruction, which was intentionally avoided here by using polynomials as a general choice known from Taylor series expansion. Additionally, including more non-linear features comes at the risk of overfitting, as more regression coefficients are added to the representation. However, this can be avoided by monitoring MSE in a hold-out test set, which was shown to be still low in the present case (Figs. 4-6). These insights hint also to the benefits of using neural network approaches for the inner optimization that come with further challenges, and were not yet tested herein.

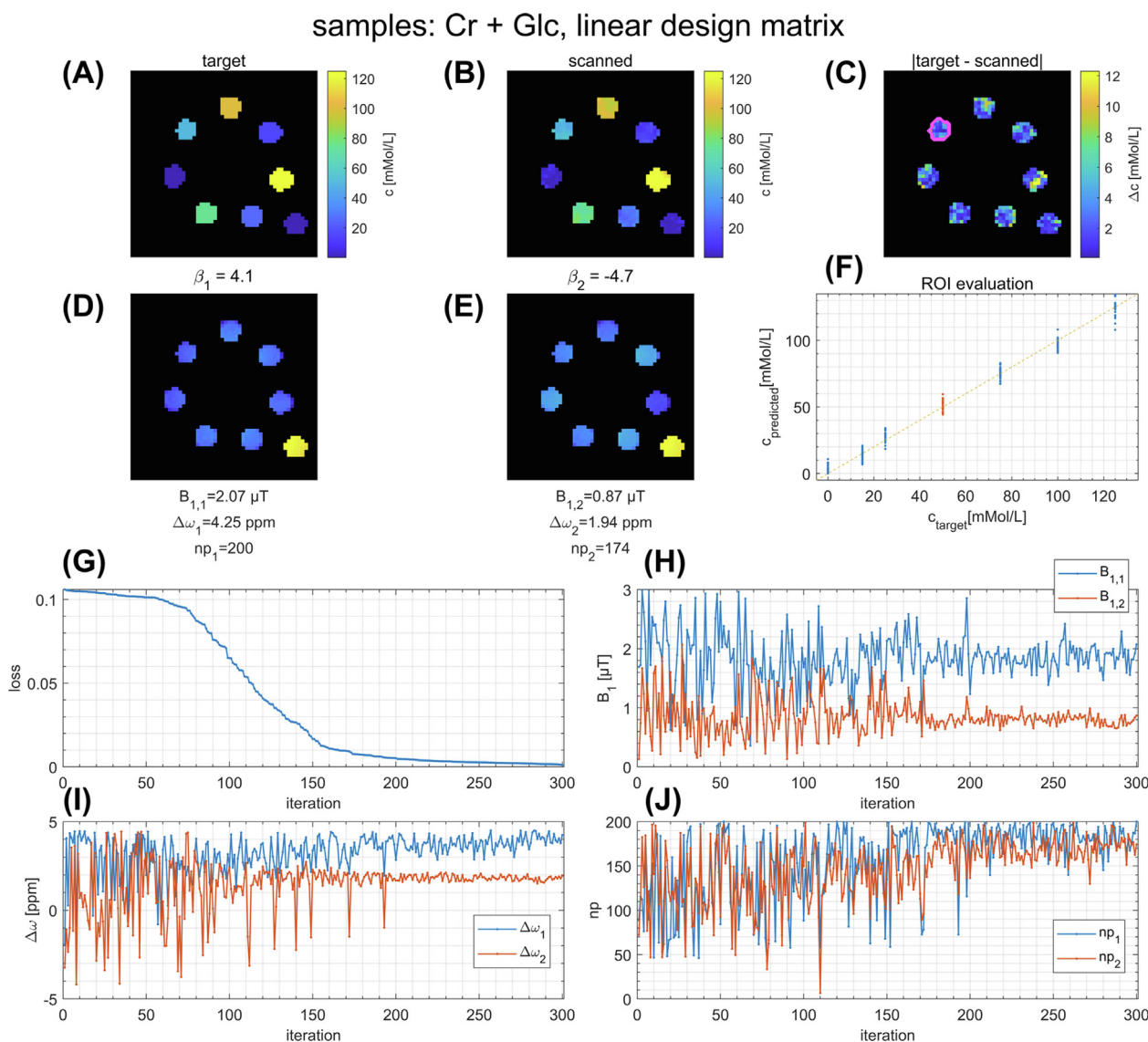


Fig. 6. Optimization process of a MR-double-zero sequence similar to the one shown in Fig. 4, but conducted on samples that contained different levels of glucose concentration as a confounding factor to the targeted creatine mapping. The final parameter set was here $\text{seq} = (2.07 \mu\text{T}, +4.25 \text{ ppm}, 200 | 0.87 \mu\text{T}, +1.94 \text{ ppm}, 174)$. The first row shows: (A) the target, (B) the experimentally derived and (C) the difference in concentrations. Second row shows the two images (D,E) with respective sequence parameters given below. In (F) the predicted and target data are scattered for ROIs within the different vials. The test vial (50 mMol/L) that was not included in the optimization process is highlighted in (C) and (F). Subplots (G-J) were retrospectively sorted by loss instead of the actual time course of acquisition. (G) shows the loss for the sequence parameters shown in (H)-(J). Subscripts 1 and 2 refer to the image number for all parameters.

4.3. Discovered strategies in the context of existing methods

A CEST pool can affect T1 and T2 relaxation times, thus adding agar and contrast agent is crucial to make this direct influence negligible and the samples indiscernible in conventional contrasts. By doing this, the actual contrast of interest can be considered unknown. Still, not on-resonant preparation pulses, which would lead to T1/T2-weighting, but off-resonant pulses are chosen by MR-double-zero to encode the creatine concentration. In contrast to conventional CEST imaging, the optimized sequence required as little as two RF preparation offsets. The optimized sequence in case of the simple design matrix without additional non-linear transforms (Fig. 4) yields the parameters $\text{seq} = (0.96 \mu\text{T}, +2.09 \text{ ppm}, 86 | 1.04 \mu\text{T}, -2.11 \text{ ppm}, 97)$ and closely resembles the traditional asymmetry metric at 2 ppm: $\text{seq} = (B_1, +2 \text{ ppm}, np | B_1, -2 \text{ ppm}, np)$.

Interestingly, for the run with non-linear terms shown in Fig. 5, the offsets are not chosen symmetrically around the water reso-

nance, where they are typically placed in a conventional CEST measurement, but instead at $\text{seq} = (0.75 \mu\text{T}, +2.06 \text{ ppm}, 33 | 1.10 \mu\text{T}, +4.03 \text{ ppm}, 139)$, leading to improved prediction performance. This is interesting, as asymmetric approaches are known to be most prone to B_0 inhomogeneity artefacts [12], while same side approaches are more robust against B_0 shifts [13]. Furthermore, also different B_1 levels and number of pulses are chosen, which together can provide more insight into T1- and T2-dependent direct saturation, that has to be eliminated to achieve absolute concentration mapping [11]. Thus, MR-double-zero is not only able to find 'unknown' contrast-generating concepts, but can also learn better strategies for existing approaches and small but smart tricks for more robust preparation/detection/sampling schemes.

The finding that different methods are discovered that yield similar accuracy can be seen as a limitation that no global minimum is found. However, it actually fits perfectly to the experience that a plethora of chemical-exchange-weighted methods were published that generate similar contrast correlation [14-18].

4.4. Related work in the context of MRI

The presented method has some similarity with MR fingerprinting [19], which has also been demonstrated for CEST parameter mapping [17,20]. For the latter, only saturation pulse amplitudes (B_1) were varied in a pseudo-random manner to obtain unique signal trajectories, from which e.g. CEST pool concentrations could be inferred by means of dictionary matching. This, however, also requires the use of Bloch equations or extended phase graph formalism as a numerical model. Thus, MR-double-zero can be seen as model-free joint optimization of a fingerprinting schedule and reconstruction based on real measurements.

The idea of optimizing both acquisition and reconstruction of MRI data at the same time was already presented by others in the context of ‘active acquisition’ [21–22]. Jin et al. [21] split the optimization process into separately optimizing acquisition and reconstruction of MRI data by training “two deep networks that are tied together”. The so-called SampleNet predicts which k-space points should be acquired next based on previous acquisitions, and the ReconNet learns the reconstruction given the provided sampling strategy. To some extent, the present approach behaves similarly, as the outer optimization (CMA-ES) optimizes the data acquisition while in the inner optimization the coefficients for linear regression are determined. Although such active acquisition policies could in principle be executed directly at a real MR scanner, in these works they are evaluated purely retrospectively on brain and knee MRI data sets. In contrast, the proposed approach optimizes a real data acquisition with live optimization. This might be beneficial as it enables full flexibility in terms of data acquisition and is not limited to any existing data that gets re-sampled.

4.5. Real-world optimization

Running optimization algorithms on real physical systems instead of theoretical models or simulations is known from other disciplines like robotics or autonomously driving cars. Particularly, reinforcement learning [23] can be applied to learning robot policies in realistic environments, e.g. [24–25]. In fact, the model and derivative-free optimization algorithm chosen in the present work reminds of the popular Q-learning algorithm [26], which learns to take appropriate actions (here: MR sequences) in a certain state (previously tested sequences) and environment (scanner and samples). Learning in realistic environments brings the benefit of including all possible real-world error sources like sensor noise, complex mechanical interactions and friction. However, a common disadvantage of all such real-world optimizations is that they are expensive, hard to reproduce exactly and usually more time-consuming (in terms of possible optimization iterations per time) than pure simulations. Because of that, it appears promising to combine simulation and real world based optimizations to hybrid approaches, which, for example, might intermittently update and improve a simulation-based optimization by real measurements.

However, also in the case of MRI, even simple systems may be challenging to model as the model has to be extended by experimental imperfections, e.g. eddy currents, gradient delays, and amplifier heating [27] in case of MR image encoding. Consequently, potential theoretical benefits of pure simulations – such as computational speed, reduced costs – are counterbalanced by the fact that simulating the real world accurately is arbitrarily complicated. This may not be an issue for some applications, but as the final goal of MRI in most cases is the real experimental implementation, it may actually be a severe bottleneck.

Moreover, instead of discovery of novel contrasts, one could exactly take such imperfections as a task for an optimization. For instance, the current off-resonant pulses could be optimized to

generate a fast/robust fat-saturation, using an expensively acquired fat-artifact-free image as a target. In addition, B_0 or B_1 inhomogeneity-robust sequences optimized at the scanner are conceivable to be found. In general, not only complete novel strategies can be aimed for, but also small optimizations of existing approaches can be performed elegantly with the MR-double-zero approach. The optimization parameters are not limited to $\text{seq} = (B_1, \Delta\omega, np)$ as shown in this proof-of-concept, but could also be parameters such as echo time, repetition time or flip angle $\text{seq} = (TE, TR, FA)$. For instance, variable flip angle approaches could potentially be efficiently optimized with the proposed framework.

4.6. Future ideas and outlook

For the described proof of principle, a well known contrast mechanism was investigated. The ultimate goal could be to provide any target of interest. The proposed framework would then be used to learn how to map from the object/sample to the target by exploiting MR methodology. Here it is important, that not only the feature of interest is well-prepared in the used samples, but also to rule out correlations by ‘randomizing’ other properties that are not targeted, as shown in the present case for relaxation effects, as well as for the glucose contamination. In general, all contaminations against which the developed sequence should be robust, must be part of the training data established by the samples. Well-prepared samples are therefore a crucial step for the presented approach. Until now, we only showed re-discovery of a CEST contrast mechanism, but novel discoveries are in principle possible for samples already.

In contrast, for learning directly in vivo, the rather lengthy scan time in the order of several hours might be challenging, but it is still conceivable if the dimensionality can be reasonably reduced. Furthermore, one could split the learning phase into several sessions or run the optimization on multiple scanners with similar targets in parallel.

As a speculative future application, MR-double-zero might be used complementary to the radiomics approach that is of increasing popularity in the medical context of MRI [28]. Radiomics relies on using all available multi-modal imaging information to find correlations with pathology, e.g. brain tumors. Instead of looking for correlations in already existing data from conventional imaging methodologies, real-world based optimization of MR sequences and reconstructions that map to a known outcome, prognosis etc., thus explicitly designing the data generation process to correlate with the desired target information, might be a promising step towards novel, targeted MRI methods applied for medical diagnosis.

However, also well-designed experiments in samples can lead to novel concepts that can subsequently be translated for in vivo application, similar to many previous MRI breakthroughs found by ‘trial-and-error’ or grid search approaches in samples and in vivo in the past. The found glucose-invariant creatine mapping in the present work, by using different B_1 and offsets, is such a concept that could now be investigated in more detail using human intuition, Bloch simulations, or more detailed grid-search measurements.

5. Conclusion

MR-double-zero is able to discover completely new MRI contrasts without requiring an explicit description of the underlying mechanism in form of a theoretical model. This was exemplarily demonstrated for a specific chemical-exchange-weighting, but it is conceivable that MR-double-zero could also discover yet

unknown MRI contrast correlations given suitable samples and targets are provided.

Declaration of Competing Interest

The authors declare that they have no known competing financial interests or personal relationships that could have appeared to influence the work reported in this paper.

Acknowledgements

The financial support of Max Planck Society, German Research Foundation (Reinhart Koselleck project DFG SCHE658/12 and ZA 814/7-1) and ERC Advanced Grant, No 834940 is gratefully acknowledged. We would like to thank Georg Martius for helpful discussions about gradient-free optimization.

Appendix A. Supplementary data

Supplementary data to this article can be found online at <https://doi.org/10.1016/j.jmr.2022.107237>.

References

- [1] A. Loktyushin, K. Herz, N. Dang, et al., MRzero - Automated discovery of MRI sequences using supervised learning, *Magnetic Resonance in Medicine* 86 (2021) 709–724, <https://doi.org/10.1002/mrm.28727>.
- [2] Scheffler, K. (1995), Design of B1-Insensitive and B1-Selective RF Pulses by Means of Stochastic Optimization. *Journal of Magnetic Resonance Series B*, 109 (2), 175–183. <https://doi.org/10.1006/jmrb.1995.0007>.
- [3] S. Mueller, K. Scheffler, M. Zaiss, On the interference from agar in chemical exchange saturation transfer MRI parameter optimization in model solutions, *NMR in Biomedicine* 34 (2021) e4403.
- [4] A. Deshmane, M. Zaiss, T. Lindig, et al., 3D gradient echo snapshot CEST MRI with low power saturation for human studies at 3T, *Magnetic Resonance in Medicine* 81 (2019) 2412–2423, <https://doi.org/10.1002/mrm.27569>.
- [5] K.J. Layton, S. Kroboth, F. Jia, et al., Pulseq: A rapid and hardware-independent pulse sequence prototyping framework, *Magnetic Resonance in Medicine* 77 (2017) 1544–1552, <https://doi.org/10.1002/mrm.26235>.
- [6] Herz K, Mueller S, Perlman O, et al. Pulseq-CEST: Towards multi-site multi-vendor compatibility and reproducibility of CEST experiments using an open-source sequence standard. *Magnetic Resonance in Medicine* n/a doi: 10.1002/mrm.28825.
- [7] N. Hansen, A. Ostermeier, Adapting arbitrary normal mutation distributions in evolution strategies: the covariance matrix adaptation, in: In: Proceedings of IEEE International Conference on Evolutionary Computation, 1996, pp. 312–317, <https://doi.org/10.1109/ICEC.1996.542381>.
- [8] Rabin J, Teytaud O. Nevergrad - A gradient-free optimization platform. <https://github.com/facebookresearch/nevergrad>. 2018.
- [9] V. Guivel-Scharen, T. Sinnwell, S.D. Wolff, R.S. Balaban, Detection of Proton Chemical Exchange between Metabolites and Water in Biological Tissues, *Journal of Magnetic Resonance* 133 (1998) 36–45, <https://doi.org/10.1006/jmre.1998.1440>.
- [10] K. Herz, T. Lindig, A. Deshmane, et al., T1ρ-based dynamic glucose-enhanced (DGEp) MRI at 3 T: method development and early clinical experience in the human brain, *Magnetic Resonance in Medicine* 82 (2019) 1832–1847, <https://doi.org/10.1002/mrm.27857>.
- [11] M. Zaiss, J. Xu, S. Goerke, et al., Inverse Z-spectrum analysis for spillover-, MT-, and T1-corrected steady-state pulsed CEST-MRI – application to pH-weighted MRI of acute stroke, *NMR in Biomedicine* 27 (2014) 240–252, <https://doi.org/10.1002/nbm.3054>.
- [12] A. Singh, M. Haris, K. Cai, et al., Chemical exchange saturation transfer magnetic resonance imaging of human knee cartilage at 3 T and 7 T, *Magnetic Resonance in Medicine* 68 (2012) 588–594, <https://doi.org/10.1002/mrm.23250>.
- [13] P.Z. Sun, C.T. Farrar, A.G. Sorensen, Correction for artifacts induced by B0 and B1 field inhomogeneities in pH-sensitive chemical exchange saturation transfer (CEST) imaging, *Magnetic Resonance in Medicine* 58 (2007) 1207–1215, <https://doi.org/10.1002/mrm.21398>.
- [14] J. Yuan, J. Zhou, A.T. Ahuja, Y.-X.-J. Wang, MR chemical exchange imaging with spin-lock technique (CESL): a theoretical analysis of the Z-spectrum using a two-pool $R_{1\rho}$ relaxation model beyond the fast-exchange limit, *Phys. Med. Biol.* 57 (2012) 8185–8200, <https://doi.org/10.1088/0031-9155/57/24/8185>.
- [15] Z. Zu, V.A. Janve, J. Xu, M.D. Does, J.C. Gore, D.F. Gochberg, A new method for detecting exchanging amide protons using chemical exchange rotation transfer, *Magnetic Resonance in Medicine* 69 (2013) 637–647, <https://doi.org/10.1002/mrm.24284>.
- [16] N.N. Yadav, C.K. Jones, J. Xu, et al., Detection of rapidly exchanging compounds using on-resonance frequency-labeled exchange (FLEX) transfer, *Magnetic Resonance in Medicine* 68 (2012) 1048–1055, <https://doi.org/10.1002/mrm.24420>.
- [17] O. Perlman, K. Herz, M. Zaiss, O. Cohen, M.S. Rosen, C.T. Farrar, CEST MR-Fingerprinting: Practical considerations and insights for acquisition schedule design and improved reconstruction, *Magnetic Resonance in Medicine* 83 (2020) 462–478, <https://doi.org/10.1002/mrm.27937>.
- [18] F.T. Gutjahr, E. Munz, P.M. Jakob, Positive chemical exchange contrast in MRI using Refocused Acquisition of Chemical Exchange Transferred Excitations (RACETE), *Zeitschrift für Medizinische Physik* 29 (2019) 184–191, <https://doi.org/10.1016/j.zemedi.2018.05.005>.
- [19] D. Ma, V. Gulani, N. Seiberlich, et al., Magnetic resonance fingerprinting, *Nature* 495 (2013) 187–192, <https://doi.org/10.1038/nature11971>.
- [20] O. Perlman, H. Ito, K. Herz, et al., Quantitative imaging of apoptosis following oncolytic virotherapy by magnetic resonance fingerprinting aided by deep learning, *Nat Biomed Eng* (2021) 1–10, <https://doi.org/10.1038/s41551-021-00809-7>.
- [21] Jin KH, Unser M, Yi KM. Self-Supervised Deep Active Accelerated MRI. arXiv:1901.04547 [cs] 2019.
- [22] Z. Zhang, A. Romero, M.J. Muckley, P. Vincent, L. Yang, M. Drozdal, Reducing Uncertainty in Undersampled MRI Reconstruction With Active Acquisition, in: 2019 IEEE/CVF Conference on Computer Vision and Pattern Recognition (CVPR), 2019, pp. 2049–2053, <https://doi.org/10.1109/CVPR.2019.00215>.
- [23] Kober J, Bagnell JA, Peters J. Reinforcement Learning in Robotics: A Survey. :38.
- [24] S. Mahadevan, J. Connell, Automatic programming of behavior-based robots using reinforcement learning, *Artificial Intelligence* 55 (1992) 311–365, [https://doi.org/10.1016/0004-3702\(92\)90058-6](https://doi.org/10.1016/0004-3702(92)90058-6).
- [25] Bagnell JA, Schneider JG. Autonomous helicopter control using reinforcement learning policy search methods. In: Proceedings 2001 ICRA. IEEE International Conference on Robotics and Automation (Cat. No.01CH37164). Vol. 2. ; 2001. pp. 1615–1620 vol.2. doi: 10.1109/ROBOT.2001.932842.
- [26] C.J.C.H. Watkins, P. Dayan, Q-learning, *Mach Learn* 8 (1992) 279–292, <https://doi.org/10.1007/BF00992698>.
- [27] Voelker MN, Kraff O, Goerke S, et al. The traveling heads 2.0: Multicenter reproducibility of quantitative imaging methods at 7 Tesla. *NeuroImage* 2021;232:117910 doi: 10.1016/j.neuroimage.2021.117910.
- [28] R.J. Gillies, P.E. Kinahan, H. Hricak, Radiomics: Images Are More than Pictures, They Are Data. *Radiology* 278 (2016) 563–577, <https://doi.org/10.1148/radiol.2015151169>.

References

- [1] Haacke EM, Brown RW, Thompson MR, Venkatesan R. *Magnetic resonance imaging: physical principles and sequence design*. Wiley-Liss, New York [u.a.], 1999. ISBN 978-0-471-35128-3
- [2] Gutowsky HS, McCall DW, Slichter CP. Nuclear Magnetic Resonance Multiplets in Liquids. *The Journal of Chemical Physics*, 1953;21(2):279–292. doi:10.1063/1.1698874
- [3] Gutowsky HS, Saika A. Dissociation, Chemical Exchange, and the Proton Magnetic Resonance in Some Aqueous Electrolytes. *The Journal of Chemical Physics*, 1953; 21(10):1688–1694. doi:10.1063/1.1698644
- [4] Zaiss M. Chemical exchange saturation transfer (CEST) and MR Z-spectroscopy in vivo: a review of theoretical approaches and methods. *Physics in Medicine and Biology*, 2013;Volume 58(22):221–269. doi:10.1088/0031-9155/58/22/R221
- [5] van Zijl PC, Yadav NN. Chemical Exchange Saturation Transfer (CEST): what is in a name and what isn't? *Magnetic Resonance in Medicine*, 2011;65(4):927–948. doi:10.1002/mrm.22761
- [6] Bloch F. Nuclear Induction. *Physical Review*, 1946;70(7-8):460–474. doi:10.1103/PhysRev.70.460
- [7] Hahn EL. Spin Echoes. *Physical Review*, 1950;80(4):580–594. doi:10.1103/PhysRev.80.580
- [8] Worthoff WA, Yun SD, Shah NJ. *CHAPTER 1 Introduction to Magnetic Resonance Imaging*. The Royal Society of Chemistry, 2019. ISBN 978-1-78801-074-0. doi: 10.1039/9781788013062-00001
- [9] Likes RS. Moving gradient zeugmatography. *US patent*, 1981;(US4307343A)
- [10] Ahn CB, Kim JH, Cho ZH. High-Speed Spiral-Scan Echo Planar NMR Imaging-I. *IEEE Transactions on Medical Imaging*, 1986;5(1):2–7. doi:10.1109/TMI.1986.4307732
- [11] Glover GH, Pauly JM. Projection Reconstruction Techniques for Reduction of Motion Effects in MRI. *Magnetic Resonance in Medicine*, 1992;28(2):275–289. doi: 10.1002/mrm.1910280209

References

- [12] Pipe JG. Motion correction with PROPELLER MRI: Application to head motion and free-breathing cardiac imaging. *Magnetic Resonance in Medicine*, 1999; 42(5):963–969. doi:10/dcvwc3
- [13] Mansfield P. Multi-planar image formation using NMR spin echoes. *Journal of Physics C: Solid State Physics*, 1977;10(3):L55–L58. doi:10.1088/0022-3719/10/3/004
- [14] Oshio K, Feinberg DA. GRASE (Gradient-and Spin-Echo) imaging: A novel fast MRI technique. *Magnetic Resonance in Medicine*, 1991;20(2):344–349. doi:10.1002/mrm.1910200219
- [15] Bruder H, Fischer H, Reinfelder HE, Schmitt F. Image reconstruction for echo planar imaging with nonequidistant k-space sampling. *Magnetic Resonance in Medicine*, 1992;23(2):311–323. doi:10.1002/mrm.1910230211
- [16] Reeder SB, Atalar E, Bolster Jr BD, McVeigh ER. Quantification and reduction of ghosting artifacts in interleaved echo-planar imaging. *Magnetic Resonance in Medicine*, 1997;38(3):429–439. doi:10.1002/mrm.1910380312
- [17] Roemer PB, Edelstein WA, Hayes CE, Souza SP, Mueller OM. The NMR phased array. *Magnetic Resonance in Medicine*, 1990;16(2):192–225
- [18] Pruessmann KP, Weiger M, Scheidegger MB, Boesiger P. SENSE: Sensitivity encoding for fast MRI. *Magnetic Resonance in Medicine*, 1999;42(5):952–962. doi:10/fvbh4d
- [19] Griswold MA, Jakob PM, Heidemann RM, et al. Generalized autocalibrating partially parallel acquisitions (GRAPPA). *Magnetic Resonance in Medicine*, 2002; 47(6):1202–1210. doi:10.1002/mrm.10171
- [20] Breuer FA, Blaimer M, Heidemann RM, Mueller MF, Griswold MA, Jakob PM. Controlled aliasing in parallel imaging results in higher acceleration (CAIPIRINHA) for multi-slice imaging. *Magnetic Resonance in Medicine*, 2005;53(3):684–691. doi:10.1002/mrm.20401
- [21] Breuer FA, Blaimer M, Mueller MF, et al. Controlled aliasing in volumetric parallel imaging (2D CAIPIRINHA). *Magnetic Resonance in Medicine*, 2006;55(3):549–556. doi:10.1002/mrm.20787
- [22] Shepp LA, Logan BF. The Fourier reconstruction of a head section. *IEEE Transactions on Nuclear Science*, 1974;21(3):21–43. doi:10.1109/TNS.1974.6499235
- [23] Forsén S, Hoffman RA. Study of Moderately Rapid Chemical Exchange Reactions by Means of Nuclear Magnetic Double Resonance. *The Journal of Chemical Physics*, 1963;39(11):2892–2901. doi:10.1063/1.1734121
- [24] Wolff SD, Balaban RS. NMR imaging of labile proton exchange. *Journal of Mag-*

netic Resonance (1969), 1990;86(1):164–169. doi:10.1016/0022-2364(90)90220-4

- [25] Guivel-Scharen V, Sinnwell T, Wolff SD, Balaban RS. Detection of Proton Chemical Exchange between Metabolites and Water in Biological Tissues. *Journal of Magnetic Resonance*, 1998;133(1):36–45. doi:10.1006/jmre.1998.1440
- [26] Zhou J, Payen JF, Wilson DA, Traystman RJ, van Zijl PCM. Using the amide proton signals of intracellular proteins and peptides to detect pH effects in MRI. *Nature Medicine*, 2003;9(8):1085–1090. doi:10.1038/nm907
- [27] Liu D, Zhou J, Xue R, Zuo Z, An J, Wang DJJ. Quantitative characterization of nuclear overhauser enhancement and amide proton transfer effects in the human brain at 7 tesla. *Magnetic Resonance in Medicine*, 2013;70(4):1070–1081. doi:10.1002/mrm.24560
- [28] Liepinsh E, Otting G. Proton exchange rates from amino acid side chains— implications for image contrast. *Magnetic Resonance in Medicine*, 1996;35(1):30–42. doi:10.1002/mrm.1910350106
- [29] Cai K, Haris M, Singh A, et al. Magnetic Resonance Imaging of Glutamate. *Nature medicine*, 2012;18(2):302–306. doi:10.1038/nm.2615
- [30] Jin T, Autio J, Obata T, Kim SG. Spin-locking versus chemical exchange saturation transfer MRI for investigating chemical exchange process between water and labile metabolite protons. *Magnetic Resonance in Medicine*, 2011;65(5):1448–1460. doi:10.1002/mrm.22721
- [31] Kogan F, Haris M, Singh A, et al. Method for high-resolution imaging of creatine in vivo using chemical exchange saturation transfer. *Magnetic Resonance in Medicine*, 2014;71(1):164–172. doi:10.1002/mrm.24641
- [32] Ling W, Eliav U, Navon G, Jerschow A. Chemical Exchange Saturation Transfer by Intermolecular Double Quantum Coherence. *Journal of magnetic resonance (San Diego, Calif. : 1997)*, 2008;194(1):29–32. doi:10.1016/j.jmr.2008.05.026
- [33] Grad J, Bryant RG. Nuclear magnetic cross-relaxation spectroscopy. *Journal of Magnetic Resonance (1969)*, 1990;90(1):1–8. doi:10.1016/0022-2364(90)90361-C
- [34] McMahon MT, Gilad AA, Zhou J, Sun PZ, Bulte JWM, Zijl PCMv. Quantifying exchange rates in chemical exchange saturation transfer agents using the saturation time and saturation power dependencies of the magnetization transfer effect on the magnetic resonance imaging signal (QUEST and QUESP): Ph calibration for poly-L-lysine and a starburst dendrimer. *Magnetic Resonance in Medicine*, 2006; 55(4):836–847. doi:10.1002/mrm.20818
- [35] McConnell HM. Reaction Rates by Nuclear Magnetic Resonance. *The Journal of Chemical Physics*, 1958;28(3):430. doi:10.1063/1.1744152

References

- [36] Ernst RR, Bodenhausen G, Wokaun A. *Principles of nuclear magnetic resonance in one and two dimensions*. The International series of monographs on chemistry 14. Clarendon Press ; Oxford University Press, Oxford [Oxfordshire] : New York, 1987. ISBN 978-0-19-855629-9
- [37] Trott O, Palmer AG. $R1\rho$ Relaxation outside of the Fast-Exchange Limit. *Journal of Magnetic Resonance*, 2002;154(1):157–160. doi:10.1006/jmre.2001.2466
- [38] Zaiss M, Bachert P. Exchange-dependent relaxation in the rotating frame for slow and intermediate exchange - modeling off-resonant spin-lock and chemical exchange saturation transfer. *NMR in Biomedicine*, 2013;26(5):507–518. doi:10.1002/nbm.2887
- [39] Zaiß M, Schmitt B, Bachert P. Quantitative separation of CEST effect from magnetization transfer and spillover effects by Lorentzian-line-fit analysis of z-spectra. *Journal of Magnetic Resonance*, 2011;211(2):149–155. doi:10.1016/j.jmr.2011.05.001
- [40] Zaiss M, Xu J, Goerke S, et al. Inverse Z-spectrum analysis for spillover-, MT-, and T1 -corrected steady-state pulsed CEST-MRI—application to pH-weighted MRI of acute stroke. *NMR in Biomedicine*, 2014;27(3):240–252. doi:10.1002/nbm.3054
- [41] Solomon I. Relaxation Processes in a System of Two Spins. *Physical Review*, 1955; 99(2):559–565. doi:10.1103/PhysRev.99.559
- [42] van Zijl PC, Zhou J, Mori N, Payen JF, Wilson D, Mori S. Mechanism of magnetization transfer during on-resonance water saturation. A new approach to detect mobile proteins, peptides, and lipids. *Magnetic Resonance in Medicine*, 2003; 49(3):440–449. doi:10.1002/mrm.10398
- [43] van Zijl PCM, Lam WW, Xu J, Knutsson L, Stanisz GJ. Magnetization Transfer Contrast and Chemical Exchange Saturation Transfer MRI. Features and analysis of the field-dependent saturation spectrum. *NeuroImage*, 2018;168:222–241. doi:10.1016/j.neuroimage.2017.04.045
- [44] Jin T, Kim SG. In vivo saturation transfer imaging of nuclear Overhauser effect from aromatic and aliphatic protons: implication to APT quantification. In *Proceedings of 2013 ISMRM & SMRT Annual Meeting & Exhibition (ISMRM 2013)*. United States, 2013;
- [45] Jones CK, Huang A, Xu J, et al. Nuclear Overhauser Enhancement (NOE) Imaging in the Human Brain at 7 T. *NeuroImage*, 2013;77. doi:10.1016/j.neuroimage.2013.03.047
- [46] Zaiss M, Windschuh J, Goerke S, et al. Downfield-NOE-suppressed amide-CEST-MRI at 7 Tesla provides a unique contrast in human glioblastoma. *Magnetic Resonance in Medicine*, 2017;77(1):196–208. doi:10.1002/mrm.26100

- [47] Edzes HT, Samulski ET. Cross relaxation and spin diffusion in the proton NMR of hydrated collagen. *Nature*, 1977;265(5594):521–523. doi:10.1038/265521a0
- [48] Wolff SD, Balaban RS. Magnetization transfer contrast (MTC) and tissue water proton relaxation in vivo. *Magnetic Resonance in Medicine*, 1989;10(1):135–144. doi:10.1002/mrm.1910100113
- [49] Henkelman RM, Huang X, Xiang QS, Stanisz GJ, Swanson SD, Bronskill MJ. Quantitative interpretation of magnetization transfer. *Magnetic Resonance in Medicine*, 1993;29(6):759–766. doi:10.1002/mrm.1910290607
- [50] Ceckler TL, Balaban RS. Tritium-proton magnetization transfer as a probe of cross relaxation in aqueous lipid bilayer suspensions. *Journal of Magnetic Resonance (1969)*, 1991;93(3):572–588. doi:10.1016/0022-2364(91)90084-7
- [51] Kucharczyk W, Macdonald PM, Stanisz GJ, Henkelman RM. Relaxivity and magnetization transfer of white matter lipids at MR imaging: importance of cerebroside and pH. *Radiology*, 1994;192(2):521–529. doi:10.1148/radiology.192.2.8029426
- [52] Henkelman RM, Stanisz GJ, Graham SJ. Magnetization transfer in MRI: a review. *NMR in Biomedicine*, 2001;14(2):57–64. doi:10.1002/nbm.683
- [53] Kwiatkowski G, Kozerke S. Accelerating CEST MRI in the mouse brain at 9.4 T by exploiting sparsity in the Z-spectrum domain. *NMR in Biomedicine*, 2020; 33(9):1–14. doi:10.1002/nbm.4360
- [54] Jin T, Kim SG. Advantages of chemical exchange-sensitive spin-lock (CESL) over chemical exchange saturation transfer (CEST) for hydroxyl- and amine-water proton exchange studies. *NMR in Biomedicine*, 2014;27(11):1313–1324. doi:10.1002/nbm.3191
- [55] Li Y, Chen H, Xu J, et al. CEST theranostics: label-free MR imaging of anticancer drugs. *Oncotarget*, 2016;7(6):6369–6378. doi:10.18632/oncotarget.7141
- [56] Chávez FV, Halle B. Molecular basis of water proton relaxation in gels and tissue. *Magnetic Resonance in Medicine*, 2006;56(1):73–81. doi:10.1002/mrm.20912
- [57] Herz K, Gandhi C, Schuppert M, Deshmane A, Scheffler K, Zaiss M. CEST imaging at 9.4 T using adjusted adiabatic spin-lock pulses for on- and off-resonant T1 ρ -dominated Z-spectrum acquisition. *Magnetic Resonance in Medicine*, 2019; 81(1):275–290. doi:10.1002/mrm.27380
- [58] Glang F, Fabian M, German A, et al. Linear projection-based CEST reconstruction: the simplest explainable AI. *Proceedings of 2021 ISMRM & SMRT Annual Meeting & Exhibition (ISMRM 2021)*, 2021;
- [59] Fabian MS, Glang F, Khakzar KM, et al. Reduction of 7T CEST scan time and evaluation by L1-regularised linear projections. *Proceedings of 2021 ISMRM &*

References

- SMRT Annual Meeting & Exhibition (ISMRM 2021)*, 2021;
- [60] Glang F, Fabian MS, German A, et al. Linear projection-based CEST parameter estimation. *NMR in Biomedicine*, 2022;pages 1–17. doi:10.1002/nbm.4697
- [61] Zaiss M, Ehses P, Scheffler K. Snapshot-CEST: Optimizing spiral-centric-reordered gradient echo acquisition for fast and robust 3D CEST MRI at 9.4 T. *NMR in Biomedicine*, 2018;31(4). doi:10.1002/nbm.3879
- [62] Stirnberg R, Huijbers W, Brenner D, Poser BA, Breteler M, Stöcker T. Rapid whole-brain resting-state fMRI at 3 T: Efficiency-optimized three-dimensional EPI versus repetition time-matched simultaneous-multi-slice EPI. *NeuroImage*, 2017; 163:81–92. doi:10.1016/j.neuroimage.2017.08.031
- [63] Jones CK, Polders D, Hua J, et al. In vivo three-dimensional whole-brain pulsed steady-state chemical exchange saturation transfer at 7 T. *Magnetic Resonance in Medicine*, 2012;67(6):1579–1589. doi:10.1002/mrm.23141
- [64] Cohen O, Huang S, McMahon MT, Rosen MS, Farrar CT. Rapid and quantitative chemical exchange saturation transfer (CEST) imaging with magnetic resonance fingerprinting (MRF). *Magnetic Resonance in Medicine*, 2018;80(6):2449–2463. doi:10.1002/mrm.27221
- [65] Breitling J, Deshmane A, Goerke S, et al. Adaptive denoising for chemical exchange saturation transfer MR imaging. *NMR in Biomedicine*, 2019;0(0):1–14. doi:10.1002/nbm.4133
- [66] Deshmane A, Zaiss M, Lindig T, et al. 3D gradient echo snapshot CEST MRI with low power saturation for human studies at 3T. *Magnetic Resonance in Medicine*, 2018;81(4). doi:10.1002/mrm.27569
- [67] Spencer RGS, Horska A, Ferretti JA, Weiss GH. Spillover and Incomplete Saturation in Kinetic Measurements. *Journal of Magnetic Resonance, Series B*, 1993; 101(3):294–296. doi:10.1006/jmrb.1993.1045
- [68] Layton KJ, Kroboth S, Jia F, et al. Pulseq: A rapid and hardware-independent pulse sequence prototyping framework. *Magnetic Resonance in Medicine*, 2017; 77(4):1544–1552. doi:/10.1002/mrm.26235
- [69] Mueller S, Herz K, Scheffler K, Zaiss M. Open source Pulseq interpreter for CEST MRI on Bruker systems. *Proceedings of 2021 ISMRM & SMRT Annual Meeting & Exhibition (ISMRM 2021)*, 2021;
- [70] Gillies RJ, Kinahan PE, Hricak H. Radiomics: Images Are More than Pictures, They Are Data. *Radiology*, 2016;278(2):563–577. doi:10.1148/radiol.2015151169
- [71] Loktyushin A, Herz K, Dang N, et al. MRzero - Automated discovery of MRI sequences using supervised learning. *Magnetic Resonance in Medicine*, 2021;

86(2):709–724. doi:10.1002/mrm.28727

- [72] Hansen N, Ostermeier A. Adapting arbitrary normal mutation distributions in evolution strategies: the covariance matrix adaptation. In *Proceedings of IEEE International Conference on Evolutionary Computation*. 1996; pages 312–317. doi:10.1109/ICEC.1996.542381
- [73] Rapin J, Teytaud O. Nevergrad - A gradient-free optimization platform, 2021
- [74] Jin KH, Unser M, Yi KM. Self-Supervised Deep Active Accelerated MRI. *arXiv:1901.04547 [cs]*, 2019;
- [75] Zhang Z, Romero A, Muckley MJ, Vincent P, Yang L, Drozdal M. Reducing Uncertainty in Undersampled MRI Reconstruction With Active Acquisition. In *2019 IEEE/CVF Conference on Computer Vision and Pattern Recognition (CVPR)*. 2019; pages 2049–2053. doi:10.1109/CVPR.2019.00215
- [76] Kober J, Bagnell JA, Peters J. Reinforcement learning in robotics: A survey. *The International Journal of Robotics Research*, 2013;32(11):1238–1274. doi:10.1177/0278364913495721
- [77] Mahadevan S, Connell J. Automatic programming of behavior-based robots using reinforcement learning. In *Proceedings of the ninth National conference on Artificial intelligence - Volume 2, AAAI'91*. AAAI Press, Anaheim, California. ISBN 978-0-262-51059-2, 1991; pages 768–773
- [78] Bagnell J, Schneider J. Autonomous helicopter control using reinforcement learning policy search methods. In *Proceedings 2001 ICRA. IEEE International Conference on Robotics and Automation (Cat. No.01CH37164)*, volume 2. 2001; pages 1615–1620 vol.2. doi:10.1109/ROBOT.2001.932842
- [79] Mueller S, Scheffler K, Zaiss M. On the interference from agar in chemical exchange saturation transfer MRI parameter optimization in model solutions. *NMR in Biomedicine*, 2020;34(1):1–12. doi:10.1002/nbm.4403
- [80] Zhu H, Jones CK, Zijl PCMV, Barker PB, Zhou J. Fast 3D chemical exchange saturation transfer (CEST) imaging of the human brain. *Magnetic Resonance in Medicine*, 2010;64(3):638–644. doi:10.1002/mrm.22546
- [81] Ellingson BM, Yao J, Raymond C, et al. pH-weighted molecular MRI in human traumatic brain injury (TBI) using amine proton chemical exchange saturation transfer echoplanar imaging (CEST EPI). *NeuroImage: Clinical*, 2019;22:1–11. doi:10.1016/j.nicl.2019.101736
- [82] Krishnamoorthy G, Nanga RPR, Bagga P, Hariharan H, Reddy R. High quality three-dimensional gagCEST imaging of in vivo human knee cartilage at 7 Tesla. *Magnetic Resonance in Medicine*, 2017;77(5):1866–1873. doi:10.1002/mrm.26265

References

- [83] Lam F, Liang ZP. A subspace approach to high-resolution spectroscopic imaging: High-Resolution Spectroscopic Imaging. *Magnetic Resonance in Medicine*, 2014; 71(4):1349–1357. doi:10.1002/mrm.25168
- [84] Ma C, Lam F, Ning Q, Johnson CL, Liang ZP. High-resolution ^1H -MRSI of the brain using short-TE SPICE. *Magnetic Resonance in Medicine*, 2017;77(2):467–479. doi:10.1002/mrm.26130
- [85] Lustig M, Donoho D, Pauly JM. Sparse MRI: The application of compressed sensing for rapid MR imaging. *Magnetic Resonance in Medicine*, 2007;58(6):1182–1195. doi:10.1002/mrm.21391
- [86] Xu X, Lee JS, Jerschow A. Ultrafast Scanning of Exchangeable Sites by NMR Spectroscopy. *Angewandte Chemie*, 2013;125(32):8439–8442. doi:10.1002/ange.201303255
- [87] Döpfert J, Zaiss M, Witte C, Schröder L. Ultrafast CEST imaging. *Journal of Magnetic Resonance*, 2014;243:47–53. doi:10.1016/j.jmr.2014.03.008
- [88] Zaiss M, Deshmane A, Schuppert M, et al. DeepCEST: 9.4 T Chemical exchange saturation transfer MRI contrast predicted from 3 T data – a proof of concept study. *Magnetic Resonance in Medicine*, 2019;81(6):3901–3914. doi:10.1002/mrm.27690
- [89] Van Rossum G, Drake FL. *Python 3 Reference Manual*. CreateSpace, 2009. ISBN 1-4414-1269-7
- [90] Pedregosa F, Varoquaux G, Gramfort A, et al. Scikit-learn: Machine Learning in Python. *Journal of Machine Learning Research*, 2011;12(85):2825–2830
- [91] Hastie T, Tibshirani R, Friedman JH. *The elements of statistical learning: data mining, inference, and prediction*. Springer series in statistics. Springer, New York, NY, 2. ed. edition, 2009. ISBN 978-0-387-84857-0
- [92] Mueller S, Glang F, Scheffler K, Zaiss M. pH mapping of brain tissue by a deep neural network trained on 9.4T CEST MRI data: pH-deepCEST. In *Proceedings of the 2020 International Society of Magnetic Resonance in Medicine*. 2020;
- [93] Moon RB, Richards JH. Determination of Intracellular pH by ^{31}P Magnetic Resonance. *Journal of Biological Chemistry*, 1973;248(20):7276–7278
- [94] Korzowski A, Weinfurtner N, Mueller S, et al. Volumetric mapping of intra- and extracellular pH in the human brain using ^{31}P MRSI at 7T. *Magnetic Resonance in Medicine*;84(4):1707–1723. doi:10.1002/mrm.28255
- [95] Zaiss M, Schuppert M, Deshmane A, et al. Chemical exchange saturation transfer mri contrast in the human brain at 9.4 T. *NeuroImage*, 2018;179:144–155. doi:10.1016/j.neuroimage.2018.06.026

Acknowledgments

There are many people to whom I am deeply grateful for their support. Without you, my Ph.D. would for sure not have been possible. Thanks a lot for all your input, patience and support! I would especially like to thank:

Moritz, for being way more than a supervisor as good as one could anyhow imagine. Your motivation, knowledge and patience are impressive and I am thankful that you gave me the opportunity to become part of the CEST team!

Everybody in the Kinderzimmer - you made me feel home from the very first day. Especially Felix, for numerous incredibly helpful discussions on physics, politics, arts, as well as for bicycle rides and sport sessions way longer than healthy. Dario for your patience for giving me insights into the heart of a 9.4T scanner, for all your insider tips for life in Tübingen and showing me the beauty of programming in C++. Kai for always helping me in case of questions on IDEA, Bloch simulations and how to handle the turtle. Praveen for your support with toolboxes and blobs of all kinds. Guys it was an honor, I hope we can continue this for a little longer.

I would like to thank all my colleagues at MPI, for creating an atmosphere that made me come to the institute everyday with pleasure.

Thank you Klaus for always having an open ear, even when it was CEST, and for providing us with both support and freedom for all our ideas.

And of course, I would like to thank all the others that I did not yet mention explicitly: Aaron, Anagha, Cihan, Edyta, Jörn, Jonas, Kengo, Mark, Nico, Nina, Ole, Paul, Remy, Rolf, and Tina.

Last but not least, I want to thank my family, for all your support that gave me the freedom to get to where I am today!

Erklärung / Declaration

Ich erkläre, dass ich die zur Promotion eingereichte Arbeit mit dem Titel:

Advances in Quantitative CEST MRI at 3T and 9.4T

selbständig verfasst, nur die angegebenen Quellen und Hilfsmittel benutzt und wörtlich oder inhaltlich übernommene Stellen als solche gekennzeichnet habe. Ich versichere an Eides statt, dass diese Angaben wahr sind und dass ich nichts verschwiegen habe. Mir ist bekannt, dass die falsche Abgabe einer Versicherung an Eides statt mit Freiheitsstrafe bis zu drei Jahren oder mit Geldstrafe bestraft wird.

I hereby declare that I have produced the work entitled:

Advances in Quantitative CEST MRI at 3T and 9.4T

submitted for the award of a doctorate, on my own (without external help), have used only the sources and aids indicated and have marked passages included from other works, whether verbatim or in content, as such. I swear upon oath that these statements are true and that I have not concealed anything. I am aware that making a false declaration under oath is punishable by a term of imprisonment of up to three years or by a fine.

Tübingen, den
Datum / Date

.....
Unterschrift / Signature